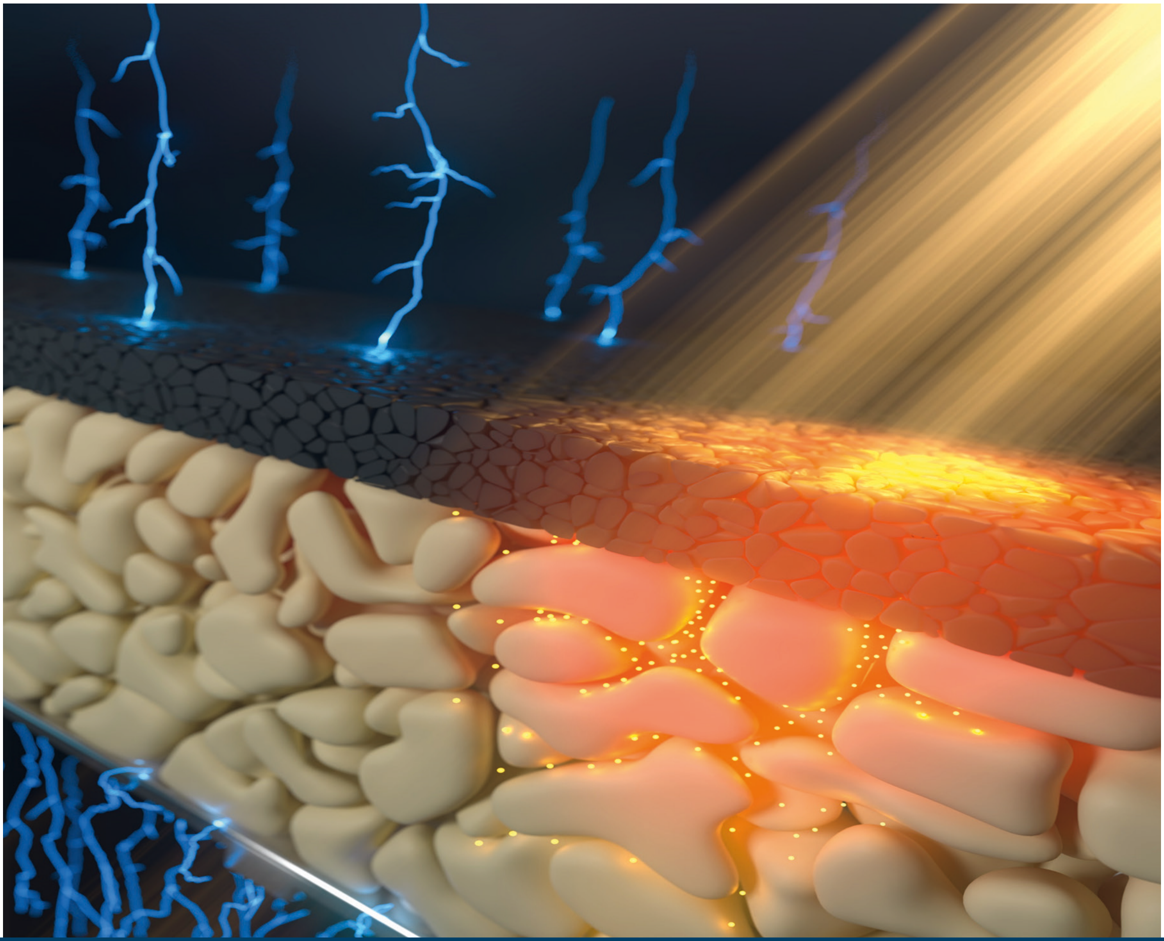

Photonic Sintering of Garnet-Based Solid-State Batteries

Walter Sebastian Scheld

Energie & Umwelt / Energy & Environment
Band / Volume 620
ISBN 978-3-95806-737-0

Mitglied der Helmholtz-Gemeinschaft

JÜLICH
Forschungszentrum

Schriften des Forschungszentrums Jülich
Reihe Energie & Umwelt / Energy & Environment Band / Volume 620

Forschungszentrum Jülich GmbH
Institut für Energie- und Klimaforschung (IEK)
Werkstoffsynthese und Herstellungsverfahren (IEK-1)

Photonic Sintering of Garnet-Based Solid-State Batteries

Walter Sebastian Scheld

Schriften des Forschungszentrums Jülich
Reihe Energie & Umwelt / Energy & Environment Band / Volume 620

ISSN 1866-1793 ISBN 978-3-95806-737-0

Bibliografische Information der Deutschen Nationalbibliothek.
Die Deutsche Nationalbibliothek verzeichnet diese Publikation in der
Deutschen Nationalbibliografie; detaillierte Bibliografische Daten
sind im Internet über http://dnb.d-nb.de abrufbar.

Herausgeber und Vertrieb: Forschungszentrum Jülich GmbH
Zentralbibliothek, Verlag
52425 Jülich
Tel.: +49 2461 61-5368
Fax: +49 2461 61-6103
zb-publikation@fz-juelich.de
www.fz-juelich.de/zb

Umschlaggestaltung: Grafische Medien, Forschungszentrum Jülich GmbH

Titelbild: The graphical cover of this dissertation was reproduced with permission from the cover picture of volume 33, issue 43 of Advanced Functional Materials, which belongs to the following publication: Walter Sebastian Scheld, Kwangnam Kim, Christian Schwab, Alexandra C. Moy, Shi-Kai Jiang, Markus Mann, Christian Dellen, Yoo Jung Sohn, Sandra Lobe, Martin Ihrig, Michael Gregory Danner, Chia-Yu Chang, Sven Uhlenbruck, Eric Wachsman, Bing Joe Hwang, Jeff Sakamoto, Liwen Wan, Brandon C. Wood, Martin Finsterbusch, Dina Fattakhova-Rohlfing: The Riddle of Dark LLZO: Cobalt Diffusion into the Garnet-based Separator of Solid-State Lithium Batteries. Advanced Functional Materials. 2023. Volume 33. Issue 43. 2302939. Copyright Wiley-VCH GmbH. Reproduced with permission.

Druck: Grafische Medien, Forschungszentrum Jülich GmbH

Schriften des Forschungszentrums Jülich
Reihe Energie & Umwelt / Energy & Environment, Band / Volume 620

D 464 (Diss. Duisburg-Essen, Univ., 2023)

ISSN 1866-1793
ISBN 978-3-95806-737-0

Vollständig frei verfügbar über das Publikationsportal des Forschungszentrums Jülich (JuSER)
unter www.fz-juelich.de/zb/openaccess.

Abstract

Ceramic solid-state batteries (SSBs) are attracting significant attention worldwide as an alternative to lithium-ion batteries (LIBs). As the organic electrolyte is replaced by a ceramic electrolyte, unprecedented cell-level safety, a greatly extended operating temperature range and a potentially high energy density are expected. Li-ion conductive oxide ceramics such as the garnet type $Li_7La_3Zr_2O_{12}$ (LLZO) are promising solid electrolytes for future lithium SSBs because they have sufficient ionic conductivity up to 1 mS cm^{-1} at room temperature that can be tuned by doping elements, can be processed in air, have a wide electrochemical stability window, and have a high stability to Li metal, enabling the use of Li metal anodes. The garnet material is usually obtained in form of powders. Therefore, a sintering step is required to densify the powder and achieve good contact at the various interfaces, which is critical for adequate electrochemical performance. However, the high sintering temperatures, which can exceed 1000 °C for garnet materials, lead to the interdiffusion of elements at the interface and the formation of undesirable secondary phases. In particular, most common cathode materials such as layered $LiCoO_2$ (LCO) and $LiNi_{1-x-y}Mn_xCo_yO_2$ (NMC) or spinel $LiMn_2O_4$ (LMO) are known to react with LLZO at temperatures as low as 400 °C to 600 °C to form resistive secondary phases that drastically degrade battery performance. Material degradation during processing could be avoided by kinetically controlling the sintering process and drastically shortening the sintering times. Apart from numerous undesirable material interactions, protracted sintering at high temperatures is also energy consuming and thus has a negative impact on production costs. New, fast, scalable, and energy-efficient sintering technologies need to be explored to demonstrate viable manufacturing routes for oxide-ceramic batteries.

The objective of this work was to investigate the suitability of radiation-based sintering processes for sintering garnet-based battery components. Radiation-based sintering (photonic sintering) such as rapid thermal processing (RTP) and laser sintering are non-contact processes that combine extremely high heating rates with short exposure times to selectively sinter the surface of a sample. The light sources can range from high-power lamps and flash lamps to lasers. Radiation-based sintering and annealing processes are commercialized and well-established for inorganic thin films, but have not been investigated for ceramic garnet-based battery components, yet.

Sintering ceramic electrode layers directly on metal substrates, which serve as current collectors or housing, is advantageous for various battery designs. However, the low oxidation stability of metals and their relatively low melting temperatures often lead to the formation of passivation oxide layers, chemical reactions with electrode materials, or substrate melting during conventional sintering. To overcome these processing challenges, RTP in a lamp furnace with heating rates up to 1200 K min^{-1} was used, which enabled LCO cathodes to be sintered in a very short time of only 90 s, resulting in homogenous, electrochemically active, dense layers with small amounts of secondary phases. In contrast, pure LLZO films did not sinter during RTP processing and showed minor impurities of the $La_2Zr_2O_7$ pyrochlore phase. The presence of the pyrochlore phase was attributed to the formation of oxides on the steel substrate, since the LLZO layer was more stable in an Ar atmosphere than in air. Accordingly, the composite cathode layers containing LCO and LLZO showed a high reactivity in the RTP process with high amounts of side phases and insufficient sintering.

To overcome the material incompatibility during sintering of LCO-LLZO composite cathodes on steel substrates and to mitigate the formation of secondary phases, laser sintering was investigated as an alternative sintering technique. It was shown that laser irradiation enables selective sintering of ceramic cathodes layers within a few milliseconds of interaction time, while heating the substrate significantly less, thus minimizing the substrate oxidation. Laser sintering produces homogenous, porous composite cathodes with low secondary phase formation. Due to the porous structure of the sintered cathode, infiltration of polymer electrolyte for battery testing was possible. Laser sintering allows the processing of ceramic battery materials on substrates with low thermal stability, thus opening the way to many new material combinations and process routes for cell fabrication.

In addition to sintering of thin films on metal substrates, the suitability of radiation-based sintering processes for the fabrication of all-ceramic cells was investigated. For this purpose, LCO-LLZO composite cathodes were sintered on LLZO separators using RTP. The RTP parameters were optimized to produce mechanically stable and phase-pure ceramic half cells. In a total processing time of 15 min, phase-pure, electrochemically active cathodes could be produced. Compared to several hours required for conventional sintering, this process significantly reduces the overall production time. The resulting composite cathode microstructure had a relative density of 85% and was well bound to the LLZO separator. After attaching an indium anode, the cells could be electrochemically cycled. Considering these properties, RTP shows to be a good alternative to the conventional time-consuming sintering process for ceramic SSBs.

The chemical processes between the composite LCO-LLZO cathode and the LLZO separator are less studied compared to the material interaction in the composite cathodes, and little is known about their effect on the battery performance. Therefore, the RTP sintered half-cells were used to study the diffusion of Co-ions within the LLZO separator, which leads to the often-observed LLZO darkening. It was demonstrated that the Co-ion diffusion has a significant impact on ionic conductivity, electronic conductivity, and dendrite stability of the separator. Experimental data coupled with large-scale molecular dynamics simulations uncovered the diffusion mechanism for Co-ions and identified secondary phases that form during these interactions. In addition to extensive Co-ion diffusion within the grains, a non-uniform segregation of Co-ions at the grain boundaries was found with the formation of three distinct Co-containing phases. These results provide a general approach to investigate the basic ion diffusion processes that occur during the fabrication of oxide SSBs in order to find potential preventive strategies.

Kurzfassung

Keramische Festkörperbatterien (SSB) erregen als Alternative zu Lithium-Ionen-Batterien (LIB) weltweit große Aufmerksamkeit. Durch den Austausch des flüssigen organischen Elektrolyten durch einen keramischen Elektrolyten, wird eine noch nie dagewesene Sicherheit auf Zellebene, ein breiterer Betriebstemperaturbereich und eine höhere Energiedichte erwartet. Li-Ionen-leitfähige Oxidkeramiken wie der Granattyp $Li_7La_3Zr_2O_{12}$ (LLZO) sind vielversprechende Festkörperelektrolyte für künftige Lithium-SSBs. Diese können in Luft verarbeitet werden und besitzen ein breites elektrochemisches Stabilitätsfenster und eine hohe Stabilität gegenüber Li-Metall, was die Verwendung von Li-Metall-Anoden ermöglicht. Außerdem weisen sie bei Raumtemperatur eine ausreichende Ionenleitfähigkeit von bis zu 1 $mS\ cm^{-1}$ auf, welche durch Elementdotierung beeinflusst werden kann. Das Granatmaterial wird normalerweise in Form von Pulvern gewonnen. Daher ist ein Sinterungsschritt erforderlich, um das Pulver zu verdichten und einen guten Kontakt an den verschiedenen Grenzflächen zu erreichen, was für eine hohe elektrochemische Leistung entscheidend ist. Die hohen Sintertemperaturen, die bei Granatwerkstoffen über 1000 °C liegen können, führen jedoch zur Interdiffusion von Elementen an der Grenzfläche und zur Bildung unerwünschter Sekundärphasen. Es ist bekannt, dass die meisten gängigen Kathodenmaterialien wie die Schichtstrukturen $LiCoO_2$ (LCO) und $LiNi_{1-x-y}Mn_xCo_yO_2$ (NMC) oder das Manganspinell $LiMn_2O_4$ (LMO) bereits bei Temperaturen von 400 °C bis 600 °C mit LLZO reagieren und Sekundärphasen bilden, die die Batterieleistung drastisch durch hohe Widerstände beeinträchtigen. Die Materialdegradation während der Verarbeitung könnte durch eine kinetische Steuerung des Sinterprozesses und einer drastischen Verkürzung der Sinterzeiten vermieden werden. Abgesehen von den zahlreichen unerwünschten Materialwechselwirkungen ist eine langwierige Sinterung bei hohen Temperaturen energieaufwendig und wirkt sich somit negativ auf die Produktionskosten aus. Neue, schnelle, skalierbare und energieeffiziente Sintertechnologien müssen erforscht werden, um praktikable Herstellungswege für oxidkeramische Batterien aufzuzeigen.

Ziel dieser Arbeit war es, die Eignung von strahlungsbasierten Sinterverfahren für das Sintern von Batteriekomponenten auf Granatbasis zu untersuchen. Strahlungsbasierte Sinterverfahren (photonisches Sintern) wie Rapid Thermal Processing (RTP) und Lasersintern sind berührungsfreie Verfahren, die extrem hohe Heizraten mit kurzen Belichtungszeiten kombinieren, um die Oberfläche einer Probe zu sintern. Die Lichtquellen können von herkömmlichen Hochleistungslampen und Blitzlampen bis hin zu Lasern reichen. Strahlungsbasierte Sinter- und Glühverfahren sind für anorganische Dünnschichten kommerziell verfügbar und gut etabliert, wurden aber bisher nicht für keramische Batteriekomponenten auf Granatbasis untersucht.

Das Sintern von keramischen Elektrodenschichten direkt auf Metallsubstrate, welche als Stromsammler oder Gehäuse dienen, ist für verschiedene Batteriekonzepte von Vorteil. Jedoch führen die geringe Oxidationsstabilität von Metallen und deren relativ niedrige Schmelztemperatur häufig zur Bildung von Passivierungsoxidschichten, zu chemischen Reaktionen mit Elektrodenmaterialien oder zum Schmelzen des Substrats während des herkömmlichen Sinterns. Zur Überwindung dieser Prozessierungsherausforderung wurde RTP in einem Lampenofen mit Heizraten von bis zu 1200 K min^{-1} eingesetzt, wodurch LCO-Kathoden in einer sehr kurzen Zeit von nur 90 s gesintert werden konnten. Dies führte zu homogenen, elektrochemisch aktiven, dichten Schichten mit geringen Mengen an Sekundärphasen. Im Gegensatz dazu sinterten reine LLZO-Schichten während der RTP Verarbeitung nicht und wiesen geringe Verunreinigungen der Pyrochlorphase $La_2Zr_2O_7$ auf. Das Vorhandensein der Pyrochlorphase wurde auf die Bildung von Oxiden auf dem Stahlsubstrat zurückgeführt, da die LLZO-Schicht in einer Ar-Atmosphäre stabiler war als in Luft. Dementsprechend zeigten die zusammengesetzten Kathodenschichten, die LCO und LLZO enthielten, eine hohe Reaktivität im RTP-Prozess mit hohem Nebenphasenanteil und unzureichender Sinterung.

Um die Materialinkompatibilität während des Sinterns von LCO-LLZO-Kompositkathoden auf Stahlsubstraten zu überwinden und die Bildung von Nebenphasen zu vermindern, wurde Lasersintern als alternative Sintertechnik untersucht. Es wurde gezeigt, dass die Laserbestrahlung ein selektives Sintern der keramischen Kathodenschichten mit einer Interaktionszeit von wenigen Millisekunden ermöglichte, während das Substrat deutlich weniger erhitzt wurde und so dessen Oxidation minimiert werden konnte. Durch das Lasersintern entstanden homogene, poröse Kompositkathoden mit geringer Sekundärphasenbildung. Aufgrund der porösen Struktur der gesinterten Kathode war die Infiltration mit Polymerelektrolyt für Batterietests möglich. Das Lasersintern ermöglichte somit die Verarbeitung von keramischen Batteriematerialien auf Substraten mit geringer thermischer Stabilität und eröffnet damit den Weg zu vielen neuen Materialkombinationen und Prozessrouten für die Zellherstellung.

Neben dem Sintern von Dünnschichten auf Metallsubstraten wurde die Eignung von strahlungsbasierten Sinterverfahren für die Herstellung von vollkeramischen Zellen untersucht. Zu diesem Zweck wurden mittels RTP LCO-LLZO-Kompositkathoden auf LLZO-Separatoren gesintert. Die RTP-Parameter wurden optimiert, um mechanisch stabile und phasenreine keramische Halbzellen herzustellen. In einer Gesamtbearbeitungszeit von 15 min konnten phasenreine, elektrochemisch aktive Kathoden hergestellt werden. Im Vergleich zu einer Bearbeitungszeit von mehreren Stunden, die für das herkömmliche Sintern benötigt wird, verkürzt dieses Verfahren die Gesamtproduktionszeit erheblich. Die resultierende Mikrostruktur der Kompositkathode hatte eine relative Dichte von 85% mit einhergehendem Verbund der Kathoden|Separator Grenzfläche. Nach dem Anbringen einer Indiumanode konnten die Zellen elektrochemisch zykliert werden. In Anbetracht dieser Eigenschaften erweist sich die RTP Prozessierung als eine gute Alternative zum herkömmlichen zeitaufwändigen Sinterverfahren für keramische SSBs.

Die chemischen Prozesse zwischen der LCO-LLZO-Kompositkathode und dem LLZO-Separator sind im Vergleich zu den Materialinteraktionen innerhalb der Kompositkathode weniger gut untersucht, und es ist wenig über ihre Auswirkungen auf die Batterieleistung bekannt. Daher wurden die gesinterten RTP-Halbzellen verwendet, um die Diffusion von Co-Ionen innerhalb des LLZO-Separators zu untersuchen, welche zu der häufig beobachteten LLZO-Verdunkelung führt. Es konnte gezeigt werden, dass die Co-Ionendiffusion einen erheblichen Einfluss auf die Ionenleitfähigkeit, die elektronische Leitfähigkeit und die Dendritenstabilität des Separators hat. Mithilfe von experimentellen Daten in Verbindung mit Molekulardynamiksimulationen konnte der Diffusionsmechanismus der Co-Ionen aufgeklärt werden und Sekundärphasen, die sich während dieser Wechselwirkungen bilden, identifiziert werden. Zusätzlich zur ausgeprägten Co-Ionen-Diffusion innerhalb der Körner wurde eine ungleichmäßige Segregation von Co-Ionen an den Korngrenzen mit der Bildung von drei verschiedenen Co-haltigen Phasen festgestellt. Diese Ergebnisse bieten einen allgemeinen Ansatz zur Untersuchung der grundlegenden Ionendiffusionsprozesse bei der Herstellung von oxidischen SSBs, und können genutzt werden um potenzielle Präventionsstrategien zu finden.

List of Abbreviations

AC	Alternating current
AE	Auger electron
ALD	Atomic layer deposition
BSE	Backscattered electrons
CAM	Cathode active material
CCD	Critical current density
c-LLZO	Cubic lithium lanthanum zirconium oxide
Conv.	Conventional sintering
CV	Cyclic voltammetry
DC	Direct current
EDS	Energy-dispersive X-ray spectroscopy
EIS	Electrochemical impedance spectroscopy
EN	European standard
FAST/SPS	Field assisted sintering technique/spark plasma sintering
FLA	Flash lamp annealing
GB	Grain boundary
GCPL	Galvanostatic cycling with potential limitation
HOMO	Highest occupied molecular orbital
HT	High temperature
ICDD	International centre for diffraction data
ILT	Fraunhofer institute for laser technology
ITO	Indium thin oxide ($(In_2O_3)_{0.9}\cdot(SnO_2)_{0.1}$)
LCO	Lithium cobalt oxide ($LiCoO_2$)
LFP	Lithium iron phosphate ($LiFePO_4$)
LIB	Lithium-ion battery
LIPON	Lithium phosphorus oxynitride (Li_2PO_2N)
LiTFSI	Lithium bis(trifluoromethanesulfonyl)imide ($LiC_2F_6NO_4S_2$)
LLZO	Lithium lanthanum zirconium oxide ($Li_7La_3Zr_2O_{12}$)
LLZO:Al	Lithium lanthanum zirconium oxide with Al substitution

LLZO:Nb	Lithium lanthanum zirconium oxide with Nb substitution
LLZO:Ta	Lithium lanthanum zirconium oxide with Ta substitution
LLZO:Ta-Al	Lithium lanthanum zirconium oxide with Al, Ta co-substitution
LMO	Lithium manganese oxide ($LiMnO_2$)
LNMO	Lithium nickel manganese oxide ($LiNi_{0.5}Mn_{1.5}O_4$)
LSV	Linear sweep voltammetry
LT-LLZO	Low temperature cubic lithium lanthanum zirconium oxide
LTO	Lithium titanate ($Li_4Ti_5O_{12}$)
LUMO	Lowest unoccupied molecular orbital
MD	Molecular dynamic
MSD	Mean squared displacement
n.a.	Not availabe
NaSICON	(**Na**) **S**uper **I**onic **CON**ductor
NIR	Near-infrared
NMC	Lithium nickel manganese cobalt oxide ($LiNi_{1-x-y}Mn_xCo_yO_2$)
NMC811	Lithium nickel manganese cobalt oxide ($LiNi_{0.8}Mn_{0.1}Co_{0.1}O_2$)
OCV	Open circuit voltage
PAN	Poly(acrylonitrile) ($(C_3H_3N)_n$)
PEC	Poly(ethylene carbonate) ($(C_{39}H_{32}O_7)_n$)
PEO	Poly(ethylene oxide) ($C_{2n}H_{4n+2}O_{n+1}$)
PLD	Pulsed layer deposition
PVDF	Poly(vinylidene fluoride) ($(C_2H_2F_2)_n$)
Ref.	Literature reference
RF	Radio frequency
RTP	Rapid thermal processing
RT	Room temperature
SE	Solid electrolyte
SEI	Solid electrolyte interphase
SEL	Secondary electron
SEM	Scanning electron microscope
SHE	Standard hydrogen electrode

SIMS	Secondary ion mass spectrometry
SoC	State of charge
SSB	Solid-state battery
t-LLZO	Tetragonal lithium lanthanum zirconium oxide
ToF	Time of flight
UHS	Ultra-fast high-temperature sintering
UV	Ultraviolet radiation
Vis	Visible spectra of electromagnetic radiation
vol.-%	Volume percentage
wt%	Weight percentage
XPS	X-ray photoelectron spectroscopy
XRD	X-ray crystallography

Table of contents

1 Motivation

Batteries are essential in almost all aspects of our daily lifes, from small portable electronic and medical devices to large-scale applications such as electromobility or stationary energy storage in power grids [1-4]. Among the available battery systems, lithium-ion batteries (LIBs) have the highest energy density and longest cycle life, making them the dominant energy storage technology for portable electronic devices and electromobility [1-5]. A major advantage of lithium batteries comes from the physical properties of Li itself, with the most negative potential and the lowest molar mass among known battery materials, resulting in the highest available specific storage capacity of electrode materials [6, 7]. LIBs achieve high practical energy densities close to the theoretical limit, which are accomplished by the continuous improvement of battery materials and the optimization of manufacturing and stacking processes [8, 9]. Despite this already excellent performance, the ever-increasing demands of applications require even higher energy densities, which are however already coming close to the theoretical limit in the LIB technology. Further increase in energy density is limited not only by the storage capacity of the active electrode materials but also by their stability in the liquid organic electrolytes used in the modern LIBs. In particular, the flammability of organic electrolytes and their limited electrochemical stability window leading to possible reactions with the battery materials pose major thermodynamic limitation and safety concerns [10].

On the way to batteries with higher energy densities, the transition from liquid to solid electrolytes leading to solid-state batteries (SSB) is considered as one of the promising options that is receiving much attention in current battery research [11]. SSBs have the potential to overtake conventional LIBs in terms of energy storage capacity, temperature operating range, and especially safety characteristics [11-14]. One of the most intensively studied classes of solid-state electrolytes is the garnet $Li_7La_3Zr_2O_{12}$ (LLZO). LLZO is a ceramic material with a sufficiently high Li-ion conductivity, a wide electrochemical stability window, and a particularly high reduction stability that allows the use of Li metal anodes [11-22]. Eventually, LLZO is expected to completely replace the liquid electrolyte in LIBs. The appropriate cell architecture is supposed to mimic that of conventional LIBs with a thick three-dimensional composite cathode consisting of a cathode active material (CAM) with LLZO [18, 22-27], an LLZO separator processed as a dense layer [22, 24, 25, 27-29], and a Li metal anode. The technical difficulty in the practical implementation of a ceramic SSB design is that LLZO is processed as a ceramic powder that requires high sintering temperatures above 1000 °C for sufficient contact between particles [15, 20, 30-35]. Conventional sintering methods used for laboratory-scale production of garnet-based batteries are often very time and energy consuming, while large-scale production methods have not yet been developed [36, 37]. New, fast, scalable sintering technologies that shorten fabrication time and reduce energy consumption need to be explored to make ceramic SSBs competitive.

Furthermore, the material challenge in high-temperature sintering is that at the temperatures required for LLZO densification, undesirable chemical reactions with different battery components occur, leading to material degradation and even a complete loss of electrochemical activity. For example, during sintering of CAM-LLZO composite cathodes, most CAMs react with LLZO and form high-resistance secondary phases that degrade battery performance [38-42]. So far $LiCoO_2$ (LCO) is one of the most suitable CAM for composite cathodes in garnet-based SSBs [22, 23, 25, 26, 41], which is due to its high thermal stability with LLZO of up to 1050 °C [25, 38, 40, 41]. However various secondary phases have also been found for the LCO-LLZO system [25, 38, 41, 43-45]. In addition to the CAM, the metallic current collectors are also very sensitive to sintering conditions, as they oxidize and react with battery materials when exposed to high temperatures for extended periods of time [43, 46]. The material stability would also benefit greatly from sintering techniques that allow selective heating over a very short period of time.

An approach that has great potential to reduce unwanted reactions by drastically shortening sintering time is photonic sintering. Photonic sintering is a collective term for various non-contact processes in which the sample is heated by a radiation source. Due to the high heating rates that can be achieved, the total heating time can be reduced drastically, that is to a few minutes or even seconds, compared to several hours for a conventional sintering process. Photonic sintering is suitable for highly absorbing materials, particularly for thin layers up to ~100 µm. For such layers, energy transfer is more efficient than for thicker geometries of hundreds of µm, where large temperature gradients can cause cracking or spalling in the material. Because of their selectivity and very short processing time, photonic sintering techniques are broadly used on an industrial scale for a variety of processes such as printed electrode processing in solar cell production [47] or semiconductor wafer processing [48], but they have not yet been tested for sintering garnet-containing battery components.

One attractive photonic sintering technique is laser sintering, which has become a successful commercial process for the selective sintering of numerous materials since it was first described in 1975 [48]. In laser sintering, a sample is moved under a laser beam resulting in short interaction times. This way, the heat generated by the absorption of the laser radiation (which depends on the optical properties of the material and the laser wavelength) is mainly transferred to the processed layer, while the underlying materials are not strongly affected, avoiding possible temperature-induced reactions with the substrate [49].

Another interesting technique is rapid thermal processing (RTP). In this process, layers are heated by absorption of light in a quartz-lined furnace with lamps from all sides and high heating rates of up to 100 $K\ s^{-1}$. As with photonic sintering, this non-contact rapid heating of flat layers from one or both sides can be used to reduce unwanted diffusion and/or side reactions by dramatically shortening the processing time.

To investigate the suitability of laser sintering and rapid thermal processing for sintering garnet-based ceramic components, two different battery designs were examined in this work. In the metal-supported battery design, the electrode layers were printed on steel substrates and sintered using RTP or laser sintering. The steel substrate acts as a current collector and provides mechanical support for the ceramic layer [46].

In the second concept, an electrolyte-supported design was investigated in which electrode layers were screen printed on dense LLZO pellets to fabricate all-ceramic SSBs. In this approach, the cathodes were sintered with RTP only, followed by a detailed analysis of ion diffusion in the separator itself. The screen-printing method stands out for its easily adjustable and larger layer thickness, simplicity and low cost, making it suitable for large-scale industrial applications [50-52].

2 Theoretical background

2.1 Electrochemical energy storage in batteries

In a battery, electrical energy is stored by a conversion to chemical energy in the electrode materials. In the electrochemical cell, ion transport between the electrodes takes place *via* the electrolyte, which must have ionic conductivity but at the same time be electrically insulating to prevent self-discharge. Electron transport occurs *via* an external circuit with current collectors at both electrodes. The redox reactions that take place at the electrodes can be reversible or irreversible. In primary batteries, irreversible redox reactions occur when the battery is discharged, while secondary batteries can be charged and discharged multiple times due to reversible redox reactions [53]. Examples of secondary battery types (Figure 2.1) are Ni-Cd, Ni-metal hydride, lead-acid and Li-ion battery (LIB).

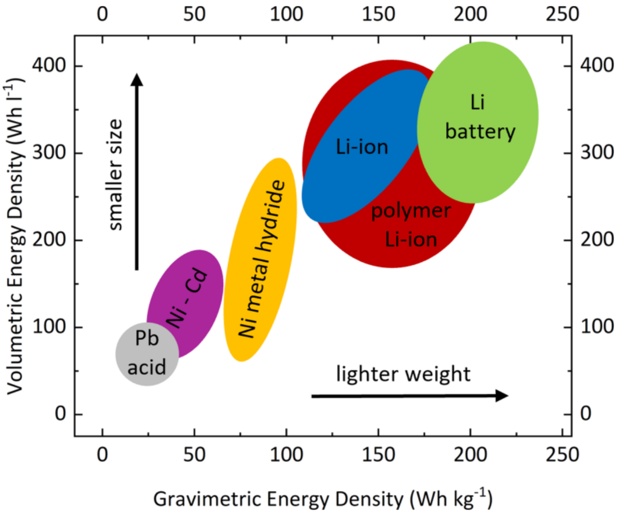

Figure 2.1: Collection of battery technologies in terms of volumetric and gravimetric energy density. Reproduced from [5] with permission from Springer Nature.

The LIB, which was introduced to the market by Sony in 1991, has the best characteristics in terms of operating voltage, energy density, absence of memory effect, low self-discharge, and operating temperature range [54, 55]. Commercial LIBs are based on a liquid organic electrolyte with dissolved Li salts for ionic conductivity (typically $LiPF_6$ in a mixture of propylene carbonate and diethyl carbonate), a graphite anode, and a porous cathode layer containing lithium metal oxides or lithium metal phosphates as CAMs. The electrodes are spatially and electrically separated from each other by a porous separator filled with an organic electrolyte. Electrical contact is made by current collectors, usually Al for the cathode side and Cu for the anode side. The schematic of a LIB is shown in Figure 2.2 [46, 54-57].

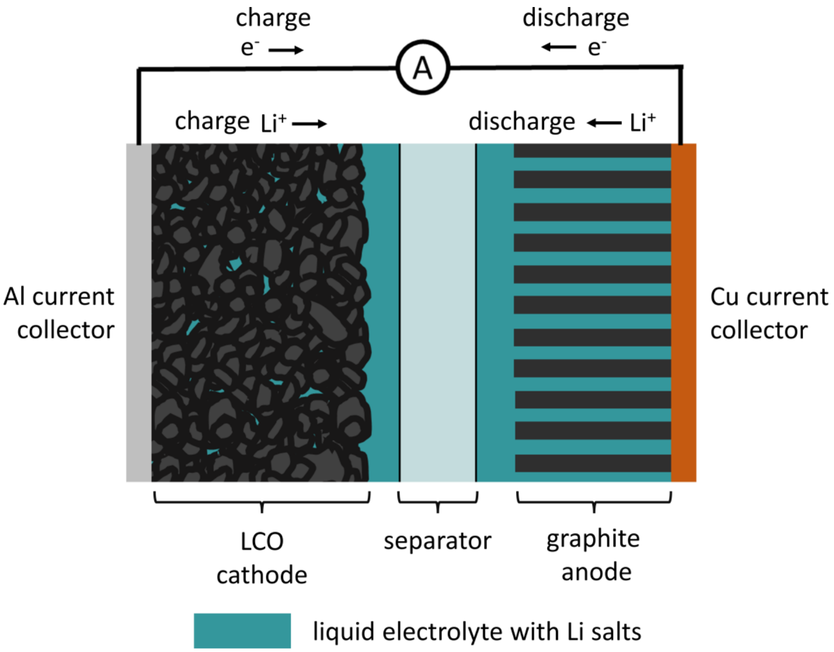

Figure 2.2: Schematic representation of a LIB with cathode, separator and anode, as well as current collectors and external circuit [46, 54-57].

LCO is one of the oldest CAMs used in the first generation of LIBs and is still widely used in modern batteries. In a battery operating with LCO as the CAM, the following reactions take place at the electrodes during discharge (Equation 2.1 to Equation 2.3) [8, 58].

Anode	$x \cdot LiC_6 \rightleftharpoons x \cdot C_6 + x \cdot Li^+ + x \cdot e^-$	Equation 2.1
Cathode	$Li_{1-x}CoO_2 + x \cdot Li^+ + x \cdot e^- \rightleftharpoons LiCoO_2$	Equation 2.2
Cell reaction	$Li_{1-x}CoO_2 + x \cdot Li^+ \rightleftharpoons LiCoO_2$	Equation 2.3

Graphite and LCO belong to the intercalation type electrode with a layered structure in which covalently bond layers containing redox active atoms are connected by van der Waals forces. The Li-ions can be intercalated or deintercalated from the van der Waals gaps during charge and discharge without significantly changing the crystal structure [8, 58].

The driving force for this energy conversion is the change in Gibbs free energy (standard reaction energy) ΔG^0 during the electrode reactions. Using the relationship from Equation 2.4, this energy can be calculated for the conversion of one mole of an electrode material to the corresponding electrode reaction product with the electrochemical equivalent z, E^0 as the standard cell potential, and the Faraday constant F (product of the Avogadro constant N_A and the elementary charge e) [59].

$$\Delta G^0 = -z\,F\,E^0 \qquad \text{Equation 2.4}$$

A positive cell potential corresponds to a negative free reaction energy, so that the products of the electrode reaction are formed spontaneously. If the potential is negative, the reaction is reversed and the starting materials are formed again. The standard cell potential can be calculated from the difference in the standard electrode potentials of anode and cathode (Equation 2.5) [59].

$$E^0 = E^0_{(\text{Kathode})} - E^0_{(\text{Anode})} \qquad \text{Equation 2.5}$$

The change of the Gibbs free energy per concentration of the respective species c_i determines the individual chemical potentials μ_i of these species (Equation 2.6) [60].

$$\mu_i = \frac{\partial G}{\partial c_i} \qquad \text{Equation 2.6}$$

Using the chemical potentials of both electrodes, the open circuit voltage (OCV), the potential between two electrical poles in an open circuit, can be calculated (Equation 2.7) [61].

$$U_o = -\frac{\mu_{\text{cathode}} - \mu_{\text{anode}}}{z\,F} \qquad \text{Equation 2.7}$$

The mass of the electrode material together with the charge transferred per mass gives the capacity C of an electrode. Using the molecular mass M_m, the number of electrons transferred per mole of the material z, and the Faraday constant F, the theoretical gravimetric capacity C_{grav} of the electrode material can be calculated (Equation 2.8) [62].

$$C_{\text{grav}} = \frac{z\,F}{M_m} \qquad \text{Equation 2.8}$$

The capacity of a battery is mainly limited by the capacity of the cathode, as it is generally much lower than the capacity of the anode. In addition to the gravimetric capacity, it is also possible to specify the electrode materials by their volumetric capacity C_{vol}, which is the product of the gravimetric capacity and the material density. When thin film electrodes are used, the gravimetric capacity is usually multiplied by the density of the thin film and normalized to an electrode area of 1 cm^2 and a film thickness of 1 µm to compare different electrodes.

The specific capacity C_{spec} indicates the total capacity of the active materials of the battery without considering other non-active components. Together with the standard potential of a material E^0 or the open circuit voltage U_o of the cell, the energy density ρ_E of the material or the cell, can be calculated (Equation 2.9) [63].

$$\rho_E = C_{\text{spec}}\ U_o \qquad \text{Equation 2.9}$$

The energy density can also be specified gravimetrically or volumetrically. The state of charge (SoC) is measured as a fraction of full capacity, where 100% SoC stands for a fully charged battery, and 0% SoC stands for a fully discharged battery [64].

2.2 Lithium solid-state batteries

As discussed in the Motivation section, the replacement of liquid organic electrolytes with solid electrolytes resulting in solid-state batteries (SSB) is one of the promising battery concepts that has received much attention. An important advantage of solid electrolytes (SEs) is their lower flammability and often lower toxicity, which minimizes safety concerns [6, 7, 11, 65]. Furthermore, many SEs exhibit higher reduction stability to lithium metal, which allows the use of Li metal anodes. For this reason, SSBs can be expected to deliver much higher theoretical cell energy densities of up to ~400 Wh kg^{-1} and ~800 Wh l^{-1}, compared to 260 Wh kg^{-1} and 770 Wh l^{-1} for modern LIBs [11, 65]. Other expected advantages of SEs include a high transference number and thus no concentration polarization at high powers in the electrolytes, and a much wider operating temperature range [32, 66-68]. However, the ionic conductivity of many SEs is still lower than that of liquid electrolytes at about 10^{-2} S cm^{-1} [69]. Moreover, SEs often require more complex processing to achieve highly conducting interfaces [17, 70-73]. Nevertheless, as the research on solid-state batteries continues to evolve, improvements in conductivity are constantly being achieved through material developments and new process engineering approaches [1, 8, 10, 66, 70, 74-77].

2.2.1 Solid electrolytes

There are major differences between various solid-state batteries, which depend on the choice of SEs. Different electrolytes have different physical and chemical properties and therefore require different processing methods. The four main SE classes are oxides, sulfides, halides, and polymers [17, 70-73, 78-82]. The polymer electrolytes are the only class of SE that requires an addition of Li salts for ionic conductivity. The most common polymer electrolytes are poly(ethylene oxide) (PEO), poly(vinylidene fluoride) (PVDF), poly(acrylonitrile) (PAN), and poly(ethylene carbonate) (PEC) [83]. The most common inorganic SEs are garnets, perovskites, antiperovskites, Na-superionic-conductors (so called NASICON), sulfides, argyrodites, lithium nitrides, lithium phosphorus oxynitrides (so called LIPON), and halides. The basic properties of these SEs are summarized in Table 2.1 [17, 70-73, 78-82].

Table 2.1: Major classes of inorganic SEs with their basic molecular formulas, ionic conductivity, electrochemical window, and some specific remarks [17, 70-73, 82].

Material class	Composition[a, b]	Ionic conductivity[c] (S cm^{-1})	Electro-chemical window[d]	Specific remarks
Garnet	$Li_7La_3ZrO_{12}$	$10^{-4} - 10^{-3}$	0.0 – 3.6	Processable in air, formation of Li_2CO_3 on the surface, stable with Li^0
Perovskite	$Li_{3X}La_{2/3-x}TiO_3$	$10^{-5} - 10^{-4}$	1.0 – 4.5	High grain boundary resistance
Antiperovskite	Li_3OX	$10^{-4} - 10^{-2}$	> 6.0	Hygroscopic
NASICON	$LiTi_2(PO_4)_3$	$10^{-4} - 10^{-2}$	> 2.5	Low reduction stability, reaction with Li metal
Sulfide	Li_4GeS_4 $Li_{10}GeP_2S_{12}$ Li_2S-P_2S_5	$10^{-5} - 10^{-2}$	1.6 – 2.5	Unstable in air, H_2S formation
Argyrodite	Li_6PS_5X	$10^{-7} - 10^{-3}$	0.0 – 0.7	Unstable in air, H_2S formation
Lithium nitride	Li_3N	$10^{-7} - 10^{-4}$	1.7 – 2.8	Electrochemically unstable
LIPON	Li_2PO_2N	10^{-6}	0.0 – 4.1	Low ionic conductivity
Halide	Li_3MX_6, $LiMX_4$	$> 10^{-3}$	0.5 – 7.0	Unstable in air

[a] M = Y, Al, Ga, In, Sc, Er, Ho, Zr, Fe, La

[b] X= Cl, Br, I

[c] represents the ionic conductivity of several different compositions of the material class

[d] represents the electrochemical window of several different compositions of the material class

The properties of SEs depend on their composition and microstructure [76], which are often influenced by the processing method. SEs are continuously optimized to achieve higher ionic conductivity, higher electrochemical stability, material compatibility, and increased material safety [84].

Since this work mainly deals with garnet SE, it will be described in more detail in the following chapters.

2.3 Garnet-based solid-state batteries

2.3.1 Battery design

Several possible garnet-based cell concepts are investigated, including thin-film [85], hybrid [26], or full ceramic SSBs [25]. To achieve the highest possible energy density, the architecture of a garnet-based SSB should mimic that of a conventional LIB with a thick three-dimensional composite cathode consisting of CAM and LLZO, an anode (ideally Li metal), and a LLZO separator (Figure 2.3). The LLZO separator should be produced as a dense layer of several micrometer in thickness to minimize the cell resistance [86] (in comparison, the separator thickness in LIBs is about 25 µm [87]).

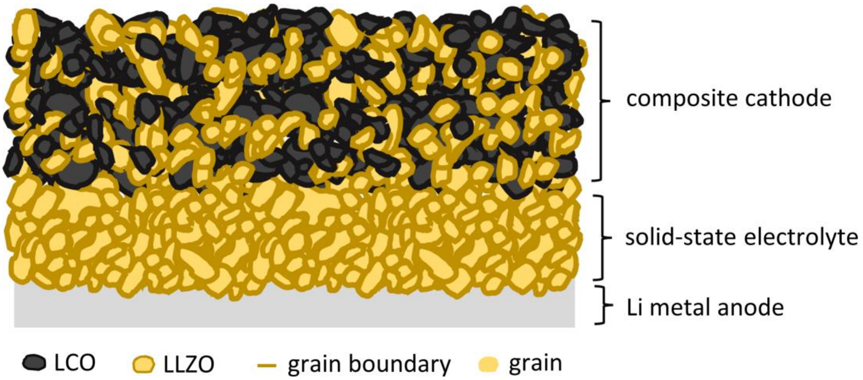

Figure 2.3: Schematic of a garnet-based SSB with the components of the composite cathode, SE, and Li metal anode [27].

2.3.2 Garnet LLZO electrolyte

LLZO has three different crystal structures: a high-temperature cubic phase with the highest ionic conductivity (c-LLZO), a tetragonal phase (t-LLZO), and a low-temperature cubic phase

(LT-LLZO), the last two have a lower ionic conductivity [88, 89]. The higher conductivity of the high-temperature cubic phase is the result of a disordered sublattice and uniform Li-ion movement in the x, y, z directions [90, 91]. In contrast, the tetragonal phase has an ordered Li sublattice and only movement in x and y direction is possible [90, 91]. However, due to the ordered structure, the Coulombic repulsion among Li-ions is reduced, resulting in a lower electrostatic energy, which makes the t-LLZO phase more thermodynamically stable [91]. The difference in ionic conductivity is about two orders of magnitude, which shows the importance of stabilizing the cubic phase [15, 19, 88, 89, 92]. This is usually done by substituting the structure with different elements, *e.g.*, Ta [25, 93, 94], Y [93], Cr [95], Te [96], Nb [94, 97], Al [98, 99], Ge [88], Ga [100] and theoretically many others [101]. Substitution can take place on the Li-, La-, or Zr-sites depending on the element and oxidation state [101, 102]. Two examples are shown in Figure 2.4, with an Al substitution on a Li site and a Ta substitution on a Zr site [103]. In this work, the c-LLZO phase was stabilized by co-doping Al and Ta with the composition $Li_{6.45}Al_{0.05}La_3Zr_{1.6}Ta_{0.4}O_{12}$. The maximum atomic Li content in the c-LLZO is 7.5, while the highest theoretical conductivity occurs at an atomic Li content of 6.4 ± 0.1 [104].

The properties of the substituted LLZO should meet the following criteria to be integrated into an SSB: The SE should have high ionic conductivity at room temperature (RT) of around 10^{-3} S cm^{-1}, electrical conductivity below 10^{-8} S cm^{-1}, high reduction and oxidation stability, low toxicity and cost, high chemical stability with the electrode materials in the temperature application range as well as in the high-temperature processing step, and sintering temperatures and thermal expansion coefficients similar to those of the electrode materials used [25].

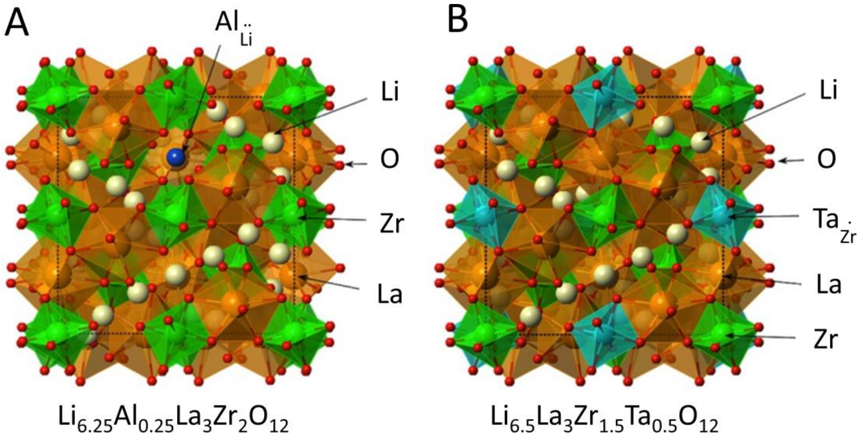

Figure 2.4: Cubic crystal structures of LLZO with different element substitutions. A) Al substitution on Li site; B) Ta substitution on Zr site. Adapted with permission from [103]. Copyright 2023 American Chemical Society.

The surface of LLZO is not stable in the ambient atmosphere and is slowly degraded over time. The reason for this degradation is the so-called H^+/Li^+ exchange due to the reaction with water, where lithium ions are replaced by protons inside the LLZO structure and LiOH is formed on the surface. The LiOH reacts with CO_2 from the atmosphere to form Li_2CO_3 at the grain boundaries, which is the most common surface contaminant of LLZO materials (Equation 2.10 and Equation 2.11) [75, 105-108].

1. $Li_7La_3Zr_2O_{12} + x\ H_2O \rightarrow Li_{7-x}H_xLa_3Zr_2O_{12} + x\ LiOH$ Equation 2.10
2. $2\ LiOH + CO_2 \rightarrow Li_2CO_3$ Equation 2.11

Since Li_2CO_3 has a low ionic conductivity, it increases the interfacial resistance of LLZO when deposited at the grain boundaries of LLZO particles [75, 105-108]. Prolonged contact with an air atmosphere can also change the distribution of elements such as Al or La on the LLZO surface [72], which is why the samples are usually stored in a glovebox.

The presence of Li_2CO_3 on the surface or at the grain boundaries generally has a detrimental effect on the electrochemical properties, so several procedures have been developed for its removal. The carbonates can be easily removed from the surface by mechanical polishing, but it is only possible for mechanically stable samples. Another very common method is the heat treatment at about 750 °C, which leads to the decomposition of Li_2CO_3 [109]. Another approach to remove the carbonates is the chemical conversion to another phase. This can be realized with the sintering aid $Li_{2.3}C_{0.7}B_{0.3}O_3$, which reacts with the Li_2CO_3 to form a $Li_{2.3-x}C_{0.7+x}B_{0.3-x}O_3$ phase that has good ionic conductivity while providing better interparticle bonding [110]. Moreover, hydrated LLZO can also be reactively sintered in the presence of Li salts at moderate temperatures of about 400 °C (decomposition of LLZO:H with hydrogen release) in a pressure-assisted process, resulting in dense LLZO bodies [111].

2.3.3 Electrochemical stability window

If the potential difference between the electrodes is outside the electrochemical stability window of the electrolyte, it may decompose. If the chemical potential of the battery anode is more negative than the lowest unoccupied molecular orbital (LUMO) of liquid electrolyte or the conduction band of the SE, the electrolyte is reduced, and if the chemical potential of the battery cathode is more positive than the highest occupied molecular orbital (HOMO) of the liquid electrolyte or the valence band of SE, it is oxidized, as shown in Figure 2.5 [63, 112].

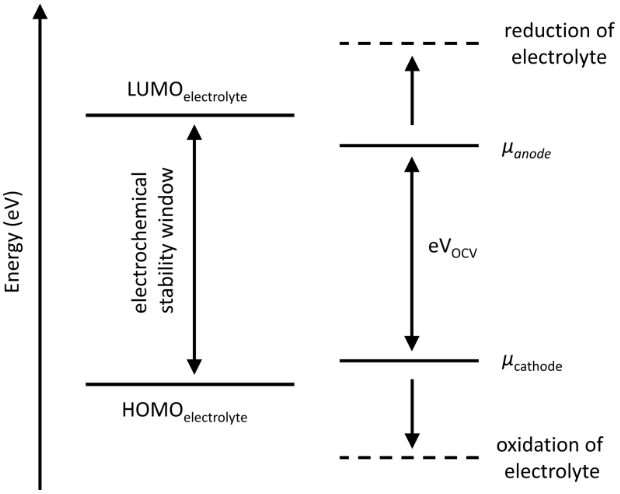

Figure 2.5: Energy diagram of the electrolyte and the corresponding electrochemical stability window between the HOMO and LUMO, as well as a stable potential difference of anode and cathode and examples of potentials in which reduction and oxidation of the electrolyte occurs. Adapted with permission from [63]. Copyright 2016 Elsevier.

The electrochemical stability window of liquid electrolytes is about 1.0 V – 4.7 V depending on the solvent and the lithium salt used [112]. As a result of electrolyte decomposition, an interfacial layer with a complex heterogeneous composition and morphology is formed at the electrode surface, which is called solid electrolyte interface (SEI). The properties of the SEI are important for the battery performance. An ideal SEI should be an electronic insulator to prevent the chemical and electrochemical reaction between the electrodes and the electrolyte thus increasing the lifetime of the battery, and a good ionic conductor to allow ion transport in the battery [63, 112, 113]. The garnet electrolyte has a low reduction potential of 0.05 V against Li/Li^+ and a high decomposition reaction energy of 49 kJ mol^{-1} at 0 V, so that the reduction of the electrolyte is kinetically inhibited [114]. The high reduction stability of LLZO allows the use of metallic Li anodes so that a high energy density can be achieved [32, 67]. However, at higher temperatures of about 300 °C, LLZO shows a decreased stability with Li metal [115]. The theoretical oxidation potential of LLZO is 2.91 V, resulting in the formation of La_2O_3, $La_2Zr_2O_7$ and O_2 as oxidation products. The origin of the gas is the oxidation of Li_2O_2 to Li_2O at 2.9 V. When the intrinsic decomposition of LLZO is taken into account, the electrochemical stability window further increases to 0.0 – 3.6 V [73]. This is due to large overpotentials caused by the slow kinetics of nucleation of the reaction products, O_2 release, slow diffusion of the non-Li elements, and the electrically insulating character of the products [115].

2.3.4 Anode half cell

Li metal is a very attractive anode due to its very high theoretical specific capacity of 3860 mAh g^{-1}, a very low potential of −3.04 V vs. standard hydrogen electrode (SHE), and a low density of 0.59 g cm^{-3}, resulting in an extremely high theoretical gravimetric capacity of 3860 mAh g^{-1} [116]. However, the Li metal anode has some major problems, such as its high reactivity with virtually all known liquid electrolytes [117] and its poor morphological stability during multiple stripping and plating events, leading to so called “dendrite” or “mossy” growth during electrochemical cycling [116]. The formation of dendrites is a consequence of the lack of spatial control of Li nucleation, which leads to infinite volume expansion [118]. The dendrites lead to short circuits when they penetrate the separator and reach the cathode, which is a critical safety issue due to the heat generation and fire hazard of the battery. The safety issues are greatly reduced in SSBs due to the non-flammability of SEs and their higher stability to Li metal. However, Li dendrites are also a major problem in the solid systems, reducing the cycling stability of SSBs [119, 120]. There are many reasons for the formation of Li dendrites in SSBs. The viscosity, yield strength, and low diffusion coefficient of Li metal cause various morphological instabilities at the Li|electrolyte interface [121]. These instabilities are due to undesirable contact losses of the Li metal caused by pore formation during an anodic load and Li dendrite growth through the electrolyte during a cathodic load. The inhomogeneities at the Li|electrolyte interface caused by the Li anode or surface defects of the electrolyte lead to a decrease in contact area with formation of point contacts, which act as hotspots for the Li plating due to the much higher current density at these point contacts. The insufficient contact area can also be the reason for high interfacial impedances. Dendrite growth through the electrolyte is mainly caused by the focusing of current flow and the imbalance of Li^0 and Li^+ flux at the interface. The dendrite propagation can be explained by the Poiseuille pressure and the Maxwell stress in the SE. The ionic conductivity, fracture toughness, shear modulus and Youngs modulus of the electrolyte also play a role in dendrite propagation. The kinetics of charge transfer and space charge layers at the interface are also rate-limiting but contribute less to the interfacial impedance. Here, insufficient contacts and high-resistance interfacial layers are the more important effects [121]. In addition, high Li|electrolyte interface resistances, interfacial reactions or incongruent ion diffusion at the interface, grain boundary defects, electrolyte electronic conductivity, and non-uniform heat distribution can be reasons for dendrite growth [122-126]. Dendrite formation can also be observed at high temperatures, although to a much lesser degree, which has a positive effect on stable Li stripping and plating [121, 127].

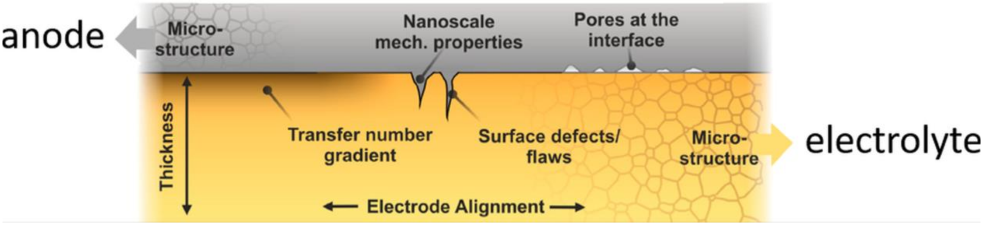

Figure 2.6: Schematic illustration of aspects of and reasons for Li dendrites on an anode half-cell. Adapted with permission from [121]. Copyright 2020 American Chemical Society.

Dendrite formation can be minimized by reducing the interfacial resistances and increasing the mechanical moduli and ionic conductivity of the SE [128]. Another approach is to coat the SE surface with materials with high mechanical moduli and high ionic conductivities and surface energies, for example, Li_3N-LiF, to prevent Li penetration into the SE [129]. An alternative possibility is to anchor the Li dendrites and simultaneously repair cracks by dynamic decomposition of unstable interlayers [130].

In addition to dendrite formation and low coulombic efficiency of Li metal anodes, there are problems such as large volume expansions, poor cycle life, capacity decay, overpotential increase and safety hazards. To improve the performance of Li metal anodes, several strategies are being investigated, such as creating an artificial SEI or regulation the Li ion pathway [121, 131]. Another approach is to use other anode material with lower theoretical capacities but better electrochemical cycling properties. The examples are insertion anodes such as graphite or $Li_4Ti_5O_{12}$, conversion anodes such as metal hydrides, or alloying metal anodes such as Si, Sn, Bi or Sb [131]. Graphite, which is already used in commercial LIBs, offers an advantage of low volume changes and a stable structure during electrochemical cycling, but is less stable at high temperatures and has a low theoretical capacity of 371 mAh g^{-1} for LiC_6 [132]. Metal hydrides such as MgH_2, TiH_2 or LiAlH are already well studied for LIBs and show good performances such as high theoretical capacity of 2038 mAh g^{-1} for MgH_2 anodes. However, the research on their use in SSB is still in its infancy. Narrow operating temperatures, poor interfacial contact with SEs and poor cycling performance are the major challenges. The $Li_4Ti_5O_{12}$ (LTO) oxide anode has a wide operating temperature range, high intrinsic safety, long cycle life and high diffusion coefficients of Li-ions that enable high charging rates, but a low specific capacity of 175 mAh g^{-1}. As regards alloy anodes, the $Li_{15}Si_4$ alloy reaches the highest theoretical capacity at 3580 mAh g^{-1}, but the strongest volume expansions are also found for this material, which can lead to fracture and delamination. To counteract the volume expansion, the particle size of the Si can be reduced to the nanometer range or modified current collector surfaces and adhesives can suppress the strong volume change. Carbon nanotubes, nanofibers and graphene can also be used to enhance electron transport within the anode. Due to its energy density, electrochemical performance, low cost, and processability, the Si anode has a great potential for use in future SSBs [131].

2.3.5 Cathode half cell

Cathode active materials (CAMs) typically contain transition metal ions in their composition to achieve a positive oxidation potential and a high theoretical capacity. The CAMs should have a good electronic conductivity, a high chemical and electrochemical stability to the electrolyte, a low material cost, and a low toxicity [133]. The CAMs commonly used in LIBs and

SSBs are intercalation compounds from the three classes of material, namely layered oxides such as $LiCoO_2$, $LiNi_{1-x-y}Mn_xCo_yO_2$ and $LiNi_{0.8}Co_{0.15}Al_{0.05}O_2$, spinels such as $LiMn_2O_4$ and olivines such as $LiFePO_4$ (Table 2.2) [58, 133, 134].

Table 2.2: The different CAMs in their discharged molecular formula with name, structure type and abbreviation, potential against Li/Li$^+$, and specific capacity [58, 133, 134].

Structure	Composition	Abbreviation	Potential vs. Li/Li$^+$ (V)	Practical specific capacity (mAh g^{-1})
Layered	$LiCoO_2$	LCO	3.9	140
	$LiNi_{1-x-y}Mn_xCo_yO_2$	NMC	3.8	160 – 170
	$LiNi_{0.8}Co_{0.15}Al_{0.05}O_2$	NCA	3.8	180 – 200
Spinel	$LiMn_2O_4$	LMO	4.1	100 – 120
Olivine	$LiFePO_4$	LFP	3.5	150 – 170

Mn-containing NMC cathodes are the cheapest and safest, but they are electrochemically less active than Co- and Ni-rich NMCs [135]. The highest capacities of 265 mAh g^{-1} have been achieved in Li- and Mn-rich materials such as $Li_{1.2}Ni_{0.2}Mn_{0.6}O_2$ (LNMO) [136]. The capacity can also be increased by increasing the Ni content, such as in $LiNi_{0.8}Mn_{0.1}Co_{0.1}O_2$ (NMC811) with a capacity of ∼200 mAh g^{-1} [137]. However, these CAMs often exhibit capacity degradation due to structural transformation and O_2 release from the lattice during cycling [74, 136, 137]. Due to the high cost and limited resources of Co, many research efforts are directed toward Co-free CAMs such as LMO, LNMO, and LFP or replacement of Co-ions in LCO, NMC and NCA with other elements. However, decreasing the Co content leads to lower electronic conductivity because it is provided mainly by Co-ions [138, 139]. In this work, LCO was mainly used as CAM for battery production. LCO has several thermodynamically stable phases, the most important one being the rhombohedral LCO phase in the $R\bar{3}m$ space group with CoO_6 and LiO_6 octahedra in the Li and Co layers (Figure 2.7) [140-142].

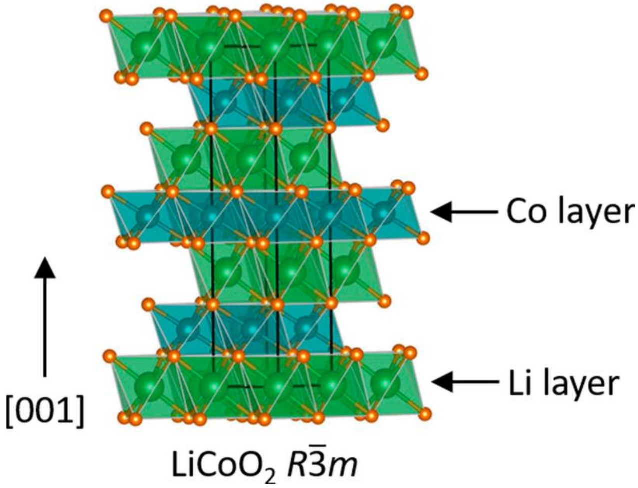

Figure 2.7: Schematic illustration of the rhombohedral LCO phase in the R$\bar{3}$m space group with CoO_6 and LiO_6 octahedra in the Li and Co layers. Graphic adapted from. Adapted with permission from [142]. Copyright 2021 APL Materials.

The LCO has a high electronic conductivity of 10^{-3} S cm^{-1} [143] and also exhibits a high practical specific capacity of 140 mAh g^{-1} [58]. The theoretical capacity of LCO is actually twice as high at ~280 mAh g^{-1}, but only half the amount of Li can be extracted since Li-ions are essential for the stability of the LCO phase as a counterforce to the repulsive forces between the CoO_2 during delithiation [63]. The ionic conductivity of the LCO depends on its orientation, since Li ion diffusion within the Li layers is different from that through the Co layers [144].

During electrochemical cycling, the Li atoms are inserted into and extracted from the cathode lattice. In both cases, the change of Li content leads to the lattice distortion, resulting in volume expansion and contraction. The distortion depends on the state of charge and is different for different CAM compositions as illustrated in Figure 2.8, where the volume strain $\Delta V/V$ is shown as a function of lithiation. Starting from a complete Li occupation, LCO shows first an increase and then a decrease in volume upon delithiation. In contrast, the various NMC compositions and NCA continuously decrease in volume during delithiation [145]. Especially for SSBs, such volume changes are critical because the contact between particles can be lost, and cracks can develop. In addition, the Li diffusion coefficient and the electronic conductivity are also affected by the lithiation state of the cathode [146-148]. LCO, for example, shows a drastic loss of electronic conductivity in the region of complete lattice lithiation [148].

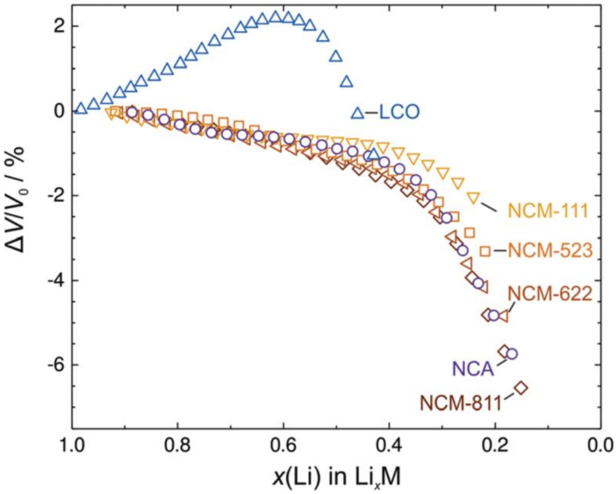

Figure 2.8: Volumetric strain of the unit cell volume form different CAMs obtained from crystallographic data as a function of the state of lithiation. Graphic taken with permission from. Adapted with permission from [145]. Copyright 2018 the American Chemical Society.

2.3.5.1 Composite cathodes

Since most CAMs do not have high ionic conductivity, the ion transport in thick cathode layers of SSB must be increased by forming a composite cathode with the SE, as shown in Figure 2.3. The composition and the fabrication of composite cathodes play a crucial role in the SSB performance. Ideally, CAM and SE should be homogeneously distributed in the composite cathode. For garnet-containing composite cathodes that require sintering, CAM should be thermodynamically stable during sintering with LLZO, and both materials should ideally have similar coefficients of thermal expansion and similar sintering temperatures to prevent undesired reactions or cracking. In addition, high ionic conductivity of the electrolyte and a high electronic conductivity of the cathode are important, as well as low volume change of the CAM during charge and discharge [25, 149]. A suitable ratio of CAM to SE in the composite cathode is critical to achieve sufficient percolation of the electrolyte in the cathode layer [23]. The optimum properties of the composite cathode can only be achieved if the interfacial resistances between the CAM and SE particles is low [25, 149]. For that, degradation reactions during sintering must be prevented.

2.3.5.2 Thermal stability of CAMs with LLZO

Many CAMs such as LMO and LFP react with LLZO already at relatively low temperatures around 500 °C, while NMCs have a higher stability of up to 700 °C [38, 40, 42]. If the temperature is too high, the decomposition starts and various secondary phases are formed, *e.g.,* $LaCoO_3$, La_2O_3, La_3TaO_7, $LaMnO_3$ and $La_2Zr_2O_7$. These phases increase the interfacial impedance and deteriorate the battery performance [38, 40, 42]. An exception is LCO, which is thermally stable up to 1085 °C when sintered with LLZO [38, 40, 41]. Therefore, LCO is the most suitable CAM for the fabrication of garnet-based composite cathode at elevated temperatures [22, 23, 25, 26, 41]. Nevertheless, numerous minor phases can also form in the LCO-LLZO composite cathodes during sintering. Detailed analyses of thermally processed LCO-LLZO composite cathodes revealed various secondary phases such as $La_2Zr_2O_7$ [38, 41], CoO [43, 44], Co_3O_4 [43, 44], La_2O_3 [38], $Li_{0.5}La_2Co_{0.5}O_4$, $LaCoO_3$ [41], La_2CoO_4 [45], and a Co-doped LLZO [25].

In addition to the reactions between CAMs and LLZO in composite cathodes, sintering can also lead to reactions between the cathode and the LLZO separator [18, 22-25, 38-42, 101]. For example, Kim *et al*. observed formation of a ~50 nm thick interfacial diffusion layer consisting of La_2CoO_4 after pulsed laser deposition (PLD) of LCO layers on a dense LLZO pellet at 664 °C [45], which was attributed to formation of Co^{2+} species due to the low partial pressure of O_2 [150]. Ihrig *et al*. reported the amorphization of grain boundaries between crystalline LCO and LLZO particles after processing composite cathodes with high-pressure spark plasma sintering (FAST/SPS) at 675 °C [22]. Park *et al*. demonstrated the interdiffusion of Co, Al, Zr and La atoms during sintering of an LCO cathode on an LLZO:Al separator at 700 °C. Diffusion of Al-ions from the LLZO:Al separator into the LCO resulted in the formation of the low-conductivity t-LLZO phase and increased interfacial resistance [19, 72]. Zarabian *et al*. demonstrated mutual diffusion of Co, Zr and La atoms from LCO and LLZO at the cathode|separator interface for spin-coated thin films processed at 400 °C [151]. Vardar *et al*. found a 100 nm cross-diffusion area at the cathode|separator interface after processing the thin films at 500 °C with formation of Li_2CO_3, $La_2Zr_2O_7$ and $LaCoO_3$ as reaction products [152].

To prevent the side reactions or to increase the stability of the components, various approaches have been proposed, such as modifying the LLZO composition [101], introducing protective layers such as Li_3BO_3 [153], $Li_{2.3}C_{0.7}B_{0.3}O_3$ [110] or Li-Nb-O [154], or using low-temperature processes such as FAST/SPS [22].

2.4 Garnet-based batteries: current state of research

In the last decade, several garnet-based battery concepts and the possibilities of their fabrication have been investigated. There are a large number of publications on thin film battery fabrication using atomic layer deposition (ALD) [155], PLD [82], radio frequency (RF) magnetron sputtering [85], or aerosol deposition [25]. Thin film batteries can be charged at high rates but have low energy densities due to the small amount of active material in the thin electrode layers [156]. Various ceramic processing methods such as powder pressing [32], tape casting [24], and screen printing [27] have been explored to fabricate SSBs with thick electrode layers and high energy densities (bulk batteries). There are also numerous publications on sintering of garnet-based battery components and complete batteries, which include conventional sintering in a furnace or more elaborate techniques such as hot-pressing [157], FAST/SPS [22], or ultra-fast high-temperature sintering (UHS) [158]. Many publications address sintering aids such as Li_3BO_3 or $LiBO_2$ to increase densification and lower processing temperature, or conductive additives such as $(In_2O_3)_{0.9}\cdot(SnO_2)_{0.1}$ (ITO) to increase the electronic conductivity of the electrodes. Table 3 provides an overview of the reports on LCO-LLZO based bulk batteries published in the last decade. It can be seen that progress is being made toward higher capacities, current densities, and cycle numbers. However, most batteries exhibit poor capacity retention after several cycles due to various degradation mechanisms [159, 160], and the capacity utilization of the active electrode materials is often low. Nevertheless, the data show that there is a continuous progress in the development of LLZO-based SSBs.

Table 3: Listing of publications in which LCO-LLZO based solid-state batteries were fabricated *via* a sintering process with the corresponding reference (Ref.), year, used materials, sintering process (Conv. for conventional sintering), LCO loading, current density applied, first cycle discharge capacity, first cycle discharge cathode utilization, electrochemical cycle

Ref.	Year	Material	Fabrication	LCO loading ($mg\ cm^{-2}$)	current density	1st discharge capacity	Cathode utilization	*T* (°C)	Cycle	Capacity retention
[161]	2022	LLZO:Ta	Conv.	6	50 $\mu A\ cm^{-2}$	0.63 $mAh\ cm^{-2}$	75%	100	100	81%
[162]	2022	LLZO:Ta, Li_3BO_3	FAST/SPS	14.4	50 $\mu A\ cm^{-2}$	1.1 $mAh\ cm^{-2}$	55%	60	50	60%
[22]	2021	LLZO:Ta-Al	FAST/SPS	14.15	50 $\mu A\ cm^{-2}$	1.2 $mAh\ cm^{-2}$	61%	80	5	64%
[163]	2020	LLZO:Nb, $LiBO_2$, ITO	Conv.	1.27	3 $\mu A\ cm^{-2}$	1.1 $mAh\ cm^{-2}$	86%	80	40	50%
[157]	2020	LLZO:Ta, $Li_{2.95}B_{0.05}OCl$	Hot-pressing	1.85	5 $\mu A\ cm^{-2}$	0.17 $mAh\ cm^{-2}$	67%	90	50	64%
[158]	2020	LLZO:Ta, $LiBO_2$	UHS	n.a.	30 $\mu A\ g^{-1}$	87 $mAh\ g^{-1}$	62%	25	450	69%
[18]	2020	LLZO:Ta	Conv. + liquid	0.73	51 $\mu A\ cm^{-2}$	0.085 $mAh\ cm^{-2}$	84%	80	14	97%
[25]	2019	LLZO:Ta	Conv.	12.6	50 $\mu A\ cm^{-2}$	1.62 $mAh\ cm^{-2}$	92%	50	100	30%
[23]	2018	LLZO:Ta-Al	Conv.	7.1	100 $\mu A\ cm^{-2}$	0.84 $mAh\ cm^{-2}$	85%	100	100	42%
[110]	2018	LLZO:Ta, $LiCO_3$, $Li_{2,3}C_{0,7}B_{0,3}O_3$	Conv.	1	5.8 $\mu A\ cm^{-2}$	0.094 $mAh\ cm^{-2}$	67%	25	100	94%
[40]	2017	LLZO:Ta-Al	Conv.	2.9	6.4 $\mu A\ cm^{-2}$	0.051 $mAh\ cm^{-2}$	13%	80	10	72%
[164]	2017	LLZO:Ta, ITO	Conv.	1.9	15 $\mu A\ cm^{-2}$	0.19 $mAh\ cm^{-2}$	71%	80	20	86%
[165]	2016	LLZO:Ta, TO, Li_3BO_3	Conv.	4	5 $\mu A\ cm^{-2}$	0.056 $mAh\ cm^{-2}$	10%	25	6	87%
[166]	2013	LLZO:Nb, Li_3BO_3	Conv.	2.35	10 $\mu A\ cm^{-2}$	0.20 $mAh\ cm^{-2}$	61%	25	5	~100%

3 Manufacturing techniques

3.1 LLZO synthesis

Ta- and Al-substituted LLZO ($Li_{6.45}Al_{0.05}La_3Zr_{1.6}Ta_{0.4}O_{12}$, referred to hereafter as LLZO) powder was produced by a three-step solid-state reaction [30-32]. $LiOH{\cdot}H_2O$ (APPLICHEM, 99.00%), La_2O_3 (MERCK, 99.90%, pre-dried at 900 °C for 10 h), ZrO_2 (TREIBACHER, 99.70%), Ta_2O_5 (TREIBACHER, 99.99%), and Al_2O_3 (INFRAMAT, 99.82%) were dry-milled and then mixed stoichiometrically with an excess of 10 mol% $LiOH{\cdot}H_2O$. The resulting powder was pressed into pellets (45 mm in diameter, 19 MPa uniaxial pressure) and calcined in Al_2O_3 crucibles at 850 °C and 1000 °C for 20 h. Between the calcination steps, the powder was homogenized and pressed again into pellets. In the sintering step, 6 g pellets were pressed (13 mm in diameter, 113 MPa uniaxial pressure) and sintered in Al_2O_3 crucibles at 1175 °C with a dwell time of 10 h, using a MgO plate covered with an LLZO powder layer as a diffusion barrier. For LLZO without Al content ($Li_{6.2}La_3Zr_{1.2}Ta_{0.8}O_{12}$) the same steps were done without Al_2O_3 and a ZrO_2 crucible was used. Some of the sintered pellets were sliced into thin discs for battery fabrication and the rest were ground for the fabrication of a screen-printing ink. For LLZO without Al content ($Li_{6.2}La_3Zr_{1.2}Ta_{0.8}O_{12}$) the same steps were done without Al_2O_3 and a ZrO_2 crucible was used. The resulting sintered LLZO pellets were cut into pieces for further processing.

A Co-ion contaminated LLZO reference material was prepared by conventional heating of a LLZO mixture with 1 wt% of $CoCO_3$ (ALFA AESAR, 99.50%) in an Al_2O_3 crucible and heated up to 1175 °C for 4 h.

3.2 Screen-printing

Screen-printing is an economical and simple method for printing layers and controlling their shape [50, 167]. The principle of this printing process is to use a screen consisting of wire mesh made of polyamide, polyester or steel as a shaping unit. The mesh is placed on a substrate and an ink is spread over the screen using a rubber squeegee with a certain pressure. The screen itself only has certain open meshes where the ink penetrates through, which determines the printing shape (Figure 3.1).

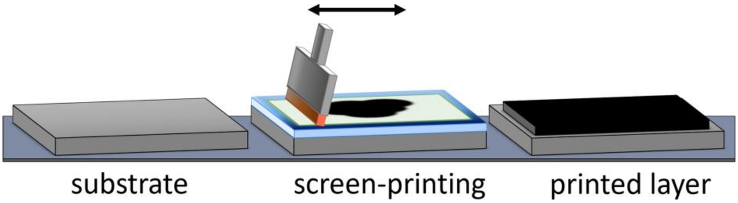

Figure 3.1: Screen printing scheme of a black screen-printing paste on a metal substrate with a rectangular open print area [43].

The open area inside the screen consists of woven wires with a certain diameter and mesh, while the surface around it is coated with a layer of polyvinyl alcohol and cross-linkable acrylic resin or diazonium compounds, produced *via* photo catalytic processes. The selection of the wire material of the screen is decisive for its stability against temperatures, acid, bases, friction and determines its elasticity. The mesh fineness is specified by the number of threads and their diameter, determining the accuracy of the resulting print. Additionally, the thread distance must be optimized for different particle sizes in the ink to ensure a controlled print. The wet layer thickness h_w in the printing process can be determined by the wire diameter d_w and the mesh count per unit length M_u (Equation 3.1) [168].

$$h_\mathrm{w} = 2 \cdot d_\mathrm{w} \cdot \left(\frac{M_\mathrm{u}^{-1} - d_\mathrm{w}}{M_\mathrm{u}^{-1}} \right)^2 \qquad \text{Equation 3.1}$$

When the printed layer dries, the thickness is reduced until all the liquid components have evaporated and only the solid remains. The thickness of the final dried layer depends on the thickness of the wet layer and the concentration of the solid in the ink. The ink contains the solid to be printed, an organic matrix of ethyl cellulose, polyacrylates, or polyvinyl butyral, and a solvent such as terpineol or diethylene glycol monobutyl ether actetate [167]. The solid loading depends on the mass ratio between the solid and the solvent with the binder and is expressed in weight percent. In this work, ethyl cellulose dissolved in terpineol as a dispersant is used as a binder with a solid loading of 50 wt% to 55 wt%.

During printing, the ink must roll off in front of the squeegee, and the squeegee must wipe the ink off the screen surface. The screen must be placed on a substrate with a small gap to prevent the ink from smearing. The squeegee then applies a certain amount of pressure to the screen so that the ink is printed onto the substrate. The screen then snaps off, while the printed ink must remain on the substrate. To make this possible, the ink must meet the correct hydrodynamic conditions and the angle and pressure of the squeegee must be adjusted [167-169].

In this work, screen-printing was performed with commercial LCO powder (MTI CORPORATION, battery grade) mixed with the synthesized LLZO powder for composite cathode production (60 wt% LCO : 40 wt% LLZO) and milled in 2-propanol (ALFA AESAR, 99.50%) in a micro-planetary mill (PULVERISETTE 7, FRITSCH). For pure LCO or LLZO layers the material was not mixed before the milling process. After drying in air overnight at 50 °C, the particles were mixed with a solution of an isomeric mixture of terpineol (SIGMA-ALDRICH, 99.50%) with 6 wt% ethyl cellulose (SIGMA-ALDRICH, 46 cps, 48.00%) and homogenized in a three-roll mill (50l, EXAKT) with a minimum roll distance of 10 µm. The resulting ink with a solid loading of the composite cathode of 55 wt% was printed on polished LLZO pellets and ethanol rinsed steel substrates (EN 1.4767 for RTP samples and EN 1.4301 for laser sintering samples) by screen-printing (E2, EKRA) with a polyester screen (27-120×22.5°, KOENEN). The wet layers were dried in air for 1 h at 60 °C. Subsequently, the ethyl cellulose binder in the dried samples was removed in air as part of a preheating step in a conventional furnace with a heating rate of 2 K min^{-1} up to 500 °C without a dwell time, followed by free cooling. The pure LCO cathodes were pre-densified with a warm press (40 EH-SERVO, P/O/WEBER) at 150 °C with 200 kN for 2 min before the binder removal. The mass of the layers was determined by the difference in weight of the LLZO or steel substrate before the screen-printing process and after the removal of the binder.

3.3 Sintering

The solidification of powdered materials is achieved by a sintering process below the melting point of the materials. Instead of melting, atomic diffusion in the solid-state is used to generate a microstructure of crystalline grains separated by grain boundaries with lower porosity than in the initial state. The driving force of this solid-state sintering is a decrease in the surface free energy of the system and can be expressed by the specific surface energy γ_s, the specific grain boundary energy γ_{gb} and the changes in the corresponding surfaces ΔA_s and ΔA_{gb} (Equation 3.2) [170].

$$\Delta E = \gamma_s \cdot \Delta A_s + \gamma_{gb} \cdot \Delta A_{gb} \qquad \text{Equation 3.2}$$

The decrease in energy is due to the reduction in free surface area caused by the reduction in porosity as the microstructure becomes more compact or the grains begin to grow. In addition to atomic diffusion which leads to densification, coarsening of the microstructure can also occur, leading to a rearrangement of matter just at the surface. However, coarsening does not lead to an increase in relative density and thus does not reduce the driving force for densification. Both processes can be enhanced by higher temperatures and smaller particle sizes. Densification can be further enhanced by external pressure or by the addition of small amounts of low-melting additives called sintering aids. The sintering aids accelerate particle binding by rapid diffusion through the liquid, what is referred to as liquid phase sintering. However, the sintering aids form an additional phase at the grain boundaries that can affect the desired properties of the sintered material. Pressure-assisted sintering increases the driving force for densification without significantly affecting the coarsening rate. Inhomogeneities in density, particle size, and composition of the initial powder result in lower densities and poorer control of the microstructure [170]. In general, the starting material should have a high degree of purity, a small particle size (ideally around or below 1 µm) with a narrow or monodisperse particle size distribution, no formation of hard agglomerates, and a spherical or equiaxial particle shape to achieve optimum sintering [170].

Matter transport

During sintering, matter is transported from areas of high chemical potential to areas of lower potential. In polycrystalline materials, this transport can occur *via* six different mechanisms (Figure 3.2), all of which lead to the growth and bonding of necks between particles. However, only some of them lead to densification, such as grain boundary diffusion, lattice diffusion, and plastic flow by dislocation motion (more common in metal powder sintering). In contrast, surface diffusion, lattice diffusion from the particle surface to the neck, and vapor transport are among the mechanisms that do not lead to densification because they do not reduce the curvature of the neck surface and thus the driving force for sintering. During the transport of the various ionic species, the stoichiometry and electroneutrality of the compound are maintained so that the slowest species control the rate of densification. The temperature supplied to the system affects the transport mechanisms in an Arrhenius dependence, with higher temperatures leading to higher densification rates [170].

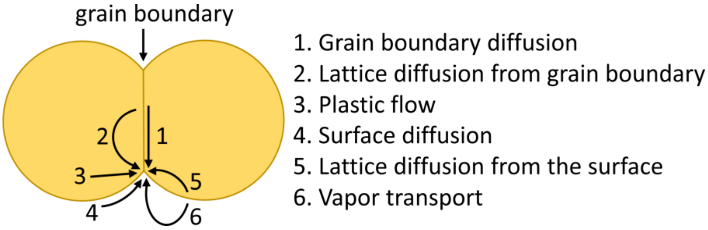

Figure 3.2: The six different mass transport mechanisms shown in a scheme of two polycrystalline particles during sintering. 1. Grain boundary diffusion; 2. lattice diffusion from grain boundary; 3. plastic flow; 4. surface diffusion; 5. lattice diffusion from the surface; 6. vapor transport. Adapted with permission from [170]. Copyright 2003 CRC Press.

As previously indicated, particle size is an influencing factor for sintering. Considering a powder system in which grain boundary diffusion and lattice diffusion are the dominant transport mechanisms, the grain boundary diffusion rate k_{gb} and the lattice diffusion rate k_{lat} are strongly dependent on the grain size G, as shown in Equation 3.3 and Equation 3.4 [170, 171].

$$k_{gb} \sim G^{-4} \qquad \text{Equation 3.3}$$

$$k_{lat} \sim G^{-3} \qquad \text{Equation 3.4}$$

This dependence shows that small particles strongly influence the diffusion mechanisms and increase the sintering rate. However, when the size of the particles is below ~1 µm, the interaction between the particles is more pronounced and the formation of agglomerates increases. The agglomerates lead to inhomogeneous particle packing and pore distribution in the green body (initial state of the material before sintering) and affect the sintering behavior of the material. Therefore, the powder has to be optimized by using small particle sizes, but without causing the detrimental effect of agglomerates [170].

Sinter Stages

Sintering takes place in several successive stages, each stage representing a time or density interval with a well-defined microstructure. In the initial stage, differences in surface curvature are eliminated by rapid growth of interparticle necks due to diffusion, vapor transport, plastic or viscous flow. At this stage, the spherical particles come into contact and a relative density of up to 65% can be achieve. Then the intermediate stage begins, which accounts for most of the sintering and leads to a relative density of up to 90%. At this stage, the pores are still continuous and sit along the grain edges, while they become smaller and their radius decreases. When isolated pores form, the third and final stage begins, leading to relative densities greater than 90%. At this stage, the spherical pores shrink continuously along the corners and may even disappear completely. In addition to the fundamental material properties, which are due to the chemical composition, the properties of the material are also determined by the final microstructure. Therefore, controlling and maintaining the desired microstructure is crucial for achieving material properties for the specific applications [170].

Constrained Sintering

The term constrained sintering is commonly used for systems where the shape constraint is necessary and is an intentionally imposed property. Examples include sintering of a material applied to a substrate, multilayer systems with different materials, or insertions in a powder matrix (Figure 3.3) [170].

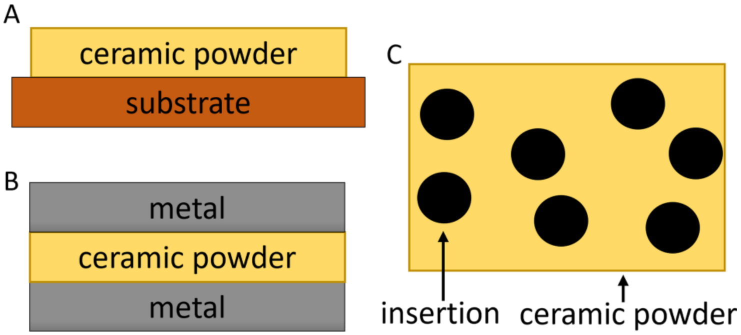

Figure 3.3: Examples for constrained sintering. A) ceramic powder on a substrate of another material; B) ceramic powder in a multilayer system with metal; C) ceramic powder with insertion of another material. Adapted with permission from [170]. Copyright 2003 CRC Press.

The proportion of another material insertion in the primary powder matrix strongly influences the sintering process and the resulting properties of the composite. The sintering rate in the composite differs from the sintering of the two materials by themselves. This is due to transient stresses, the formation of percolation networks and disrupted powder packing. Transient stresses are caused by different sintering rates of the two materials, which can lead to reduced densification and damage to the microstructure. Percolation networks can form as a result of the insertion, inhibiting densification or even preventing it altogether. The powder packing surrounding the insertion can be disrupted, affecting densification, especially in polycrystalline materials. When the shrinkage rates of the matrix and the insertion are different, mechanical forces occur. The maximum force at the interface between the insertion and the matrix can be determined using the composite sphere model, in which finely distributed insertions are surrounded by spheres of matrix powder, all having the same volume fraction. According to this model, the maximum force decreases with r^{-3}, where r is the radius of the insertion center. The direction of the force depends on which material is sintering faster or slower. For example, if the matrix sintered faster than the insertion, compressive stresses would develop in the insertion and tensile stresses in the matrix. Apart from the stresses, radial cracks around the insertion or circumferential cracks are also possible (Figure 3.4) [170, 172].

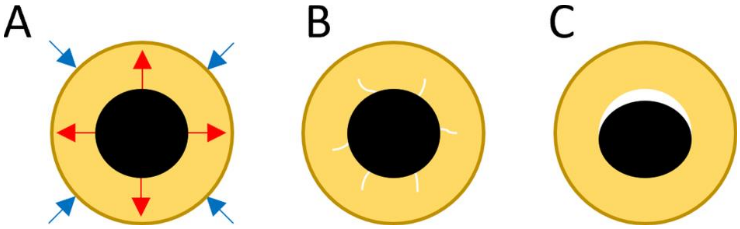

Figure 3.4: Scheme of the different effects of mismatch in the sintering behavior of different materials. A) tensile (red) and compressive (blue) stresses; B) radial cracks; C) circumferential cracks. Adapted with permission from [170]. Copyright 2003 CRC Press.

When mechanical stress builds up in the system, it is relieved by viscous flow or creep. As Borfia and Scherer have shown, it can be assumed that stress reduction occurs only *via* the viscous response of the porous material, since the elastic strain is much smaller than the strain during sintering and thus the elastic side can be neglected [173]. For the calculation of densification rates and stresses, the composite sphere model or the self-consistent model can be used for insertion fractions below 20%. In the self-consistent model, a microscopic region of the powder matrix is considered as an inclusion of sintering material in the composite, which contracts at a slower rate. Therefore, stresses are generated that affect the densification rate in each region. It differs from the composite sphere model in that the shear viscosity of the composite is replaced by the shear viscosity of the matrix. However, for insertion fractions less than ~10-15%, the model predictions are close to those using the rule of mixtures, where the composite is assumed to have the sintering behavior of the individual components [170, 174].

Percolation network

If the volume fraction of the insertions in the composite is high enough, they can form a continuous percolation network. The stage at which it is first formed is the percolation threshold, which depends on the shape and dimensionality of the lattice. For a triangular lattice, the volume fraction of the percolation threshold is reached at 50 vol.-%, for a square two-dimensional lattice at 59 vol.-%, and for a cubic lattice at 31 vol.-%. During sintering, however, the lattice is not present. Therefore, for a three-dimensional system of equiaxial particles without agglomerates or repulsion, the percolation threshold is reached when the insertion particles have a volume fraction of 16 vol.-%. The percolation network has important effects on the sintering and the final properties of the composite. If the network is continuous throughout the sample and the insertion material has certain properties, these properties will be transferred to the composite. This is used in the fabrication of composite cathodes, where the electrolyte provides higher ionic conductivity in the cathode compared to pure CAMs. When the insertion is rigid, the composite will be mechanically rigid. However, the increased stiffness affects the sintering kinetics and can reduce or stop sintering. Even before the percolation threshold, larger clusters of insertions can have a local effect on the sintering [170, 175, 176].

3.4 Photonic sintering processes

Photonic sintering is a term used to describe a range of thermal processing methods in which the sample is sintered with light. In photonic sintering, radiation is absorbed in the surface layers to generate heat that is transferred to the deeper layers. These processes depend on the optical and thermal transfer properties of the material and the energy of the radiation. The fast transient heating of the surface allows very short heating times of minutes to nanoseconds, so that the surface can be selectively treated, while the bulk temperature is kept low, enabling the processing of heat-sensitive substrates. The slowest of the photonic sintering processes is RTP. In RTP samples are heated with broadband halogen lamps to temperatures up to 1300 °C over a period of seconds and minutes. During this rather long heating, the substrate is also heated, so that the temperature gradient between surface and bulk is lower compared to the other photonic sintering methods [48].

A faster method in the time range of milliseconds is flash lamp annealing (FLA). Here, Xe flash lamps with a broad wavelength around 400 nm are used to heat the samples up to 2000 °C with pulsed irradiation. Due to the shorter interaction time, a much stronger temperature gradient is generated between the surface and the bulk, which enables selective sintering of the surface [48].

Even shorter interaction times in the nanosecond and millisecond range can be achieved by using lasers for the annealing. Temperatures of up to 2000 °C can be achieved with a variety of lasers such as excimer lasers (KrF, λ = 0.25 µm), Nd:YAG lasers (λ = 1.06 µm) or CO_2 lasers (λ = 10.60 µm) [49]. This technique can be used to process different classes of material such as polymers, metals, ceramics, or cermets. Unlike the other techniques, the sample is heated with a discrete wavelength, which allows selective heating of the better absorbing fractions. This creates a strong temperature gradient between the surface and the bulk as well as a lateral gradient. The laser can be used as a focused point or as a line. To process the entire sample surface, the sample is moved under the laser focus. The temperature gradients of RTP, LFA and laser sintering are shown schematically in Figure 3.5 [48].

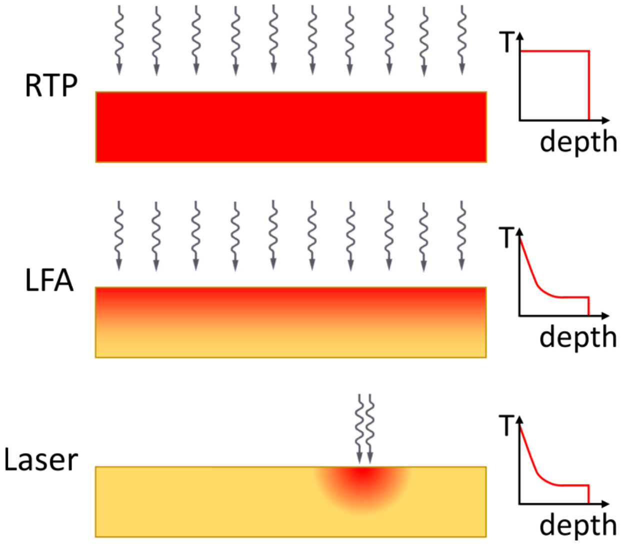

Figure 3.5: Schematic representation of the temperature gradient of the photonic sintering methods RTP, LFA and laser sintering, with the temperature plotted as a function of the sample depth. Adapted with permission from [48]. Copyright 2016 IOP Publishing Ltd.

In this work, the RTP and laser methods were used for the sintering of cathode layers on different substrate materials. The RTP sintering process was carried out with a lamp furnace

(Xerion), with a Pt-Rh thermocouple control with contact to a stainless steel substrate (EN 1.4767 steel, VDM Metals) as a reference. The source of radiation in the RTP are halogen lamps with a W filament (13136V, Philips) and a color temperature of 3000 K. The samples were placed inside the RTP with the cathode side up. When electrolyte supported samples were sintered, the samples were placed on a protective powder sheet of the synthesized LLZO material to prevent loss of Li from the LLZO lattice into the quartz [177]. Metal and electrolyte supported samples were additionally covered by a quartz crucible (V = 15 ml) as furnace protection. During the sintering process, only the lamps above the cathode were used and the lamps below the sample were switched off when sintering the electrolyte supported samples. For the metal supported samples both lamp sides were used. The heating and cooling rates of the RTP were varied for the electrolyte supported samples between 120 K min^{-1} and 600 K min^{-1} to a maximum temperature of 1000 °C with dwell times between 60 s and 180 s. The final parameters for the battery production and Co-ion diffusion investigation were 10 s dwell time at 400 °C, 10 s dwell time at 700 °C, and 90 s dwell time at 1000 °C with a heating rate of 3 K s^{-1} for each step and a cooling rate of 5 K s^{-1} [27]. The same parameters were used for the current collector supported composite cathodes sintered by RTP.

For the laser sintering process, which was developed by Fraunhofer ILT [178], the samples were placed on a hot plate (FLE100640/TR400, Bach Resistor Ceramics GmbH) pre-heated to 500 °C. The temperature of the hot plate surface near the sample was controlled with a thermocouple (GOF130 Typ K, GREISINGERElectronic) and maintained 500 °C. The hot plate with the sample was located on a two-axis handling system (Kreuztisch 10-V, isel Germany AG) for bidirectional moving with a feed velocity of 16 mm s^{-1} during the laser treatment in ambient atmosphere. Pre-heating is used to enhance the adhesion of the layer to the substrate during laser sintering, since low surface temperatures of the substrate tend to decrease the wetting of (partly) molten material and, thus, the adhesion [179, 180]. A laser (LIMO250-L6×0.07-DL1470-EX1682, LIMO GmbH) with a wavelength λ of 1470 nm, a maximum output power of 250 W, and line-shaped beam (6.3 mm × 0.084 mm) was used in continuous wave mode. The parameters for the laser sintering were chosen with respect to the sintering performance and phase stability of the cathode [178]. The laser power was set to 53.5 W, resulting in an interaction time of 5.3 ms and a power density of approx. 10.1 kW cm^{-2}, and the temperature at the laser focus can be assumed to be around 1000 °C to 1100 °C according to previous IR camera measurements [178]. After sintering, the samples were placed on a large metal plate at RT for cooling.

Optical properties

The conversion of light energy into thermal energy by absorption is called the photothermal effect [181]. As far as the various interactions between light and matter are concerned, there are three major photothermal conversion mechanisms. The first is plasmonic localized heating of metals, which takes place when a suitable wavelength excites free electrons to a collectively oscillating frequency called localized surface plasmon resonance. This resonance can decay in a radiative or non-radiative manner. Non-radiative decay occurs *via* intraband or interband transitions involving energetic electrons that produce particle heating through electron-phonon interaction. However, this process applies only to metals and is therefore relevant to the metal substrate but not to the ceramic materials. The second conversion mechanism is found in semiconductors, where photons with energy equal to or higher than the bandgap excite an electron to the conduction band, while a hole is generated in the valence band. The electron-hole pair can recombine and relax in a radiative or non-radiative manner. In the non-radiative relaxation, the energy is converted into vibrational energy of the lattice. In the third mechanism, an electron in the LUMO is excited by a photon to the HOMO. The relaxation of the excited electron occurs *via* an electron-phonon coupling, which transfers the energy to the vibrational modes of the atomic lattice, resulting in a temperature rise. In particular, for materials with a large number of π-orbitals, such as some carbonaceous materials, the excitation energy is reduced due to the low energy barrier of the excitation. This leads to a larger absorption range at longer wavelengths [181].

To ensure efficient energy transfer in photonic sintering using the photothermal effect, the absorption of the material must match the wavelength of the radiation source and have a high absorption rate [181, 182]. Therefore, a broad absorption of the materials to be sintered is especially important for RTP and LFA applications, which have a broader spectrum. In contrast, discrete energy, as used in lasers, can be used to match the radiation source with the absorption bands of the material to be processed. For example, in materials mixtures with different sintering temperatures, certain fractions can be selectively heated to a greater or lesser extent. To do this, the absorption of the materials must be known, which is usually determined by absorption spectroscopy. Most ceramics have a bandgap in the range of 2.5 eV to 5 eV [183] impeding high absorptions of visible light, since the absorption maximum is reached at photon energies higher than the bandgap. Therefore, radiation with an even smaller wavelength is necessary for high absorption in ceramics.

Since the band gap energy tends to decrease with increasing temperature, it becomes smaller when the material is heated to the sintering temperature. Depending on the material and the temperature, the band gap can be reduced by 1 eV [184-187]. When a sample is heated with a discrete radiation source with a photonic energy below the absorption maximum, the reduction of the bandgap is clearly reflected in the temperature when a certain temperature is reached. Then the absorption becomes much more efficient and rapid heating occurs. An example of such a process is shown in Figure 3.6, where a $Li_{6.4}La_3Zr_{1.4}Ta_{0.6}O_{12}$ sample is heated with a 450 nm laser. After the temperature of above 800 °C has been reached and the bandgap was sufficiently reduced, the energy conversion efficiency increased from below 10 % to over 80 % [182]. In addition to the sample temperature, Figure 3.6 shows the emission of infrared radiation, which represents a loss of thermal energy. The total radiation emission E_{em} of a hot body per area is given by the Stefan-Boltzmann law with the Stefan-Boltzmann constant σ ($5.67 \cdot 10^{-8}$ W m^{-2} K^{-4}), the emission coefficient ε, and the temperature T (Equation 3.5) [188].

$$E_{\mathrm{em}} = \varepsilon \sigma T^4 \qquad \text{Equation 3.5}$$

The law shows a direct proportionality of the emission to the fourth power of the temperature of the body and therefore the emission is strongly temperature dependent. However, the emission coefficient is $\varepsilon = 1$ only for ideal black bodies, and for all other subjects absorbing and emitting less than a black body, the value is $0 < \varepsilon < 1$.

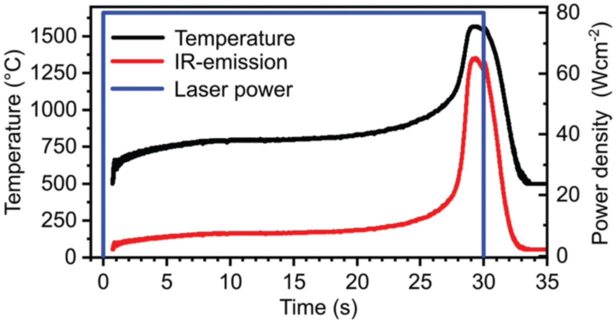

Figure 3.6: Sample temperature, infrared emission and applied laser heating shown with temperature and power density as a function of time during constant laser illumination of a $Li_{6.4}La_3Zr_{1.4}Ta_{0.6}O_{12}$ polycrystalline ceramic sample. Reproduced from [182] with permission from the Royal Society of Chemistry.

The penetration depth of the radiation decreases with increasing absorption, so that the thickness of the processable layer decreases. Deeper layers are heated by heat conduction, hence the thermal conductivity of the materials also plays a role in photonic sintering. The penetration depth of the radiation is determined not only by the transmission and absorption of the material, but also by the reflectivity of the individual particles [189].

3.5 Battery fabrication

The full cell assembly were performed in an Ar-protective atmosphere. The cell assembly of the sintered pure LCO layers on EN 1.4767 steel substrates were carried out in an ECC-Ref cell housing (EL-Cell®) with a liquid electrolyte (Sigma Aldrich, 99.9%), consisting of 1M $LiPF_6$ in ethylene carbonate and dimethyl carbonate (50:50 vol.-%), glass fiber separator (EL-Cell®) and lithium metal as anode. The full cell had a diameter of 1.70 cm ($A_{\text{cathode}} = 2.27\ \text{cm}^2$) and the total mass of CAM in the cathode was around 14 mg, resulting in a theoretical capacity of 1.96 mAh and an areal capacity of 0.86 mAh cm^{-2}.

For the polymer infiltration and cell assembly of the laser sintered composite cathodes, PEO (Sigma-Aldrich, $M\text{v} = 600{,}000$) was mixed with lithium bis(trifluoromethanesulfonyl)imide (LiTFSI) (Sigma-Aldrich, 99.95%) in a molar ratio of the repeat unit, ethylene oxide, to Li^+ of 20. Next, carbon black (Alfa Aesar, 99.99%) was added as an electronically conductive additive and all components were dissolved in acetonitrile (Honeywell, 99.8%). The laser-sintered composite cathodes were infiltrated by the prepared polymer solution and were dried at 50 °C for 1 h. Sliced LLZO discs were polished with sandpaper and conditioned by an annealing step at 750 °C for 2 h in Ar. Metallic Li was pressed to obtain a thin foil, which was subsequently pressed onto the LLZO disc. The attached Li foil was then heated until it was molten to increase the contact between the anode and the electrolyte. This anodic half-cell was placed on the PEO composite cathode and the assembled full cell was placed in an ECC-REF cell housing (EL-CELL®). The full cell had a diameter of 1.12 cm ($A_{\text{cathode}} = 0.99\ \text{cm}^2$). The total mass of active material in the composite cathode was around 2.2 ± 0.2 mg, resulting in a theoretical capacity of 0.31 ± 0.03 mAh.

For the cell assembly of the electrolyte supported samples, the anode side of the resulting half-cells were polished with SiC sandpaper to reduce the pellet thickness to ~400 µm and to remove carboxyl- and hydroxyl-based impurities. Subsequently, a thin Au film was sputtered on both sides of the sample. This film acts as the current collector on the cathode side and increased the adhesion of indium and Li metal on the anode side [22, 25]. The In foil was manually attached as the anode and subsequently heated until the In was molten to improve the contact between the anode and the electrolyte. The assembled full cell was finally placed in a cell housing consisting of a modified Swagelok® T union body. The full cell had a diameter of 1.15 cm ($A_{\text{cathode}} = 1.04\ \text{cm}^2$), while the anode had a diameter of 1 cm ($A_{\text{anode}} = 0.79\ \text{cm}^2$). The total mass of CAM in the composite cathode was around 2 ± 0.1 mg, resulting in a theoretical capacity of 0.28 ± 0.01 mAh and an areal capacity of 0.27 ± 0.01 mAh cm^{-2}.

4 Characterization methods

4.1 Raman Spectroscopy

Raman spectroscopy uses scattered light to measure the vibrational energy modes of a sample. Since vibration modes dependent strongly on chemical structure, they can be used to identify species and quantify (or semi-quantify) their amount [190, 191].

When a photon interacts with matter, it may be absorbed if the photon's energy matches the difference between two energy levels, or it may be scattered elastically or inelastically. A major part of the light (0.01% – 0.1% of a radiation source) is scattered elastically (Rayleigh scattering) without changing its energy. The intensity of Rayleigh scattering depends strongly on the wavelength and increases with λ^{-4}. Raman spectroscopy is based on Raman scattering that occurs when light is scattered inelastically involving nuclear motion. In this process, photons excite the sample into a virtual energy state that emits photons with the different energy and direction than the incident photon. In this process, the energy of the photon is transferred to the sample or vice versa, while the species relaxes to the vibrational ground state (Figure 4.1) [190, 191]. The intensity of Raman scattering is much lower than that of Rayleigh scattering, affecting only one photon out of $10^6 – 10^8$ [190, 191].

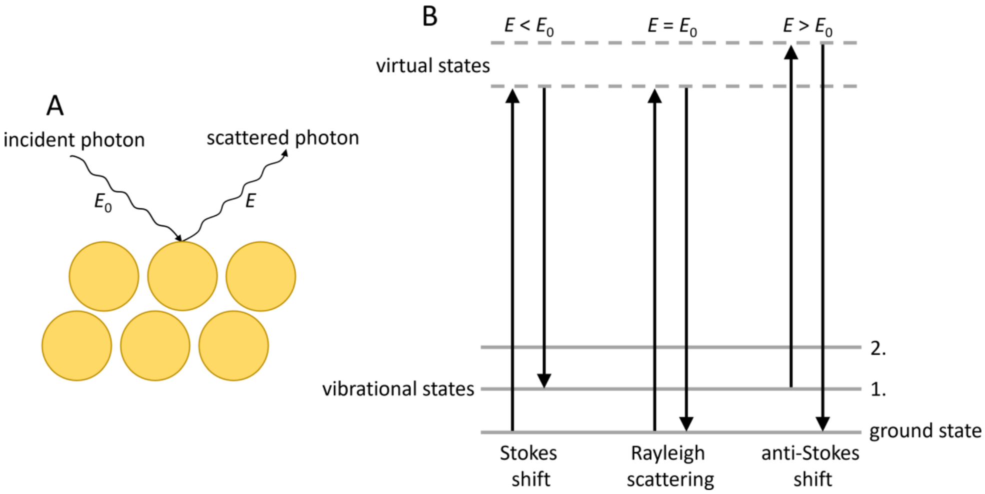

Figure 4.1: Schematic illustration of a scatter process of a photon on a sample. A) incident and scattered photon with E_0 and E; B) energy diagram with the transitions between the different vibrational and virtual states with the corresponding labeling of Rayleigh scattering, Stokes shift and anti-Stokes shift. Adapted with permission from [190]. Copyright 2005 John Wiley & Sons, Ltd.

The photon energy shift (Raman shift) corresponds to the energy difference between two vibrational states (or more precisely, rotational-vibrational-electronic states) of the species. When the incident photon transfers its energy to the species, the energy of the scattered photon shifts to lower values ($E < E_0$) and a Stokes shift (downshift) is observed. When the energy of the scattered photon E is higher than the energy of the incident photon E_0 ($E > E_0$), an anti-Stokes shift is observed. This occurs when a species is already at a higher vibrational level. The relative intensity of these two shifts depends on the population of vibrational states. Since most measurements are performed at RT, the ground state is the most common vibrational level in most species, so Raman scattering with the Stokes shift is more intense and most commonly measured. Since the energy shift depends on the wavelength, a monochromatic radiation source must be used for the measurement. Usually, laser sources are used that provide a high number of photons, compensating the low number of Raman scattering interactions. The Raman shifts are then separated into the individual wavelengths by optics and detected by a charge-coupled device, while the wavelength of the laser is filtered out (the larger part, due to Rayleigh scattering and reflection). The measured wavelengths are usually given in wavenumbers λ^{-1}, since they are directly proportional to the energies, and are plotted against intensity. By convention, the laser wavelength is set to 0 cm^{-1}. This allows comparison of spectra from lasers with different wavelengths [190, 191].

Raman spectroscopy can be used for gases, liquids, solids (including powders) and is suitable for the study of small objects and surface layers. In addition, this method can be used at both low and high temperatures, although small temperature-induced changes in Raman shifts must be taken into account. With Raman spectroscopy, it is possible to measure single points on the sample or to map a specific area with multiple spectra. In conjunction with a light microscope or electron microscope, it is possible to obtain spatially resolved information about the sample. By averaging multiple spectra from the mapping, statistically meaningful spectra of the sample can be obtained. Cosmic rays and emission from room light or cathode ray tubes may appear in the spectra and must be eliminated by software tools, otherwise their intensity may distort the spectrum of the sample [190, 191]. It is also possible that a material has an electronic transition that resonates with the incident photons from the laser. This results in photoluminescence that can be detected as a new signal or background. To detect or possibly avoid the photoluminescent signals, a laser with lower photon energy can be used, i.e. below the energy of the resonance [192].

In this work Raman spectroscopy was performed with the device INVIA QONTOR from the company RENISHAW with a 532 nm and 785 nm laser. For Raman mappings a 2400 l mm^{-1} (for 532 nm laser) or 1800 l mm^{-1} (for 532 nm laser) grating was used. The single spectra of the mapping were collected with an integration time of 1 s per spectrum and a step size of (x, y) = (1 µm, 1 µm) over an area of 80 µm × 40 µm, resulting in a total number of 3321 spectra. Cosmic ray removal, background subtraction, and normalization were applied to the spectra. Finally, LCO and LLZO signals were extracted by a component analysis and the spectra for each phase were averaged. For the mapping of the separator cross section of the Co-ion contaminated LLZO separators, the sample was embedded and polished and an area of 1050 µm × 30 µm was analyzed and each line along the separator was averaged to a single spectrum.

4.2 X-ray diffraction

X-ray diffraction (XRD) is a nondestructive analytical technique based on the elastic scattering of X-rays by a sample with a higher order structure of its constituents and is a primary technique for characterizing crystalline materials to obtain information about their structural and phase composition [170]. For the measurement, the atomic spacing in the material must be in the wavelength of the X-rays and the scattering centers must be distributed in a spatially ordered manner. The X-rays are diffracted by the electron shell of the atoms in the lattice planes. A schematic of a constructive interference condition in a lattice is shown in Figure 4.2. The X-rays diffracted at the lower lattice plains have a different path than the upper ones, which is indicated by the dashed lines in the figure [170].

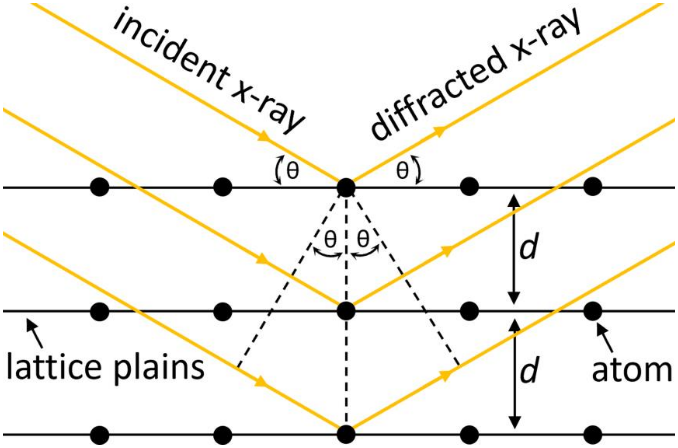

Figure 4.2: Scheme of a crystalline lattice on which X-ray beams are diffracted. The dashed lines indicate the path difference of the diffracted beams of the lower lattice plains. Adapted with permission from [170]. Copyright 2003 CRC Press.

The condition for constructive interference is given in the Bragg equation (Equation 4.1) [170],

$$2 \cdot d \cdot \sin\theta = \mathrm{n} \cdot \lambda \qquad \text{Equation 4.1}$$

with the spacing between the lattice planes d, the angle of incidence θ, the wavelength λ, and the integer n. The XRD technique can be applied to single crystals, polycrystalline dense bodies, layers, and powders. The diffraction pattern is a superposition of the patterns of the individual phases, which can be identified and quantified by comparing the positions and intensity of their reflections with standard patterns of materials. For known crystal phases, Rietveld refinement, which calculates the theoretical patterns for a given crystalline structure, can be used to determine the concentration of the individual phase. To determine a unit cell, a set of unit cell parameters must be found that fits the measured reflections. However, there are some artifacts that can occur due to sample preparation, such as preferred orientation of crystals or texturing and particle size broadening, which must be avoided to obtain valid data. The XRD technique has a detection limit of around 0.1 wt% – 1.0 wt% for crystalline phases. Amorphous materials show a broad background that is superimposed on a crystalline pattern [170, 191].

The XRD measurements in this work were mainly performed with the device D4 ENDEAVOR from BRUKER in the Bragg-Brentano geometry with two-theta values between 10° and 80° using Cu Kα radiation. Additionally, *in situ* high temperature (HT) XRD measurements were performed on the XRD device EMPYREAN from MALVERN PANALYTICAL with a heating rate of 5 K min^{-1}, where the XRD-data were collected again with two-theta values between 10° and

80° for every 100 °C step up to 1300 °C, starting at 600 °C. The total data collection time at each temperature yielded ~24 min.

4.3 Scanning electron microscopy

Scanning electron microscopy (SEM) can be used to obtain information about the surface topography and composition of samples [193]. This is done by using an electron beam that is scanned across the sample surface. For each position of the beam, the signals resulting from the interactions of the electrons with the sample are recorded to produce a magnified image of the area. The electron beam is generated using a thermionic Schottky or field emission cathode with a voltage difference to the anode between 0.1 keV to 50 keV to accelerate the electrons. The beam is focused and collimated using a two- to three-stage electron lens system with apertures to produce an electron probe 1 nm to 10 nm in diameter with a current of 10^{-9} A to 10^{-12} A. The beam then passes through a deflection coil system in the final lens to scan the sample in a raster mode. A variety of electron-sample interactions can be detected and used to create an image in greyscale or to obtain qualitative or quantitative information. The interaction consists of secondary electrons (SEL), backscattered electrons (BSE), Auger electrons (AE), and X-rays, which are illustrated in Figure 4.3 [193].

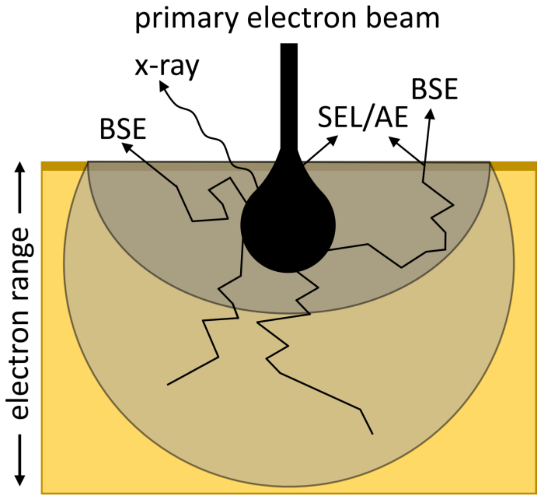

Figure 4.3: Schematic representation of the origin of SEL, BSE, AE and X-ray photons. SEL and AE are generated only in the uppermost layer of the sample, while the BSE can penetrate deeper into the sample, along with multiple collisions. Adapted with permission from [193]. Copyright 1998 Springer-Verlag Berlin Heidelberg.

By convention, the energy of the SEL is up to 50 keV, followed by BSE > 50 keV, and AE with energies of 50 keV up to 200 keV. The electron range of the primary beam depends on the electron energy and the density of the sample, leading to a theoretical range of 10 nm to 10 µm. SEL are generated by inelastic collisions of the electron beam or BSE with the sample and can leave the sample only in the upper nanometers of the material. Therefore, SEL are mostly used to image the surface topography with a positively polarized collector grid on the side of the sample as a detector. Since the sample is negatively polarized, contrast differences in the image are generated by differently polarized regions on the sample surface. To compensate for strongly negatively charged areas that would result in bright contrasts, the sample is usually coated with a thin electronic conducting layer, such as Au or Pt. BSE have a broad energy range from 50 keV to primary electron energy. The broad behavior is due to multiple energy losses during different scattering processes. The BSE can originate from much deeper regions compared to the SEL, with a maximum information depth of about half the electron range. The BSE are commonly detected with a semiconductor or scintillation detector that provides signals proportional to the BSE energy, contributing to the final image. The contrast mechanism in BSE imaging depends on the backscattering coefficient of the mean atomic number $\bar{Z}$. Therefore, phases with different $\bar{Z}$ can be recognized. In addition, the backscattering coefficient also depends on the relative orientation of the electron beam to the lattice planes and can distinguish coefficients in the order of 1% to 10% [193].

When an electron of an inner shell is ionized and an electron from an upper shell fills the vacancy, the released energy can be converted into a characteristic X-ray photon or transferred to another atomic electron leaving the sample as an Auger electron. However, this is only possible if the primary electron exceeds the ionization energy of the inner shell of the sample atoms. Additional effects that can occur are X-ray fluorescence, electron beam-induced currents, cathode luminescence, and heat. During the cascade of inelastic scattering of the primary electron beam, most of energy is converted to heat. In most materials, the thermal conductivity is high enough so that the generated heat does not interfere [193].

For the microstructural sample analysis in this work, cross-sections were prepared by fracturing, polishing, or Ar-ion milling. The fracture edges of the metal supported samples were made by breaking the specimens after cooling in liquid nitrogen. The cross-sections of the polymer infiltrated samples were prepared by Ar-ion milling (SM-09010 CROSS-SECTION

POLISHER, JEOL) for 6 h with an operating voltage of 6 kV. After sputtering of a thin Pt or Au layer the analysis was done with the SEM devices EVO-15 from ZEISS, LEO 1455 EP from CARL ZEISS AG, and MERLIN from CARL ZEISS utilizing a SEL and a BSE detector with an acceleration voltage of 5 kV to 15 kV were used. The density of the samples was measured with digital image analysis by the IMAGEJ software (WAYNE RASBAND).

4.4 Energy-dispersive X-ray spectroscopy

Most SEM instruments are equipped with a lithium-drifted silicon detector for energy-dispersive X-ray spectroscopy (EDS). With the detector, it is possible to measure the characteristic X-ray lines described above with a resolution of $\Delta E \simeq 100$ eV to 200 eV in a range from 0.1 keV to 30.0 keV [193, 194]. Lighter elements such as Li and Be with X-ray energies down to ~0.052 keV can also be measured, but require a special setup with thin polymer or highly transparent windows. To generate characteristic X-rays, the critical excitation energy E_c must be exceeded by the incident electron beam energy E_0. The dependency is parameterized with the overvoltage U_0 (Equation 4.2) [194].

$$U_0 = \frac{E_0}{E_c} \qquad \text{Equation 4.2}$$

U_0 can be used to determine the intensity I_{ch} of the characteristic X-ray generation (Equation 4.3) [194].

$$I_{ch} = I_b \, a \, (U_0 - 1)^n \qquad \text{Equation 4.3}$$

with the beam current I_b and the constants a and n with values of $1.5 \leq n \leq 2.0$. In addition to the characteristic X-rays, a continuum radiation, called bremsstrahlung, is also produced. The intensity of the X-ray continuum I_{cm} can also be determined by taking into account the mass-concentration-averaged atomic number Z of the sample and another constant b (Equation 4.4) [194].

$$I_{cm} = I_b \, b \, Z \, (U_0 - 1) \qquad \text{Equation 4.4}$$

The generation of X-rays therefore depends strongly on the energy of the primary electron beam. EDS is typically performed with a beam energy of 10 keV to 30 keV, since this energy is capable of producing characteristic X-rays for all elements of the periodic table except hydrogen and helium, so they cannot be detected in EDS. The analysis is usually combined with SEM imaging to provide information about the chemical composition of the sample in addition to topographic analysis. It is possible to measure individual points or to create a mapping of multiple individual point spectra for each coordinate of the map. Both can be performed as qualitative elemental analysis or as quantitative compositional analysis. Finally, the assignment of the characteristic signals to specific elements is done with the help of analysis software. Due to signal superposition, qualitative analysis can be difficult for a large number of element combinations in the sample, for example Ti and Ba, or S, Mo and Pb [194]. In this work EDS single spectra point measurements and mappings were performed with the device ULTIM MAX 100 and X-MAX 80, both from OXFORD INSTRUMENTS, with an electron beam energy of 15 kV.

4.5 X-ray photoelectron spectroscopy

X-ray photoelectron spectroscopy (XPS) is a surface analysis technique that provides semi-quantitative elemental information about the chemical state and electronic structure of the top 10 nm of a sample. The analysis is based on the process of photoelectron emission. In this process, an incident photon with the energy $h\nu$ is absorbed by an atom and subsequently a photoelectron with the kinetic energy E_{kin} is emitted, see Figure 4.4 [191].

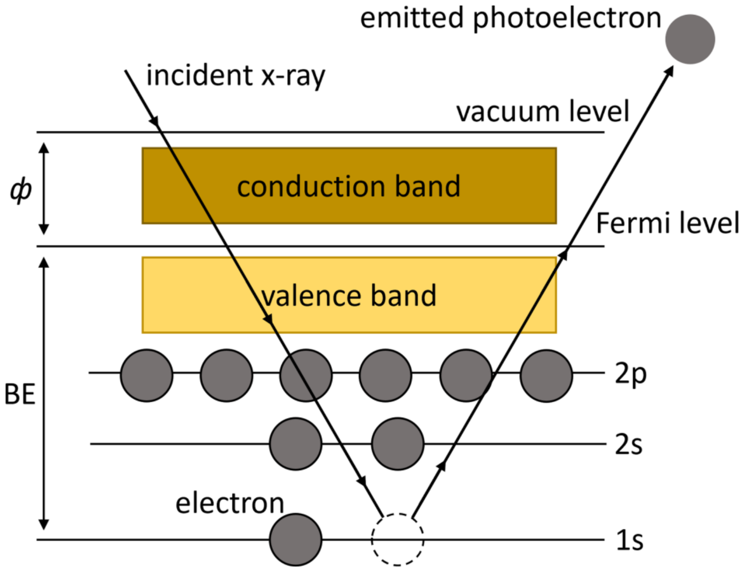

Figure 4.4: Schematic representation of a photoelectron emission initiated by an X-ray photon, with the binding energy BE and the work function ϕ of the spectrometer. Adapted with permission from [191]. Copyright 2014 Springer Science + Business Media New York.

With the binding energy BE and the work function ϕ, the E_{kin} of the photoelectron can be determined (Equation 4.5) [191].

$$E_{kin} = h\nu - BE - \phi \qquad \text{Equation 4.5}$$

The work function ϕ gives the difference in energy between the vacuum level and the Fermi level and represents the energy barrier that the electron must overcome to be emitted. Here ϕ varies with the chemical and electronic structure of the material surface and depends on the exposed crystallographic site. To reduce the influence of the radiation source on the E_{kin} of the photoelectron, monochromatic radiation is used, resulting in discrete binding energies. In addition, the results are plotted on a binding energy scale to avoid plotting the kinetic energy, which in turn depends on the radiation source (Equation 4.6) [191].

$$BE = h\nu - E_{kin} - \phi \qquad \text{Equation 4.6}$$

After photoelectron emission, the atom is in an excited state. During relaxation, an electron from an upper shell fills the previous position of the photoelectron. As a result, the orbital energy difference is released by X-ray fluorescence, emitting an X-ray photon or an Auger electron, as described in the previous chapter. The kinetic energy of the Auger electrons also depends on the energy of the X-ray source. Therefore, the energy is usually expressed in E_{kin} and can be compared with Auger spectra generated with electron beams. The emitted photoelectrons are collected by an electron energy analyzer consisting of a series of extraction lenses, a hemispherical energy filter, and a detector. The grounded sample is located next to the analyzer and the electrons are focused electrostatically. With this setup, it is possible to measure the orbital binding energy of Li and heavier elements with an energy resolution of < 0.3 eV. The binding energy of the different elements is strongly dependent on their atomic number and the respective orbital. In general, there is a trend toward increasing binding energies with increasing atomic number and increasing principal quantum number and angular momentum quantum number. This makes it possible to assign the measured binding energies to the corresponding elements. In addition, small shifts in the binding energy can occur, indicating a change in the chemical state and electronic structure of the material or its environment [191].

In this work XPS spectra were measured using a PHI5000 VERSAPROBE^{TM} III from PHYSICAL ELECTRONICS with a monochromatic A1 source with an energy of 1486.6 eV. XPS were measured for pristine LLZO powder, pressed *via* a hydraulic press, and on a fresh polished cathode side.

All energies of the spectra were calibrated with a gold foil before measurement, and an electron neutralization gun has been applied to avoid charge accumulation during measuring. The data were collected for 20 ms per step with 3 to 50 accumulation steps. The XPS fitting were done using Gaussian shaped line.

4.6 Time-of-flight secondary ion mass spectrometry

In time-of-flight secondary ion mass spectrometry (ToF-SIMS), a sample surface is bombarded with a beam of primary ions to generate secondary ions, which are measured based on their mass/charge ratio to quantitatively and qualitatively analyze elemental composition. During the measurement, the solid state character of the sample is maintained so that the chemical distribution is preserved. To generate secondary ions, the primary ion beam must be collimated and accelerated to a sufficient energy. When the primary ion beam hits the sample surface, the energy is transferred by elastic and inelastic collisions to particles on the surface, as well as to particles in deeper atomic layers. When a single atom on the sample surface or a group of them receives enough energy in a suitable direction, it can overcome the surface binding forces and leave the sample (desorption ionization) from the top 0.3 nm to 0.5 nm. Most secondary ions are the result of collisions with other atoms in the non-primary ion beam. The secondary ion is then generated at a distance of up to 10 nm from the initial impact, as shown in Figure 4.5. Therefore, the chemistry of the secondary ion is not directly affected by the primary beam. However, the primary ions can be implanted into the sample and their concentration can be increased [191, 195].

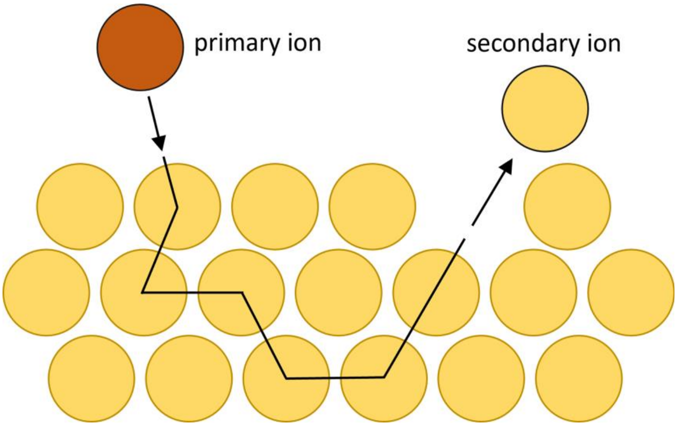

Figure 4.5: Schematic illustration of the collision of a primary ion with a sample, leading to energy distribution of energy to different atoms (indicated by the black line) and finally to the ejection of a secondary ion that, can be analyzed. Graphic adapted from [195].

In addition to monoatomic and polyatomic secondary ions, the impact can also produce electrons, photons, and re-sputtered primary ions. The secondary ions can be negatively or positively charged, and neutrally charged fragments can also occur. Various ion sources can be used for the primary ion beam, for example Ar_n^+, C_{60}^+, and Bi_n^+. The large cluster sources based on carbon fullerenes, Ar gas cluster and Bi cluster ions are mainly used for organic molecules. For ceramic materials, a primary ion beam of Bi^+ from a liquid metal source is usually used. For sputtering and depth profiling, Cs^+ and O^- ions are used, while $Cs^+$is used to detect negative secondary ions and O^- for positive ions. Charges are generated in the sample due to impinging ion beam. To compensate for this, a low-pressure Ar flow and/or a low-energy electron flood gun can be used [191, 195].

Mass analysis is then performed using a time-of-flight (ToF) system that separates the secondary ions according to their time in a flight tube without an electric or magnetic field. The ions are accelerated into this tube with a fixed potential extraction plate, which gives all ions the same kinetic energy. Since the kinetic energy E_{kin} (Equation 4.7) depends on the mass m, the velocity v can be used to separate the ions by their flight time through the tube [191, 195].

$$E_{\mathrm{kin}} = \frac{1}{2}\, m\, v^2 \qquad \text{Equation 4.7}$$

After passing through the tube, the ions are detected, and the time of flight is used to determine the mass (light ions travel the fast and heavy ions travel slow) [191, 195].

In this work a TOF.SIMS 5 machine from IONTOF GmbH was used, which was equipped with a Bi Nanoprobe primary ion gun, a Cs sputter gun and a low-energy electron flood gun for charge compensation. Additional charge compensation was applied by Argon main flooding at a pressure of $2 \cdot 10^{-6}$ mbar. Secondary ions were detected on an extended dynamic range detector. Bi^+ primary ions were chosen for analysis at an energy of 30 keV. The sputter gun operated at an energy of 2 keV. Depth profiles were taken in spectrometry mode in negative polarity in an analysis raster of 20 µm × 20 µm and a 64 × 64 pixel raster. The sputter raster was set to 100 µm × 100 µm. Before recording, the surface was pre-sputtered for 60 s to remove contaminants due to polishing and handling in air. During acquisition, the ion guns operated in non-interlaced mode using one analysis frame and one sputter frame. To analyze Co and Al gradients in the LCO-LLZO system, embedded, polished cross-sections were investigated *via* ToF-SIMS. Therefore, small field-of-view depth profiles of 20 µm × 20 µm were taken along the cross-section of the separator with 100 µm to 150 µm spacing between the analyzed areas, starting 50 µm apart from the original cathode interface. To mitigate beam fluctuations, intensity ratios of $^{59}Co^{16}O^-$ and $^{27}Al^{16}O^-$ species are normalized to the $^{16}O^-$ intensity. Averaged intensity ratios of each sputter area and over the sputter time are used for further analysis.

4.7 Electrochemical characterization

4.7.1 Electrochemical impedance spectroscopy

Electrochemical impedance spectroscopy (EIS) allows the nondestructive characterization of systems with multiple impedance elements, making it well suited for the study of batteries [196]. To measure impedance, a small-amplitude periodic perturbation (potential or current) is applied to the electrochemical cell at various frequencies from mHz to MHz and the response of the system is measured [197]. Usually, an AC potential is applied as the perturbation signal and the current is measured. To obtain accurate results, the system must be in steady state. This is achieved by holding the cell at a certain potential and superimposing a small sinusoidal potential with an amplitude of about ∼10-30 mV to obtain a pseudolinear cell response [196, 198]. In battery research, EIS measurements are often combined with galvanostatic charge/discharge measurements to monitor the change in cell impedance during cycling. The EIS measurements are usually performed at OCV potential after each charge and discharge cycle.

Impedance is a generalized complex and time-dependent form of the classical electrical resistance described by Ohm`s law ($R = \frac{E}{I}$). When an AC potential is applied to the cell, the impedance Z can be expressed by the Ohm's law for an AC circuit (Equation 4.8) [199-201],

$$Z\,(\omega) = \frac{E_t}{I_t} \qquad \text{Equation 4.8}$$

where ω is the angular frequency (related to the linear frequency f with $\omega = 2\,\pi\,f$). E_t and I_t are the potential and current at time t, respectively, which can be expressed by the following equations (Equation 4.9 and Equation 4.10) [199-201].

$$E_t = E_0\ \sin(\omega\, t) \qquad \text{Equation 4.9}$$

$$I_t = I_0\ \sin(\omega\, t + \phi) \qquad \text{Equation 4.10}$$

E_0 and I_0 are the amplitude (maximum values) of the potential and the current, and ϕ is the phase shift of the responding current versus the potential. With Equation 4.9 and Equation 4.10, impedance can be expressed as Equation 4.11 [199-201].

$$Z\,(\omega) = \frac{E_0\ \sin(\omega\, t)}{I_0\ \sin(\omega\, t + \phi)} = Z_0 \frac{\sin(\omega\, t)}{\sin(\omega\, t + \phi)} \qquad \text{Equation 4.11}$$

The impedance is generally represented by a complex function (Equation 4.12) [199-201],

$$Z\,(\omega) = Z_0 \exp\,(i\,\phi) = Z_R + i\,Z_I \qquad \text{Equation 4.12}$$

where i = $\sqrt{-1}$ is the complex number, Z_R is the real part, and Z_I is the imaginary part of the impedance [199-201].

The electrochemical impedance spectrum can be represented in different ways. Very common is the complex representation of the impedance (Nyquist plot), where the x-axis (Z_R), the real part represents the resistive part of the impedance and the y-axis (Z_I), the imaginary part represents the reactive part, which can be attributed to, e.g., capacitive behavior. Another possible plot is the Bode plot, which shows the amplitude and the phase shift as a function of frequency, with log $|Z|$ against log f or ϕ against log f [200]. The impedance data is usually analyzed by mathematical correlation using a physico-electrical model called the equivalent electrical circuit. In this model, electronic circuit components such as resistors R, capacitors C, constant phase elements CPE, inductors L, and Warburg diffusion elements Z_W are connected in series or parallel to model a real electrochemical process, for example charge transfer processes at various interfaces, diffusion processes, and electrical and ionic conductivity of the electrolyte or electrode materials [200, 202]. Resistors represent charge transfer reactions across interfaces and can also describe the movement of mobile charges (electrons or ions) through solid or liquid. The impedance of a resistor is equal to its resistance and is not frequency dependent (Equation 4.13). Capacitors model the capacitive charge (double layer capacitance) at various interfaces. The impedance of a capacitive element changes inversely with ω (Equation 4.14). The impedance of an inductor L is opposite to that of a capacitor, and is often used to model the inductive effects of metal contacts and wiring in the cell (Equation 4.15). Constant phase elements are used to model non-ideal capacitors due to surface roughness, irregularities, surface termination, porosity, or geometrical complexity. Their impedance is similar to that of the capacitors, but is additionally affected by Q, a non-ideal capacitance coefficient with a unit F $s^{\beta-1}$, with β as the ideality factor (β = 1 for an ideal capacitor, often between 0.8 – 1 for non-ideal capacitors) (Equation 4.16). The Warburg diffusion element is used to describe finite or infinite diffusion of mobile charges in solids and liquids. Here, the finite or infinite behavior is an important distinction, representing either open/reflecting boundaries or shortened/absorbing boundaries. The impedance of Warburg element is given by the equation in Equation 4.17, where σ_{rd} is the resistance associated with diffusion [202].

Table 4.1: Equivalent electrical circuit elements for the EIS analysis with their name, element symbol and the corresponding impedance contribution [202].

Element	Symbol	Impedance	Equation
Resistor		$Z_R = R$	Equation 4.13
Capacitor		$Z_C = \frac{1}{i\,\omega\,C}$	Equation 4.14
Inductor		$Z_L = i\,\omega\,L$	Equation 4.15
Constant phase element		$Z_{\mathrm{CPE}} = \frac{1}{(\omega\ \ C)^{\beta}\,Q}$	Equation 4.16
Warburg diffusion	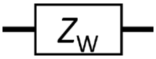	$Z_W = \frac{\sigma_{\mathrm{rd}}\sqrt{2}}{(\omega\ C)^{0.5}}$	Equation 4.17

To match the equivalent circuits to their physical counterparts in polycrystalline ceramics, the capacitance *C* can be used, which can be calculated according to Equation 4.18 [203-205].

$$C = \frac{(Q\,R)^{\frac{1}{\beta}}}{R} \qquad \text{Equation 4.18}$$

The capacitance values can then be used to assign the electronic circuit elements to the corresponding physical counterparts by comparison with the literature (Table 4.2) which often provides a good approach to the physics behind a semicircle [203].

Table 4.2: Capacitance values of different physical and electrochemical phenomena [203].

capacity (F)	physical counterparts
10^{-12}	bulk
10^{-11}	minor, second phase
$10^{-11} - 10^{-8}$	grain boundary
$10^{-10} - 10^{-9}$	bulk ferroelectric
$10^{-9} - 10^{-7}$	surface layer
$10^{-7} - 10^{-5}$	sample|electrode interface
10^{-4}	electrochemical reaction

In this work, EIS has been used to characterize the ionic conductivity of polycrystalline LLZO electrolytes in sintered pellets. The Nyquist plots of polycrystalline ceramics ideally show two semicircles corresponding to bulk and grain boundary resistance. However, for the LLZO pellets used in this work, the individual contributions could not be resolved with sufficient accuracy at RT, so a total resistance R_{tot} (the sum of all semicircles) was measured. The total ionic conductivity σ_{tot} was then calculated from R_{tot} and the pellet geometry (height *h* and area *A*) (Equation 4.19) [206].

$$\sigma_{\text{tot}} = \frac{h}{A\,R_{\text{tot}}} \qquad \text{Equation 4.19}$$

EIS were measured in this work with the potentiostat VMP-300 (BIOLOGIC) in a climate chamber (VT 4002EMC, VÖTSCH INDUSTRIETECHNIK) at 25 °C and 60 °C using an ECC-REF cell housing (EL-CELL®) or a modified T union body (SWAGELOK®). Before the measurement the surface of the samples were polished and subsequently coated with Au to generate a sufficient electrical contact to the complete sample surface. For the analysis of the Co-ion contaminated LLZO separators the sintered composite cathode was polished off. The measurement was done at frequencies between 7 MHz to 100 mHz with an electrical field perturbation of 10 mV. EIS measurements were done for electrolyte analysis, for battery cell analysis, and for critical current density measurements before and during electrochemical cycling. Measured impedance spectra in this work were fitted with the software ZView (SCRIBNER).

4.7.2 Galvanostatic charge and discharge

Galvanostatic charge and discharge is an important electrochemical characterization technique in battery research to obtain information about the capacity, rate performance and cycling stability of the cell and its components [207]. In this technique, a constant current (often expressed as a C-rate) is applied for a specified time and the voltage response of a battery is recorded [207]. In a variation of this technique, called galvanostatic cycling with potential limitation (GCPL), a current is applied until a specified upper cutoff potential is reached; then the direction of the current is inverted and the battery is polarized until the lower cutoff potential is reached. The charge and discharge cycle can be repeated several times to test the cycling stability of the battery.

The product of the applied current and time gives the charge (capacity), which is usually normalized to the active material loading (Ah g^{-1}) or electrode area (Ah cm^{-2}) [207]. In battery research, the charge and discharge rate is usually expressed as the C-rate (h^{-1}), which indicates how many times the full theoretical capacity can be reached within 1 hour at constant current. For example, 1C is equivalent to charging or discharging full capacity in 1 hour. Higher and lower C-rates correspond to faster and slower charge and discharge rates, respectively [207]. Coulombic efficiency is calculated as the ratio of the capacities during discharge and charge (Equation 4.20) [207].

$$\text{Coulombic efficiency (\%)} = \frac{Q_{\text{discharge}}}{Q_{\text{charge}}}\ 100\% \qquad \text{Equation 4.20}$$

During initial charging, an irreversible process often occurs in which a certain amount of energy is used for secondary reactions such as oxidation or reduction of active electrode materials, electrolyte, surface impurities or water with formation of interfacial layers[207, 208].

In this work, GCPL characterization was performed using VMP-300 potentiostat from BIOLOGIC. The pure LCO cathodes were analyzed at 25 °C with an applied current density of 0.44 µA cm^{-2}. The full cell tests of the laser sintered and electrolyte supported composite cathodes were performed in a climate chamber (VT 4002EMC, VÖTSCH INDUSTRIETECHNIK) at 60 °C with GCPL. The laser sintered battery was charged in GCPL between 3 V and 4 V vs. Li with different currents depending on the C-rate, and the voltage was then kept at 4 V until the current declined to 1 µA. The electrolyte supported cell was electrochemically cycled between 2.8 V and 3.6 V vs. Li-In with a constant current of 20 µA (current density of 25.3 µA cm^{-2} and a C-rate of 0.1 C with respect to the anode area). In the charging process, the voltage was maintained at 3.6 V vs. Li-In until the current declined to 10 µA. EIS started after 5 min of OCV with a frequency varied from 3 MHz to 100 mHz and an electrical field perturbation of 10 mV.

4.7.3 Critical current density

Lithium dendrite formation can be studied with capacity-controlled galvanostatic cycling with increasing current density. When the critical current density (CCD) is reached, the dendrite forms. Between galvanostatic charge and discharge steps, the cells can also be measured with EIS. When a dendrite starts to form, the thickness of the separator is virtually reduced, thus changing its impedance. The stripping and plating of the Li metal anode is verified by observing the voltage plateaus during each charge and discharge step. When the anode no longer has complete wetting of the anode|electrolyte interface, this can be seen by a change in the voltage plateaus [209, 210].

For the CCD investigation in this work, thin Li foils were pressed onto both sides of the LLZO pellets and heated for a better contact. The symmetric cell was then placed inside a modified T union body (SWAGELOK®). The CCD measurements were performed with the potentiostat VMP-300 (BIOLOGIC) in a climate chamber (VT 4002EMC, VÖTSCH INDUSTRIETECHNIK) at 60 °C with capacity controlled galvanostatic cycling with an increasing current density, starting at 50 µA cm^{-2} with an increment of 50 µA cm^{-2} per cycle (three times stripping and plating), recording a datapoint every 30 s. Every 100 µA cm^{-2} EIS were measured between 3 MHz to 1 Hz and additional datapoints were recorded if the voltage showed a deviation of more than 10 mV from the previous datapoint and fitted with the equivalent circuit shown in Figure 4.6.

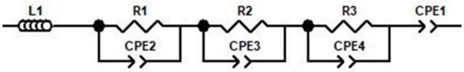

Figure 4.6: Equivalent circuit for the fitting of the symmetric Li cells for the CCD measurements (L is inductance, R is ohmic resistance, and CPE is constant phase element). Copyright Wiley-VCH GmbH. Reproduced with permission [211].

4.7.4 Linear sweep voltammetry and cyclic voltammetry

In linear sweep voltammetry (LSV), the potential is swept linearly as a function of time with a defined scan rate in a specified potential range and the current is recorded [212-214]. In another variation of this technique, cyclic voltammetry (CV), the direction of potential scan is reversed and the measurement is repeated several times. The resulting current-potential curve (voltammogram) provides general information about the processes at the electrode, such as the type of process (capacitive or faradaic), the number of redox reactions or redox steps, and the oxidation or reduction potentials of the electrochemical reactions. The scan rate can be varied over a very wide range, allowing the study of the kinetics of electrochemical reactions [212]. The LSV and CV are widely used in battery research to study the electrochemical performance of active electrode materials or to determine the electrochemical stability window of electrolytes [207, 213, 214].

In this work, LSV was used to investigate the electrochemical performance of solid cathodes and separators of garnet-based batteries. To investigate the electrochemical properties of LLZO pellets, they were polished and then coated with a Au electrodes to ensure sufficient electrical contact [215]. The LSV measurements were done with the potentiostat VMP-300 (BIOLOGIC) in a climate chamber (VT 4002EMC, VÖTSCH INDUSTRIETECHNIK) at 25 °C from −1 V up to 2 V with a voltage change of 5 mV s^{-1}.

4.8 Further characterization methods

Particle size analysis were performed by laser diffraction (LA 950V2, HORIBA) with the Mie-theory in ethanol.

Optical absorption, transmission and reflection measurements were performed with a UV-Vis NIR spectrometer (1050 LAMBDA, PERKIN ELMER).

Electron backscatter diffraction (EBSD) the LLZO electrolyte was polished using 0.5 µm and 0.1 µm diamond polishing compounds with glycol-based diamond extender (EcoMET 300 Pro, Buehler). For each polishing step, 10 N of force was applied to the LLZO electrolyte sample, and the head and base were rotated at 210 rpm and 60 rpm, respectively. An additional polishing step was performed with 0.03 µm colloidal silica suspension on a felt pad using a lapping fixture (PELCO 15000 micrometer-controlled lapping fixture, Ted Pella). The EBSD measurements were conducted using an EBSD detector and TEAM software on a MIRA3 FEG-SEM (Tescan). The collected data was analyzed using the EDS OIM data collection software. The EBSD datasets were refined by dilating the grains in a single iteration and correcting for pseudosymmetry, where appropriate.

Molecular dynamic (MD) simulations were performed using *LAMMPS* software with the Verlet integration algorithm and the Nosé–Hoover thermostat [216, 217]. The interatomic potentials were described by neural-network-based machine-learning models trained for pure and Co-doped LLZO and LCO|LLZO interfaces using the *n*2*p*2 code [218-220]. The cubic $Li_{6.625}La_3Zr_2O_{12}$ structure without Co-ions was modeled using a 2 × 2 × 2 replica of a cubic $Li_7La_3Zr_2O_{12}$ unit cell with a = 13.0035 Å lattice constant [104] and by removing three Li-ions per unit cell. The cubic $[Li_{6.625}Co_{0.125}]La_3Zr_2O_{12}$ structure was modeled by adding one Co-ion per unit cell at Li sites in the cubic $Li_{6.625}La_3Zr_2O_{12}$ model. To extract diffusion properties, the MD simulations were performed for 1 ns (with a 0.5 fs time step) under the NVT ensemble at 800 K, 1000 K, 1200 K, and 1400 K. The diffusivity D was calculated using the mean squared displacement (MSD) of Li ions over time (Equation 4.21),

$$D = \frac{1}{2\,n\,d\,t}\sum_{i=1}^{n}|\boldsymbol{r}_\mathrm{i}(t_0 + t) - \boldsymbol{r}_\mathrm{i}(t_0)|^2 \qquad \text{Equation 4.21}$$

where d is the dimensionality of the system, n is the total number of mobile species in concern, and $\boldsymbol{r}_\mathrm{i}(t_0)$ and $\boldsymbol{r}_\mathrm{i}(t_0 + t)$ are the positions of ion i at initial time t_0 and after time t passes from t_0. The average and standard deviation of the diffusivity were obtained from ten separate MD simulations at each temperature. The activation energy E_a of ion migration was obtained from the Arrhenius equation (Equation 4.22),

$$D = D_0 \mathrm{e}^{\frac{-E_\mathrm{a}}{k_\mathrm{B} T}} \qquad \text{Equation 4.22}$$

where D_0 is the prefactor, k_B is the Boltzmann constant, and T is temperature. The coherent $\sum 13(230)/[001]$ symmetric tilt grain boundary model was generated by rotating the cubic $Li_7La_3Zr_2O_{12}$ lattice grains along [001] axis by 22.62° and overlaying them to create a (230) GB plane with a ∑13 coincident-site lattice and 2 Å vacuum thickness between grains [221]. The grain boundary model was equilibrated at 1300 K under the NPT ensemble for 2.5 ns (with a 0.5 fs time step) and the lattice cell and atomic positions were relaxed while maintaining α, β, and γ lattice angles as 90°. Then, three Li-ions within the grain interior regions were replaced by one Co-ion randomly to model ∑13(230)/[001] grain boundary with $[Li_{6.625}Co_{0.125}]La_3Zr_2O_{12}$ stoichiometry. The final structure has 416 formula units (9880 atoms) with $a = 26.171$, $b = 46.718$, and $c = 96.121$ Å lattice parameters. For this grain boundary model, an MD simulation was performed for 10 ns (with a 2 fs time step) at 1300 K under the NVT ensemble. The concentration profile was obtained by counting ions within 53 contiguous rectangular regions in the grain boundary cell and normalized by the total number of ions for each species, which was averaged with a time window between ± 100 ps at a given time for smoothening (using atomic snapshots every 1 ps). The positional probability densities were evaluated by subdividing the cell into a grid of 0.26 × 0.26 × 0.26 $Å^3$ cubes. The density was determined by the number of time steps for which each mesh was occupied by ions [222], which was normalized by the total number of ions and time steps and divided by the cube volume. The trajectories for 1 ns every 5 fs and for 10 ns every 50 fs were used for the c-LLZO and the grain boundary, respectively, to calculate the probability density. The heatmap of the probability density for the grain boundary was obtained by integrating the density along the direction normal to the structure figure in S-Figure 27A (*a*-direction). Visualization of atomic structures was done by *VESTA* software [223].

5 Sintering of LCO layers on steel substrates using rapid thermal processing

This chapter was published in *Thin Solid Films*, **2022**, *749*, 139177, with the title *Rapid thermal sintering of screen-printed $LiCoO_2$ films*, by Walter Sebastian Scheld, Sandra Lobe, Sven Uhlenbruck, Christian Dellen, Yoo Jung Sohn, Linda Charlotte Hoff, Frank Vondahlen, Olivier Guillon, Dina Fattakhova-Rohlfing. Copyright Elsevier (**2022**).

Link to the published article: https://doi.org/10.1016/j.tsf.2022.139177

Walter Sebastian Scheld fabricated the samples, performed the electrochemical and phase characterization, analyzed all data, and wrote the manuscript with contributions from all authors. Christian Dellen took the SEM images and performed the EDS measurements. Yoo Jung Sohn conducted the HT-XRD measurements. Linda Charlotte Hoff measured the UV-Vis. Frank Vondahlen assisted the RTP processing. Sandra Lobe, Sven Uhlenbruck, Olivier Guillon, and Dina Fattakhova-Rohlfing initiated the idea, provided the resources, and supervised the work.

In previous publications concerning screen-printed LCO layers, Al_2O_3 or Si-wafers, with Pt coatings were used as current collectors and substrate materials [50, 224-226]. These current collectors however required an additional step to apply Pt and are rather cost-intensive. A more suitable setup would be to print directly onto a thin electrically conductive and comparatively low-cost substrate, like a high temperature stable stainless steel substrate. In doing so, a whole production step can be skipped by directly bonding the current collector to the cathode, which provides additional mechanical strength. With this design the current collector can be used as a bipolar interconnector for battery stacking applications.

In this study, we investigated the applicability of the RTP system to the densification of LCO layers. A rapid processing route was developed, so that dense LCO cathode layers can be fabricated on a stainless steel *via* a combination of the economical screen-printing process and photonic sintering with RTP. The resulting cathodes were tested electrochemically by using a liquid electrolyte for cell tests (Figure 5.1).

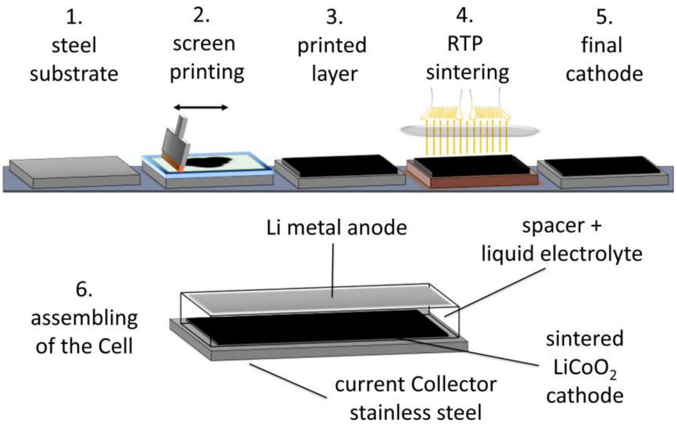

Figure 5.1: Schematic representation of the various steps in the fabrication of the cathode layers and the setup for the subsequent electrochemical testing.

5.1 Optical properties

Screen-printing of a slurry of LCO powder on a stainless steel substrate produces homogeneous, black colored and flat layers. The black color of the layer system is important for the followed densification step with the photonic sintering by RTP. Since the RTP furnace generates a continuous radiation by incandescent filaments at around 3000 K, the intensity of the radiation is very high in the visible and the near infrared range. An optical absorption measurement of a pressed and binder removed LCO layer on steel (Figure 5.2) reveals a high optical absorption of the system in the visible and near infrared range, consequently resulting in a high energy transfer from the radiation source to the sample. This high energy transfer makes photonic sintering possible, since only in this way rapid heating rates of 600 K min^{-1} can be realized inside the layer with the RTP furnace.

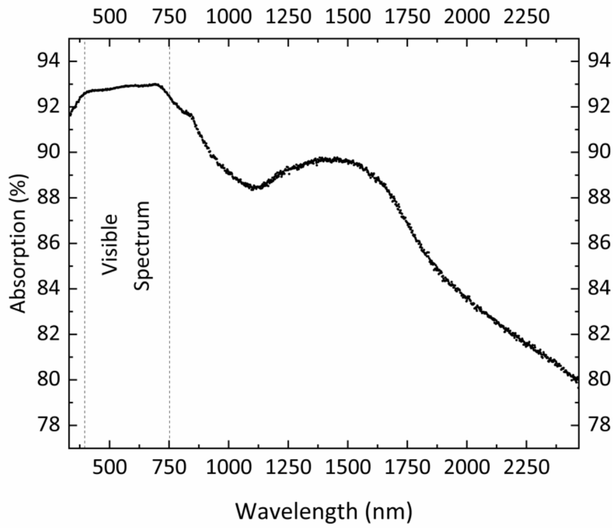

Figure 5.2: Optical absorption measurement of a pressed and binder-removed LCO layer on steel in the visible spectrum and part of the near infrared spectrum [43].

As can be seen from the optical images (Figure 5.3), the samples heated to 700 °C, 800 °C and 900 °C show no observable change of their surface after the RTP treatment, while the samples heated at 1000 °C and 1050 °C had a circular change in color. The macroscopic surface change of the sample suggests that certain processes such as sintering of the LCO could take place at around 1000 °C. The inhomogeneous surface indicates that the sample had probably a temperature gradient from the middle to the edges. In the further analysis, the inner part of the samples was investigated.

Figure 5.3: Heat treated samples of LCO printed on EN1.4767 substrate (Ø 17 mm) with their process temperature [43].

5.2 Microstructural Investigation

SEM images (Figure 5.4) confirm the suggestion that no sintering takes place at temperatures below 1000 °C. While no significant sintering is observed for the 900 °C treated sample with only slightly altered shape of the initial particles (Figure 5.4A-B), for the samples treated at

1000 °C (Figure 5.4C) a pronounced sintered smooth and homogenous surface is observable. The lower limit at which the material starts to sinter in the RTP process must therefore be between 900 °C and 1000 °C. So far, pure LCO material was sintered as a cast tape at 1270 °C for 10 h, while hot pressed pellets were sintered at 950 °C for 5 h with 20 MPa [227, 228]. Using sintering additives such as Li_3BO_3, the temperature could be reduced to 700 °C and 1 h dwell time[166]. In contrast, the RTP sintering of LCO films allows an immense reduction of the processing time at the elevated temperatures, as the entire heat treatment process with heating and dwell time takes only 90 s at a maximum temperature of about 1000 °C.

The initial particles have grown into two-dimensional coherent connected structures with sizes ranging from 8 µm to 15 µm. Considering the starting particle size of D_{10} 1.7 µm, D_{50} 5.9 µm, D_{90} 11.9 µm, the particle size difference illustrates the grain growth and the associated sintering step that has taken place. The back scattered electron image (Figure 5.4D) demonstrates that some small cracks have formed. Since the coefficient of thermal expansion of the EN 1.4767 ($1.22 – 1.48 \cdot 10^{-5}\ K^{-1}$ at 100 °C – 900 °C according to the manufacturer), LCO ($1.3 \cdot 10^{-5}\ K^{-1}$ at 50 °C – 400 °C) [229] and Al_2O_3 thin films ($1.3 \cdot 10^{-5}\ K^{-1}$ at 300 °C and $3.9 \cdot 10^{-5}\ K^{-1}$ at 1073 °C) [230] are close to each other, the reason for the cracks is probably sintering mismatch induced by the densification of LCO on the stiff substrate which very likely does not shrink during the heat treatment. In addition, the image shows some planar LCO structures vertical to the sintered layer. It is possible that this orientation has an influence on the performance of the electrode, since the ionic conductivity in LCO is depending on the spatial orientation [231]. In contrast, the back scattered electron image of the 900 °C treated sample (Figure 5.4B) does not show any of these structures. For this reason, their origin is probably attributable to the sintering process at 1000 °C.

At the bottom of the fracture cross-section of the 1000 °C treated specimen (Figure 5.4E) with an average LCO layer thickness of ∼15 µm the steel substrate is visible and the sintered LCO layer is on top. Based on this image, the LCO layer is sintered through its entire thickness. A gap between the layer and the steel substrate has formed, as the layer has detached from the steel during the fracture preparation. Evidence of the bond between LCO and the steel is given by a polished cross-section image (Figure 5.4F) with an adherent layer on the substrate.

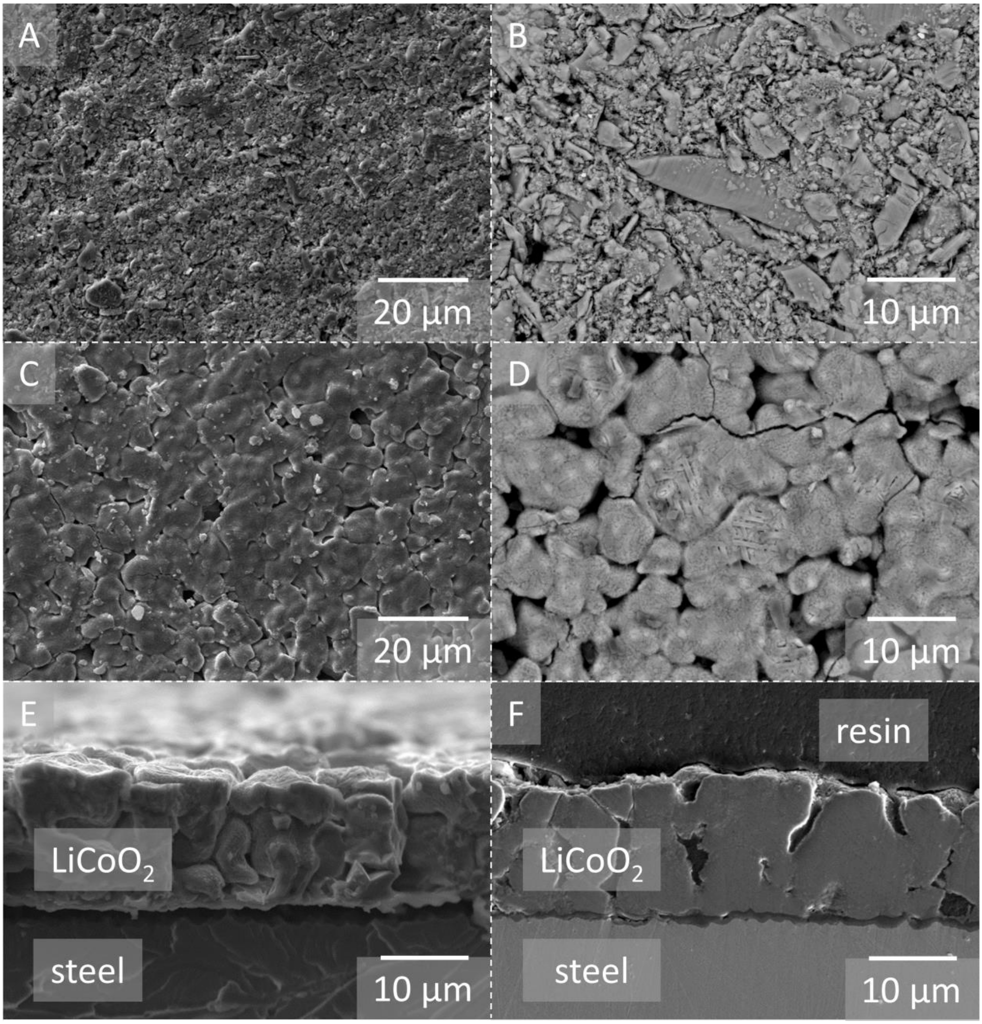

Figure 5.4: SEM images of heat treated LCO samples. A) secondary electron image of the 900 °C sample; B) back scattered electron image of the 900 °C treated sample; C) secondary electron image of the 1000 °C sample; D) back scattered electron image of the 1000 °C treated sample; E) secondary electron image of a fractured cross-section from the 1000 °C treated sample; F) secondary electron image of a polished cross-section of the LCO sample treated at 1000 °C [43].

The EN 1.4767 steel substrate consists mainly of Fe, Cr and Al. At high temperatures, an Al_2O_3 layer in general forms on the steel, which serves as a passivation layer [232]. In the polished cross-section, this passivation oxide is observable as a continuous layer below the LCO film and between the cathode and the substrate (Figure 5.4F). The cathode film has sintered with the passivation layer and these have detached from the steel together.

EDS measurements of the electrode cross-section (Figure 5.5) show clearly defined areas of each layer (Co: cathode, Al: Al_2O_3 passivation layer, Fe: steel substrate). It cannot be excluded that some ion interdiffusion takes place at the LCO|Al_2O_3|steel interface with formation of, *e.g.*, $LiAlO_2$ due to lithium diffusion into the Al_2O_3 phase [85] or $LiAl_yCo_{1-y}O_2$ [233] due to Al diffusion into the LCO structure. However, EDS measurements do not provide any unequivocal evidence of such reactions. Low intensity Al signals can be found in LCO above the passivation layer, but only in the areas where the morphology of the cathode not planar. Due to this morphology dependency the signals are not necessarily an indication for the mentioned $LiAl_yCo_{1-y}O_2$ phase but may possibly be an effect of a height difference in the measurement.

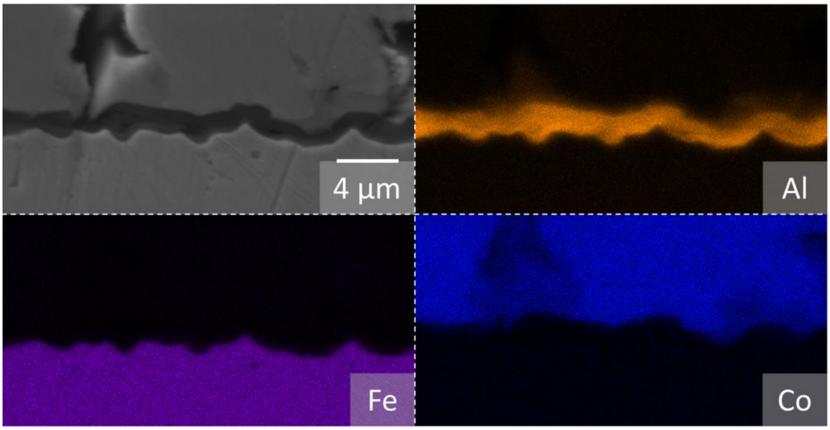

Figure 5.5: EDS Mapping of the LCO|Al_2O_3|steel between the steel substrate at the bottom and the cathode on top with a secondary electron image of the measured area and the element mappings of Al (orange), Fe (purple) and Co (blue) [43].

With an even higher sintering temperature of 1050 °C, the surface has less pores, but also the number and size of cracks are increasing (Figure 5.6A). It is possible that the origin of the cracks is given by areas with greater distance to the surrounding material, and thus at higher temperatures the sintering of the material in this area is prevented and the cracks become wider due to the sintering of the material on both sides of the initial spacing. Another origin could be a temperature induced bending of the substrate. The planar, vertical LCO structures are also observable at 1050 °C (Figure 5.6B).

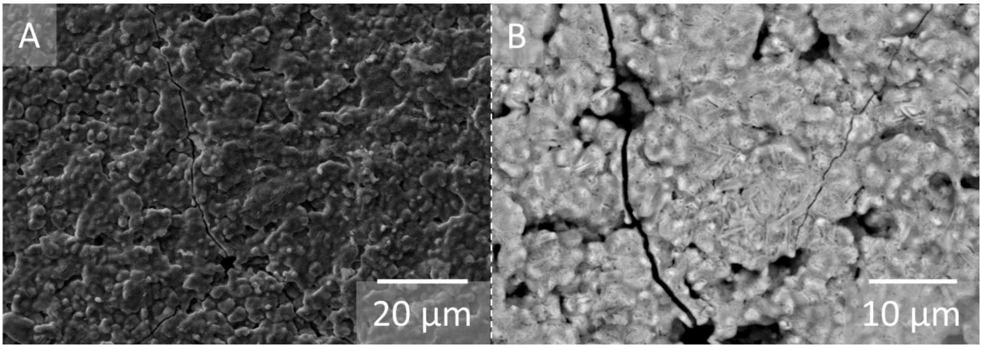

Figure 5.6: SEM images of heat treated LCO samples at 1050 °C. A) secondary electron image of the sample; B) back scattered electron image of the sample [43].

5.3 Phase characterization

The chemical stability of the LCO layers against the EN 1.4767 steel was investigated by *in situ* HT-XRD (Figure 5.7A). It must be mentioned that the Bragg reflections have a shift to lower angles due to the thermal expansion of the sample. The shown LCO reference (ICDD 00 016 0427) refers to RT. The LCO phase is observable up to 1000 °C. However, a decomposition of the LCO phase starts at 1000 °C, and an additional CoO phase (ICDD 01 070 2855) is detected. At 1100 °C a full decomposition takes place and the reflections of LCO are no longer present, and only the CoO phase can be observed. It can be however concluded, that even if a small amount of side phases is formed, the selected steel provides a suitable chemical stability to the CAM in the required sintering temperature range up to 1000 °C.

The ex-situ XRD analysis of the RTP treated LCO samples (Figure 5.7B) reveals the existence of a phase pure rhombohedral structure until 900 °C. At higher temperatures, besides the main LCO phase, CoO is observable as secondary phase, similar to the HT-XRD measurements. Additionally, the LCO reflections are becoming broader with higher temperature, possibly due to a loss of crystallinity. Due to the layer thickness the 900 °C and 1000 °C treated samples show reflexes of the steel substrate.

The secondary phases with the steel substrate and its passivation layer discussed above could not be determined due to a large thickness of the cathode layer preventing detection of any phases beneath the LCO layer.

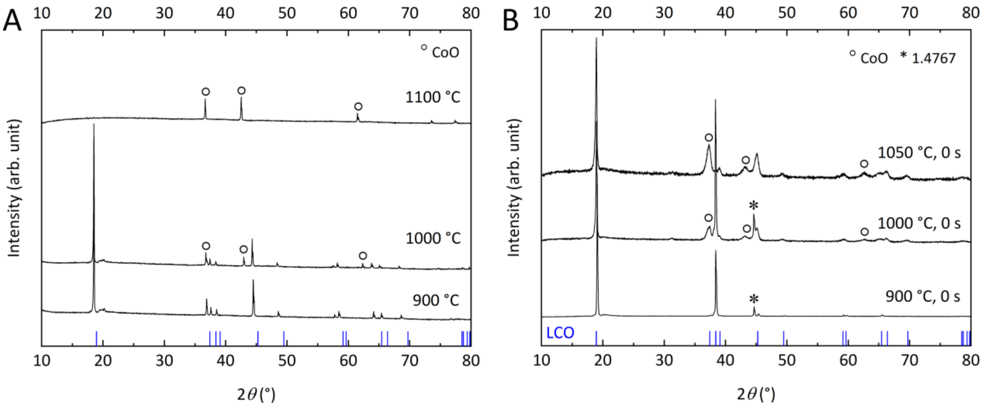

Figure 5.7: XRD measurements of LCO films on EN 1.4767 steel after different heat treatments with references of LCO (shown in blue, ICDD 00 016 0427) and CoO (ICDD 01 070 2855). A) in-situ HT-XRD measurements with a heating rate of 5 K min^{-1} and each measurement took 24 min. The reflections show a shift to lower angles due to the increased temperature; B) RTP sintered samples [43].

In addition to the XRD data, Raman spectra of the LCO samples treated at different temperatures were measured to assess the phase composition (Figure 5.8). The LCO material has two vibrational modes (A_{1g} and E_g), which are observable by Raman spectroscopy and belong to the rhombohedral lattice with the space group $R\bar{3}m$ [234-236]. These two signals are observable at all measured spectra (Figure 5.8) at 488 cm^{-1} (E_g), 597 cm^{-1} (A_{1g}) and at 1170 cm^{-1} where a broad A_{1g} overtone is existing and thus show evidence of the presence of the LCO phase in the RTP treated samples [234, 237]. With higher temperatures, the wavenumber shows a small shift to lower wavenumbers. The 1000 °C sample has the A_{1g} at 595 cm^{-1} and at the 1050 °C sample the A_{1g} is at 593 cm^{-1}. The shift indicates a loss of Li atoms within the lattice, which is more pronounced at higher temperatures [238].

Besides LCO, signals of Co_3O_4 are observable at 534 cm^{-1} and 680 cm^{-1} as side phase, signed with (°) [239]. The line broadening of the LCO signals indicates an increased disorder in the crystal structure. Including the stronger signal of Co_3O_4 a loss of lithium atoms is the most probable. However, since no other Li residues like Li_2O and just small signals of Li_2CO_3 at 1090 cm^{-1} are detected, there could also be a random distribution of Li atoms between the LCO layers in the lithium planes of the crystal [240]. This random distribution, which is already described in literature [235], is possibly leading to the observed broadening. Nevertheless, the Raman measurements, like the XRD measurements, show the main phase is LCO even after the high temperature treatment.

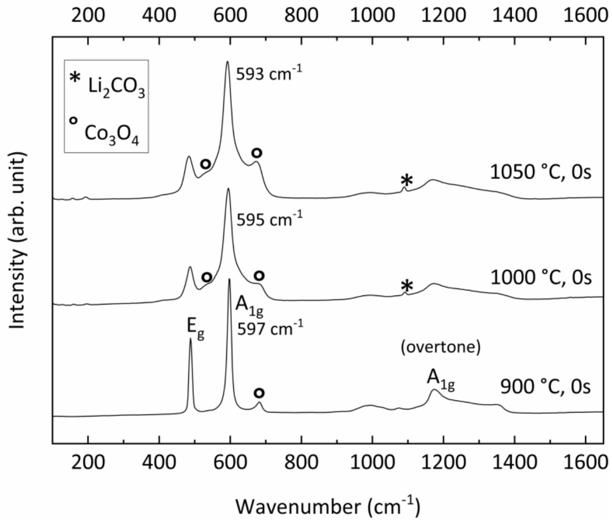

Figure 5.8: Raman spectra of differently treated LCO samples with signed secondary phases and the wavenumber of the A_{1g} LCO Signal [43].

5.4 Electrochemical investigation

Although the results of the SEM, XRD and Raman measurements demonstrate a densification of the LCO layers at 1000 °C without significant phase changes, the electrochemical performance of such layers still needs further optimization. The first three galvanostatic cycles (Figure 5.9A) with liquid electrolyte demonstrate that the screen-printed LCO layers are electrochemically active after the RTP sintering process at 1000 °C, as the characteristic plateaus of LCO charge and discharge are observed at a potential around 3.9 V [241]. However, the capacity utilization in a thick layer is relatively low, as only around 52 mAh g^{-1} has been reached in the first charging cycle, with a fast capacity degradation in the subsequent cycles. Due to the low ionic conductivity of LCO, the thickness of the cathode layer is probably hindering efficient lithiation and delithiation inside the cathode. Compared to conventional LCO cathodes, the relative layer thickness of the RTP sintered layer is larger, considering the aspects that the layer is sintered and thus has a higher density than the binder-bonded cathodes, and additionally it is a pure LCO layer without conductive additives such as carbon black. Also, some cobalt oxides side phases were found by Raman spectroscopy and XRD

measurements. These oxides are a direct result of the lithium loss in the LCO and therefore also generate a reduction in capacity.
In comparison, cell tests with cathodes produced at 900 °C and 1050 °C show (Figure 5.9B) a significantly lower capacity utilization in the lower µAh g^{-1} region for the 1050 °C treated sample and even lower capacity utilization for the 900 °C treated sample. The low capacity values for the 900 °C treated sample are not surprising, since a large part of the cathode is inaccessible due to insufficient sintering and a poor contact with the current collector. For the sample produced at 1050 °C, the loss of connectivity within the electrode layer and the respective reduction in capacity utilization can be attributed to the formation of cracks discussed above. Furthermore, for this sample formation of the higher amount of cobalt oxides is detected by the Raman spectroscopy and XRD measurements, which can also reduce the specific capacity of the cathode. Cell tests demonstrate a very strong effect of the temperature on the performance of RTP sintered cathodes. The temperature should be therefore selected very precisely within a narrow range between 900 °C to 1050 °C to achieve satisfactory electrochemical performance.

The time and energy savings mentioned above compared to conventional production routes offer great potential for the commercial application of battery technology using screen-printing and RTP. However, the capacity of the cathodes must be increased, and a suitable method of electrolyte deposition and sintering must be developed for a functional half-cell production. The use of a composite instead of a pure cathode layer is also conceivable to increase the ionic conductivity within the cathode layer. If these obstacles are overcome, industrial upscaling of the manufacturing processes would be easy, since the layer thickness can be adjusted and the printed area can be increased and handled in RTP, allowing significantly higher throughputs of material to be processed.

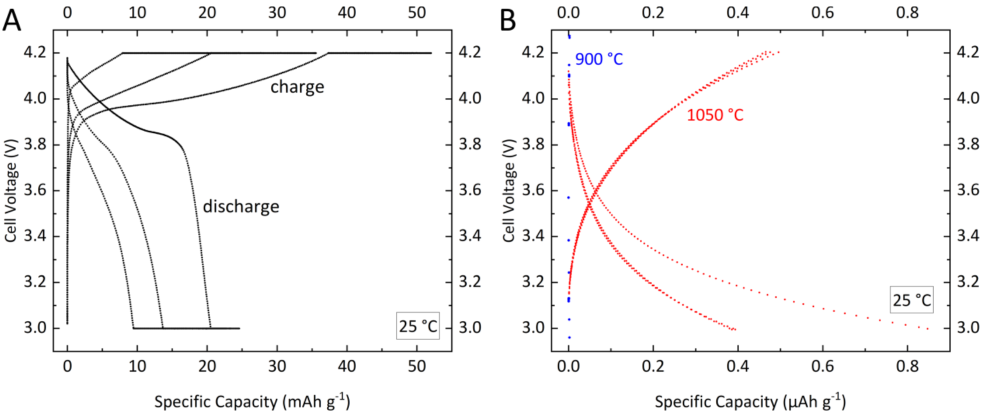

Figure 5.9: Charge and discharge capacity vs. cell voltage different sintered LCO films performed with 1 M LiPF6 in EC/DMC as electrolyte and Li metal as anode between 3.0 V and 4.2 V. A) LCO layer sintered at 1000 °C; B) LCO layers sintered at 900 °C (blue) and 1050 °C (red) [43].

5.5 Sintering of LLZO layers on steel substrates using rapid thermal processing

The sintering of LCO on the steel substrate was an important first step towards the sintering of a composite cathode of LLZO and LCO on steel. To study the components and their reaction with the substrate individually, LLZO was printed on steel substrates using the screen-printing processes and sintered subsequently with RTP. In contrast to the LCO coatings, which were successfully sintered at 1000 °C without a holding time, LLZO proved to be much more difficult to sinter. Even after a holding time of 5 min, no initial signs of sintering behavior like sinter necks were evident and the first minor phases such as pyrochlore $La_2Zr_2O_7$ appeared in the XRD (Figure 5.10A-B).

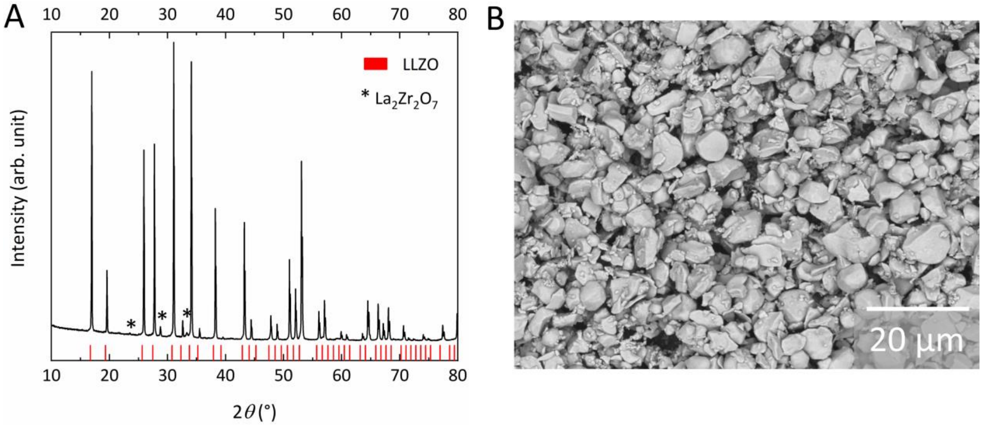

Figure 5.10: XRD measurement and SEM image of the RTP sintered LLZO films on the steel substrate RTP sintered at 1000 °C for 5 min. A) XRD measurement with LLZO reference pattern (ICDD 99 000 0032); B) SEM top view image.

With longer holding time, also no sintering could be achieved and the phase formation of $La_2Zr_2O_7$ was enhanced.

5.5.1 Influence of the sintering atmosphere

The $La_2Zr_2O_7$ phase is formed mainly by the loss of Li from the LLZO structure. Since passivating oxide layers form at higher temperatures or longer holding times on steel substrates, which have already been discussed for the LCO layers, it is also conceivable that these layers can incorporate Li from the LLZO structure and thus cause delithiation of the LLZO. To test this degradation theory, HT-XRD measurements of LLZO layers on steel were performed in air and in Ar atmosphere (Figure 5.11A-B).

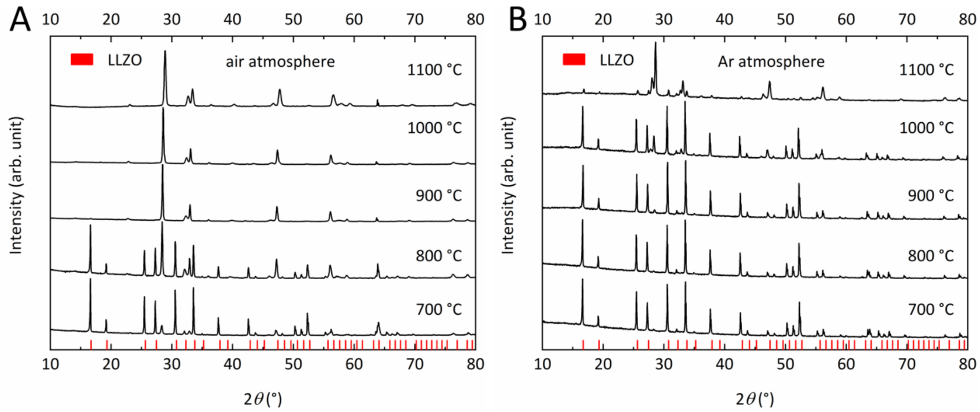

Figure 5.11: In-situ HT-XRD measurements with a heating rate of 5 K min^{-1} and each measurement at different temperatures took 24 min with LLZO pattern (ICDD 99 000 0032). A) air atmosphere; B) Ar atmosphere.

The measurements show that already at 900 °C in air the LLZO phase was decomposed. The main secondary phase is again the pyrochlore phase $La_2Zr_2O_7$ with the prominent reflex at 28.8°. In contrast, the sample heated in Ar shows significantly higher stability up to 1100 °C. At 1100 °C, the sample also decomposes and the pyrochlore phase is also formed. These two measurements are a clear indication that in oxidative atmospheres the LLZO phase is less stable and thus strengthens the theory that Li from the LLZO phase is incorporated into the passivation layer of the steel.

5.6 Sintering of composite cathode layers on steel substrates using rapid thermal processing

The attempt to sinter the two components LLZO and LCO together as a composite cathode on the steel substrate led to a strong degradation of both. Already at 700 °C it can be seen in the XRD (Figure 5.12A) that on the one hand the reflections of LLZO have a very low intensity and on the other hand reflections of $LaCoO_3$ and CoO can be seen as decomposition products. In the SEM image of the sample (Figure 5.12B), an initial sintering can already be found, but the porosity is still high. Attempts to increase the density by means of higher temperatures resulted in significantly stronger degradation. At 800 °C the LLZO phase pattern disappeared completely and $LaCoO_3$ and CoO reflexes become stronger, while at 900 °C also the LCO phase pattern disappeared and the side phases become the main phase. These measurements show that the combination of the LCO and LLZO phases on steel is significantly less stable than the two phases individually. While the LLZO phase alone is stable in the RTP process at 1000 °C (Figure 5.10A) and LCO at 1050 °C (Figure 5.7B), the LLZO phase in the composite already decomposes at 800 °C and the LCO phase at 900 °C. However, in literature full ceramic cells with the same composition on LLZO substrates show a much higher stability up to 1050 °C in conventional furnaces [25]. The instability must therefore be conditioned to the steel substrate. This instability can probably be explained by the fact that the delithiated phases, which lose their Li to the passivation layer, exhibit increased reactivity, thus enhancing the formation of $LaCoO_3$. For successful sintering of the composite, the ion diffusion between the cathode and the passivation layer would have to be reduced. Conceivable possibilities for this would be a protective layer between the passivation oxide of the steel and the cathode, or the cathode would have to be selectively heated. In the latter case, the steel would be heated less and thus form less passivation oxide. Additionally, the reactivity of the oxide would also be lowered due to the lower temperature.

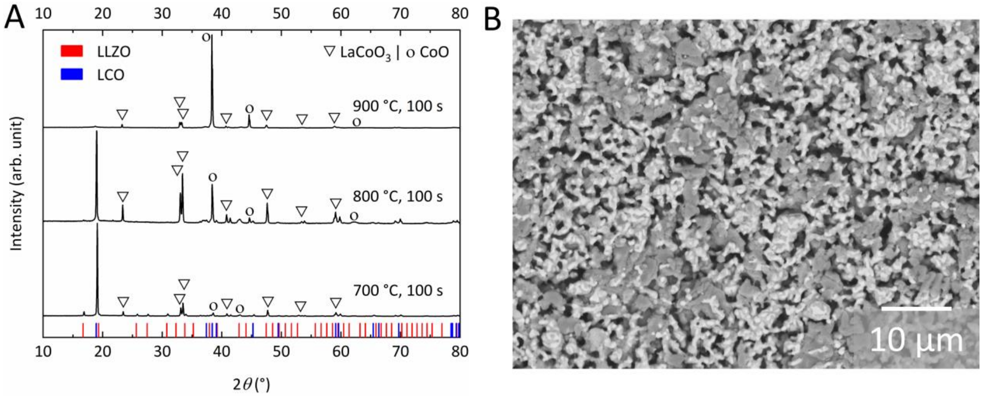

Figure 5.12: XRD measurement and SEM image of the RTP sintered composite cathode layers on the steel substrate RTP sintered at different temperatures for 100 s. A) XRD measurement with LLZO (ICDD 99 000 0032) and LCO (ICDD 00 016 0427) reference pattern; B) SEM top view image of the sample treated at 700 °C.

6 Laser sintering of composite cathodes on steel substrates

This chapter was published in *Applied Energy*, **2023**, *345*, 121335, with the title *Enabling metal substrates for garnet-based composite cathodes by laser sintering*, by Walter Sebastian Scheld, Linda Charlotte Hoff, Christian Vedder, Jochen Stollenwerk, Sandra Lobe, Daniel Grüner, Melanie Rosen, Martin Ihrig, Ah-Ram Seok, Martin Finsterbusch, Sven Uhlenbruck, Olivier Guillon, Dina Fattakhova-Rohlfing. Copyright Elsevier (**2023**).

Link to the published article: https://doi.org/10.1016/j.apenergy.2023.121335

Walter Sebastian Scheld fabricated the samples, performed the electrochemical and phase characterization, analyzed all data, and wrote the manuscript with contributions from all authors. Linda Charlotte Hoff fabricated the samples, and performed the laser sintering. Daneil Grüner took the SEM images and performed the EDS measurements. Martin Ihrig assisted the electrochemical characterization. Ah-Ram Seok prepared samples for parameter testing. Christian Vedder, Jochen Stollenwerk, Sandra Lobe, Martin Finsterbusch, Sven Uhlenbruck, Olivier Guillon, and Dina Fattakhova-Rohlfing initiated the idea, provided the resources, and supervised the work.

Sintering of the composite cathodes on stainless steel substrates leads to detrimental chemical reactions in the cathode and the formation of insulating passivation layers [43] on the current collector. Therefore, the development of a sintering technique that selectively heats the cathode layer without excessively heating the current collector is of great interest for the future development of ceramic cell processing. A promising technique is laser sintering of garnet-based composite cathodes on steel substrates [48], which has recently been published by some authors [178]. However, a detailed study on the microstructure, phase analysis, and electrochemical performance of the cathode layer, which is important for the evaluation of the potential of the technology, was lacking.

To investigate the suitability of laser irradiation for selective sintering of ceramic composite cathodes on metal substrates LCO-LLZO layers were screen-printed on steel substrates and then laser sintered [178]. Finally, the sintered porous composite cathode was infiltrated with a PEO electrolyte to connect the cathode to an LLZO separator and a Li metal anode without an additional sintering step. This model cell was used to evaluate the electrochemical activity, microstructure, and phase stability of the laser-sintered composite cathodes.

6.1 Phase characterization

The screen-printed composite cathode layers were pre-heated first to remove the organic binder molecules. The resulting flat black layers were analyzed by XRD, revealing only c-LLZO (ICDD 99 000 0032) and rhombohedral LCO (ICDD 00 016 0427) phases after the pre-heating step (Figure 6.1A). After laser sintering (for more details check the earlier publication [178]), the c-LLZO and rhombohedral LCO phases were present as the main phases. However, the formation of several secondary phases assigned to rhombohedral $LaCoO_3$ (ICDD 00 025 1060), cubic CoO (ICDD 01 071 1178) [44], and tetragonal $Li_{0.5}La_2Co_{0.5}O_4$ (ICDD 01 083 1842) [242] were detected.

To investigate whether the formation of secondary phases is due to the specifics of laser sintering (e.g., locally higher temperatures when irradiated with a laser beam compared to other sintering methods) or to a reaction with the steel substrate, the same cathode layers were sintered using both another light-absorption-based sintering method, namely sintering with a RTP lamp furnace, and conventional furnace sintering. The conventional furnace has slow heating rates and long dwell times so that the entire sample, including the steel substrate, is heated without temperature gradients in a processing time of hours. The RTP furnace has higher heating rates and short dwell times in the range of minutes, and heats only the surface of the cathode layer by absorption, creating a temperature gradient during heating that is homogenized by heat conduction over the dwell time [48]. In laser sintering, the sample is heated at a moving position below the laser beam at extremely high heating rates with no dwell time, resulting in short interaction times in the range of milliseconds and producing much higher temperature gradients in the sample compared to other processes [48].

The optimal sintering parameters for RTP and conventional sintering of electrolyte-supported composite cathodes with complete phase retention have been described in previous publications [25, 27]. In this context, the LCO-LLZO system showed high thermal stability in electrolyte-supported cell designs at temperatures up to 1050 °C [25, 38, 41, 42]. The optimum sintering parameters [25, 27] were used to process composite cathodes by RTP and conventional sintering on the stainless steel substrate. This experiment was designed to evaluate the influence of the substrate on the stability of the composite cathodes during sintering.

XRD analysis of the steel-supported cathodes sintered with RTP and conventional sintering (Figure 6.1B) shows that the LLZO phase was completely decomposed, as indicated by the absence of the most intense LLZO reflection at 16.7°. $LaCoO_3$, $LiFeO_2$, $LiAl_2Cr_3O_8$ and $Al_{95}Fe_4Cr$ formed as secondary phases in the RTP process and $LaCoO_3$, $La_2Zr_2O_7$, and FeO in the conventional sintering process.

Since electrolyte supported LCO-LLZO composite cathodes sintered by RTP and conventional sintering [25, 27] as well as other sintering techniques [22, 26, 72, 154, 159] exhibit phase retention, this result indicates that the thermal stability of the composite cathodes are drastically lower when sintered on steel substrates. While the LLZO substrate [25, 27] likely serves as a Li reservoir, supporting the stability of the LCO-LLZO composite during sintering, the steel substrate does not provide Li-ions. On the contrary, it may withdraw Li-ions from the composite cathode by reacting with the oxide layers which form on the steel surface during thermal processing [43]. In addition, undesirable reaction products are possible due to the diffusion of elements contained in the steel such as Fe, Cr, Al, Mn, or Ni.

Therefore, sintering of composite cathodes in a metal-supported cell design is much more challenging compared to electrolyte-supported cell designs. Laser sintering has been shown to be the only method for sintering LCO-LLZO composite cathodes on steel substrates that retains the LLZO phase. This is due to much shorter interaction times resulting in high temperature gradients, so that the steel substrate is less heated (selective sintering of the cathode) and consequently less oxidized and less reactive.

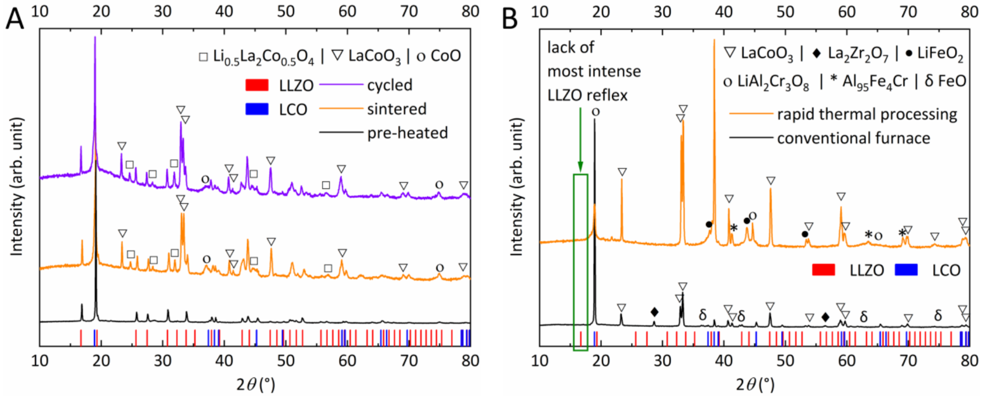

Figure 6.1: XRD measurements with respectively labeled major and minor phases. A) pre-heated composite cathode on steel with the laser-sintered and the electrochemically cycled cathode; B) sintered composite cathodes on EN 1.4767 steel substrates using a conventional furnace and rapid thermal processing with a insert hihglighting missing LLZO reflexes due to decomposition [243].

Raman spectroscopy was performed to obtain deeper insights into the phase composition of the LCO-LLZO composite cathode layers on the steel substrate after the different treatment steps, i.e. the pre-heating step, the laser sintering step, and the electrochemical cycling step (as described below). Evaluation of the individual phases in a typical Raman spectrum (Figure 6.2A) is difficult due to a strong superposition of the Raman signals. To deconvolute the contribution of the LCO phase, its spectrum was extracted by component analysis (see Experimental part for more details) (Figure 6.2B). Due to the low intensity of the LLZO signals, extraction of the LLZO signals was not possible.

The E_g and A_{1g} LCO signals of the pre-heated, binder-removed sample show a shift to lower wavenumbers at 472 cm^{-1} and 583 cm^{-1} compared to the pristine rhombohedral LCO phase (space group $R\bar{3}m$), which has signals at 488 cm^{-1} and 597 cm^{-1} [244]. It is possible that preheating to 500 °C converted some of the LCO phase to the low-temperature cubic LCO phase (space group $Fd3m$), resulting in the strong shift to lower wavenumbers [245]. After laser sintering, the rhombohedral LCO phase appears to be restored, as indicated by LCO Raman signals at 484 cm^{-1} and 592 cm^{-1}. However, a 5 cm^{-1} shift to lower wavenumbers compared to the fully lithiated LCO phase (488 cm^{-1} and 597 cm^{-1} [244]) suggests that some amount of Li evaporated during sintering [238]. An additional signal at 684 cm^{-1} can be assigned to Co_3O_4, which was not detected by XRD measurements [246]. Since Raman spectroscopy is more surface sensitive than XRD, it is possible that Co_3O_4 formed at the surface of the cathode layer, while CoO was confirmed in deeper regions. In this context, it should be noted that direct heating during laser sintering of highly absorbing material, such as the LCO-LLZO composite cathode layers that have an absorbance of 73% at the laser wavelength of 1470 nm [178], mainly results in absorption of radiation in the upper parts of the cathode layer, while the underlying material is heated by thermal conduction. The energy transfer in deeper layers is thereby mainly influenced by the physical parameters of the specific heat capacity C_p ($C_{p(LLZO)}$ = 0.55 to 0.80 J g^{-1} K^{-1} [21], $C_{p(LCO)}$ = 0.73 J g^{-1} K^{-1} [247]) and heat conductivity k ($k_{(LLZO, RT to 900 K)}$ = 1.45 to 1.55 W m^{-1} K^{-1} [21], $k_{(LCO)}$ = 5.4 W m^{-1} K^{-1} [248]), as well as the green density of the layer. Therefore, it is possible that the surface of the cathode layer reaches a higher temperature during laser sintering than the material in the deeper parts of the cathode. The $LaCoO_3$ phase detected in the XRD measurements was not observed in the Raman spectra, which can most likely be explained by the different penetration depths and probe volumes of the two methods.

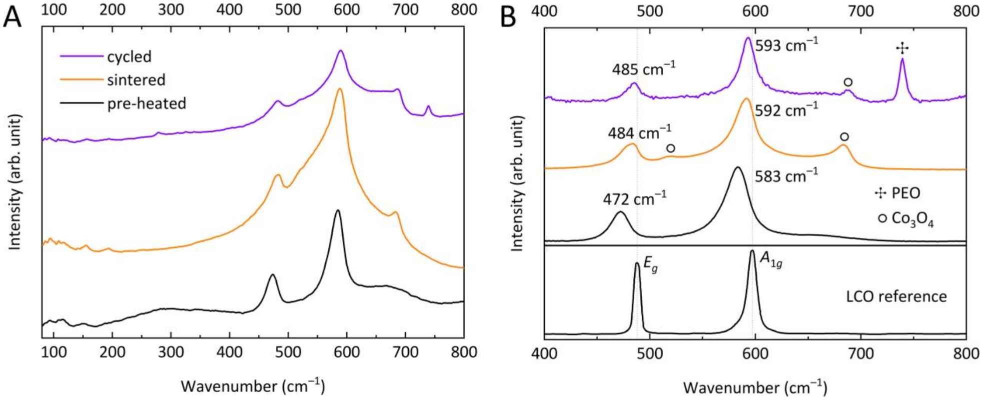

Figure 6.2: Raman spectroscopy measurements of the pre-heated, laser-sintered and electrochemically cycled composite cathode. A) average spectra of the Raman mapping; B) extracted LCO signals with wavenumbers of the signals, side phases and a pristine LCO reference spectrum with marked vibrational modes [234, 243, 244].

6.2 Microstructural Investigation

Top view SEM images of the laser-sintered layers (Figure 6.3A-B) show the formation of a coherent structure with homogenously distributed macropores and a porosity of about 30%, as determined by digital analysis using IMAGEJ software. A cross-section of a polymer-infiltrated and electrochemically cycled composite cathode polished with Ar-ions shows sintering necks between the LCO and the LLZO particles, indicating that sintering was successful even in deeper regions (Figure 6.3C). However, the densification of the composite cathode during laser sintering is limited, as many pores can also be seen in the cross-section. In addition, the LCO, LLZO and secondary phases are inhomogeneously distributed in the layer. The relative density of the layer and homogenization of the phase distribution need to be improved for future optimization of electrode performance.

Based on the elemental contrast of the different materials and their mean atomic number $\bar{Z}$, the darker regions can be assigned to LCO, while the lighter regions correspond to LLZO. LCO and LLZO are unevenly distributed over the layer thickness and the microstructure of the laser-sintered layer is not uniform. Regions with different microstructures can be distinguished. The areas labeled “1” in Figure 6.3C show well-sintered LCO-LLZO composite cathodes with low porosity and sintering necks between the particles. In addition to these regions, which closely resemble the targeted microstructure of co-sintered composite cathodes, much denser regions are also visible (labeled “2” in Figure 6.3C), consisting mainly of sintered LCO particles. The LLZO phase can be detected in these areas as light inclusions in the large LCO crystals. Since these areas are mainly located on the surface of the layers (“2”) that were directly exposed to the laser beam, it is very likely that they were formed as a result of the very rapid sintering. The growth of the LCO particles takes place at sites with a locally high temperature, which can be well above the sintering temperature of the LCO phase. LLZO particles do not form such large domains.

In addition to the dark LCO and light LLZO regions, some areas of intermediate gray-scale contrast were also detected (labeled “3”), probably corresponding to one of the detected cobalt-containing secondary phases such as $LaCoO_3$, $Li_{0.5}La_2Co_{0.5}O_4$, CoO, Co_3O_4, or a partially delithiated LCO. The latter three phases could be formed by the evaporation of Li from the LCO, which fits the results of the Raman spectroscopy analysis. The highest concentration of the secondary phases is visible at the surface of the laser-sintered layers, where they form separate domains (labeled “3”). These gray particles were also detected in regions consisting of small co-sintered LLZO and LCO particles (labeled “4”). This suggests that the secondary phases form preferentially in areas of high temperature, such as the surface directly exposed to laser radiation, and in areas with increased reactivity, such as small particles with a large interfacial area. Furthermore, some needle-like particles with light contrast were detected (labeled “5”), which have not yet been identified and could correspond to one of the secondary phases.

The fact that sintering takes place even at quite deep levels is very encouraging and indicates that the heat supply via laser penetration depth and heat conduction is sufficient, rendering laser sintering a suitable method for densifying relatively thick composite cathode layers. It is also important to note that the steel substrate (labeled “6”) does not appear to be damaged by laser sintering or react with the cathode layer, as no oxide or secondary phase layers were detected on the steel|cathode interface. Considering the coefficients of thermal expansion (CTE) of EN 1.4301 steel with $1.8 \cdot 10^{-5}\,K^{-1}$ for 20 °C to 500 °C (according to the manufacturer), LCO with $1.3 \cdot 10^{-5}\,K^{-1}$ for 50 °C to 400 °C [229], and LLZO with $1.55 \cdot 10^{-5}\,K^{-1}$ for 25 °C to 700 °C [249], the question arises whether the mismatch of the CTEs of the different components can lead to cracking and delamination. In particular, LCO and the steel substrate exhibit large difference in CTEs. However, since laser processing produces a strong thermal gradient, the metal is heated less and the adverse effects of different CTEs during sintering are reduced [20]. This is also evident in the SEM cross-section, which shows good adhesion between the steel substrate and the cathode layer without large gaps or cracks at the interface. The black regions (labeled “7”) and the gray area on the top correspond to the polymer PEO (which was infiltrated after laser sintering). The PEO was used to connect the cathode to an LLZO separator and a Li metal anode without an additional sintering step. Some artifacts from the Ar-ion milling during the sample preparation for SEM can be seen labeled “8”, which originates from material being removed and deposited elsewhere.

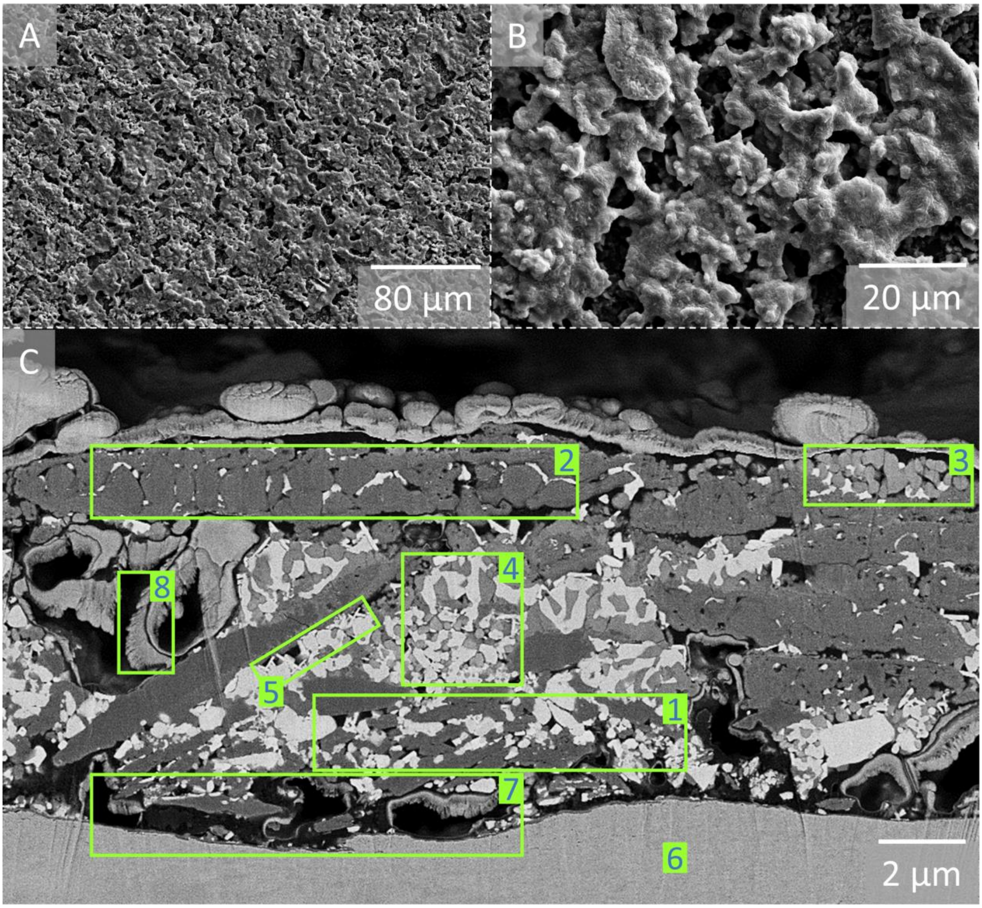

Figure 6.3: SEM images of the laser-sintered composite cathode. A) & B) top view images (SEL) with different magnifications of the sintered cathode; C) cross-section view (BSE) of the PEO infiltrated and electrochemically cycled sample after Ar-ion milling. For details of the different highlighted areas, see the main text. During the Ar-ion milling process, material may be removed and deposited in other places, especially in pores ("8") [243].

The element analysis of individual particles using EDS measurements (Figure 6.4A-B) confirms the presence of LLZO (spectrum 1) and LCO (spectrum 2) as the main phases. The detection of minor signals of Fe in both spectra can be explained by the previously mentioned deposited material from the Ar-ion milling, while the signals of La in the LCO spectrum (spectrum 2) can be assumed to be due to the excitation volume extending into the surrounding material. Since the Fe signals are present in both spectra (LLZO and LCO), the substitution of Fe into the LLZO lattice can probably be excluded and no evidence for any other possible substitution in LLZO [101] was found. One of the regions with the gray contrast scale, which can be assumed to contain secondary phases, is measured in spectrum 3, where strong signals of Co, La, Zr, and

O can be observed. It should be emphasized that these signals are probably influenced by the excitation volume, since the particles with the gray scale are much smaller than the LCO and LLZO particles. However, it is possible that $LaCoO_3$ and $Li_{0.5}La_2Co_{0.5}O_4$ formed right next to LLZO, which could explain the existence of the Co signal next to the LLZO particle. On the other hand, a Zr-rich phase must also form during decomposition of LLZO into La-Co phases. Such a phase was not detected by XRD and Raman spectroscopy and is still under investigation. The measurement performed on the PEO electrolyte (spectrum 4) shows a signal of S, corresponding to LiTFSI in the polymer electrolyte. The signals of other elements such as Fe, Cr, Ni, Si, and Mn originate from the steel substrate and those of Co and Zr from the composite cathode, as a result of the excitation volume extending into surrounding material. Spectrum 5 shows the elements of the steel substrate without any diffusion of La, Zr, or Co.

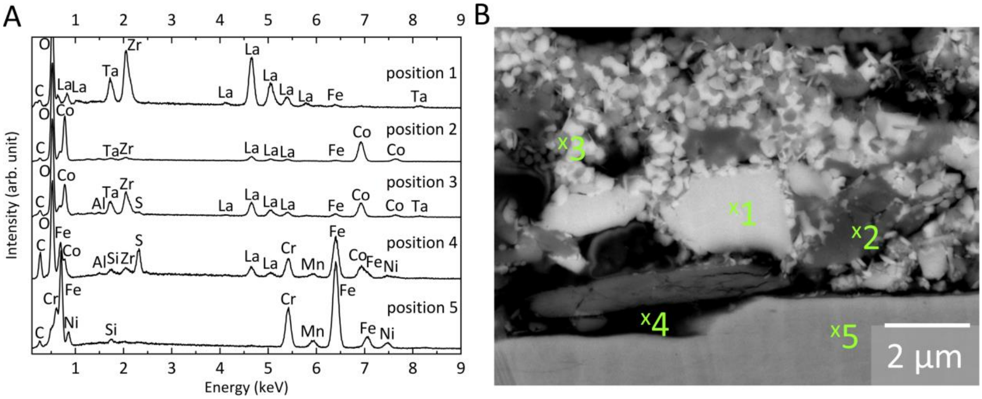

Figure 6.4: Cross sectional SEM image (BSE) with labeled EDS point measurements. A) EDS spectra from the different positions: (1) LLZO particle, (2) LCO particle, 3) area of secondary phases, 4) PEO, 5) steel substrate; B) SEM image [243].

To get a better idea of the diffusion of the elements in different regions, EDS mapping was performed in addition to point measurements (Figure 6.5). As expected, the lighter particles in the BSE image, which are associated with the LLZO phase, show a light element contrast of La, Zr, Ta and O. In contrast, the darker particles in the BSE image of LCO show mainly Co and O, but La signals are also present. The La-EDS mapping indicates La-ion diffusion to the cathode particles, but at lower concentration than in LLZO particle. This result agrees well with the $LaCoO_3$ and $Li_{0.5}La_2Co_{0.5}O_4$ phases determined by XRD.

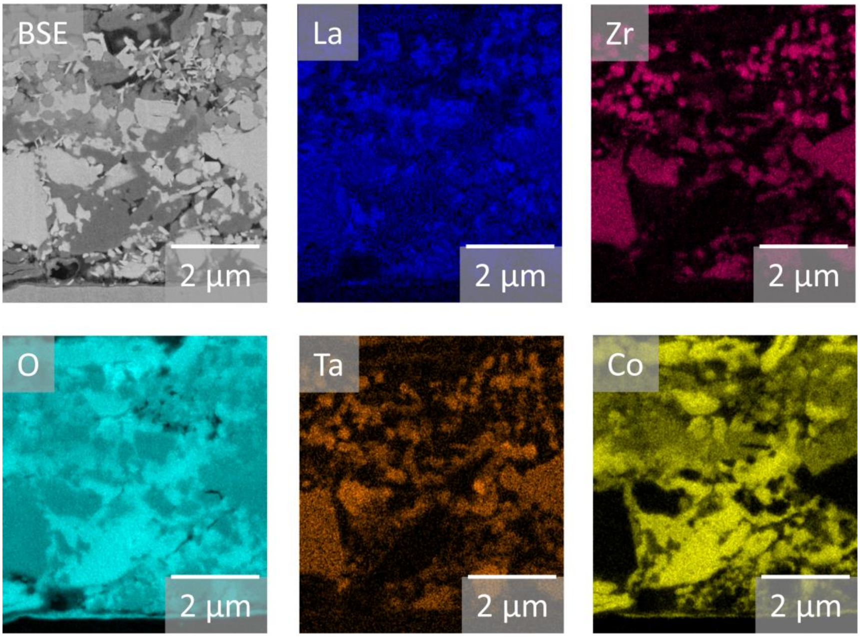

Figure 6.5: Cross sectional SEM image (BSE) with EDS mappings of La, Zr, O, Ta, and Co [243].

6.3 Electrochemical characterization

The electrochemical performance of the laser-sintered ceramic composite cathodes on the steel substrate was evaluated in a hybrid cell setup, which was previously used for ceramic composite cathodes by some of the authors of this study [24]. For this purpose, the porous cathode layer was infiltrated with the PEO polymer electrolyte, which was used to support ionic conductivity and to connect the cathode to an LLZO separator and a Li metal anode without an additional sintering step (Figure 6.6A). Further optimization of the cell design would ultimately require sintering a ceramic separator onto the cathode so that PEO infiltration is no longer necessary. However, the cell design with PEO and LLZO pellets is suitable for the model cells in the current study for the purpose of evaluating the electrochemical performance of the laser-sintered composite cathodes.

In the cross-section image (Figure 6.3C) of the cathode, the infiltrated PEO can be seen in the open pores as material with black contrast (partially gray due to Ar-ion milling residues, see the area of Figure 6.3C labeled “8”). The infiltrated PEO can mainly be observed within the pores and on the surface of the composite cathode. Of particular note is the localization of PEO close to the steel substrate (labeled “7”), indicating successful infiltration.

The electrochemical activity of the laser-sintered and PEO-infiltrated composite cathode was characterized by galvanostatic charge/discharge with different current densities and C-rates (Figure 6.6B). In the first discharge cycle, a specific capacity of 102 mAh g^{-1} was achieved. Since the cathode was cycled only to 4.0 V, to prevent polymer electrolyte degradation at higher potentials, the cathode active material utilization is ~86% of the theoretical capacity of 118 mA g^{-1} (specific capacity of LCO charged/discharged at 4.2 V: 140 mAh g^{-1}) [58, 250].

In the subsequent cycles, a capacity fade was observed with a capacity loss of about ~5% per cycle. The capacity reduction was significantly increased by increasing the C-rate by about ~9% per cycle. This trend continued in the subsequent electrochemical cycles until finally, in the 12th cycle, a specific discharge capacity of only 54 mAh g^{-1} was reached, corresponding to a capacity fade of 47%. The individual discharge capacities and the respective coulombic efficiency are summarized in Figure 6.6C, which illustrates the increased capacity loss for the different C-rates and shows a decreased coulombic efficiency, especially in the first electrochemical cycles with a higher C-rate. Overall, the coulombic efficiency increases with a higher number of electrochemical cycles.

The XRD patterns (Figure 6.1A) and Raman spectra (Figure 6.2B) of the electrochemically cycled layer are practically indistinguishable from those of the as-prepared layers. They show no signs of phase change induced by the electrochemical cycling, indicating no strong degradation of the crystal phase after electrochemically cycling (a signal was observed at 740 cm^{-1} which can be assigned to the PEO electrolyte [251]). Therefore, the observed capacity fading could be due to the phase transformation in a very thin interfacial layer, as described in a previous study on LCO-LLZO cathodes by Ihrig et al. [159]. However, it should be noted that the observed capacity fade of the laser-sintered LCO-LLZO cathode on the steel substrate is comparable to electrolyte supported LCO-LLZO based cathodes processed by other sintering techniques [22, 25-27, 72, 154, 159, 252]. This suggests the cause of the observed capacity fade as the intrinsic electrochemical instability of unprotected LCO-LLZO composite cathodes and not by the laser sintering process [159]. In comparison, electrolyte supported and conventional sintered LCO-LLZO based batteries showed capacity retentions after electrochemical cycling between 30% to 72% (30% [25], 42% [23], 50% [163], 72% [40]), while cells processed with SPS or FAST/SPS showed capacity retentions of 60% [162] and 64% [22]. Hot-pressed cells lead to a capacity retention of 64% [157] and UHS to a value of 69% [158]. The cathodes presented in the study are in the middle range with a capacity retention of 53%, which demonstrates that the laser-sintered cathode does not result to increased electrochemical degradation.

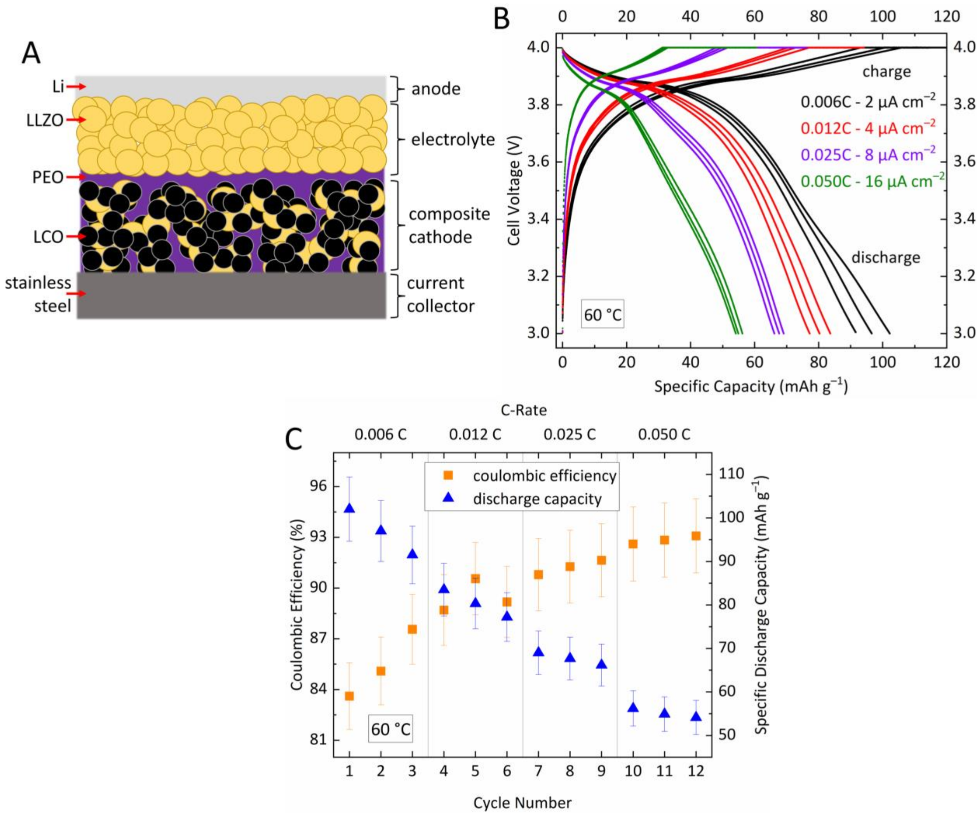

Figure 6.6: Electrochemical measurements of the cell. A) scheme of the manufactured battery with descriptions of the individual components; B) GCPL measurements of the polymer infiltrated battery at 60 °C, progressing from small C-rates and current densities to larger ones; C) the coulombic efficiency with the discharge capacity of the individual electrochemical cycles shown with the different C-rates [243].

7 Fabrication of ceramic solid-state-batteries with rapid thermal processing

This chapter was published in *Journal of Power Sources*, **2022**, *545*, 231872, with the title *Rapid thermal processing of garnet-based composite cathodes*, by Walter Sebastian Scheld, Sandra Lobe, Christian Dellen, Martin Ihrig, Grit Häuschen, Linda Charlotte Hoff, Martin Finsterbusch, Sven Uhlenbruck, Olivier Guillon, Dina Fattakhova-Rohlfing. Copyright Elsevier (**2022**).

Link to the published article: https://doi.org/10.1016/j.jpowsour.2022.231872

Walter Sebastian Scheld optimized the sintering parameters and fabricated the samples, performed the electrochemical and phase characterization, analyzed all data, and wrote the manuscript with contributions from all authors. Sandra Lobe conducted the phase separation in the Raman analysis. Christian Dellen took the SEM images and performed the EDS measurements. Martin Ihrig assisted the electrochemical characterization. Grit Häuschen provided the LLZO powder. Linda Charlotte Hoff measured the UV-Vis. Sandra Lobe, Martin Finsterbusch, Sven Uhlenbruck, Olivier Guillon, and Dina Fattakhova-Rohlfing initiated the idea, provided the resources, and supervised the work.

The fabrication of LCO-LLZO-based composite cathodes has not yet been established on an industrial level, and the methods used in research often consume too much time and energy. Therefore, new, fast, scalable, and energy-efficient sintering technologies must be explored to demonstrate feasible fabrication routes for oxide-ceramic SSB. The classical fabrication method for sintering a composite cathode of LCO and LLZO on a LLZO separator uses a conventional furnace and has a dwell time of 30 min at 1050 °C [25].

By using the H^+/Li^+ exchange for pressure-assisted reactive sintering, it is possible to lower the temperature to 400 °C [75, 111]. FAST/SPS utilizes ohmic heating and high pressures to allow the sintering of the powders already at 675 °C [22]. The UHS process can be used to fabricate electrolyte and cathode films with very short sintering times of around ∼3 s at ∼800 °C – 1500 °C to produce dense batteries [28, 253]. Currently, the major drawback of these advanced sintering techniques is their limited sample size and rather complex preparation steps.

In contrast, photonic sintering with RTP could provide a fast and scalable production route without creating unwanted secondary phases. To demonstrate the feasibility of this method for the fabrication of oxide-ceramic-based SSB, RTP was used to sinter a screen-printed LCO-LLZO composite cathode on an LLZO separator, which is shown schematically in Figure 7.1. The sintering parameters were optimized and the resulting samples were characterized chemically and also electrochemically by applying an In anode to prepare full cells.

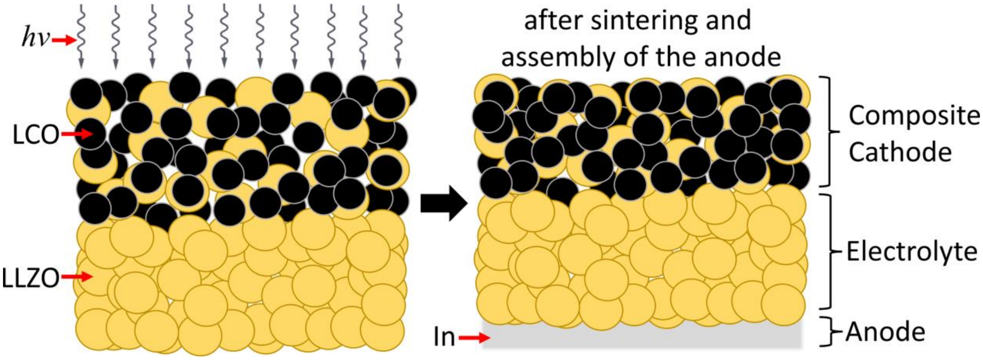

Figure 7.1: Schematic overview of the screen-printed half-cell (left) with a composite cathode of LLZO and LCO on an LLZO electrolyte, shown in a RTP sintering process, where radiation heats the sample and causes the cathode to sinter. The half-cell with a densified cathode (right) is finally contacted with an indium metal anode [27].

7.1 Optical properties

Screen-printing slurries on LLZO pellets followed by a preheating step at 500 °C results in black, homogenous, flat layers with an average thickness of ~30 µm and a smooth surface (Figure 7.2B and Figure 7.3C). The preheating step aims at removing the binder molecules to prevent possible fractures within the composite cathode during the sintering process due to the release of H_2O and CO_2. High absorption within the operating wavelengths of the RTP radiation source is a prerequisite for a high heating rate in the RTP sintering. The UV-Vis spectrum (Figure 7.2A) shows strong absorption in the visible and the near-infrared region (spectral regions with the highest intensity of the 3000 K lamp) of the screen-printed LCO-LLZO films, while almost no transmission occurs through the sample. The majority of the spectral range generated by the halogen lamps in our RTP setup is therefore suitable for the RTP sintering.

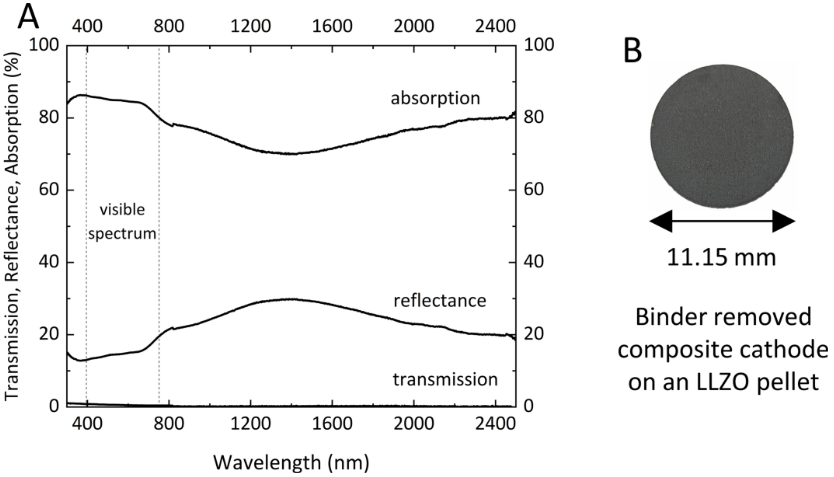

Figure 7.2: UV-VIS measurement of the binder-removed composite cathode. A) absorption, reflectance and transmission of the sample; B) picture of the cathode side (diameter = 11.15 mm) [27].

7.2 Optimization of the sintering parameter

One of the major challenges in the sintering of garnet-based composite cathodes is a reaction between the LLZO and the CAM at elevated temperatures, which leads to the formation of highly resistive secondary phases. The mixture of LCO and LLZO is stable up to 1050 °C according to previous investigations [25, 41]. However, if the elevated temperature is maintained for too long, interdiffusion of ions at the LCO|LLZO interface and the formation of resistive interphases or secondary phases [39, 40] may occur. Besides the undesired chemical reactions, mechanical deformations due to stresses caused by the temperature gradient, should also be considered when optimizing RTP sintering. Heating is limited to the exposed surface of the composite cathode, while the LLZO separator is heated only indirectly by heat transfer ($k_{(\mathrm{LLZO,RT-900\,K})}$ = 1.45-1.55 W m^{-1} K^{-1} [21], $k_{(\mathrm{LCO})}$ = 5.4 W m^{-1} K^{-1} [248]). Therefore, temperature gradients can arise in photonic sintering methods or RTP. As a result of the temperature gradient, stresses can occur at the cathode|separator interface and inside the LLZO separator, which can lead to mechanical deformation or even cracks.

Various RTP parameters were tested to sinter the cathode and reduce the formation of secondary phases or mechanical deformation at the same time. The most important sintering parameters are the heating temperature and the irradiation time. Both parameters can be adjusted by a dwell time at a given temperature or by a heating rate, with faster heating rates resulting in shorter total irradiation times. If the irradiation time is too long, the temperature of the cathodes may rise too high, leading to the decomposition of the material. On the other hand, if the irradiation time is too short (which may mean a short dwell time or a high heating rate), the temperature may be too low for the powder to sinter, but the temperature gradient may still be too high, causing mechanical deformation. The overall sintering process can be optimized by a combination of different heating and cooling steps (*e.g.*, stepwise heating at different temperatures by dwell or ramp steps or pulse sintering) to achieve an optimal heat distribution within the electrode.

Different RTP parameters were studied individually to evaluate their effects on the sintering process in more detail (Table 7.1). Analysis of the microstructure and phase composition of the resulting cathodes by SEM, Raman spectroscopy, and XRD (S-Figure 1-S-Figure 15) shows that the slower heating rates lead to better sintering. However, when the samples were irradiated in a single heating rate step, cracks were observed in the ceramic separator independent of heating rates, indicating the presence of temperature gradients. Aside from the heating rate, the total irradiation time can also be controlled by the dwell time. The irradiation of samples for 90 s at 1000 °C after a heating rate of 5 K s^{-1} was not sufficient for sintering. When longer dwell times of 180 s were used, the cathode layer was sintered, but secondary phase formation was observed. A dwell time of 120 s showed good results for sintering and phase stability, but cracks also appeared in the electrolyte. The cooling rate variation resulted in three similar samples with cracks in the electrolyte, showing that this parameter had no relevance on the resulting sample in the tested range.

The heating program with ramps resulted in a better sintering behavior without the formation of secondary phases in the cathode layer, but cracks in the electrolyte were also observed. Dense cathodes with crack-free electrolytes were finally achieved by sequential steps of heating, likely due to a reduced temperature gradient in the pellet. From the parameter study described here, the following optimized sintering parameters were obtained: 10 s dwell time at 400 °C, 10 s dwell time at 700 °C, and 90 s dwell time at 1000 °C with a heating rate of 3 K s^{-1}

for each step and a cooling rate of 5 K s^{-1}. These parameters were used for RTP sintering of all samples described below. The total heating time (heating + dwell time) was 7 min and 15 s, starting from RT. The free cooling step took about 15 min.

Table 7.1: Summary of the results of the optimization of the RTP program. The individual columns contain information about the RTP process such as the varied parameter (while other parameters were kept constant), the parameter value and the RTP program, as well as the properties of the resulting half-cells such as the phase purity of the sintered cathode layers (✓ indicates the absence and **X** the presence of impurity phases); the sintering behavior (✓ sintering occurred, **X** no sintering), and the mechanical stability of the LLZO pellet (✓ indicates a crack-free pellet, **X** the occurrence of cracks). The initial program had a dwell time of 3 s and a cooling rate of 5 K s^{-1}. The program was then changed from top to bottom according to the table by selecting the optimized parameter from the previous step [27].

Parameter	Value	Program	Phase	Sintering	LLZO pellet
Heating rate	3 K s^{-1}	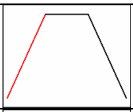	✓	✓	X
	5 K s^{-1}		✓	X	X
	10 K s^{-1}		✓	X	X
Dwell time	90 s	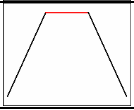	✓	X	X
	120 s		✓	✓	X
	180 s		X	✓	X
Cooling rate	3 K s^{-1}	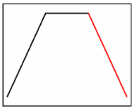	✓	✓	X
	5 K s^{-1}		✓	✓	X
	10 K s^{-1}		✓	✓	X
Temperature ramps[A]	1x	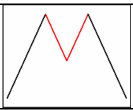	✓	✓	X
	2x		✓	✓	X
Heating steps[B]	1x	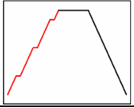	X	X	X
	2x		✓	✓	✓
	3x		✓	X	X

[A] Ramps are used to cool the sample down to 700 °C after reaching 1000 °C and then to re-heat the sample up to 1000 °C.

[B] Steps are used to heat the sample up to 1000 °C with breaks at different temperatures to reduce temperature gradients

7.3 Microstructural investigation

The optimized sintering parameters lead to dense composite cathode layers on the LLZO pellets, as can be demonstrated by SEM (Figure 7.3). The thickness of the cathode layer decreases from about 30 µm (Figure 7.3C) to about 13 µm after RTP sintering (Figure 7.3A), indicating a significant densification of the initial layer due to sintering. The density of the sintered layer is estimated to be 85% based on digital analysis of the SEM images, with pores attributed to macropores in the cathode layer. The black areas correspond to pores, which reduce the interfacial connection of the cathode and separator. SEM images of the electrode cross section (Figure 3A-B) show that the LCO particles in the composite cathode and the LLZO particles in the pellet are well sintered and form a close contact without any delamination. Even though some macroscopic pores are present between the cathode layer and the LLZO pellet, the remaining contact areas are well sintered and should be sufficient for adequate electronic and ionic contact between the cathode layer and the separator. The SEM cross-sectional images of both the fractured (Figure 7.3A) and the polished (Figure 7.3B) samples show a homogenous distribution of LCO (dark) and LLZO (bright) particles in the cathode layer. In addition to the decrease in layer thickness, a clear difference in the shape of individual particles before and after RTP sintering is also observed. The LLZO particles in the sintered layer are more spherical and the LCO particles are more coherent than in the initial layers, which can be attributed to the grain growth during RTP sintering. The LLZO particles have a roughly spherical shape whereas the LCO particles are more elongated, thus the layered structure of the LCO is still present after the sintering process. The SEM cross-sectional images of the polished surface show that the LLZO and LCO particles are well connected and have clear edges (Figure 7.3B). An electronic and ionic percolation network is expected in these areas. A network of LLZO particles can be seen in the region highlighted in red in Figure 7.3B, indicating a percolation path from the LLZO pellet across the composite cathode. The percolation pathways are essential for a sufficient ionic conductivity throughout the composite cathode to utilize thick composite cathodes and achieve a high areal capacity. A higher magnification of the fracture surface (Figure 7.3D) reveals round outcrops in the LCO that were most likely previously filled with the LLZO grains. Thus, the LLZO is partially surrounded by LCO during sintering.

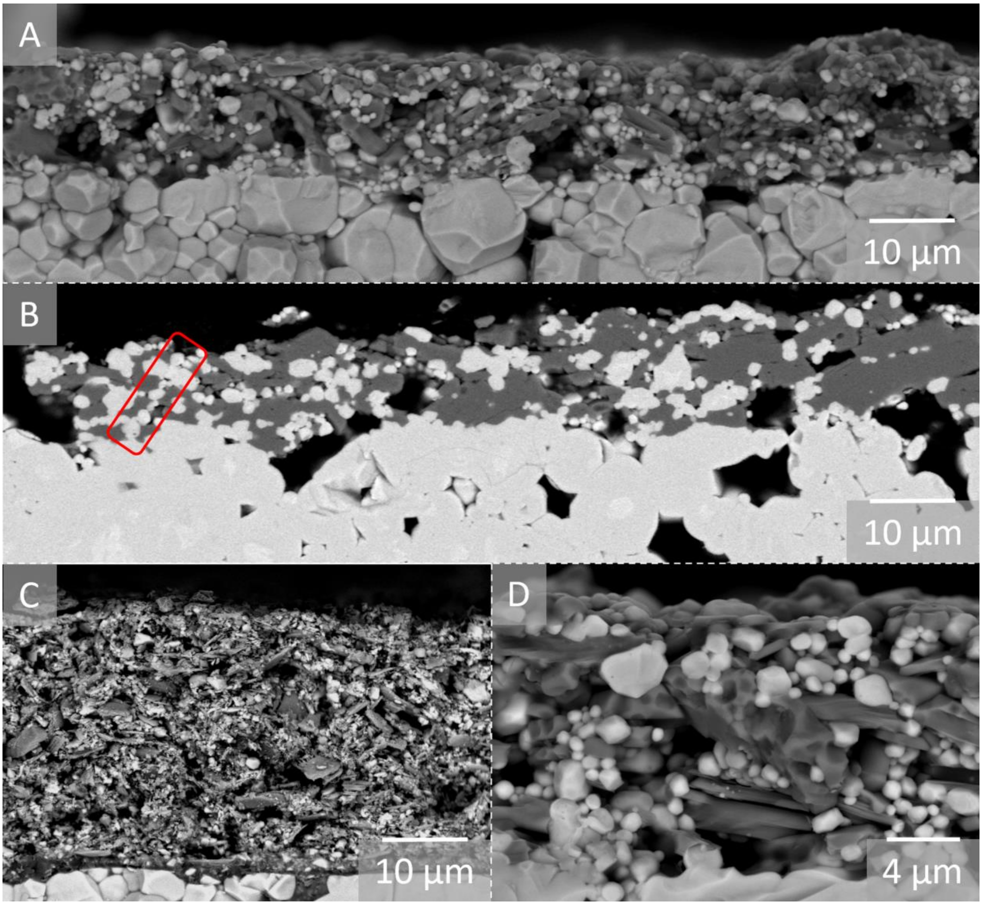

Figure 7.3: Back-scattered electron SEM images of samples prepared with the optimized sintering parameters. A) fractured sample; B) polished cross section with a red area indicating a LLZO percolation path; C) fracture of a binder-removed sample without RTP sintering; D) fractured sample with a higher magnification [27].

To detect possible ion interdiffusion with the formation of secondary phases in the composite cathode as well as in the LLZO separator, EDS measurements were performed at different locations of the half cell. As expected, the spectrum of the LCO particle (spectrum 3, Figure 7.4A) shows a strong Co signal. In addition, low-intensity signals from Zr, La, Ta, and Al are detected, but most likely originating from the surrounding LLZO due to the large excitation volume of the EDS measurements. The EDS spectrum of an LLZO particle in the composite cathode (spectrum 2, Figure 7.4A) mainly shows Zr, La, and Ta, as well as a low-intensity signal of Co, which likely originates from the surrounding LCO. The EDS measurements on the LLZO separator (spectrum 1, Figure 7.4A) show only the expected elements of LLZO and no other signs of ion interdiffusion in the LLZO separator.

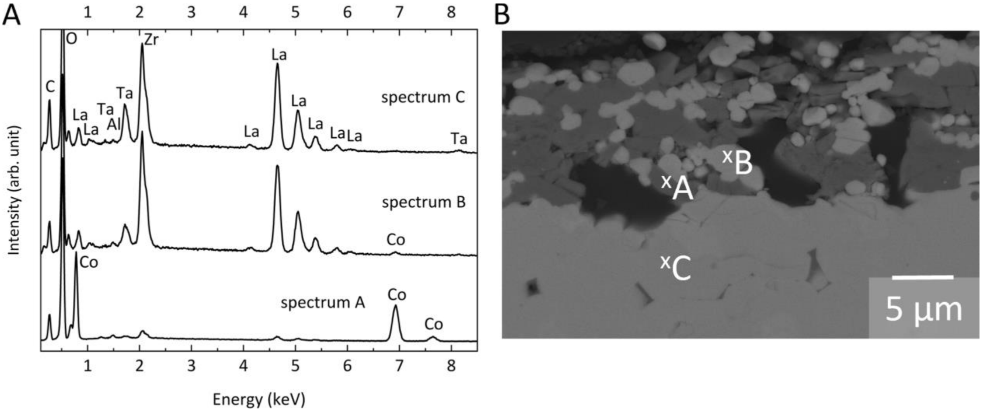

Figure 7.4: EDS point measurements on a polished cross section of an RTP-sintered composite cathode. A) EDS spectra with (1) the CAMin the composite cathode, (2) the electrolyte material in the composite cathode, and (3) the separator electrolyte material; B) SEM image of the investigated area, with the locations of the EDS measurements [27].

7.4 Phase characterization

The main results of the EDS measurements are confirmed by the XRD characterization of both the pre-heated and the RTP-sintered samples (Figure 7.5A), which only show the presence of rhombohedral LCO (ICDD 01 070 2685) and c-LLZO phases (ICDD 99 000 0032). No secondary phases were detected in the XRD patterns of the pre-heated cathode, but a slight shift of diffraction lines by around 0.1° was observed.

Due to the low sensitivity of the XRD technique, the formation of impurity phases cannot be completely excluded, for this reason the more sensitive Raman spectroscopy analysis was performed. The deconvolution of individual phases from the average Raman spectra (Figure 7.5B) of the pre-heated, RTP-sintered, and electrochemically cycled composite cathode is difficult due to the strong intensity of the LCO signals. Therefore, the spectra of LCO and LLZO were extracted by component analysis. For each sample, the average of the extracted spectra of LCO is shown in Figure 7.5C and the average of the extracted spectra of LLZO is shown in Figure 7.5D. Through this step, it is possible to analyze both phases separately to prevent the superposition of signals.

The Raman signal of the LCO phase in the pre-heated cathodes is shifted to lower wavenumbers (586 cm^{-1}) compared to the signal reported for the fully lithiated LCO phase at 597 cm^{-1} (Figure 7.5C) [234, 244]. This shift to a lower wavenumber is a clear indication of a loss of Li in the LCO lattice [238]. Moreover, the LCO signals of the sample pre-heated at 500 °C are broadened compared to those of the sintered sample, indicating a larger disorder in the crystal structure [235]. One of the possible explanations is the reaction of rhombohedral LCO with organic residues during heating to 500 °C, with the formation of disordered rhombohedral LCO or perhaps partially a low-temperature cubic LCO phase ($Fd3m$). However, the crystalline rhombohedral LCO phase is fully recovered after RTP sintering, demonstrating the typical signals of the rhombohedral LCO lattice (space group $R\overline{3}m$) with signals at 488 cm^{-1} (E_g) and 597 cm^{-1} (A_{1g}) [234, 244]. Therefore, the observation of the pre-heated state can be ignored for the evaluation of the cathode.

The extracted LLZO spectra (Figure 7.5D) of the pre-heated composite cathode show signals at 115 cm^{-1}, 285 cm^{-1}, and 670 cm^{-1}, which are likely related to the LT-LLZO phase formed in a reaction with the decomposition products of organic residues during heating [89]. The presence of some LT-LLZO may explain the slight shift in XRD lines described above. However, the formation of LT-LLZO does not seem to negatively affect the phase purity after sintering, where the LCO and LLZO phases are present without any shifts or additional signals. The Raman spectrum of the RTP-sintered composite cathode shows the typical signals of c-LLZO with the vibrational modes of La-ions at 109 cm^{-1} (T_{2g}) and 122 cm^{-1} (E_g); the signals of O-bending at 215 cm^{-1} (T_{2g}), and 251 cm^{-1} (A_{1g}); the Li vibrations at 372 cm^{-1} (T_{2g}), and 417 cm^{-1} (E_g or T_{2g}); the signals corresponding to ZrO_6 octahedron stretching at 647 cm^{-1} (A_{1g}); and the signal of the TaO_6 octahedron stretching at 741 cm^{-1} due to Ta substitution [19, 20, 254, 255]. The low-intensity signal of the c-LLZO phase at 514 cm^{-1} (E_g or T_{2g}) was not detected, which is likely due to an overlap with the intense LCO signals. Trace amounts of Li_2CO_3 were detected at 157 cm^{-1}, 193 cm^{-1}, and 1090 cm^{-1} in the sintered sample, which was formed during exposure to ambient atmosphere during measurements, most likely [75, 256]. Additionally, a signal is detected at 694 cm^{-1}. A possible explanation for this signal is the formation of $LaCoO_3$ due to the reaction of LLZO with LCO, for which the Raman signals were reported around 685 cm^{-1} to 691 cm^{-1} [40]. However, the more likely explanation is the formation of a Co-substituted LLZO phase generating a photoluminescence signal at 693 cm^{-1} [25], which was observed as a side product during the sintering of LLZO and LCO at 1050 °C in a conventional furnace. This signal was not observed with a less energetic laser (785 nm), which confirmed the photoluminescence character of the signal, as this effect is wavelength-specific (S-Figure 16).

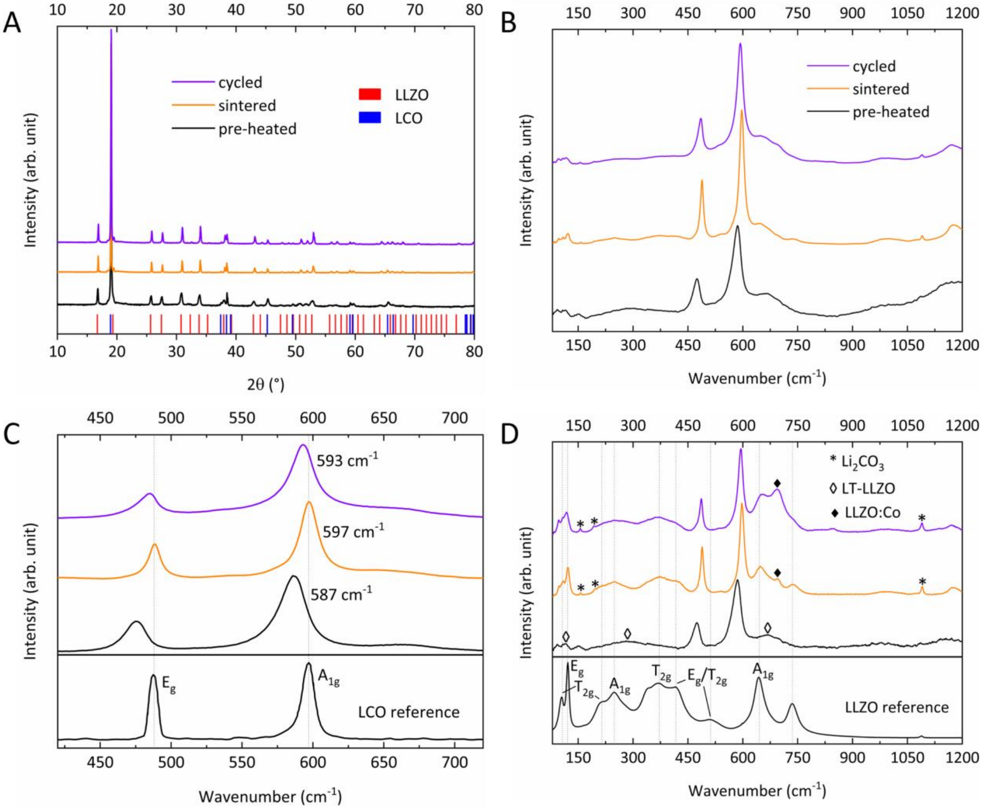

Figure 7.5: XRD and Raman analysis of the pre-heated (black), sintered (orange), and electrochemically cycled (purple) samples. A) XRD measurement, with LCO (ICDD 00 016 0427) and LLZO (ICDD 99 000 0032) reference pattern at the bottom; B) full Raman spectra of the composite cathodes; C) extracted Raman spectra of the LCO phase with a reference spectrum of the pristine LCO; D) extracted Raman spectra of the LLZO phase with a reference spectrum of pristine LLZO [27].

The results of the XRD and Raman spectroscopy analysis show that the RTP-sintered LCO-LLZO composite cathodes exhibit a higher phase purity than the conventionally sintered cathodes with a similar composition. By comparison, the formation of $La_2Zr_2O_7$ at 600 °C and $LaCoO_3$ at 900 °C [39, 40] has been reported, and the formation of Co_3O_4 or CoO due to the decomposition of LCO is also conceivable. None of these secondary phases were detected in the RTP-sintered cathodes. Only a previously reported [25] Co interdiffusion into the LLZO, producing a photoluminescence with the 532 nm laser was detected. Therefore, it can be concluded that the above-mentioned secondary phases are absent or present in lower concentrations compared to conventionally sintered composite cathodes. It is possible that the formation of these phases in the rapid sintering process with the RTP device is kinetically inhibited by the short times at elevated temperatures.

7.5 Electrochemical investigation

To investigate the electrochemical performance of the RTP-sintered cathodes, full cells were manufactured from the half cells described above by attaching an indium foil as an anode to the LLZO side. As shown by the galvanostatic charge/discharge measurements, the RTP-sintered LCO-LLZO composite cathode layers are electrochemically active without the addition of polymer or liquid electrolytes (Figure 7.6A). The performance of the RTP-sintered cells is comparable to other LCO-LLZO, for example by optimized conventional sintering (the specific capacity in the first discharge with 50 µA cm^{-2} was 110 mAh g^{-1} which corresponds to 79% of the theoretical capacity, and the cell had a strong degradation in the first cycles) [25] or advanced FAST/SPS sintering (the specific capacity in the first discharge with a current density of 50 µA cm^{-2} was 94 mAh g^{-1} which corresponds to 67% of the theoretical capacity, and the cell had a strong degradation in the first cycles) [22]. The RTP-sintered LCO-LLZO composite cathode provides a specific capacity of 100 mAh g^{-1} in the first electrochemical discharge cycle, which is 71% of the practical specific capacity of LCO with 140 mAh g^{-1} [58]. Similar to other all-inorganic LCO-LLZO cells, the capacity continuously decreases in the subsequent electrochemical cycles [22, 25, 72, 154, 159]. The capacity drop is the highest in the first electrochemical cycle (10% of initial capacity) and becomes lower in the subsequent electrochemical cycles with 8.8%, 7.3% and 6.6%. The Coulombic efficiency (Figure 7.6B) increases from 66% in the first electrochemical cycles to 72% after the 5th electrochemical cycle.

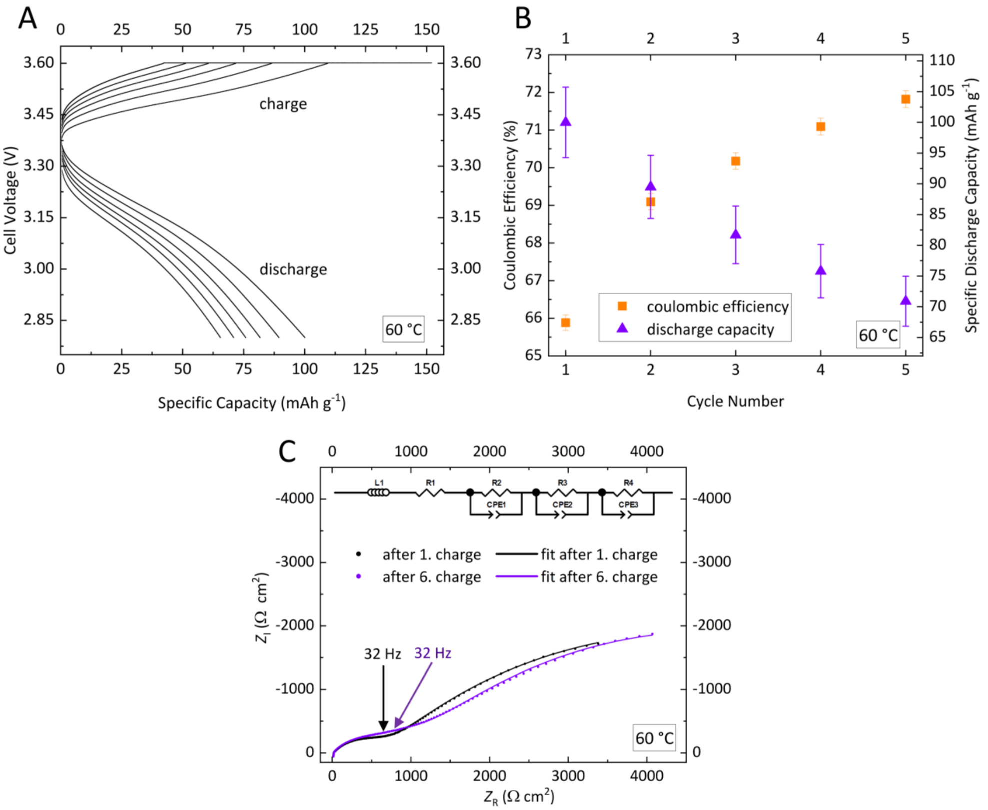

Figure 7.6: Electrochemical investigation of the prepared cells at 60 °C. A) charge and discharge capacity vs. cell voltage of the SSB with the first 6 electrochemical cycles; B) the associated coulombic efficiency with the discharge capacity of each electrochemical cycle; C) Nyquist plot after the first (black) and sixth (purple) charge with the equivalent circuit: L is the inductance, R is the ohmic resistance, and CPE is the constant phase element [27].

The Nyquist plot of the electrochemical impedance spectra (EIS) of the charged cell shows a semicircle in the high- to mid-frequency range and a semicircle in the mid- to low-frequency region (Figure 7.6C). The spectrum can be fitted using an equivalent circuit as shown in Figure 7.6C. The RC elements represent the impedance of the grain boundaries and the interfacial impedances of the anode and the cathode layers, respectively. As the semicircle corresponding to the bulk resistance cannot be resolved at this temperature, it is approximated with good accuracy by a resistance R. The high frequency inductance *L* is caused by the wiring. The high- to mid-frequency semicircle could be attributed to a superposition of the total resistance (bulk and grain boundary) of the LLZO electrolyte (S-Figure 17) [159, 257]. The mid- to low-frequency semicircle could be attributed to a superposition of the individual impedances of the anode and the cathode, as already described for comparable composite cathodes [159, 258]. Fitting these semicircles using the equivalent circuit shown in Figure 7.6C yields values of 895 Ω cm^2 and 7207 Ω cm^2. The impedance of the cell continuously increases after electrochemical cycling and after the 6th cycle the impedance of both semicircles increases to 1148 Ω cm^2 and 8095 Ω cm^2, respectively, which is likely related to the observed capacity fade.

An increasing impedance during electrochemical cycling was described in a previous investigation [159]. As mechanical fracturing was ruled out as a possible reason, an electrochemically driven ionic diffusion of Al- and Co-ions was found to cause secondary phases between LLZO and LCO [159]. XRD, Raman spectroscopy and SEM analyses of the electrochemical cycled cathode were performed to verify whether the same degradation mechanism is possible in the RTP sintered cathodes,

The XRD pattern of the electrochemically cycled sample (Figure 7.5A) gives no indication of secondary phase formation during cycling, but this could be due to the small amount of possible secondary phases or their amorphous character. In contrast, the Raman spectra of LCO and LLZO from the electrochemically cycled cathode differs from the sintered ones (Figure 7.5C-D). Thus, the signal of LCO shifts from 597 cm^{-1} to 593 cm^{-1}, indicating a loss of Li from the LCO lattice [238]. The Raman spectrum of the LLZO in the electrochemically cycled cathode also differs from the sintered one. The signal at 694 cm^{-1}, corresponding to the photoluminescence of the Co interdiffusion in the LLZO, shows a higher intensity after electrochemical cycling. Furthermore, the signal in the low-wavenumber region, corresponding to the vibrations of heavy La cations [254], shifts from 122 cm^{-1} for the as-prepared electrode to 118 cm^{-1} after electrochemical cycling.

The Raman spectroscopy results indicate some change in the LLZO crystal lattice as a result of the electrochemical cycling, which is due to a possible restructuring of La atoms in the LLZO lattice. These results confirm the previous findings [159] on electrochemically induced material degradation during electrochemical cycling as a reason for the capacity fading of the LCO|LLZO interface. In contrast, mechanical degradation, which has often been discussed as the main reason for the low electrochemically cycling stability of the rigid ceramic electrodes [25, 145], does not seem to play a significant role in the cycling stability of the RTP-sintered cathodes described in this work. SEM analysis of the electrochemical cycled LCO-LLZO composite cathode shows no effect of cycling on the cathode microstructure (S-Figure 18).

8 Cobalt-ion diffusion in LLZO separators during cathode sintering

This chapter was published in Advanced Functional Materials, **2023**, *33*, 43, 2302939, with the title *The Riddle of Dark LLZO: Cobalt Diffusion into the Garnet-based Separator of Solid-State Lithium Batteries*, by Walter Sebastian Scheld, Kwangnam Kim, Christian Schwab, Alexandra C. Moy, Shi-Kai Jiang, Markus Mann, Christian Dellen, Yoo Jung Sohn, Sandra Lobe, Martin Ihrig, Michael Gregory Danner, Chia-Yu Chang, Sven Uhlenbruck, Eric Wachsman, Bing Joe Hwang, Jeff Sakamoto, Liwen Wan, Brandon C. Wood, Martin Finsterbusch, Dina Fattakhova-Rohlfing. Copyright Wiley-VCH GmbH. Reproduced with permission.

Link to the article: https://doi.org/10.1002/adfm.202302939

W. S. Scheld initiated the idea, prepared the samples, performed the electrochemical and phase characterization, analyzed all data, and wrote the manuscript with contributions from all authors. K. Kim, L. Wan and B. C. Wood performed the large-scale molecular dynamics simulations. C. Schwab carried out the ToF-SIMS measurements. A. C. Moy and J. Sakamoto conducted the EBSD measurements. S.-K. Jiang, C.-Y. Chang, and B. J. Hwang performed the XPS measurements. M. Mann executed the CCD measurements. C. Dellen conducted the line-by-line Raman analysis. Y. J. Sohn performed the Rietveld refinement. M. Ihrig assisted with electrochemical characterization. M. G. Danner and E. Wachsman performed the Al_2O_3 coating of LLZO pellets. S. Lobe, M. Finsterbusch, S. Uhlenbruck, and D. Fattakhova-Rohlfing initiated the idea, provided the resources, and supervised the work.

While the reactions at the interface between LCO and LLZO particles in the composite cathodes have been studied in great detail [18, 22-25, 38-42, 101], much less attention has been paid to the processes taking place at the interface between the separator and the cathode layer during fabrication. Although several publications indicate that a strong ion interdiffusion occurs at the separator|cathode interface and within the separator during processing [19, 22, 40, 45, 72, 151, 152], the degree of ion interdiffusion and the nature, amount, and distribution of the phases formed are still very poorly understood. In particular, very little is known about how these processes affect the electrochemical properties of the separator, such as ion conductivity and cycling stability (dendrite formation) with Li metal anodes, although their effect can be very significant. The challenge in understanding the processes at the separator|cathode interface is mainly related to the fact that the interface is not easily accessible to most analytical methods. To address this issue, a simple approach was used to study the properties of the separator after cathode sintering. To do this, the cathode layer was deposited on a thick sintered LLZO pellet that served as a separator and then mechanically removed after RTP treatment. The RTP method was chosen as the sintering method because its fast heating rates and short sintering times generate particularly strong discoloration on the separators (compared to other techniques Figure 8.1 and S-Figure 19A-C), thus allowing better access to study the ion diffusion in the separator.

After screen-printing and RTP sintering of the cathode layer the LLZO separator, which had originally been white after its fabrication (hereafter referred to as the "untreated separator") changed, to a strongly colored separator (hereafter referred to as "LCO-treated separator"), indicating possible changes in grain boundary, bulk, or secondary phase formation (Figure 8.1). After the complete removal of the cathode, the separator remained dark, although the color and its intensity differed for opposite sides of the pellet. Thus, the top side of the pellet on which the cathode layer was deposited (hereafter referred to as the "cathode side") almost appeared black, while the bottom side (hereafter referred to as the "anode side") appeared green. The samples were characterized concerning their phase composition, ion distribution, microstructure, and the electrochemical properties of the separator. Additionally, large-scale MD simulations were used to understand the diffusion mechanism.

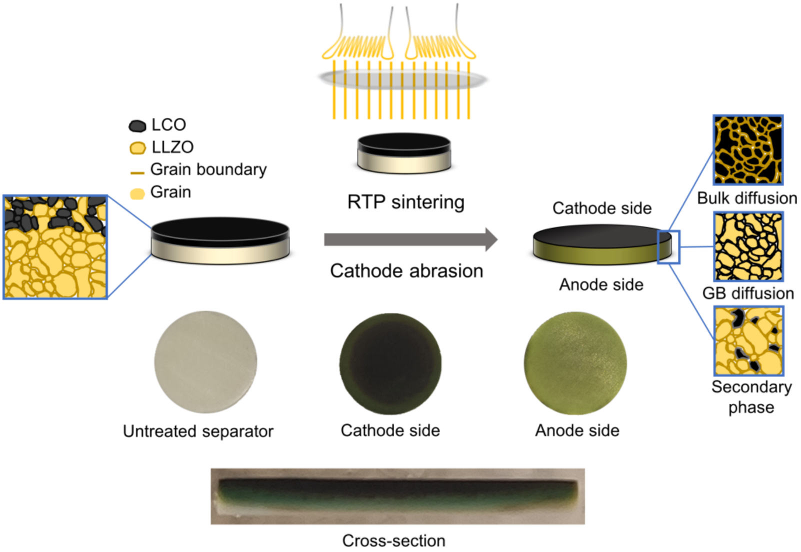

Figure 8.1: Schematic of Co-ion contamination in the LLZO separator from the pristine materials to the colored electrolyte without the abraded cathode after heat treatment. In the microstructure the change in coloration can occur from changes in the grain boundary (GB), in the grain, or by side phase formation. Photos of the untreated separator, the abraded cathode side, the anode side with a thickness of 400 µm, and an embedded cross-section of an LCO-treated separator with a thickness of 1000 µm. Copyright Wiley-VCH GmbH. Reproduced with permission [211].

8.1 Phase characterization

XRD analysis of the colored pellet reveals the presence of c-LLZO as the main phase on both sides, which is practically indistinguishable from the XRD pattern of the untreated separator (Figure 8.2A). Moreover, the Rietveld refinement shows only a slight decrease in the lattice parameters of the c-LLZO phase from 12.944 Å for the untreated separator to 12.941 Å on the anode side and 12.940 Å on the cathode side. The presence of the c-LLZO phase on both sides of the separator after RTP sintering is also confirmed by Raman spectroscopy analysis (Figure 8.2B), which shows typical signals of the high-temperature c-LLZO phase (space group *Ia*-3*d*). The vibrational modes can be assigned to La cations at 109 cm^{-1} (T_{2g}) and 122 cm^{-1} (E_g); the broad signals of O bending at 215 cm^{-1} (T_{2g}), and 251 cm^{-1} (A_{1g}); the Li vibrational modes at 372 cm^{-1} (T_{2g}), 417 cm^{-1}, and 514 cm^{-1} (E_g or T_{2g}); the signals of Zr-O bond stretching at 647 cm^{-1} (A_{1g}); and the signal of the TaO_6 octahedron stretching at 741 cm^{-1} from the Ta substitution [19, 20, 254, 255]. In addition to these peaks, another signal was detected at 693 cm^{-1} on both sides of the separator, although the intensity was much higher on the cathode side. The signal disappears when the laser wavelength is increased from 532 nm to

785 nm, thus decreasing the photon energy (Figure 8.2C, bottom), suggesting photoluminescence as the origin of the signal [192]. This signal has been previously detected for LCO–LLZO systems [25, 27], which was attributed to a Co-ion substitution of the LLZO lattice [25]. The presence of this photoluminescence signal is a clear indication of the diffusion of Co-ions into the LLZO structure (referred to hereafter as LLZO:Co) [25]. To test whether this phase forms during RTP sintering or already during preheating at 500 °C, a mixture of LCO and LLZO powders were heated to 500 °C in air for one hour. The Raman spectrum of this sample (S-Figure 20) shows only the typical signals of LCO and LLZO, proving that the LLZO:Co phase is formed during high temperature RTP sintering step. It cannot be excluded that even at such low temperatures a small amount of cross-diffusion can occur at around 100 nm, as shown by Vardar *et al.* [152], but the concentration of reaction products would be very low and below the detection limit of the characterization techniques used.

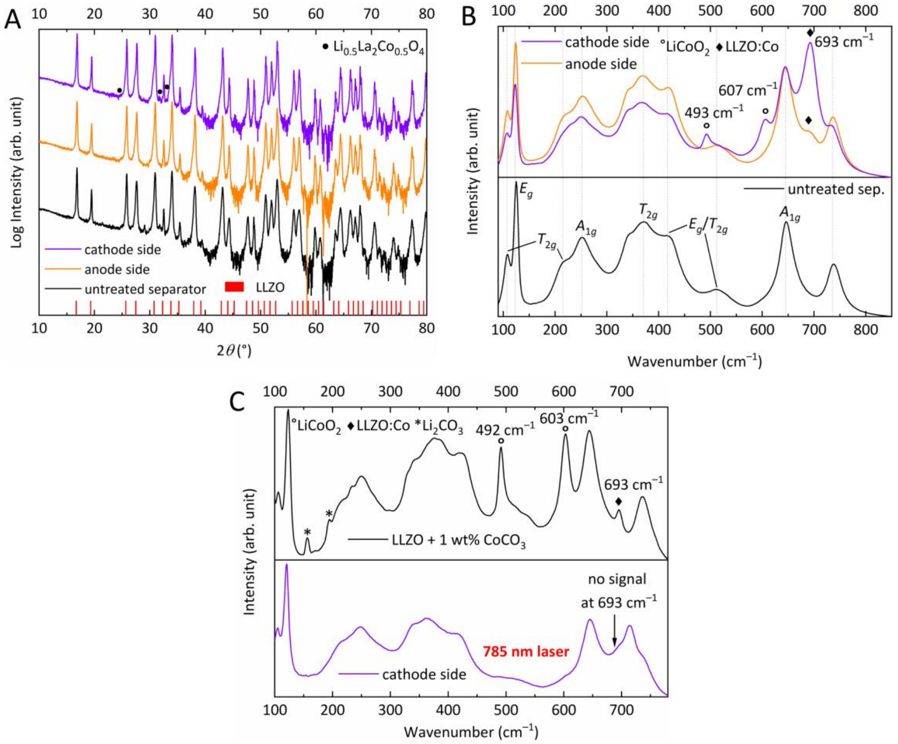

Figure 8.2: XRD and Raman spectroscopy measurements of the cathode side (purple), the anode side (orange), and the untreated separator (black). A) XRD results in logarithmic scale with the reference pattern of LLZO (ICSD 422259) in red, and marked reflexes of $Li_{0.5}La_2Co_{0.5}O_4$; B) averaged spectra from Raman mappings; C) averaged spectra from Raman mapping measurements of the mixture of LLZO with 1 wt% $CoCO_3$ processed in a conventional furnace with signs of Li_2CO_3 *[256]*, and the cathode side measured with a 785 nm laser. Copyright Wiley-VCH GmbH. Reproduced with permission [211].

In addition, XRD analysis on the cathode side revealed an insignificantly small amount of another minor phase assigned to the tetragonal $Li_{0.5}La_2Co_{0.5}O_4$ (Figure 8.2A). To confirm this result experimentally, the $Li_{0.5}La_2Co_{0.5}O_4$ phase was synthesized separately, resulting in a powder with a light brown color. The experimentally measured XRD pattern of this powder corresponds to the tetragonal $Li_{0.5}La_2Co_{0.5}O_4$ phase (ICSD 422259) with a small amount of La_2O_3 as a minor phase (Figure 8.3A). The Raman spectrum of the powder shows signals at 119 cm^{-1}, 165 cm^{-1}, 230 cm^{-1}, 371 cm^{-1}, 425 cm^{-1}, 533 cm^{-1}, and 685 cm^{-1} (Figure 8.3B). No photoluminescence effect was observed at the laser wavelengths of 532 nm and 785 nm, confirming that the above-described photoluminescence signal at 693 cm^{-1} does not belong to the $Li_{0.5}La_2Co_{0.5}O_4$ phase. Due to the small amount of $Li_{0.5}La_2Co_{0.5}O_4$ in the LLZO separator, the signals are not detectable in the averaged spectra from the Raman mapping. However, comparing the $Li_{0.5}La_2Co_{0.5}O_4$ reference signals with the individual spectra from the Raman mapping of the cathode side, the $Li_{0.5}La_2Co_{0.5}O_4$ phase can be seen in some areas, as described later.

The unabraded composite cathode after RTP sintering consisted in our earlier publication of the LCO and the LLZO phases, but the LLZO:Co photoluminescence was also detected in Raman spectra, and Li_2CO_3 residuals were found [27]. However, the $Li_{0.5}La_2Co_{0.5}O_4$ phase was not found in the cathode layer [27].

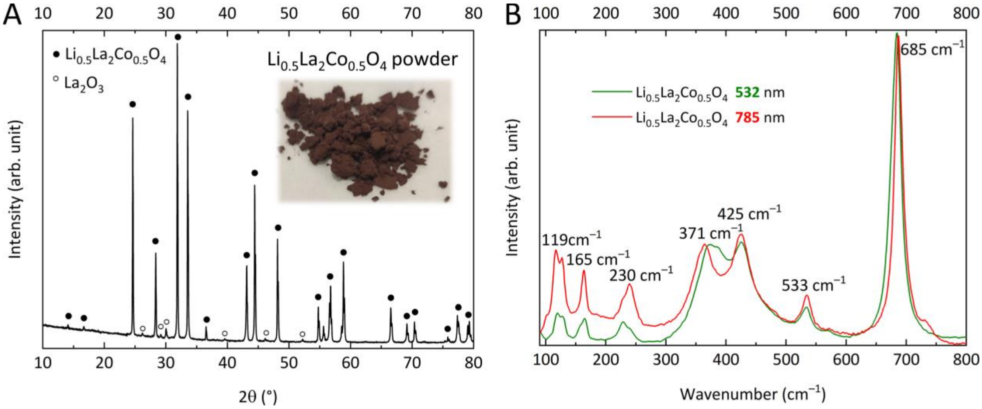

Figure 8.3: XRD and Raman measurements of the synthesized $Li_{0.5}La_2Co_{0.5}O_4$ powder. A) XRD pattern with a minor side phase of La_2O_3 and a photo of the brown powder; B) Raman spectra of the $Li_{0.5}La_2Co_{0.5}O_4$ powder measured with a 532 nm and a 785 nm laser. Copyright Wiley-VCH GmbH. Reproduced with permission [211].

In addition to the LLZO, LLZO:Co, and $Li_{0.5}La_2Co_{0.5}O_4$ phases, the Raman spectra on the cathode side show two additional signals at 493 cm^{-1} and 607 cm^{-1}, that can be assigned to the rhombohedral LCO phase (space group $R\bar{3}m$) with a slight shift to higher wavenumbers (LCO reference spectrum in S-Figure 21), as described later [234, 244].

8.2 Local distribution of phases

The measured LCO signals do not originate from the composite cathode because it has been completely removed from the separator, as can be seen in the SEM images (Figure 8.4C). It is conceivable that not only the LLZO:Co phase described above, but also the LCO phase is formed as a result of diffusion of Co-ions into the separator in a subsequent chemical reaction. In order to verify the formation of LCO in LLZO due to the reaction with Co-ions, an additional experiment was performed in which a small amount of Co(II) (1 wt% $CoCO_3$) was added to the LLZO powder and then heated to 1175 °C in a conventional furnace (Figure 8.2C, top). The Raman spectroscopy measurement shows the presence of the LLZO:Co and the LCO phase, proving that Co-ions in the presence of LLZO can react to LCO upon thermal treatment.

To determine the local distribution of the different phases as a function of the surface morphology of the separator, Raman spectroscopy mapping on the cathode side was performed. The resulting spectra were sorted by the individual phases $Li_{0.5}La_2Co_{0.5}O_4$ (374 cm^{-1}), LCO (597 cm^{-1}), and LLZO:Co (693 cm^{-1}) (Figure 8.4D–F) and correlated with the corresponding SEM images and EBSD measurements (Figure 8.4A–C and combined in Figure 8.4G–J). A strong photoluminescence signal from the LLZO:Co phase was detected throughout the cathode side of the separator. The intensity of this signal was strongest in the largest LLZO grains (approximately 20 µm in size), while a lower photoluminescence intensity, or no photoluminescence intensity, was measured in regions with small grains (less than ~5 µm). These results indicate that the LLZO:Co phase is formed by the diffusion of Co-ions in the LLZO lattice (bulk phase). In contrast, the LCO signals are mainly detected in the regions where the intensity of the photoluminescence signal (*e.g.* the LLZO:Co phase) is the lowest. The greatest amount of LCO phase is found in regions with a large number of small grains, and therefore, a higher number of grain boundaries, while LCO signals are greatly reduced in large grains.

Unlike the LLZO:Co and LCO phases, which are distributed relatively uniformly across the entire surface on the cathode side of the separator, the $Li_{0.5}La_2Co_{0.5}O_4$ phase appears to be randomly distributed and is most likely formed by precipitation. The $Li_{0.5}La_2Co_{0.5}O_4$ is not located near pores or grain boundaries and has no apparent correlation with the morphology of the separator or the presence of other phases. It is possible that the $Li_{0.5}La_2Co_{0.5}O_4$ phase forms in the part of the separator that has inhomogeneities in its composition (*e.g.* Ta- or Al-enriched domains, see S-Figure 22), but no accurate conclusion can be drawn from the obtained results at this stage. It should also be noted that although Raman spectroscopy clearly shows the presence of various Co-containing phases, no Co signal was detected by energy-dispersive X-ray spectroscopy (EDS) within the LLZO grains, suggesting that the absolute concentration of Co-ions in the LLZO is below the detection limit (with a typically EDS detection limit of ~0.1 wt%) and thus has a low concentration throughout the entire separator (S-Figure 23).

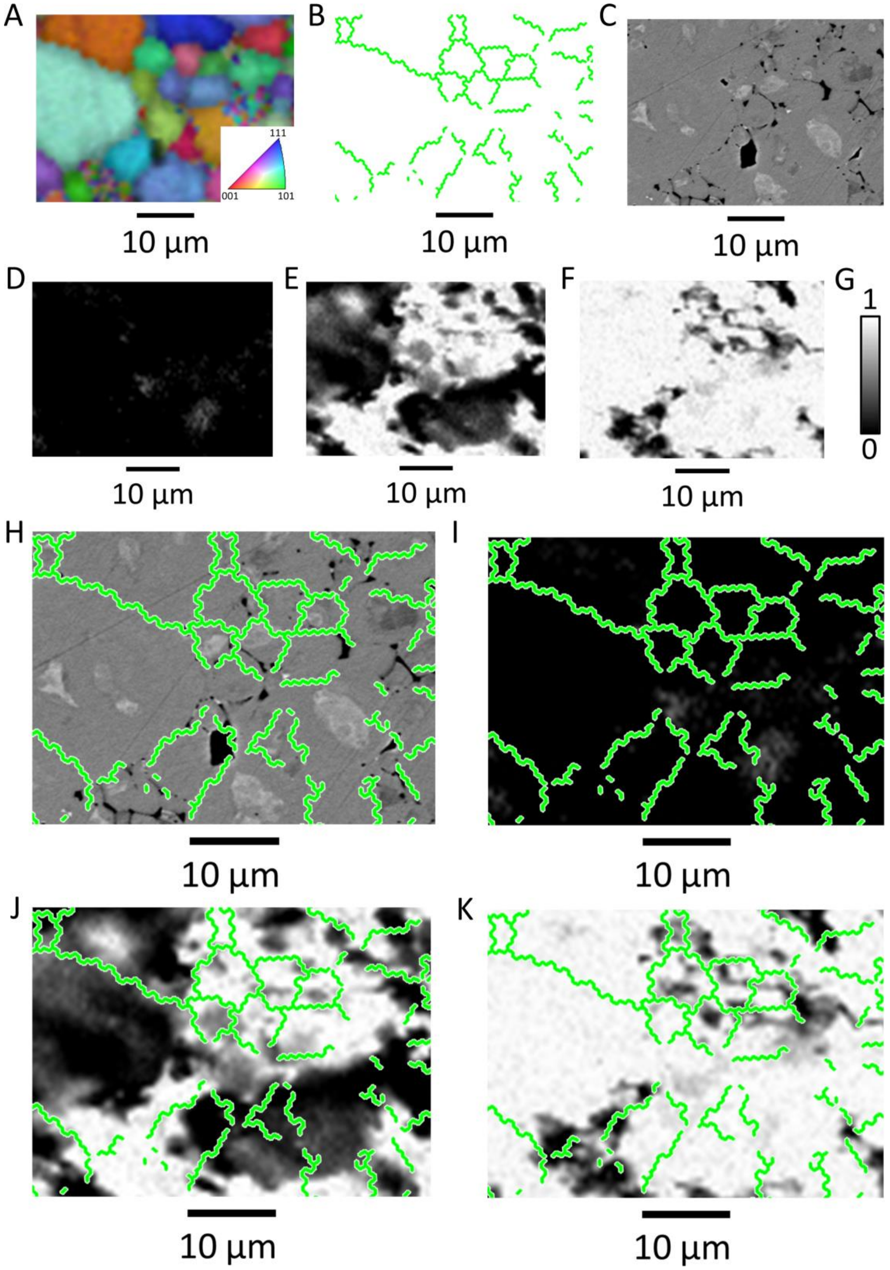

Figure 8.4: Combined measurements with SEM, Raman, and EBSD of the same top-view area at the cathode side. A) EBSD profile; B) EBSD grain contour; C) SEM image (backscattered electron); D) Raman mapping with highlighted $Li_{0.5}La_2Co_{0.5}O_4$ phase; E) Raman mapping with highlighted $LiCoO_2$ phase; F) Raman mapping with highlighted LLZO:Co photoluminesence at 693 cm^{-1}; G) Raman mapping intensity scale for all images; H) SEM image with superimposed EBSD grain contour; I) Raman mapping of the $Li_{0.5}La_2Co_{0.5}O_4$ phase with superimposed EBSD grain contour; J) Raman mapping of the $LiCoO_2$ phase with superimposed EBSD grain contour; K) Raman mapping of the LLZO:Co photoluminesence with superimposed EBSD grain contour. Copyright Wiley-VCH GmbH. Reproduced with permission [211].

8.3 Co-ion diffusion profile

Raman spectroscopy and ToF-SIMS analysis of a separator cross-section were performed to monitor the diffusion depth of Co-ions and other elements through the separator. Although the determination of absolute concentration in ToF-SIMS analysis is not straightforward, its high sensitivity enables the accurate determination of relative concentration changes. For the ToF-SIMS analysis, the polished cross-section (details in Figure 8.1) was divided into seven analysis regions of 20 µm × 20 µm along the thickness of the separator (Figure 8.5A), and the summarized intensity ratios of $^{59}Co^{16}O^-/^{16}O^-$ and $^{27}Al^{16}O^-/^{16}O^-$ were plotted as a function of distance from the cathode|separator interface, with the interface set equal to zero as the distance reference point. Raman spectroscopy mapping was also performed over the entire cross-section of the separator, and the individual spectra along the green lines in Figure 8.5A were averaged line by line. As an indication of Co-ion diffusion, the photoluminescence signal at 693 cm^{-1} from the LLZO:Co phase and the signal at 595 cm^{-1} from the LCO phase of each averaged line (corresponding to a 1 µm step) were plotted as a function of distance from the cathode (Figure 8.5A). The $Li_{0.5}La_2Co_{0.5}O_4$ phase is barely visible in the averaged line spectra due to its small overall amount and the overlap of its signals with the signals of the other spectra. It should be noted that due to the surface roughness, there is some inaccuracy in determining the zero position. The distance from the cathode is therefore subject to an error of about ± 15 µm for the ToF-SIMS and ± 3 µm for the Raman spectroscopy data.

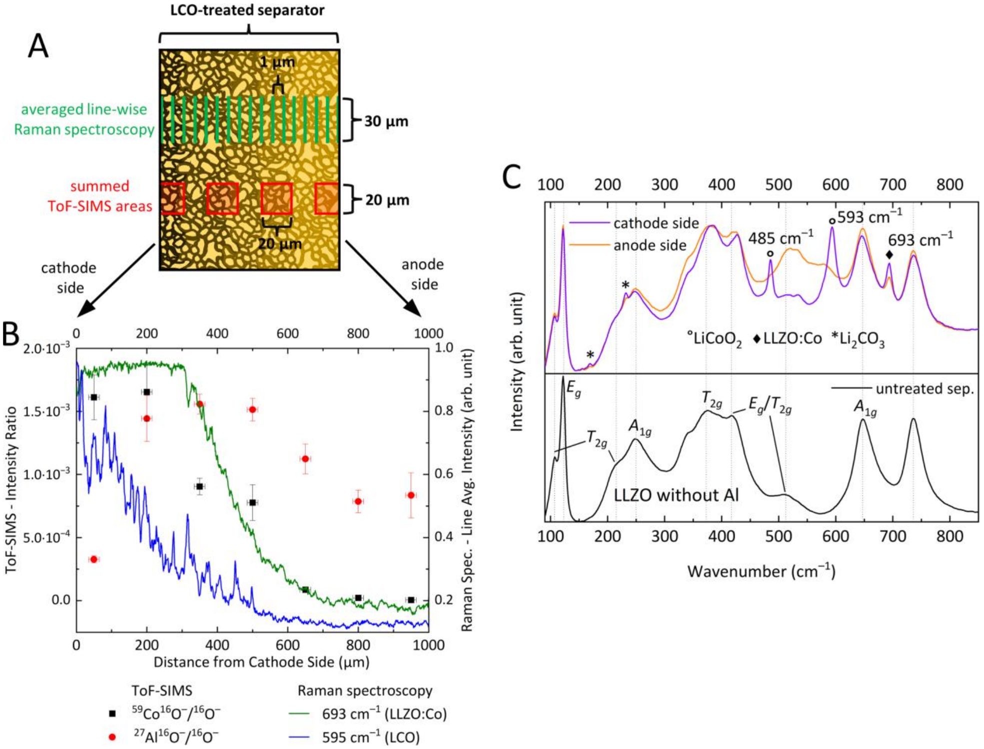

Figure 8.5: ToF-SIMS and Raman measurements to detect Co-ion diffusion into the LCO-treated separator as a function of distance from the cathode side (starting with 0 µm at the cathode|separator interface). A) ToF-SIMS, Raman scheme of the measurement through the entire cross-section thickness; B) intensity ratio of $^{59}\mathrm{Co}^{16}\mathrm{O}^-/^{16}\mathrm{O}^-$ (black) and $^{27}\mathrm{Al}^{16}\mathrm{O}^-/^{16}\mathrm{O}^-$ (red) species (ToF-SIMS) and normalized, averaged line signal intensity of the LLZO:Co photoluminescence at 693 cm^{-1} (green) and the signal at 595 cm^{-1} (blue) belonging to LCO (Raman spectroscopy) against the position at the separator cross-section (starting with 0 µm at the cathode); C) averaged Raman spectroscopy mappings of an Al-free, untreated, and LCO-treated separator (400 µm thickness). Copyright Wiley-VCH GmbH. Reproduced with permission [211].

The ToF-SIMS measurements (Figure 8.5B) clearly show the diffusion of Co-ions into the separator. High Co intensities are detected at thicknesses up to ~200 µm, after which they decrease continuously up to ~650 µm until they disappear in the background noise. Raman spectroscopy mapping also reveals the presence of LLZO:Co and LCO phases throughout the LLZO separator. The Raman spectroscopy profile of the LLZO:Co phase almost exactly matches the shape of the $^{59}\mathrm{Co}^{16}\mathrm{O}^-/^{16}\mathrm{O}^-$ signal in ToF-SIMS, with strong signals of an approximately equal intensity down to a depth of ~300 µm and a continuous decrease until no signal is measured at ~700 µm. In contrast to LLZO:Co, the signal of the LCO phase decreases continuously with increasing distance from the cathode side to a depth of ~600 µm. The temperature and dwell time are likely to be the governing sintering parameters for the diffusion distribution profile in the separator. The heating rate could also have an influence on the profile, but temperature gradients and their possible influences on diffusion in the material during RTP heating can be ruled out, since the heat capacity of 0.6 J $g^{-1}K^{-1}$ and the heat conduction of 1.5 W $K^{-1}m^{-1}$ for LLZO [21] lead to a homogeneous temperature distribution in the separator. For example, it could be that the diffusion distribution profiles change with prolonged heating, meaning that Co-ion contamination occurs at greater distances from the cathode, and its concentration increases or possibly reaches a maximum. Further studies are needed to quantify the exact diffusion kinetics.

In addition to the Co-ion diffusion, the ToF-SIMS measurements also show a change in Al concentration in the separator. LLZO is depleted of Al-ions near the cathode|separator interface and shows a high Al concentration at a distance between 200 µm and 500 µm, and a lower concentration close to the anode side between 800 µm and 1000 µm. The change in Al concentration occurs in the same region where the increase in Co concentration was observed, raising the question of whether these two processes are related. Similar effects were previously observed by Park *et al.* [72] and Ren *et al.* [259], where a strong uptake of Al from the LLZO:Al separator or an Al_2O_3 layer (between Al-free LLZO and LCO) into the LCO cathode was observed. Previous studies by some authors of this work also confirmed a very strong "aluminophilicity" of the LCO phase, which readily takes up Al-ions from LLZO:Ta-Al during co-sintering or even during electrochemical cycling [159], and forms $LiAl_xCo_{1-x}O_2$ [72, 260]. This enrichment of Al in LCO inside the separator is confirmed by Raman spectroscopy (Figure 8.2B–C), as the LCO signals are shifted to higher wavenumbers, indicating the formation of the $LiAl_xCo_{1-x}O_2$ phase [234, 244, 260]. To explain the Al concentration profile in the separator, it is important to know at which temperatures the different diffusion processes (Co → LLZO and Al → LCO) start. For this reason, an experiment was performed in which LCO and LLZO powder mixtures were heated to different temperatures and then measured by Raman spectroscopy to find the lowest temperature at which the LLZO:Co photoluminescence at 693 cm^{-1} occurs. The measurements (S-Figure 24) show that the LLZO:Co photoluminescence begins to appear in the sample processed at 700 °C, indicating the onset of Co-ion diffusion in LLZO at about 700 °C. Below 700 °C it is possible that LLZO:Co is already formed, but in a much lower concentration, so that it is below the limit of detection of the Raman spectrometer and has consequently only a minor influence on the sample. It has been reported that Al diffusion in LCO starts at 500 °C [261]. With these values, the following diffusion mechanism was assumed.

When the sample is heated, Al-ion diffusion from the separator to the cathode begins first, and the separator region near the cathode|separator interface becomes depleted of Al. The higher the temperature, the more the separator is affected by this process. When a higher temperature is reached, diffusion of Co-ions into the LLZO separator begins, and as temperature and time increase, a larger portion of the separator becomes contaminated with Co-ions up to, where aluminophilic LCO is formed inside the first ~600 µm of the separator. In the region near the cathode|separator interface, the Al concentration is already reduced due to the previous Al diffusion into the cathode, which is the largest LCO reservoir and therefore has the greatest potential for Al accumulation during heating/sintering [72, 260, 262]. Therefore, the LCO generated in the first ~200 µm is not able to accumulate much Al, and the total Al concentration in the separator region near the cathode|separator interface is kept low. Beyond a distance of ~200 µm from the cathode, the Al concentration in the separator is not affected by the Al-ion diffusion into the cathode, and the LCO formed can accumulate Al from the separator. The uncontaminated separator region, where no LCO has formed, has a lower Al content because no Al enrichment has occurred and the Al in the adjacent contaminated separator material has been taken up by the formed LCO. Consistent with this assumption, ToF-SIMS mappings of an LCO-treated separator cross-section where the cathode layer was present (not abraded) showed a strong increase in Al concentration in the cathode layer (S-Figure 25).

The experimentally observed change in Al concentration associated with Co-ion uptake in the LLZO separator raises the legitimate question of whether Al ↔ Co exchange is an important driving force for Co-ion diffusion into LLZO separators. A similar sample was prepared using an Al-free LLZO:Ta powder to confirm this assumption. The Al-free separator also shows the same coloration after RTP sintering of the cathode, suggesting that the diffusion of Al-ions is not the reason for the coloration of the separator. As in the case of the Al-containing LLZO (Figure 8.2B), the signals associated with the rhombohedral LCO were also detected on the cathode side of the Al-free separator in the Raman spectra, although the Raman lines at 485 cm^{-1} and 593 cm^{-1} did not exhibit a shift to higher wavenumbers, which would correspond to a $LiAl_xCo_{1-x}O_2$ phase formation (Figure 8.5C). On the contrary, they were slightly shifted to lower wavenumbers compared to the LCO reference spectrum (S-Figure 21). The shift of the LCO Raman bands to lower wavenumbers is well described in the literature and is typically associated with a decreased Li content in the LCO lattice [235, 263]. One of the possible reasons for the observed Raman shift in Al-free LLZO may be a sub-stoichiometric amount of Li-ions during the formation of the secondary LCO phase in the separator. Another possibility would be the loss of Li ions from the LCO due to the high temperature treatment [43]. These effects are also likely to occur in the LLZO:Ta-Al pellets (Figure 8.2B), but the possible Raman shift is likely to be outweighed by a shift in opposite direction caused by the uptake of Al-ions from the LLZO:Ta-Al particles, resulting in the formation of the $LiAl_xCo_{1-x}O_2$ phase. The Raman spectra also showed an intense photoluminescence signal of the LLZO:Co phase due to the diffusion of Co-ions into the LLZO bulk (Figure 8.5C). Raman measurements across the cross-section as a function of distance from the cathode|separator interface (S-Figure 26) also showed strong Co-ion diffusion for the Al-free LLZO separator, at similar penetration depths as for the Al-containing separator (Figure 8.5B). Although there are differences in the intensity profile, it is not possible to say whether these are due to different doping or different microstructure. The absence of Al, which acts as a sintering aid [264, 265], worsens the compaction of the powder, resulting in a less dense and mechanically more brittle separator compared to the Al-containing separator. In order to draw conclusions about the influence of doping and LLZO density on Co-ion diffusion in the LLZO separator, further investigations beyond the focus of this work are required.

However, this experiment already shows that the diffusion of Co-ions seems to be a characteristic property of the polycrystalline LLZO material even without Al doping, although it cannot be excluded that Al-ions or other dopants influence the diffusion of Co-ions in some way. Based on the obtained results, it can be suggested that there are two different pathways for the diffusion of Co-ions in polycrystalline LLZO. Considering that the formation of the LLZO:Co phase occurs mainly within large grains and that LCO is observed in the parts with a large number of grain boundaries, it is reasonable to assume that Co-ions can diffuse through the LLZO bulk lattice. There are two different possibilities of material transport for the Co-ions at the grain boundaries. The Co-ions could be transported by ion diffusion along the grain boundaries or by segregation from the bulk to the grain boundaries.

8.4 Simulation of diffusion mechanism

To reveal the transport mechanism of Co-ions in LLZO, large-scale MD simulations for cubic $[Li_{6.625}Co_{0.125}]La_3Zr_2O_{12}$ (see experimental part for simulation details) were performed. The simulations were performed in a temperature range of 800 K to 1400 K, which is similar to the highest temperature of 1273 K during RTP sintering, to capture chemical phenomena in the experiment. Figure 8.6A shows the migration pathway of Co-ions (yellow isosurface) in our cubic LLZO:Co model, indicating that Co-ion diffusion in c-LLZO follows Li-ion diffusion pathways. The activation energy E_a for Co-ion migration is predicted to be 0.539 eV, which is about 2.5 times larger than the E_a of Li-ion migration (Figure 8.6B). The diffusivity of Co-ions is about one to two orders of magnitude lower than that of Li-ions at temperatures of 800 K and above, indicating that Co-ion diffusion could be sufficiently fast to be observable on experimental timescales. Assuming the Brownian diffusion with the relation for the diffusion distance $l = \sqrt{\langle|\vec{r}|^2\rangle} = \sqrt{6\,D\,t}$, where $\langle|\vec{r}|^2\rangle$ is the mean squared displacement, D is the diffusivity, and t is time, the predicted Co-ion diffusivity of 10^{-6} cm^2 s^{-1} at 1000 °C is equivalent to a diffusion distance of 232 µm during the dwell time of 90 seconds at 1000 °C (without heating and cooling time). Accordingly, the results verify our assumption that Co-ions can diffuse through the LLZO bulk lattice *via* Li-ion sites and explain the experimental observation of Co-ions down to a depth of ~700 µm after the complete sintering process.

Note that the sintering temperature and time are closely interrelated. Accordingly, given the fast Co-ion diffusivity at high temperatures, it is recommended to reduce the sintering time to minimize Co-ion migration. However, exact conditions are difficult to recommend, given the sensitivity of densification kinetics to specific sintering approaches and green body formulations [266, 267]. Alternatively, lowering sintering temperature would help to slow Co-ion interdiffusion, but it might not completely remove the interdiffusion and could be difficult to guarantee effective densification: for instance, the predicted Co-ion diffusivity of $3 \cdot 10^{-7}$ cm^2 s^{-1} at 700 °C (Figure 6B) is corresponding to 127 µm diffusion distance, penetrating about half as deep as at 1000 °C with the same sintering time—still appreciable. Overall, a more effective strategy may be to use interlayers between the cathode and the separator that could prevent or delay the onset of interdiffusion.

Compared to Co-free LLZO (cubic $Li_{6.625}La_3Zr_2O_{12}$ without Co), the diffusivity of Li-ions decreases only slightly (Figure 8.6B). In particular, an extrapolation of the Arrhenius plot to RT

(300 K) leads to Li-ion diffusivities of $3.5 \cdot 10^{-8}$ cm^2 s^{-1} and $2.0 \cdot 10^{-8}$ cm^2 s^{-1} in our Co-free LLZO and LLZO:Co models, respectively. This is an agreement with the measured trend of decreased ionic conductivities in the untreated LLZO and LCO-treated separator ($3.0 \cdot 10^{-4}$ S cm^{-1} and $1.6 \cdot 10^{-4}$ S cm^{-1}, respectively, at 298 K in Figure 8.6B). Similarly, the activation energy increases only slightly upon the inclusion of Co-ions. Therefore, at this low Co-ion doping level, it is assumed that the mobile Co-ions do not effectively block Li diffusion pathways within grains of LLZO. However, other possible effects of the Co-ion diffusion (*e.g*. secondary phase formation) could still reduce the ionic conductivity of the LLZO separator.

In addition to bulk grains, Co-ions may also diffuse *via* grain boundaries in LLZO. Accordingly, the transport characteristics of Co-ions were further investigated using a ∑13(230)/[001] symmetric tilt grain boundary model. Co-ions, which were initially placed at the grain interior, segregate to the grain boundary during the simulation, as shown in the heatmap of integrated Co-ion positional probability density (Figure 8.6C) as well as in the atomic structure (S-Figure 27A). In Figure 8.6D, it can be seen that the Co-ion concentration at the grain boundary starts to saturate after about 5 ns of simulation time and does not vary significantly after 7.5 ns. As a result of Co-ion segregation, the overall concentration of Li-ions at the grain boundary also decreases somewhat, alongside minor redistributions of La- and Zr-ions (S-Figure 27B).

Perhaps more significantly, the heatmap shows that the Co-ions are not uniformly distributed within the grain boundary. Instead, the segregated ions exhibit a highly discontinuous distribution along the grain boundary, with some regions showing a very high concentration of Co-ions and others showing little to no Co-ion concentration buildup. Notably, this local clustering of Co-ions at the grain boundaries (*e.g*. highlighted at the bottom of the grain boundary on the right in Figure 8.6C), which may be facilitated by the greater local free volume at the grain boundaries, indicates the possible pre-nucleation and formation of other Co-rich phases. This may explain the appearance of the LCO phase at the grain boundaries, as observed in our experiment. Moreover, the fact that the probability density of Co-ions exhibits broad minima in grain boundary regions between the local clusters suggests that Co-ions are not generally transported along the grain boundaries, but are instead trapped upon segregation. Indeed, the MSD in S-Figure 27C confirms that the Co-ions segregated at grain boundaries also exhibited much slower transport compared to those within the grain interior. Grain boundaries are known to inhibit transport for Li-ions due to structural disorder disrupting migration pathways. It is therefore reasonable to assume that Co-ion migration might also be affected, given that Co-ions and Li-ions share the same pathways.

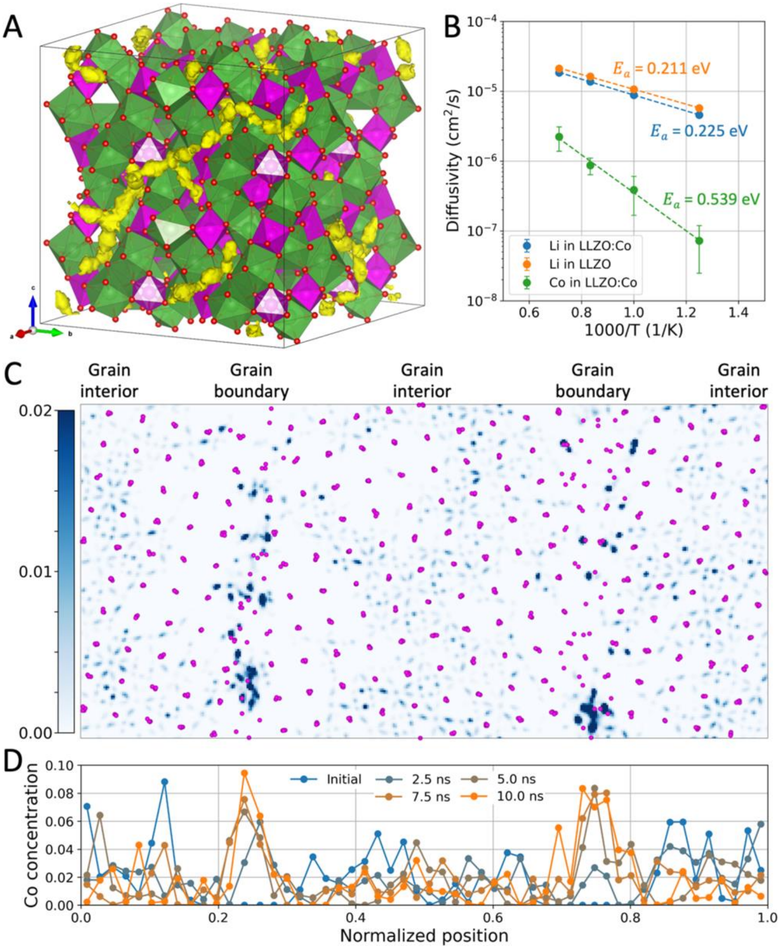

Figure 8.6: Molecular dynamics simulation results for c-LLZO systems. A) Positional probability density of Co-ions in a 2 × 2 × 2 c-LLZO supercell showing Co diffusion pathways (yellow isosurface with 10^{-4} Å^{-3} isosurface level), which was evaluated by 1 ns MD trajectory for $[Li_{6.625}Co_{0.125}]La_3Zr_2O_{12}$ at 1400 K. ZrO_6 and LaO_8 polyhedra with red O-ions at vertices are shown in magenta and green, respectively. B) Arrhenius plot of Li-ion diffusivities in $[Li_{6.625}Co_{0.125}]La_3Zr_2O_{12}$ (blue) and pure LLZO ($Li_{6.625}La_3Zr_2O_{12}$, orange), and Co-ion diffusivity in $[Li_{6.625}Co_{0.125}]La_3Zr_2O_{12}$ (green) with error bars indicating standard deviations. Dashed lines and activation energies E_a are obtained by linear fits. C) Heatmap of the integrated positional probability density of Co-ions (in Å^{-3}) in the presence of a ∑13(230)/[001] symmetric tilt grain boundary at 1300 K. Magenta spheres depict Zr-ions, showing the grain boundary configuration. D) Development over time of the corresponding concentration profile of Co-ions normal to the grain boundary plane (Co-ions were initially placed at the grain interiors). Copyright Wiley-VCH GmbH. Reproduced with permission [211].

The simulation results suggest that that the main diffusion mechanism of Co-ions is through the LLZO grain interiors and that the segregation, trapping, and clustering of Co-ions at the grain boundaries may lead to further reactions. LCO is a probable product of such reactions with residual Li-ions at LLZO grain boundaries, most likely with surficial impurities like Li_2CO_3 [35, 72, 260, 262, 264, 268], as suggested within the reaction mixture of LLZO and $CoCO_3$ (Figure 8.2C, top).

8.5 Oxidation state of phases

To obtain further information about the different phases, XPS measurements were performed on the LLZO separator. The La 3*d* signals (Figure 8.7A) of the La lattice in LLZO [269, 270] are virtually identical for untreated and LCO-treated separators, showing only minor shifts in binding energy. Moreover, the signal at 527.8 eV in the O 1*s* XPS spectrum (Figure 8.7B) corresponding to O in the LLZO lattice [270-272] has the same binding energy for the untreated and LCO-treated separator, indicating a similar chemical environment for the oxygen sublattice in the LLZO grains in both samples. However, significant differences were observed in the oxygen surface impurity signals. The O 1*s* XPS spectrum of the untreated separator shows the presence of Li_2CO_3 (530.4 eV) and/or Li_2O/LiOH (529.8 eV) surface impurities, which are formed when the LLZO surface is exposed to the ambient atmosphere [273]. The concentration of surface impurities is much higher in the untreated LLZO separator than in the LCO-treated separator, where only a small amount of Li_2O/LiOH was detected on the cathode side. Both samples were fabricated at the same time and therefore had the same time of surface exposure, but the LCO-treated separator was subject to additional heat treatment during cathode sintering. During this step, Li_2CO_3, which was formed on the LLZO particle surface, could react reversibly to LLZO, as described in [29]. In addition, Li losses due to elevated temperatures could occur [274] or a reaction with diffused Co-ions could take place to form LCO. One of the reasons for this might be that the LCO-treated sample contains significantly fewer surface impurities.

Untreated and LCO-treated separators also show significantly different Co 2*p* XPS spectra (Figure 8.7C). No Co 2*p* signals were detected on the untreated separator, while two peaks at 794.1 eV and 779.0 eV and a shoulder at 775.5 eV were measured for the LCO-treated separator. The signals at 794.1 eV and 779.0 eV can be attributed to Co^{3+} [275]. Accounting for a small shift of Δ1 eV in binding energy, the signals could be attributed to the LCO, which has signals at 780 eV and 795 eV [276]. The $Li_{0.5}La_2Co_{0.5}O_4$ phase could also be considered, which shows broad signals in this range of binding energy [277]. The shoulder at 775.5 eV could not be assigned to any known phase. Since the binding energy is lower than that of Co^{2+}, Co^{3+}, and metallic Co^0 (778 eV) [275, 278], the signal indicates a different chemical environment, possibly the LLZO:Co phase. Zarabian *et al.* found a signal at 773 eV for an LCO–LLZO system, which they attributed to an Auger peak of Co clusters with different oxidation states (Co^{x+}) [151, 279, 280]. Since the intensity and position of the Auger signals strongly depend on the oxidation state of Co, the interaction between the positive Li atoms and the transition metal Co could lead to a change in the work function and, thus, to a shift of the core electron binding energy to lower values [151, 279-281]. If the same explanation is applied to the signal at 775.5 eV, and if this signal corresponds to the LLZO:Co phase, then the photoluminescence should be strongly affected by the oxidation or reduction of the sample. To test this hypothesis, the LCO-treated separator was heated in air to 900 °C to oxidize possible Co^{x+} clusters in the LLZO:Co phase (Figure 8.7D). The photoluminescence signal, which was broadly distributed and exhibited high intensities in the LCO-treated separator, almost completely disappeared after the additional heating in air, supporting this assumption. The detection of Co^{x+} in several oxidation states below Co^{3+} challenges the widely held opinion about the structure of the LLZO:Co phase. Previously, Co^{3+} was assumed to replace Zr^{4+} sites in the LLZO structure, as predicted by Miara *et al.* [25, 101]. However, other structures can be expected if the oxidation state of Co changes.

In addition, the LCO signals from the annealed cathode side show a shift to lower wavenumbers, consistent with the previously discussed loss of Li [235, 263].

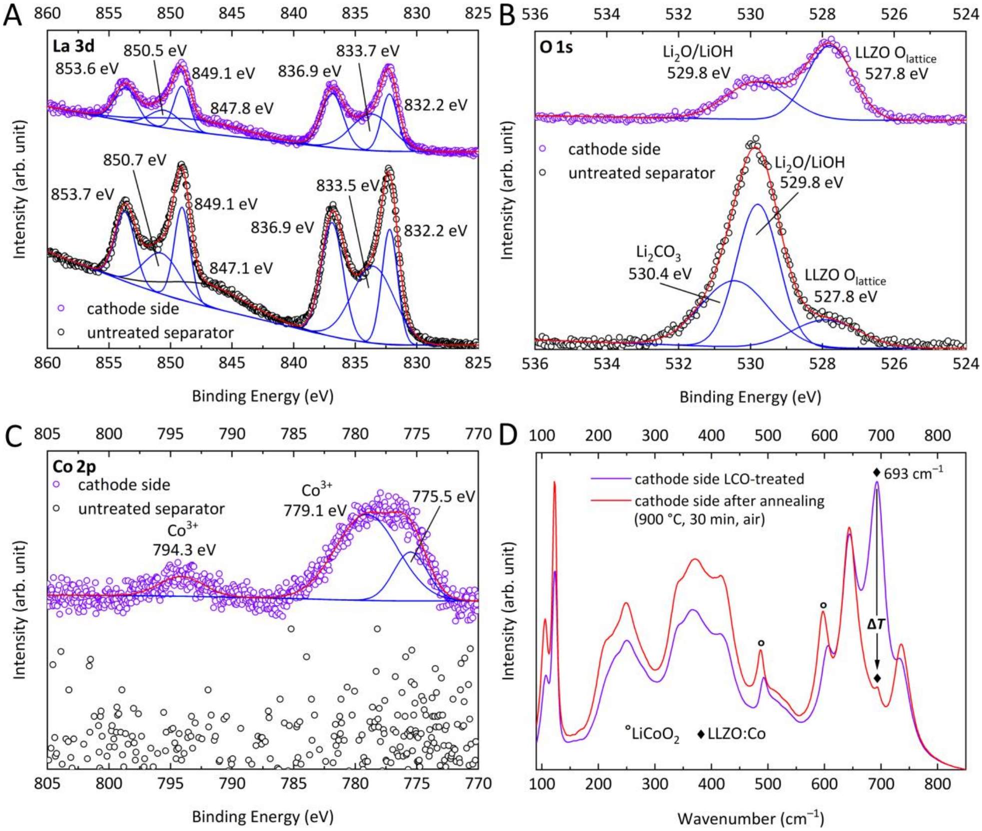

Figure 8.7: XPS measurements of the untreated and the cathode side of the LCO-treated separator. A) spectra of La 3*d*; B) spectra of O 1*s*; C) spectra of Co 2*p*; D) Raman spectra of the cathode side after additional annealing in air at 900 °C for 30 min. Copyright Wiley-VCH GmbH. Reproduced with permission [211].

8.6 Influence of Co-ion diffusion on electrochemical properties

To investigate the effect of Co-ion diffusion on the electrochemical properties of the LLZO separator, the redox potential, ionic conductivity, and Li dendrite tolerance of untreated and LCO-treated separators were analyzed. To determine the redox potential of the LCO-treated separator, it was sandwiched between two Au electrodes, and a linear potential scan was applied in a potential range from –1 V to 2 V (Figure 8.8A). The untreated LLZO separator shows virtually no redox activity in this potential range. In contrast, distinct redox features were observed for the LCO-treated sample even at low potentials, with a first oxidation peak at about 0.25 V, the second at about 1.5 V, and further increases in current at higher potentials, thus indicating a significantly increased redox activity of the LCO-treated separators. Furthermore, the onset of the reduction potential shifts to less negative values for the LCO-treated separators (–0.5 V compared to –0.75 V for the untreated separator), indicating lower reduction stability. The electrochemical impedance spectra (EIS) of the untreated and the LCO-treated separators also change significantly (Figure 8.8B). The Nyquist plots of both samples show semicircles at high frequencies, which can be attributed to the grain boundary resistance. Fitting of the impedance spectra yields a grain boundary resistance of 161 Ω cm^2 and a total ionic conductivity σ of $3.0 \cdot 10^{-4}$ S cm^{-1} for the untreated separator at 25 °C. For the LCO-treated separator, the grain boundary resistance increases by 47% to 344 Ω cm^2, and the total ionic conductivity decreases to $1.6 \cdot 10^{-4}$ S cm^{-1} at 25 °C.

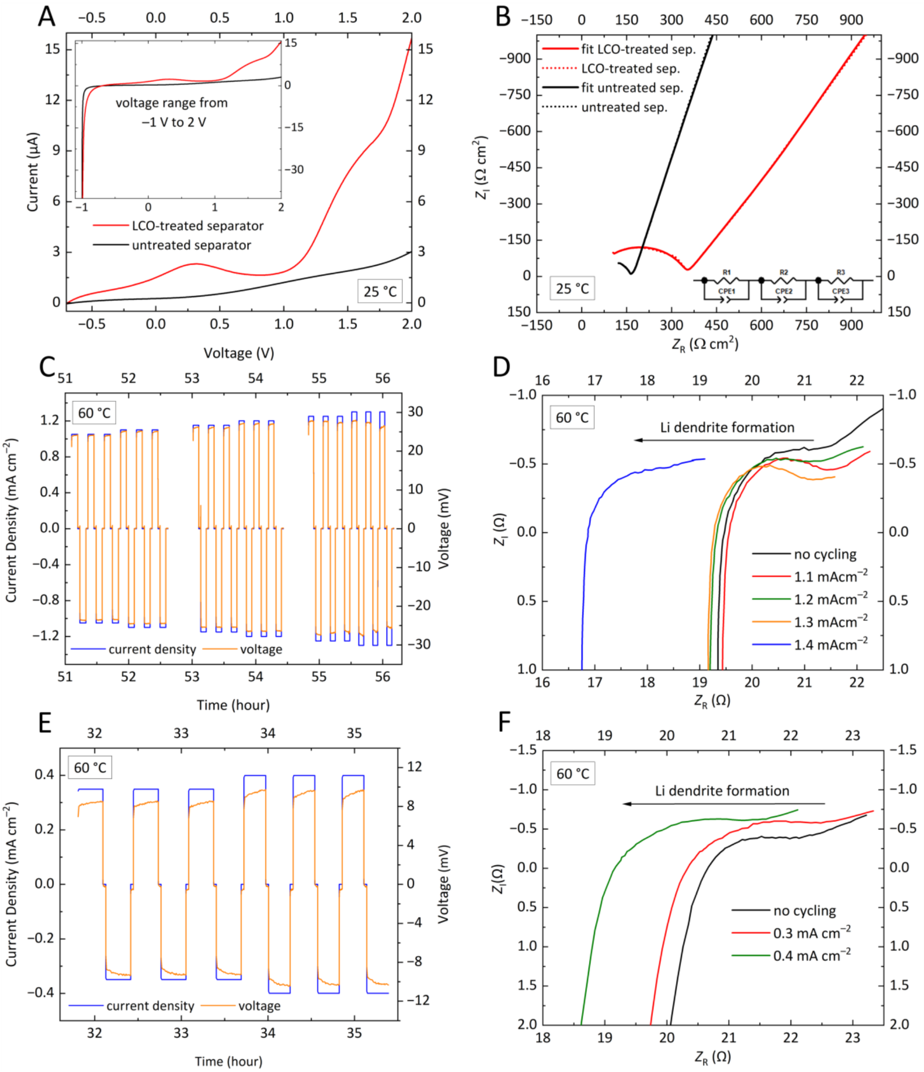

Figure 8.8: Electrochemical characterization of untreated and LCO-treated separators. A) LSV curves of symmetric Au|LLZO|Au cell at 25 °C with the full curve in potential range from –1 V to 2 V shown in the inset. Note that the potential values correspond to the potential difference applied between two Au electrodes, and not the absolute values; B) Nyquist plots of EIS spectra of symmetric Au|LLZO|Au cell at 25 °C. The equivalent circuit used for the fitting of spectra is shown in the inset (R is ohmic resistance, and CPE is constant phase element); C) lithium plating/stripping measurements (CCD), and D) the corresponding EIS measurements of the untreated separator in a symmetric Li|LLZO|Li cell performed at 60 °C; E) CCD and F) EIS measurements of the LCO-treated separator. Copyright Wiley-VCH GmbH. Reproduced with permission [211].

A high cycling stability with Li metal anodes at high current densities without dendrite formation (dendrite stability characterized by critical current density, CCD) is another important property of LLZO separators required for their sufficient performance in battery cells. To evaluate the effect of Co-ion diffusion on the dendrite stability of the separators, they were sandwiched between two Li metal electrodes, and capacity-controlled galvanostatic cycles with an increasing current density were applied between the electrodes, starting from 50 µA cm^{-2} with an increment of 50 µA cm^{-2} per cycle (Figure 8.8C–F). The untreated separator shows stable lithium stripping/plating performance with no sign of dendrites up to a current density of 1.25 mA cm^{-2} at 60 °C, after which the potential decreased due to micro dendrite formation. The dendrite formation is also evident in the EIS data, where the dendrites through the separator reduce the distances between the electrodes, thus reducing the absolute ohmic resistance. The LCO-treated separator shows a much lower critical current density for dendrite formation under the same conditions. Even at a current density of 0.40 mA cm^{-2}, dendrite formation is observed by a significant reduction in ohmic resistance in the EIS measurements. These measurements demonstrate that the Co-ion diffusion into the LLZO separator negatively affects the dendrite stability, resulting in ∼72% lower critical current densities.

The obtained data show that the diffusion of Co-ions into the LLZO separator deteriorates its electrochemical performance by changing the redox activity, decreasing the ionic conductivity, and reducing the critical currents of Li dendrite formation in combination with Li metal anodes. These results suggest that measures should be taken to prevent ion diffusion from the cathode to the separator. For the fabrication of all-ceramic garnet-based batteries with LCO cathodes in the high-temperature process, it will be almost mandatory to use modified cathode compositions [101] or to introduce protective layers between the LLZO separator and the cathode layer.

Since Al_2O_3 was already successfully used for protecting the LCO|LLZO interface reactions at 800 °C [259], it was tested if such Al_2O_3 coatings could be useful at higher temperatures. For this purpose, thin Al_2O_3 films were deposited on LLZO pellets by ALD before the LCO cathodes were screen printed (S-Figure 28A) [259]. Unfortunately, despite the Al_2O_3 coating, the separator was strongly colored on both sides after RTP sintering, and a strong photoluminescence signal of the LLZO:Co phase at 693 cm^{-1} was observed in Raman spectroscopy (S-Figure 28B). This indicates that the Al_2O_3 coating can only stop diffusion up to a certain temperature range. Therefore, other materials currently used for coating CAM powders, such as Li_3BO_3 [153], $Li_{2.3}C_{0.7}B_{0.3}O_3$ [110], or Li–Nb–O coatings [154, 210], may be tested in the future.

9 Conclusion

In this work, the suitability of radiation-based sintering processes such as RTP and laser sintering for sintering garnet-based battery components for various battery designs were investigated. It was shown that RTP and laser sintering can be used to sinter electrode layers directly on steel current collector, which was not possible with conventional sintering methods. Pure LCO layers could be successfully sintered on steel substrates using RTP to produce highly dense ~15 µm thick smooth layers in a sintering time of only 90 s. The LCO phase was largely preserved at 1000 °C, and only minor impurities of CoO and Co_3O_4 were detected. An electrochemical activity of the cathodes could be demonstrated using a liquid electrolyte. RTP sintering of pure LLZO layers and LCO-LLZO composite cathodes on a steel substrate was identified to be impacted by reactions with the metal substrate leading to material decomposition.

Nevertheless, it was demonstrated to sinter the composite cathodes on steel substrates by laser sintering because the cathode layers were heated selectively without extensively heating the metal substrate, since the overall interaction time of the composite cathode was drastically reduced [178]. The sintered cathode showed phase retention of LLZO and LCO with an occurring ion diffusion, resulting in small amounts of $LaCoO_3$, $Li_{0.5}La_2Co_{0.5}O_4$ and CoO secondary phases. The cathode layers were successfully assembled into a battery by infiltrating PEO into the porous cathode and attaching an LLZO separator with a Li metal anode. The laser-sintered cathode layers exhibited a high specific capacity of 102 mAh g^{-1} (86% cathode utilization) in the first discharge cycle and a capacity retention of 53% after 12 electrochemical cycles, that is equal to cells in literature of conventionally or FAST-SPS-sintered LCO-LLZO composite cathodes, thus proving the technical feasibility of laser sintering in SSB cell manufacture.

In a second battery design, electrolyte-supported LCO-LLZO composite cathodes were investigated for processability with radiation-based sintering. It was effectively shown that the short sintering times in the RTP process are suitable for sintering LCO-LLZO composite cathodes without secondary phase formation. Fully inorganic cells consisting of only LLZO, LCO, and a Li-In anode could be successfully fabricated and electrochemically cycled. The dense ~13 µm thick cathodes exhibited moderate capacity, utilizing 71% of the theoretical capacity.

After RTP sintering, the LLZO separator exhibited a dark coloration, which was also observed in the samples from conventional sintering and FAST/SPS. Although no secondary phases were observed using macroscopic techniques such as XRD, microscale studies have attributed the origin of this discoloration to the diffusion of Co-ions through the polycrystalline LLZO separator. It was revealed that this diffusion results in the formation of a photoluminescent Co-doped LLZO:Co phase, a $Li_{0.5}La_2Co_{0.5}O_4$ phase, and an LCO phase almost throughout the entire separator thickness. The LCO:Co phase was observed only inside the grains, while the LCO phase was mainly found at the grain boundaries, where it could be formed by a reaction with Li-containing surface impurities, *e.g.*, Li_2CO_3. Large-scale MD simulations confirmed different mechanisms of Co-ion diffusion in the grain interior and at the grain boundaries, with Co-ions segregating at the grain boundaries. Furthermore, the $Li_{0.5}La_2Co_{0.5}O_4$ phase was randomly distributed in the grains and at the grain boundaries. Since no correlation was found between the distribution of $Li_{0.5}La_2Co_{0.5}O_4$ and the microstructure of the separator, this phase was most likely formed by precipitation. Although the LLZO separator was 1000 µm thick, the LCO and LLZO:Co phases were found at a distance of up to 700 µm from the interface of the composite cathode, indicating a high diffusion coefficient under these conditions. In addition, depletion of Al was observed in the LLZO separator near the cathode interface. Here, leaching of Al from the separator into the LCO phase is likely, forming $LiAl_xCo_{1-x}O_2$ to compensate for the Co deficiency. Further analysis of the contaminated separators revealed that Co-ion diffusion adversely affects their electrochemical performance, leading to increased redox activity, decreased ionic conductivity, and lower dendrite tolerance in combination with Li metal anodes.

These results highlight the importance of the mutual cation diffusion in the LCO|LLZO system for a possible future implementation of garnet based SSB. Thereby, this study provides the basis for further research in the development of strategies to mitigate the cation diffusion during sintering.

References

1. J.F.M. Oudenhoven, L. Baggetto, P.H.L. Notten, *Adv. Energy Mater.*, **2011**, *1*, 10-33.
2. A. Yoshino, *Angew. Chem. Int. Ed.*, **2012**, *51*, 5798-800.
3. W. Liu, T. Placke, K.T. Chau, *Energy Rep.*, **2022**, *8*, 4058-4084.
4. J. Figgener, P. Stenzel, K.-P. Kairies, J. Linßen, D. Haberschusz, O. Wessels, G. Angenendt, M. Robinius, D. Stolten, D.U. Sauer, *J. Energy Storage*, **2020**, *29*, 101153.
5. J.M. Tarascon, M. Armand, *Nature*, **2001**, *414*, 359-67.
6. M.E. Wieser, T.B. Coplen, *Pure Appl. Chem.*, **2010**, *83*, 359-396.
7. S.G. Bratsch, *J. Phys. Chem. Ref.*, **1989**, *18*, 1-21.
8. T.M. Gür, *Energy Environ. Sci.*, **2018**, *11*, 2696-2767.
9. R. Korthauer, *Handbuch Lithium-Ionen-Batterien*, 1st ed., **2013**, *Springer-Verlag Berlin*, Heidelberg.
10. J.G. Kim, B. Son, S. Mukherjee, N. Schuppert, A. Bates, O. Kwon, M.J. Choi, H.Y. Chung, S. Park, *J. Power Sources*, **2015**, *282*, 299-322.
11. J. Janek, W.G. Zeier, *Nat. Energy*, **2016**, *1*.
12. Y. Xiao, Y. Wang, S.-H. Bo, J.C. Kim, L.J. Miara, G. Ceder, *Nat. Rev. Mater.*, **2019**, *5*, 105-126.
13. N. Zhao, W. Khokhar, Z. Bi, C. Shi, X. Guo, L.-Z. Fan, C.-W. Nan, *Joule*, **2019**, *3*, 1190-1199.
14. C. Wang, K. Fu, S.P. Kammampata, D.W. McOwen, A.J. Samson, L. Zhang, G.T. Hitz, A.M. Nolan, E.D. Wachsman, Y. Mo, V. Thangadurai, L. Hu, *Chem. Rev.*, **2020**, *120*, 4257-4300.
15. R. Murugan, V. Thangadurai, W. Weppner, *Angew. Chem. Int. Ed.*, **2007**, *46*, 7778-81.
16. T. Thompson, S. Yu, L. Williams, R.D. Schmidt, R. Garcia-Mendez, J. Wolfenstine, J.L. Allen, E. Kioupakis, D.J. Siegel, J. Sakamoto, *ACS Energy Lett.*, **2017**, *2*, 462-468.
17. J.F. Wu, E.Y. Chen, Y. Yu, L. Liu, Y. Wu, W.K. Pang, V.K. Peterson, X. Guo, *ACS Appl. Mater. Interfaces*, **2017**, *9*, 1542-1552.
18. K.J. Kim, J.L.M. Rupp, *Energy Environ. Sci.*, **2020**, *13*, 4930-4945.
19. T. Thompson, J. Wolfenstine, J.L. Allen, M. Johannes, A. Huq, I.N. David, J. Sakamoto, *J. Mater. Chem. A*, **2014**, *2*, 13431-13436.
20. F. Tietz, T. Wegener, M.T. Gerhards, M. Giarola, G. Mariotto, *Solid State Ion.*, **2013**, *230*, 77-82.
21. J. Neises, W.S. Scheld, A.-R. Seok, S. Lobe, M. Finsterbusch, S. Uhlenbruck, R. Schmechel, N. Benson, *J. Mater. Chem. A*, **2022**, *10*, 12177-12186.
22. M. Ihrig, M. Finsterbusch, C.-L. Tsai, A.M. Laptev, C.-h. Tu, M. Bram, Y.J. Sohn, R. Ye, S. Sevinc, S.-k. Lin, D. Fattakhova-Rohlfing, O. Guillon, *J. Power Sources*, **2021**, *482*, 228905.
23. M. Finsterbusch, T. Danner, C.L. Tsai, S. Uhlenbruck, A. Latz, O. Guillon, *ACS Appl. Mater. Interfaces*, **2018**, *10*, 22329-22339.
24. M. Rosen, M. Finsterbusch, O. Guillon, D. Fattakhova-Rohlfing, *J. Mater. Chem. A*, **2022**, *10*, 2320-2326.
25. C.-L. Tsai, Q. Ma, C. Dellen, S. Lobe, F. Vondahlen, A. Windmüller, D. Grüner, H. Zheng, S. Uhlenbruck, M. Finsterbusch, F. Tietz, D. Fattakhova-Rohlfing, H.P. Buchkremer, O. Guillon, *Sustain. Energy Fuels*, **2019**, *3*, 280-291.

26. M. Ihrig, R. Ye, A.M. Laptev, D. Grüner, R. Guerdelli, W.S. Scheld, M. Finsterbusch, H.-D. Wiemhöfer, D. Fattakhova-Rohlfing, O. Guillon, *ACS Appl. Energy Mater.*, **2021***, 4*, 10428-10432.
27. W.S. Scheld, S. Lobe, C. Dellen, M. Ihrig, G. Hauschen, L.C. Hoff, M. Finsterbusch, S. Uhlenbruck, O. Guillon, D. Fattakhova-Rohlfing, *J. Power Sources*, **2022***, 545*, 231872.
28. M. Ihrig, T.P. Mishra, W.S. Scheld, G. Hauschen, W. Rheinheimer, M. Bram, M. Finsterbusch, O. Guillon, *J. Eur. Ceram. Soc.*, **2021***, 41*, 6075-6079.
29. M. Rosen, R. Ye, M. Mann, S. Lobe, M. Finsterbusch, O. Guillon, D. Fattakhova-Rohlfing, *J. Mater. Chem. A*, **2021***, 9*, 4831-4840.
30. M. Mann, M. Küpers, G. Häuschen, M. Finsterbusch, D. Fattakhova-Rohlfing, O. Guillon, *Ionics*, **2021***, 28*, 53-62.
31. M. Mann, M. Kupers, G. Hauschen, M. Finsterbusch, D. Fattakhova-Rohlfing, O. Guillon, *Materials*, **2021***, 14*.
32. C.-L. Tsai, E. Dashjav, E.-M. Hammer, M. Finsterbusch, F. Tietz, S. Uhlenbruck, H.P. Buchkremer, *J. Electroceramics*, **2015***, 35*, 25-32.
33. F. Aguesse, W. Manalastas, L. Buannic, J.M. Lopez Del Amo, G. Singh, A. Llordes, J. Kilner, *ACS Appl. Mater. Interfaces*, **2017***, 9*, 3808-3816.
34. X. Liu, R. Garcia-Mendez, A.R. Lupini, Y. Cheng, Z.D. Hood, F. Han, A. Sharafi, J.C. Idrobo, N.J. Dudney, C. Wang, C. Ma, J. Sakamoto, M. Chi, *Nat. Mater.*, **2021***, 20*, 1485-1490.
35. C.L. Tsai, V. Roddatis, C.V. Chandran, Q. Ma, S. Uhlenbruck, M. Bram, P. Heitjans, O. Guillon, *ACS Appl. Mater. Interfaces*, **2016***, 8*, 10617-26.
36. T. Hettesheimer, S. Hirzel, H.B. Roß, *Energy Effic.*, **2018***, 11*, 1227-1245.
37. M. Castro Oliveira, M. Iten, P.L. Cruz, H. Monteiro, *Energies*, **2020***, 13*, 6096.
38. J. Wakasugi, H. Munakata, K. Kanamura, *J. Electrochem. Soc. Jpn.*, **2017***, 85*, 77-81.
39. N. Zhang, X. Long, Z. Wang, P. Yu, F. Han, J. Fu, G. Ren, Y. Wu, S. Zheng, W. Huang, C. Wang, H. Li, X. Liu, *ACS Appl. Energy Mater.*, **2018***, 1*, 5968-5976.
40. Y. Ren, T. Liu, Y. Shen, Y. Lin, C.-W. Nan, *J. Materiomics*, **2016***, 2*, 256-264.
41. S. Uhlenbruck, J. Dornseiffer, S. Lobe, C. Dellen, C.-L. Tsai, B. Gotzen, D. Sebold, M. Finsterbusch, O. Guillon, *J. Electroceramics*, **2016***, 38*, 197-206.
42. L. Miara, A. Windmuller, C.L. Tsai, W.D. Richards, Q. Ma, S. Uhlenbruck, O. Guillon, G. Ceder, *ACS Appl. Mater. Interfaces*, **2016***, 8*, 26842-26850.
43. W.S. Scheld, S. Lobe, S. Uhlenbruck, C. Dellen, Y.J. Sohn, L.C. Hoff, F. Vondahlen, O. Guillon, D. Fattakhova-Rohlfing, *Thin Solid Films*, **2022***, 749*, 139177.
44. D.H. Jung, N. Umirov, T. Kim, Z. Bakenov, J.S. Kim, S.S. Kim, *Eurasian Chem.-Technol. J.*, **2019***, 21*, 3-12.
45. K.H. Kim, Y. Iriyama, K. Yamamoto, S. Kumazaki, T. Asaka, K. Tanabe, C.A.J. Fisher, T. Hirayama, R. Murugan, Z. Ogumi, *J. Power Sources*, **2011***, 196*, 764-767.
46. A.H. Whitehead, M. Schreiber, *J. Electrochem. Soc.*, **2005***, 152*, A2105.
47. D. Angmo, T.T. Larsen-Olsen, M. Jørgensen, R.R. Søndergaard, F.C. Krebs, *Adv. Energy Mater.*, **2013***, 3*, 172-175.
48. L. Rebohle, S. Prucnal, W. Skorupa, *Semicond. Sci. Technol.*, **2016***, 31*, 103001.
49. J.P. Kruth, X. Wang, T. Laoui, L. Froyen, *Assem. Autom.*, **2003***, 23*, 357-371.
50. M.-S. Park, S.-H. Hyun, S.-C. Nam, *Electrochim. Acta*, **2007***, 52*, 7895-7902.
51. V. Shanmugam, J. Cunnusamy, A. Khanna, M.B. Boreland, T. Mueller, *Energy Procedia*, **2013***, 33*, 64-69.
52. J. Schnell, F. Tietz, C. Singer, A. Hofer, N. Billot, G. Reinhart, *Energy Environ. Sci.*, **2019***, 12*, 1818-1833.

53. W. C. H. Hamann, Vielstich, *Elektrochemie*, 4th ed., **2005**, *Wiley-VCH Verlag*, Weinheim.
54. Y. Nishi, *Chem. Rec.*, **2001***, 1*, 406-13.
55. T. Minami, M. Tatsumisago, M. Wakihara, C. Iwakura, S. Kohjiya, I. Tanaka, *Solid State Ionics for Batteries*, 1st ed., **2005**, *Springer-Verlag Tokyo*, Tokyo.
56. M. Al-Gabalawy, N.S. Hosny, S.A. Hussien, *Batteries*, **2020***, 6*, 37.
57. C.F.J. Francis, I.L. Kyratzis, A.S. Best, *Adv. Mater.*, **2020***, 32*, 1904205.
58. K. Mizushima, P.C. Jones, P.J. Wiseman, J.B. Goodenough, *Mater. Res. Bull.*, **1980***, 15*, 783-789.
59. T. Páez, A. Martínez-Cuezva, J. Palma, E. Ventosa, *ACS Appl. Energy Mater.*, **2019***, 2*, 8328-8336.
60. R.B. Smith, M.Z. Bazant, *J. Electrochem. Soc.*, **2017***, 164*, E3291-E3310.
61. A. Urban, D.-H. Seo, G. Ceder, *Npj Comput. Mater.*, **2016***, 2*.
62. E.M.D. Siriwardane, I. Demiroglu, C. Sevik, F.M. Peeters, D. Çakır, *J. Phys. Chem. C*, **2020***, 124*, 21293-21304.
63. C. Liu, Z.G. Neale, G. Cao, *Mater. Today*, **2016***, 19*, 109-123.
64. W.-Y. Chang, *ISRN Appl. Math.*, **2013***, 2013*, 1-7.
65. A. Gutiérrez-Pardo, A.I. Pitillas Martinez, L. Otaegui, M. Schneider, A. Roters, A. Llordés, F. Aguesse, L. Buannic, *Sustain. Energy Fuels*, **2018***, 2*, 2325-2334.
66. A. Sakuda, *J. Ceram. Soc. Japan*, **2018***, 126*, 675-683.
67. T. Minami, A. Hayashi, M. Tatsumisago, *Solid State Ion.*, **2006***, 177*, 2715-2720.
68. M. Pasta, D. Armstrong, Z.L. Brown, J. Bu, M.R. Castell, P. Chen, A. Cocks, S.A. Corr, E.J. Cussen, E. Darnbrough, V. Deshpande, C. Doerrer, M.S. Dyer, H. El-Shinawi, N. Fleck, P. Grant, G.L. Gregory, C. Grovenor, L.J. Hardwick, J.T.S. Irvine, H.J. Lee, G. Li, E. Liberti, I. McClelland, C. Monroe, P.D. Nellist, P.R. Shearing, E. Shoko, W. Song, D.S. Jolly, C.I. Thomas, S.J. Turrell, M. Vestli, C.K. Williams, Y. Zhou, P.G. Bruce, *JPhys Energy*, **2020***, 2*, 32008.
69. P.E. Stallworth, J.J. Fontanella, M.C. Wintersgill, C.D. Scheidler, J.J. Immel, S.G. Greenbaum, A.S. Gozdz, *J. Power Sources*, **1999***, 81-82*, 739-747.
70. F. Zheng, M. Kotobuki, S. Song, M.O. Lai, L. Lu, *J. Power Sources*, **2018***, 389*, 198-213.
71. C. Wang, J. Liang, J.T. Kim, X. Sun, *Sci. Adv.*, **2022***, 8*, eadc9516.
72. K. Park, B.-C. Yu, J.-W. Jung, Y. Li, W. Zhou, H. Gao, S. Son, J.B. Goodenough, *Chem. Mater.*, **2016***, 28*, 8051-8059.
73. T.K. Schwietert, A. Vasileiadis, M. Wagemaker, *JACS Au*, **2021***, 1*, 1488-1496.
74. P.K. Nayak, E.M. Erickson, F. Schipper, T.R. Penki, N. Munichandraiah, P. Adelhelm, H. Sclar, F. Amalraj, B. Markovsky, D. Aurbach, *Adv. Energy Mater.*, **2018***, 8*, 1702397.
75. R. Ye, M. Ihrig, N. Imanishi, M. Finsterbusch, E. Figgemeier, *ChemSusChem*, **2021***, 14*, 4397-4407.
76. K. Kerman, A. Luntz, V. Viswanathan, Y.-M. Chiang, Z. Chen, *J. Electrochem. Soc.*, **2017***, 164*, A1731-A1744.
77. N.A. Baharuddin, N.F. Abdul Rahman, H. Abd. Rahman, M.R. Somalu, M.A. Azmi, J. Raharjo, *Int. J. Energy Res.*, **2020***, 44*, 8296-8313.
78. J.C. Bachman, S. Muy, A. Grimaud, H.H. Chang, N. Pour, S.F. Lux, O. Paschos, F. Maglia, S. Lupart, P. Lamp, L. Giordano, Y. Shao-Horn, *Chem. Rev.*, **2016***, 116*, 140-62.
79. Y. Zhao, L.L. Daemen, *J. Am. Chem. Soc.*, **2012***, 134*, 15042-7.
80. K. Takada, *Acta Mater.*, **2013***, 61*, 759-770.
81. B.A. Boukamp, R.A. Huggins, *Phys. Lett. A*, **1976***, 58*, 231-233.

82. T. Kato, T. Hamanaka, K. Yamamoto, T. Hirayama, F. Sagane, M. Motoyama, Y. Iriyama, *J. Power Sources*, **2014**, *260*, 292-298.
83. J.C. Barbosa, R. Goncalves, C.M. Costa, S. Lanceros-Mendez, *ACS Omega*, **2022**, *7*, 14457-14464.
84. Y. Ren, T. Danner, A. Moy, M. Finsterbusch, T. Hamann, J. Dippell, T. Fuchs, M. Müller, R. Hoft, A. Weber, L.A. Curtiss, P. Zapol, M. Klenk, A.T. Ngo, P. Barai, B.C. Wood, R. Shi, L.F. Wan, T.W. Heo, M. Engels, J. Nanda, F.H. Richter, A. Latz, V. Srinivasan, J. Janek, J. Sakamoto, E.D. Wachsman, D. Fattakhova-Rohlfing, *Adv. Energy Mater.*, **2022**, *13*, 2201939.
85. S. Lobe, C. Dellen, M. Finsterbusch, H.G. Gehrke, D. Sebold, C.L. Tsai, S. Uhlenbruck, O. Guillon, *J. Power Sources*, **2016**, *307*, 684-689.
86. B.D. McCloskey, *J. Phys. Chem. Lett.*, **2015**, *6*, 3592-3.
87. P. Arora, Z.J. Zhang, *Chem. Rev.*, **2004**, *104*, 4419-62.
88. M. Kotobuki, B. Yan, L. Lu, E. Hanc, J. Molenda, *Funct. Mater. Lett.*, **2016**, *9*, 1642005.
89. L. Dhivya, K. Karthik, S. Ramakumar, R. Murugan, *RSC Adv.*, **2015**, *5*, 96042-96051.
90. F. Chen, J. Li, Z. Huang, Y. Yang, Q. Shen, L. Zhang, *J. Phys. Chem. C*, **2018**, *122*, 1963-1972.
91. N. Bernstein, M.D. Johannes, K. Hoang, *Phys. Rev. Lett.*, **2012**, *109*, 205702.
92. S. Toda, K. Ishiguro, Y. Shimonishi, A. Hirano, Y. Takeda, O. Yamamoto, N. Imanishi, *Solid State Ion.*, **2013**, *233*, 102-106.
93. L. Dhivya, R. Murugan, *ACS Appl. Mater. Interfaces*, **2014**, *6*, 17606-15.
94. M. Huang, M. Shoji, Y. Shen, C.-W. Nan, H. Munakata, K. Kanamura, *J. Power Sources*, **2014**, *261*, 206-211.
95. S.F. Song, B.G. Yan, F. Zheng, H.M. Duong, L. Lu, *Solid State Ion.*, **2014**, *268*, 135-139.
96. C. Deviannapoorani, L. Dhivya, S. Ramakumar, R. Murugan, *J. Power Sources*, **2013**, *240*, 18-25.
97. K. Ishiguro, Y. Nakata, M. Matsui, I. Uechi, Y. Takeda, O. Yamamoto, N. Imanishi, *J. Electrochem. Soc.*, **2013**, *160*, A1690-A1693.
98. C.A. Geiger, E. Alekseev, B. Lazic, M. Fisch, T. Armbruster, R. Langner, M. Fechtelkord, N. Kim, T. Pettke, W. Weppner, *Inorg. Chem.*, **2011**, *50*, 1089-97.
99. M. Matsui, K. Takahashi, K. Sakamoto, A. Hirano, Y. Takeda, O. Yamamoto, N. Imanishi, *Dalton Trans.*, **2014**, *43*, 1019-24.
100. R. Wagner, G.J. Redhammer, D. Rettenwander, A. Senyshyn, W. Schmidt, M. Wilkening, G. Amthauer, *Chem. Mater.*, **2016**, *28*, 1861-1871.
101. L.J. Miara, W.D. Richards, Y.E. Wang, G. Ceder, *Chem. Mater.*, **2015**, *27*, 4040-4047.
102. L. Lu, N. Hu, *Recent Advances in Energy Storage Materials and Devices*, **2017**, *Materials Research Forum LLC*, Millersville PA.
103. S. Yu, R.D. Schmidt, R. Garcia-Mendez, E. Herbert, N.J. Dudney, J.B. Wolfenstine, J. Sakamoto, D.J. Siegel, *Chem. Mater.*, **2015**, *28*, 197-206.
104. H. Xie, J.A. Alonso, Y. Li, M.T. Fernández-Díaz, J.B. Goodenough, *Chem. Mater.*, **2011**, *23*, 3587-3589.
105. L. Cheng, E.J. Crumlin, W. Chen, R. Qiao, H. Hou, S. Franz Lux, V. Zorba, R. Russo, R. Kostecki, Z. Liu, K. Persson, W. Yang, J. Cabana, T. Richardson, G. Chen, M. Doeff, *Phys. Chem. Chem. Phys.*, **2014**, *16*, 18294-300.
106. Y. Jin, P.J. McGinn, *J. Power Sources*, **2013**, *239*, 326-331.
107. R. Kun, F. Langer, M. Delle Piane, S. Ohno, W.G. Zeier, M. Gockeln, L. Colombi Ciacchi, M. Busse, I. Fekete, *ACS Appl. Mater. Interfaces*, **2018**, *10*, 37188-37197.

108. A. Sharafi, S. Yu, M. Naguib, M. Lee, C. Ma, H.M. Meyer, J. Nanda, M. Chi, D.J. Siegel, J. Sakamoto, *J. Mater. Chem. A*, **2017***, 5*, 13475-13487.
109. R.P. Rao, W. Gu, N. Sharma, V.K. Peterson, M. Avdeev, S. Adams, *Chem. Mater.*, **2015***, 27*, 2903-2910.
110. F. Han, J. Yue, C. Chen, N. Zhao, X. Fan, Z. Ma, T. Gao, F. Wang, X. Guo, C. Wang, *Joule*, **2018***, 2*, 497-508.
111. S. Ohta, M. Kawakami, H. Nozaki, C. Yada, T. Saito, H. Iba, *J. Mater. Chem. A*, **2020***, 8*, 8989-8996.
112. J.B. Goodenough, Y. Kim, *Chem. Mater.*, **2010***, 22*, 587-603.
113. E. Peled, *J. Power Sources*, **1983***, 9*, 253-266.
114. Y. Zhu, X. He, Y. Mo, *ACS Appl. Mater. Interfaces*, **2015***, 7*, 23685-93.
115. J. Wolfenstine, J.L. Allen, J. Read, J. Sakamoto, *J. Mater. Sci.*, **2013***, 48*, 5846-5851.
116. W. Xu, J. Wang, F. Ding, X. Chen, E. Nasybulin, Y. Zhang, J.-G. Zhang, *Energy Environ. Sci.*, **2014***, 7*, 513-537.
117. K. Yan, H.W. Lee, T. Gao, G. Zheng, H. Yao, H. Wang, Z. Lu, Y. Zhou, Z. Liang, Z. Liu, S. Chu, Y. Cui, *Nano Lett.*, **2014***, 14*, 6016-22.
118. H. Dai, X. Gu, J. Dong, C. Wang, C. Lai, S. Sun, *Nat. Commun.*, **2020***, 11*, 643.
119. H. Liu, X.-B. Cheng, J.-Q. Huang, H. Yuan, Y. Lu, C. Yan, G.-L. Zhu, R. Xu, C.-Z. Zhao, L.-P. Hou, C. He, S. Kaskel, Q. Zhang, *ACS Energy Lett.*, **2020***, 5*, 833-843.
120. K.N. Wood, E. Kazyak, A.F. Chadwick, K.H. Chen, J.G. Zhang, K. Thornton, N.P. Dasgupta, *ACS Cent. Sci.*, **2016***, 2*, 790-801.
121. T. Krauskopf, F.H. Richter, W.G. Zeier, J. Janek, *Chem. Rev.*, **2020***, 120*, 7745-7794.
122. J. Liu, H. Yuan, H. Liu, C.Z. Zhao, Y. Lu, X.B. Cheng, J.Q. Huang, Q. Zhang, *Adv. Energy Mater.*, **2021***, 12*, 2100748.
123. Y. Chen, K. Wen, T. Chen, X. Zhang, M. Armand, S. Chen, *Energy Stor. Mater.*, **2020***, 31*, 401-433.
124. Z. Gao, H. Sun, L. Fu, F. Ye, Y. Zhang, W. Luo, Y. Huang, *Adv. Mater.*, **2018***, 30*, e1705702.
125. Z. Wan, D. Lei, W. Yang, C. Liu, K. Shi, X. Hao, L. Shen, W. Lv, B. Li, Q.-H. Yang, F. Kang, Y.-B. He, *Adv. Funct. Mater.*, **2019***, 29*, 1805301.
126. X. Yin, L. Wang, Y. Kim, N. Ding, J. Kong, D. Safanama, Y. Zheng, J. Xu, D.V.M. Repaka, K. Hippalgaonkar, S.W. Lee, S. Adams, G.W. Zheng, *Adv. Sci.*, **2020***, 7*, 2001303.
127. A. Gupta, E. Kazyak, N. Craig, J. Christensen, N.P. Dasgupta, J. Sakamoto, *J. Electrochem. Soc.*, **2018***, 165*, A2801-A2806.
128. Y. Wang, C.J. Zanelotti, X. Wang, R. Kerr, L. Jin, W.H. Kan, T.J. Dingemans, M. Forsyth, L.A. Madsen, *Nat. Mater.*, **2021***, 20*, 1255-1263.
129. X. Ji, S. Hou, P. Wang, X. He, N. Piao, J. Chen, X. Fan, C. Wang, *Adv. Mater.*, **2020***, 32*, e2002741.
130. L. Ye, X. Li, *Nature*, **2021***, 593*, 218-222.
131. C. Liu, J. Sun, P. Zheng, L. Jiang, H. Liu, J. Chai, Q. Liu, Z. Liu, Y. Zheng, X. Rui, *J. Mater. Chem. A*, **2022***, 10*, 16761-16778.
132. Y. Nishi, *J. Power Sources*, **2001***, 100*, 101-106.
133. M.S. Whittingham, *Chem. Rev.*, **2004***, 104*, 4271-301.
134. M.M. Doeff, *Batteries for Sustainability*, 1st ed., **2013**, *Springer Science + Business Media*, New York.
135. M. Gellert, E. Dashjav, D. Grüner, Q. Ma, F. Tietz, *Ionics*, **2017***, 24*, 1001-1006.
136. W. He, W. Guo, H. Wu, L. Lin, Q. Liu, X. Han, Q. Xie, P. Liu, H. Zheng, L. Wang, X. Yu, D.L. Peng, *Adv. Mater.*, **2021***, 33*, 2005937.

137. R. Jung, M. Metzger, F. Maglia, C. Stinner, H.A. Gasteiger, *J. Phys. Chem. Lett.*, **2017**, *8*, 4820-4825.
138. G.S. Seck, E. Hache, C. Barnet, *Resour. Policy*, **2022**, *75*, 102516.
139. N. Voronina, Y.-K. Sun, S.-T. Myung, *ACS Energy Lett.*, **2020**, *5*, 1814-1824.
140. C. Julien, A. Mauger, K. Zaghib, H. Groult, *Inorganics*, **2014**, *2*, 132-154.
141. N. Yabuuchi, Y. Kawamoto, R. Hara, T. Ishigaki, A. Hoshikawa, M. Yonemura, T. Kamiyama, S. Komaba, *Inorg. Chem.*, **2013**, *52*, 9131-42.
142. S.G. Booth, A.J. Nedoma, N.N. Anthonisamy, P.J. Baker, R. Boston, H. Bronstein, S.J. Clarke, E.J. Cussen, V. Daramalla, M. De Volder, S.E. Dutton, V. Falkowski, N.A. Fleck, H.S. Geddes, N. Gollapally, A.L. Goodwin, J.M. Griffin, A.R. Haworth, M.A. Hayward, S. Hull, B.J. Inkson, B.J. Johnston, Z. Lu, J.L. MacManus-Driscoll, X. Martínez De Irujo Labalde, I. McClelland, K. McCombie, B. Murdock, D. Nayak, S. Park, G.E. Pérez, C.J. Pickard, L.F.J. Piper, H.Y. Playford, S. Price, D.O. Scanlon, J.C. Stallard, N. Tapia-Ruiz, A.R. West, L. Wheatcroft, M. Wilson, L. Zhang, X. Zhi, B. Zhu, S.A. Cussen, *APL Mater.*, **2021**, *9*, 109201.
143. H. Tukamoto, A.R. West, *J. Electrochem. Soc.*, **1997**, *144*, 3164-3168.
144. J. Xie, N. Imanishi, T. Matsumura, A. Hirano, Y. Takeda, O. Yamamoto, *Solid State Ion.*, **2008**, *179*, 362-370.
145. R. Koerver, W. Zhang, L. de Biasi, S. Schweidler, A.O. Kondrakov, S. Kolling, T. Brezesinski, P. Hartmann, W.G. Zeier, J. Janek, *Energy Environ. Sci.*, **2018**, *11*, 2142-2158.
146. R. Amin, Y.-M. Chiang, *J. Electrochem. Soc.*, **2016**, *163*, A1512-A1517.
147. H. Xia, L. Lu, G. Ceder, *J. Power Sources*, **2006**, *159*, 1422-1427.
148. J. Molenda, *Solid State Ion.*, **1989**, *36*, 53-58.
149. A. Sakuda, T. Takeuchi, H. Kobayashi, *Solid State Ion.*, **2016**, *285*, 112-117.
150. F. Girgsdies, R. Schöllhorn, *Solid State Commun.*, **1994**, *91*, 111-112.
151. M. Zarabian, M. Bartolini, P. Pereira-Almao, V. Thangadurai, *J. Electrochem. Soc.*, **2017**, *164*, A1133-A1139.
152. G. Vardar, W.J. Bowman, Q. Lu, J. Wang, R.J. Chater, A. Aguadero, R. Seibert, J. Terry, A. Hunt, I. Waluyo, D.D. Fong, A. Jarry, E.J. Crumlin, S.L. Hellstrom, Y.-M. Chiang, B. Yildiz, *Chem. Mater.*, **2018**, *30*, 6259-6276.
153. D. Wang, Q. Sun, J. Luo, J. Liang, Y. Sun, R. Li, K. Adair, L. Zhang, R. Yang, S. Lu, H. Huang, X. Sun, *ACS Appl. Mater. Interfaces*, **2019**, *11*, 4954-4961.
154. J. Sastre, X. Chen, A. Aribia, A.N. Tiwari, Y.E. Romanyuk, *ACS Appl. Mater. Interfaces*, **2020**, *12*, 36196-36207.
155. E. Kazyak, K.-H. Chen, K.N. Wood, A.L. Davis, T. Thompson, A.R. Bielinski, A.J. Sanchez, X. Wang, C. Wang, J. Sakamoto, N.P. Dasgupta, *Chem. Mater.*, **2017**, *29*, 3785-3792.
156. S. Lobe, A. Bauer, S. Uhlenbruck, D. Fattakhova-Rohlfing, *Adv. Sci.*, **2021**, *8*, 2002044.
157. W. Feng, Z. Lai, X. Dong, P. Li, Y. Wang, Y. Xia, *iScience*, **2020**, *23*, 101071.
158. W. Ping, C. Wang, R. Wang, Q. Dong, Z. Lin, A.H. Brozena, J. Dai, J. Luo, L. Hu, *Sci. Adv.*, **2020**, *6*, eabc8641.
159. M. Ihrig, M. Finsterbusch, A.M. Laptev, C.H. Tu, N.T.T. Tran, C.A. Lin, L.Y. Kuo, R. Ye, Y.J. Sohn, P. Kaghazchi, S.K. Lin, D. Fattakhova-Rohlfing, O. Guillon, *ACS Appl. Mater. Interfaces*, **2022**, *14*, 11288-11299.
160. A.A. Delluva, J. Kulberg-Savercool, A. Holewinski, *Adv. Funct. Mater.*, **2021**, *31*, 2103716.

161. A.Y. Hou, C.Y. Huang, C.L. Tsai, C.W. Huang, R. Schierholz, H.Y. Lo, H. Tempel, H. Kungl, R.A. Eichel, J.K. Chang, W.W. Wu, *Adv. Sci.*, **2023**, *10*, e2205012.
162. C. Zheng, S. Tang, F. Wen, J. Peng, W. Yang, Z. Lv, Y. Wu, W. Tang, Z. Gong, Y. Yang, *Mater. Futures*, **2022**, *1*, 045103.
163. B. Ramkumar, K. So-young, N. Chan-woo, V. Aravindan, L. Yun-Sung, *Electrochim. Acta*, **2020**, *359*, 136955.
164. T. Liu, Y.B. Zhang, R.J. Chen, S.X. Zhao, Y.H. Lin, C.W. Nan, Y. Shen, *Electrochem. commun.*, **2017**, *79*, 1-4.
165. T. Liu, Y. Ren, Y. Shen, S.-X. Zhao, Y. Lin, C.-W. Nan, *J. Power Sources*, **2016**, *324*, 349-357.
166. S. Ohta, S. Komagata, J. Seki, T. Saeki, S. Morishita, T. Asaoka, *J. Power Sources*, **2013**, *238*, 53-56.
167. H.G. Scheer, *Siebdruck Handbuch*, **1999**, *Dräger Druck GmbH & Co. KG*, Lübeck.
168. D.E. Riemer, *Ein Beitrag zur Untersuchung der physikalisch-technischen Grundlagen des Siebdruckverfahrens*, **1988**, *Dissertation, Technische Universität Berlin*, Berlin.
169. D.E. Riemer, *Microelectron. Int.*, **1989**, *6*, 8-17.
170. M.N. Rahaman, *Ceramic Processing and Sintering*, 2nd ed., **2003**, *CRC Press*, Boca Raton.
171. C. Herring, *J. Appl. Phys.*, **1950**, *21*, 301-303.
172. D. Gross, T. Seelig, *Fracture Mechanics*, 2nd ed., **2011**, *Springer Berlin*, Heidelberg.
173. R.K. Bordia, G.W. Scherer, *Acta Metall.*, **1988**, *36*, 2411-2416.
174. G.W. Scherer, *J. Am. Ceram. Soc.*, **1984**, *67*, 709-715.
175. G.W. Scherer, *Am. Ceram. Soc.*, **1991**, *70*, 1059-1063.
176. R. Zallen, *The Physics of Amorphous Solids*, 1st ed., **2008**, *Wiley-VCH*, Hoboken.
177. S.C. Jung, H.-J. Kim, J.-H. Kim, Y.-K. Han, *J. Phys. Chem. C*, **2015**, *120*, 886-892.
178. L.C. Hoff, W.S. Scheld, C. Vedder, J. Stollenwerk, *Laser-based Micro- and Nanoprocessing XVI Proceedings*, **2022**, *11989*.
179. C. Vedder, S. Wollgarten, R. Gradmann, J. Stollenwerk, K. Wissenbach, M. Eberstein, *J. Laser Appl.*, **2017**, *29*, 226031–226037.
180. H. Sändker, *Dissertation: Laserbasierte Herstellung funktionaler Beschichtungen aus partikulärem Polyetheretherketon*, **2019**, *RWTH Aachen University, Lehrstuhl für Technologie Optischer Systeme TOS*, Aachen.
181. E. Ye, Z. Li, *Photothermal Nanomaterials*, **2022**, *Royal Society of Chemistry*, Cambridge.
182. L. Porz, M. Scherer, D. Huhn, L.M. Heine, S. Britten, L. Rebohle, M. Neubert, M. Brown, P. Lascelles, R. Kitson, D. Rettenwander, L. Fulanovic, E. Bruder, P. Breckner, D. Isaia, T. Frömling, J. Rödel, W. Rheinheimer, *Mater. Horiz.*, **2022**, *9*, 1717-1726.
183. A. Jain, S.P. Ong, G. Hautier, W. Chen, W.D. Richards, S. Dacek, S. Cholia, D. Gunter, D. Skinner, G. Ceder, K.A. Persson, *APL Mater.*, **2013**, *1*, 11002.
184. Y.P. Varshni, *Physica*, **1967**, *34*, 149-154.
185. Y. Cho, A. Yamaguchi, R. Uehara, S. Yasuhara, T. Hoshina, M. Miyauchi, *J. Chem. Phys.*, **2020**, *152*, 231101.
186. V. Mishra, M.K. Warshi, A. Sati, A. Kumar, V. Mishra, R. Kumar, P.R. Sagdeo, *SN Appl. Sci.*, **2019**, *1*.
187. D. Goldschmidt, H.L. Tuller, *Phys. Rev. B Condens. Matter.*, **1987**, *35*, 4360-4364.
188. D. Halliday, R. Resnick, J. Walker, *Fundamentals of Physics*, 10th ed., **2013**, *Wiley*, New York.
189. D. Gu, Y. Yang, L. Xi, J. Yang, M. Xia, *Opt. Laser Technol.*, **2019**, *119*, 105600.

190. E. Smith, G. Dent, *Modern Raman Spectroscopy - A Practical Approach*, **2004**, *John Wiley & Sons, Ltd* Chichester.
191. M. Sardela, *Practical Materials Characterization*, **2014**, *Springer New York*, New York.
192. D. Tuschel, *Spectroscopy*, **2016***, 31*, 14-23.
193. L. Reimer, *Scanning Electron Microscopy*, 2nd ed., **1998**, *Springer Berlin*, Heidelberg.
194. J.I. Goldstein, D.E. Newbury, J.R. Michael, N.W.M. Ritchie, J.H.J. Scott, D.C. Joy, *Scanning Electron Microscopy and X-Ray Microanalysis* 4th ed., **2018**, *Springer New York*, New York.
195. S. Fearn, *An Introduction to Time-of-Flight Secondary Ion Mass Spectrometry (ToF-SIMS) and its Application to Materials Science*, **2015**, *Morgan & Claypool Publishers*, San Rafael.
196. L.A. Middlemiss, A.J.R. Rennie, R. Sayers, A.R. West, *Energy Rep.*, **2020***, 6*, 232-241.
197. F. Huet, *J. Power Sources*, **1998***, 70*, 59-69.
198. U. Tröltzsch, O. Kanoun, H.-R. Tränkler, *Electrochim. Acta*, **2006***, 51*, 1664-1672.
199. R.G. Kelly, J.R. Scully, D. Shoesmith, R.G. Buchheit, *Electrochemical Techniques in Corrosion Science and Engineering*, 1st ed., **2002**, *CRC Press*, Boca Raton.
200. M. El-Azazy, M. Min, P. Annus, *Electrochemical Impedance Spectroscopy*, **2020**, *IntechOpen*, London.
201. E. Barsoukov, J.R. Macdonald, *Impedance Spectroscopy: Theory, Experiment, and Applications*, 2nd ed., **2005**, *John Wiley & Sons, Inc.*, New Jersey.
202. A.R.C. Bredar, A.L. Chown, A.R. Burton, B.H. Farnum, *ACS Appl. Energy Mater.*, **2020***, 3*, 66-98.
203. J.T.S. Irvine, D.C. Sinclair, A.R. West, *Adv. Mater.*, **1990***, 2*, 132-138.
204. C.H. Hsu, F. Mansfeld, *Corrosion*, **2001***, 57*, 747-748.
205. M.E. Orazem, I. Frateur, B. Tribollet, V. Vivier, S. Marcelin, N. Pébère, A.L. Bunge, E.A. White, D.P. Riemer, M. Musiani, *J. Electrochem. Soc.*, **2013***, 160*, C215-C225.
206. M.S. Grewal, K. Kisu, S.I. Orimo, H. Yabu, *iScience*, **2022***, 25*, 104910.
207. X. Yang, A.L. Rogach, *Adv. Energy Mater.*, **2019***, 9*.
208. Y. Matsumura, S. Wang, J. Mondori, *J. Electrochem. Soc.*, **2019***, 142*, 2914-2918.
209. Y. Lu, C.Z. Zhao, H. Yuan, X.B. Cheng, J.Q. Huang, Q. Zhang, *Adv. Funct. Mater.*, **2021***, 31*, 2009925.
210. M. Mann, C. Schwab, M. Ihrig, M. Finsterbusch, M. Martin, O. Guillon, D. Fattakhova-Rohlfing, *J. Electrochem. Soc.*, **2022***, 169*, 40564.
211. W.S. Scheld, K. Kim, C. Schwab, A.C. Moy, S.K. Jiang, M. Mann, C. Dellen, Y.J. Sohn, S. Lobe, M. Ihrig, M.G. Danner, C.Y. Chang, S. Uhlenbruck, E.D. Wachsman, B.J. Hwang, J. Sakamoto, L.F. Wan, B.C. Wood, M. Finsterbusch, D. Fattakhova-Rohlfing, *Advanced Functional Materials*, **2023***, 33*.
212. V.D. Parker, *Chapter 3 Linear Sweep and Cyclic Voltammetry*, in *Comprehensive Chemical Kinetics*, **1986**, *Elsevier B.V.*, 145-202.
213. T. Dagger, C. Lürenbaum, F.M. Schappacher, M. Winter, *J. Power Sources*, **2017***, 342*, 266-272.
214. Z. Wang, Z. Wang, W. Peng, H. Guo, X. Li, J. Wang, A. Qi, *Ionics*, **2014***, 20*, 1525-1534.
215. A. Mery, S. Rousselot, D. Lepage, M. Dolle, *Materials*, **2021***, 14*, 3840.
216. A.P. Thompson, H.M. Aktulga, R. Berger, D.S. Bolintineanu, W.M. Brown, P.S. Crozier, P.J. in 't Veld, A. Kohlmeyer, S.G. Moore, T.D. Nguyen, R. Shan, M.J. Stevens, J. Tranchida, C. Trott, S.J. Plimpton, *Comput. Phys. Commun.*, **2022***, 271*, 108171.

217. K. Kim, A. Dive, N. Adelstein, S. Kang, B.C. Wood, L.F. Wan, *Probing interfacial degradation and Interdiffusion at interfaces between $Li_7La_3Zr_2O_{12}$ and $LiCoO_2$ in all-solid-state batteries using machine-learning interatomic potential, work in preparation*.
218. K. Kim, A. Dive, A. Grieder, N. Adelstein, S. Kang, L.F. Wan, B.C. Wood, *J. Chem. Phys.*, **2022***, 156*, 221101.
219. A. Singraber, T. Morawietz, J. Behler, C. Dellago, *J. Chem. Theory Comput.*, **2019***, 15*, 3075-3092.
220. A. Singraber, J. Behler, C. Dellago, *J. Chem. Theory Comput.*, **2019***, 15*, 1827-1840.
221. P. Lejcek, *Grain Boundary Segregation in Metals*, 1st ed., **2010**, *Springer Berlin*, Heidelberg.
222. Y. Wang, W.D. Richards, S.P. Ong, L.J. Miara, J.C. Kim, Y. Mo, G. Ceder, *Nat. Mater.*, **2015***, 14*, 1026-31.
223. K. Momma, F. Izumi, *J. Appl. Crystallogr.*, **2011***, 44*, 1272-1276.
224. S.-T. Lee, S.-W. Jeon, B.-J. Yoo, S.-D. Choi, H.-J. Kim, S.-M. Lee, *J. Power Sources*, **2006***, 155*, 375-380.
225. M.S. Park, S.H. Hyun, S.C. Nam, *J. Power Sources*, **2006***, 159*, 1416-1421.
226. M.S. Park, S.H. Hyun, S.C. Nam, *J. Electroceramics*, **2006***, 17*, 651-655.
227. H. Zhang, P.J. Baker, P.S. Grant, *J. Am. Ceram. Soc.*, **2010***, 93*, 1856 - 1859.
228. H. Yamada, T.S. Suzuki, T. Uchikoshi, M. Hozumi, T. Saito, Y. Sakka, *APL Mater.*, **2013***, 1*, 42110.
229. E.J. Cheng, N.J. Taylor, J. Wolfenstine, J. Sakamoto, *J. Asian Ceram. Soc.*, **2018***, 5*, 113-117.
230. G. Balakrishnan, R. Thirumurugesan, E. Mohandas, D. Sastikumar, P. Kuppusami, J.I. Songl, *J. Nanosci. Nanotechnol.*, **2014***, 14*, 7728-33.
231. Y. Takahashi, Y. Gotoh, J. Akimoto, S. Mizuta, K. Tokiwa, T. Watanabe, *J. Solid State Chem.*, **2002***, 164*, 1-4.
232. M. Stanislowski, E. Wessel, T. Markus, L. Singheiser, W. Quadakkers, *Solid State Ion.*, **2008***, 179*, 2406-2415.
233. Y.-I. Jang, B. Huang, D.S. H. Wang, Y.C. G. Ceder, H. Liu, H. Tamurab, *J. Electrochem. Soc.*, **1999***, 146*, 862-868.
234. T. Gross, C. Hess, *J. Power Sources*, **2014***, 256*, 220-225.
235. M. Inaba, Y. Iriyama, Z. Ogumi, Y. Todzuka, A. Tasaka, *J. Raman Spectrosc.*, **1997***, 28*, 613-617.
236. C. Julien, *Solid State Ion.*, **2000***, 136-137*, 887-896.
237. K. Kushida, K. Kuriyama, *Solid State Commun.*, **2001***, 118*, 615-618.
238. T. Nishi, H. Nakai, A. Kita, *J. Electrochem. Soc.*, **2013***, 160*, A1785-A1788.
239. V.G. Hadjiev, M.N. Iliev, I.V. Vergilov, *Solid State Phys.*, **1988***, 21*, L199-L201.
240. F.S. Gittleson, K.P.C. Yao, D.G. Kwabi, S.Y. Sayed, W.-H. Ryu, Y. Shao-Horn, A.D. Taylor, *ChemElectroChem*, **2015***, 2*, 1446-1457.
241. D. Deng, *Energy Sci. Eng.*, **2015***, 3*, 385-418.
242. P. Ghosh, S. Mahanty, R.N. Basu, *Electrochim. Acta*, **2009***, 54*, 1654-1661.
243. W.S. Scheld, L.C. Hoff, C. Vedder, J. Stollenwerk, D. Grüner, M. Rosen, S. Lobe, M. Ihrig, A.R. Seok, M. Finsterbusch, S. Uhlenbruck, O. Guillon, D. Fattakhova–Rohlfing, *Applied Energy*, **2023***, 345*.
244. B.G.A. Freitas, J.M. Siqueira, L.M. da Costa, G.B. Ferreira, J.A.L.C. Resende, *J. Braz. Chem. Soc.*, **2017***, 28*, 2254-2266.

245. W. Huang, R. Frech, *Solid State Ion.*, **1996***, 86-88*, 395-400.
246. B. Rivas-Murias, V. Salgueiriño, *J. Raman Spectrosc.*, **2017***, 48*, 837-841.
247. K. H., M. Takematsu, T. Tojo, T. Atake, A. Hirano, R. Kanno, *J. Therm. Anal. Calorim.*, **2002***, 68*, 833-839.
248. J. Cho, M.D. Losego, H.G. Zhang, H. Kim, J. Zuo, I. Petrov, D.G. Cahill, P.V. Braun, *Nat. Commun.*, **2014***, 5*, 4035.
249. A.A. Hubaud, D.J. Schroeder, B.J. Ingram, J.S. Okasinski, J.T. Vaughey, *J. Alloys Compd.*, **2015***, 644*, 804-807.
250. D. Carlier, L. Croguennec, G. Ceder, M. Menetrier, Y. Shao-Horn, C. Delmas, *Inorg. Chem.*, **2004***, 43*, 914-22.
251. I. Rey, J.C. Lassègues, J. Grondin, L. Servant, *Electrochim. Acta*, **1998***, 43*, 1505-1510.
252. M. Ihrig, L.Y. Kuo, S. Lobe, A.M. Laptev, C.A. Lin, C.H. Tu, R. Ye, P. Kaghazchi, L. Cressa, S. Eswara, S.K. Lin, O. Guillon, D. Fattakhova-Rohlfing, M. Finsterbusch, *ACS Appl. Mater. Interfaces*, **2023***, 15*, 4101-4112.
253. W. Ping, C. Wang, R. Wang, Q. Dong, Z. Lin, A.H. Brozena, J. Dai, J. Luo, L. Hu, *Sci. Adv.*, **2020***, 6*, eabc8641.
254. G. Larraz, A. Orera, M.L. Sanjuán, *J. Mater. Chem. A*, **2013***, 1*, 11419.
255. S. Uhlenbruck, C. Dellen, S. Möller, S. Lobe, C.-L. Tsai, M. Finsterbusch, M. Bram, O. Guillon, *Solid State Ion.*, **2018***, 320*, 259-265.
256. D. Peltzer, J. Múnera, L. Cornaglia, *RSC Adv.*, **2016***, 6*, 8222-8231.
257. A.J. Samson, K. Hofstetter, S. Bag, V. Thangadurai, *Energy Environ. Sci.*, **2019***, 12*, 2957-2975.
258. R. Koerver, I. Aygün, T. Leichtweiß, C. Dietrich, W. Zhang, J.O. Binder, P. Hartmann, W.G. Zeier, J. Janek, *Chem. Mater.*, **2017***, 29*, 5574-5582.
259. Y. Ren, E.D. Wachsman, *J. Electrochem. Soc.*, **2022***, 169*, 40529.
260. N. Amdouni, H. Zarrouk, F. Soulette, C. Julien, *Mater. Chem. Phys.*, **2003***, 80*, 205-214.
261. Y. Zhao, J. Li, J.R. Dahn, *Chem. Mater.*, **2017***, 29*, 5239-5248.
262. K.H. Kim, T. Hirayama, C.A.J. Fisher, K. Yamamoto, T. Sato, K. Tanabe, S. Kumazaki, Y. Iriyama, Z. Ogumi, *Mater. Charact.*, **2014***, 91*, 101-106.
263. M. Otoyama, Y. Ito, A. Hayashi, M. Tatsumisago, *J. Power Sources*, **2016***, 302*, 419-425.
264. M. Kotobuki, K. Kanamura, Y. Sato, T. Yoshida, *J. Power Sources*, **2011***, 196*, 7750-7754.
265. Y. Wang, P. Yan, J. Xiao, X. Lu, J.-G. Zhang, V.L. Sprenkle, *Solid State Ion.*, **2016***, 294*, 108-115.
266. M. Wood, X. Gao, R. Shi, T.W. Heo, J.A. Espitia, E.B. Duoss, B.C. Wood, J. Ye, *J. Power Sources*, **2021***, 484*, 229252.
267. R. Shi, M. Wood, T.W. Heo, B.C. Wood, J. Ye, *J. Eur. Ceram. Soc.*, **2021***, 41*, 211-231.
268. Y. Chen, E. Rangasamy, C.R. dela Cruz, C.D. Liang, K. An, *J. Mater. Chem. A*, **2015***, 3*, 22868-22876.
269. Y. Matsuki, K. Noi, M. Deguchi, A. Sakuda, A. Hayashi, M. Tatsumisago, *J. Electrochem. Soc.*, **2019***, 166*, A5470-A5473.
270. R. Dubey, J. Sastre, C. Cancellieri, F. Okur, A. Forster, L. Pompizii, A. Priebe, Y.E. Romanyuk, L.P.H. Jeurgens, M.V. Kovalenko, K.V. Kravchyk, *Adv. Energy Mater.*, **2021***, 11*, 2102086.
271. A. Sharafi, E. Kazyak, A.L. Davis, S. Yu, T. Thompson, D.J. Siegel, N.P. Dasgupta, J. Sakamoto, *Chem. Mater.*, **2017***, 29*, 7961-7968.
272. K.P.C. Yao, D.G. Kwabi, R.A. Quinlan, A.N. Mansour, A. Grimaud, Y.-L. Lee, Y.-C. Lu, Y. Shao-Horn, *J. Electrochem. Soc.*, **2013***, 160*, A824-A831.

273. W. Xia, B. Xu, H. Duan, X. Tang, Y. Guo, H. Kang, H. Li, H. Liu, *J. Am. Ceram. Soc.*, **2017***, 100*, 2832-2839.
274. X. Huang, J. Tang, Y. Zhou, K. Rui, X. Ao, Y. Yang, B. Tian, *ACS Appl. Mater. Interfaces*, **2022***, 14*, 33340.
275. C. Yuan, J. Li, L. Hou, L. Yang, L. Shen, X. Zhang, *J. Mater. Chem.*, **2012***, 22*, 16084.
276. L. Dahéron, R. Dedryvère, H. Martinez, M. Ménétrier, C. Denage, C. Delmas, D. Gonbeau, *Chem. Mater.*, **2007***, 20*, 583-590.
277. T. Takami, Y. Morita, M. Yonemura, Y. Ishikawa, S. Tanaka, M. Mori, T. Fukunaga, E. Matsubara, *ACS Appl. Energy Mater.*, **2018***, 1*, 2546-2554.
278. L.E. Klebanoff, D.G. Van Campen, R.J. Pouliot, *Phys. Rev. B Condens. Matter*, **1994***, 49*, 2047-2057.
279. J. Haber, L. Ungier, *J. Electron Spectrosc. Relat. Phenom.*, **1977***, 12*, 305-312.
280. J.A. Villoria, M.C. Alvarez-Galvan, S.M. Al-Zahrani, P. Palmisano, S. Specchia, V. Specchia, J.L.G. Fierro, R.M. Navarro, *Appl. Catal. B*, **2011***, 105*, 276-288.
281. H.P. Bonzel, *Surf. Sci. Rep.*, **1988***, 8*, 43-125.

Supplementary Information

The SEM images for the evaluation of the RTP parameter variation in *Table 7.1* were captured with a TM3000 from HITACHI and the electron acceleration voltage was set to 15 kV. The detailed analysis of the samples from the parameter optimization are shown in the following figures.

Heating Rate variation

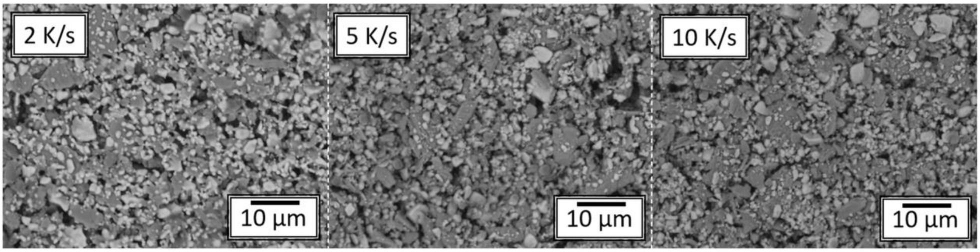

S-Figure 1: SEM images of the varied heating rate in the RTP to a temperature of 1000 °C without a dwell time and with a cooling rate of 5 K s^{-1} [27].

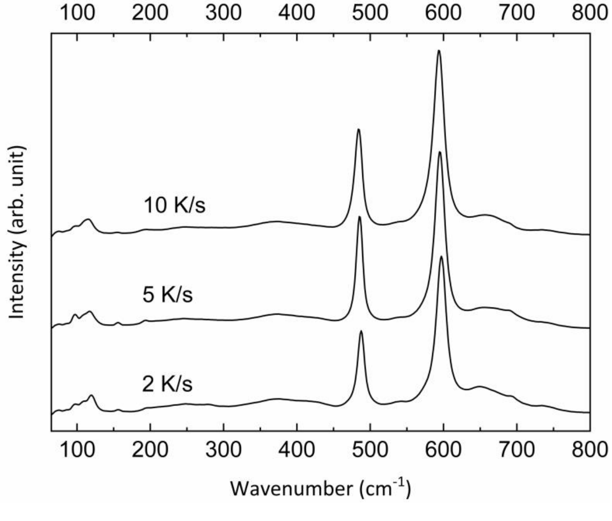

S-Figure 2: Raman measurements of the varied heating rate in the RTP to a temperature of 1000 °C without a dwell time and with a cooling rate of 5 K s^{-1} [27].

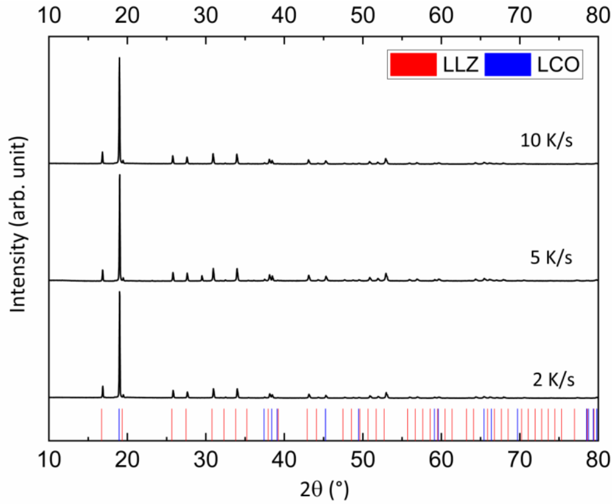

S-Figure 3: XRD measurements of the varied heating rate in the RTP to a temperature of 1000 °C without a dwell time and with a cooling rate of 5 K s^{-1} [27].

Dwell Time

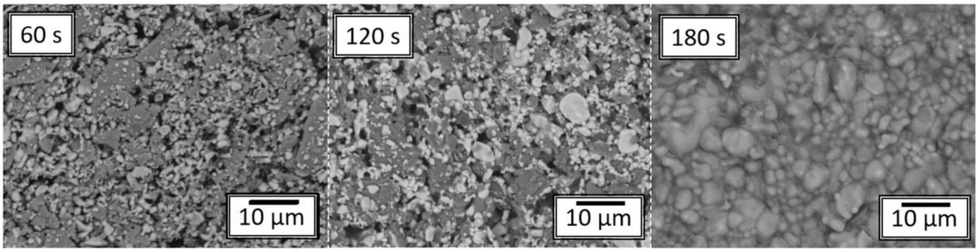

S-Figure 4: SEM images of the varied dwell time in the RTP to a temperature of 1000 °C with a heating rate of 10 K s^{-1} and with a cooling rate of 5 K s^{-1} [27].

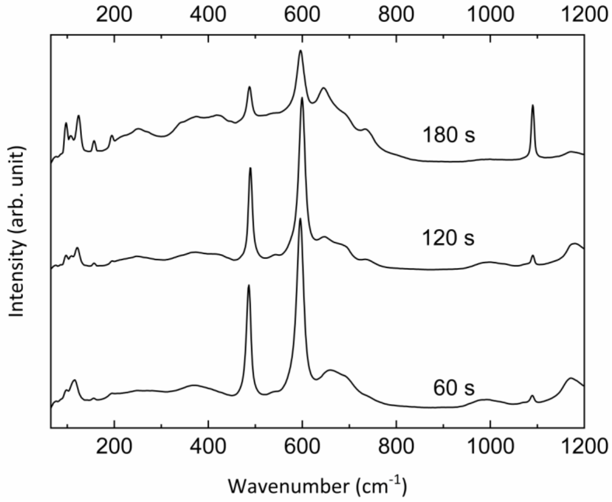

S-Figure 5: Raman measurements of the varied dwell time in the RTP to a temperature of 1000 °C with a heating rate of 10 K s^{-1} and a cooling rate of 5 K s^{-1} [27].

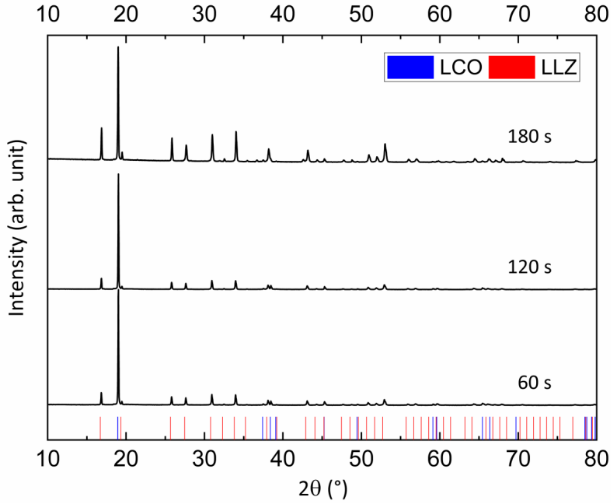

S-Figure 6: XRD measurements of the varied dwell time in the RTP to a temperature of 1000 °C with a heating rate of 10 K s^{-1} and a cooling rate of 5 K s^{-1} [27].

Cooling Rate

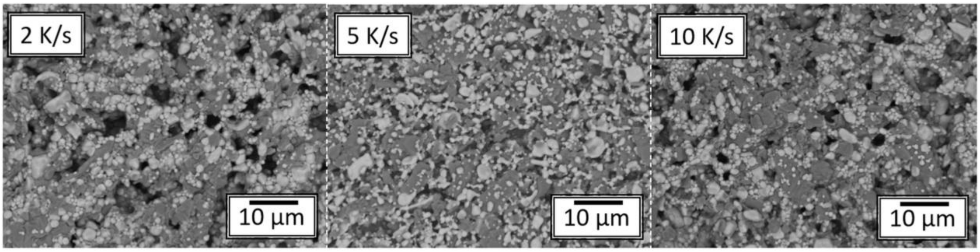

S-Figure 7: SEM images of the varied cooling rate in the RTP to a temperature of 1000 °C with a heating rate of 3 K s^{-1} and without a dwell time [27].

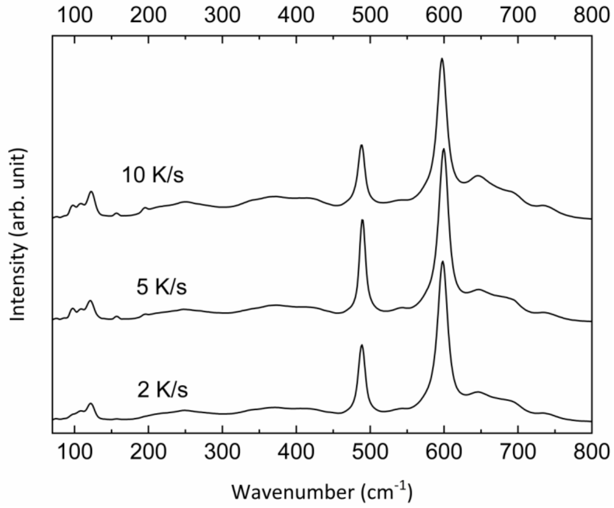

S-Figure 8: Raman measurements of the varied cooling rate in the RTP to a temperature of 1000 °C with a heating rate of 3 K s^{-1} and without a dwell time [27].

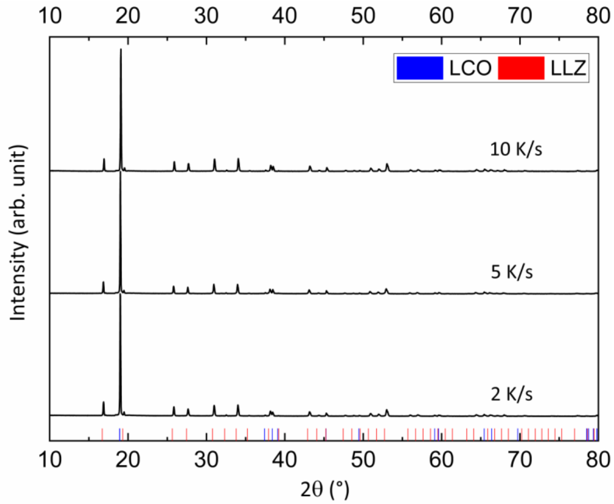

S-Figure 9: XRD measurements of the varied cooling rate in the RTP to a temperature of 1000 °C with a heating rate of 3 K s^{-1} and without a dwell time [27].

Heating Ramps

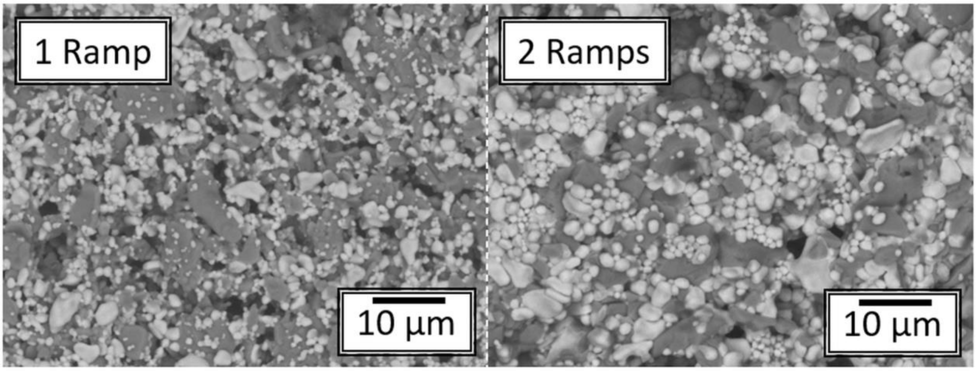

S-Figure 10: SEM images of the ramp sintering with the RTP with a heating rate of 3 K s^{-1} to 1000 °C followed by a ramp with 5 K s^{-1} to 700 °C and 5 K s^{-1} to 1000 °C and a cooling rate of 5 K s^{-1} [27].

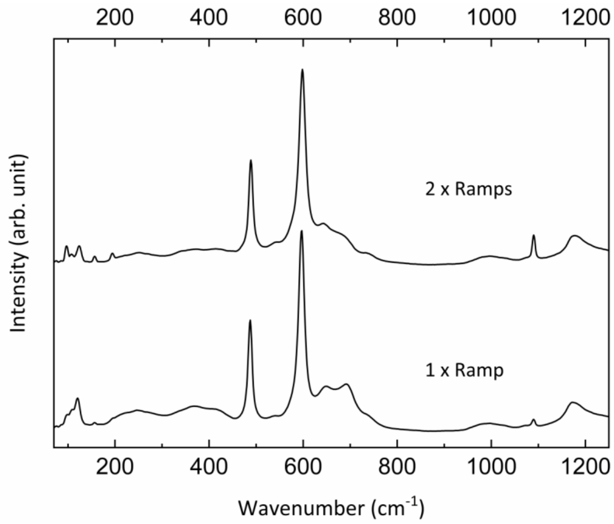

S-Figure 11: Raman measurements of the ramp sintering with the RTP with a heating rate of 3 K s^{-1} to 1000 °C followed by a ramp with 5 K s^{-1} to 700 °C and 5 K s^{-1} to 1000 °C and a cooling rate of 5 K s^{-1} [27].

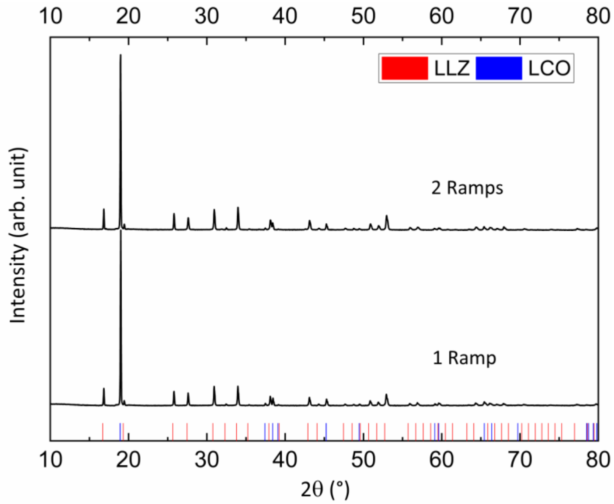

S-Figure 12: XRD measurements of the ramp sintering with the RTP with a heating rate of 3 K s^{-1} to 1000 °C and without a dwell time followed by a ramp with 5 K s^{-1} to 700 °C and 5 K s^{-1} to 1000 °C without a dwell time and with a cooling rate of 5 K s^{-1} [27].

Heating Steps

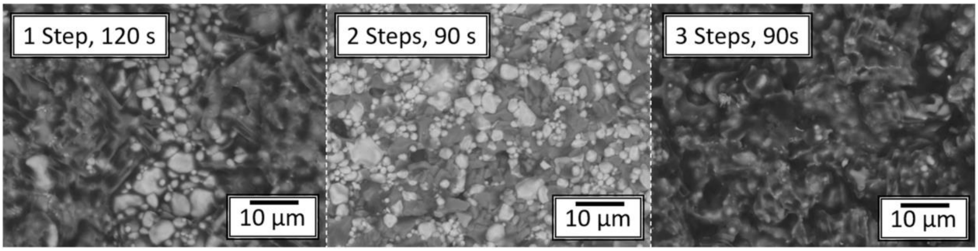

S-Figure 13: SEM images of the step sintering program with the RTP with a dwell time of 10 s in the steps. The heating rates were 3 K s^{-1} in the first step and 3 K s^{-1} in the second and third steps. All samples were heated to 1000 °C. The steps were 1: 400 °C, 2: 400 °C + 700 °C, 3: 400 °C + 550 °C + 700 °C. The dwell time was first 120 seconds at first and was reduced due to a too strong heating, to 90 s. The cooling rate was 5 K s^{-1} [27].

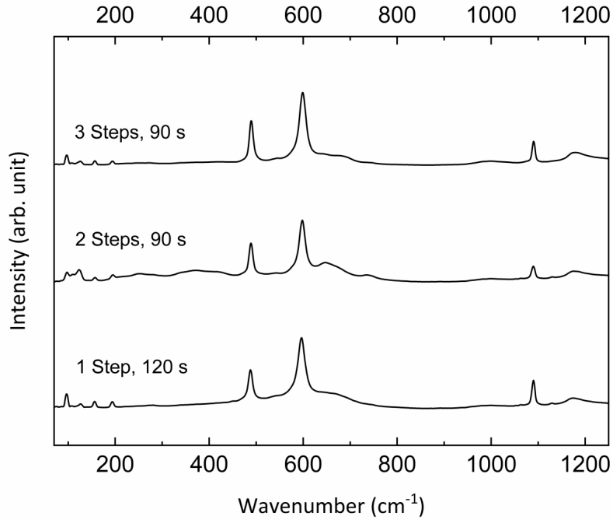

S-Figure 14: Raman measurements of the step sintering program with the RTP with a dwell time of 10 s in the steps. The heating rates were 3 K s^{-1} in the first step and 3 K s^{-1} in the second and third steps. All samples were heated to 1000 °C. The steps were 1: 400 °C, 2: 400 °C + 700 °C, 3: 400 °C + 550 °C + 700 °C. The dwell time was first 120 seconds and was reduced due to a too strong heating to 90 s. The cooling rate was 5 K s^{-1} [27].

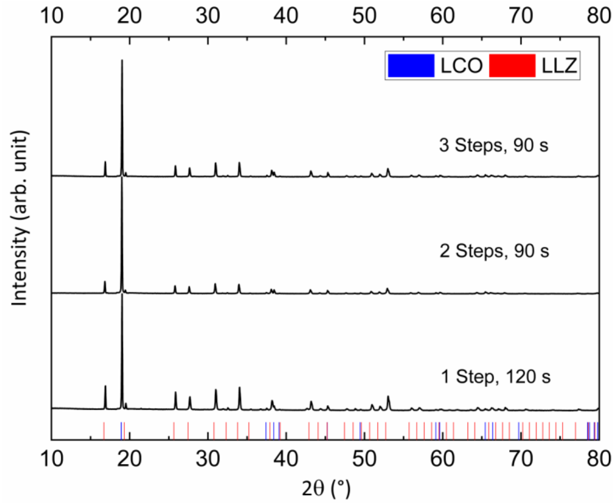

S-Figure 15: XRD measurements of the step sintering program with the RTP with a dwell time of 10 s in the steps. The heating rates were 3 K s^{-1} in the first step and 3 K s^{-1} in the second and third steps. All samples were heated to 1000 °C. The steps were 1: 400 °C, 2: 400 °C + 700 °C, 3: 400 °C + 550 °C + 700 °C. The dwell time was first 120 seconds and was reduced due to a too strong heating to 90 s. The cooling rate was 5 K s^{-1} [27].

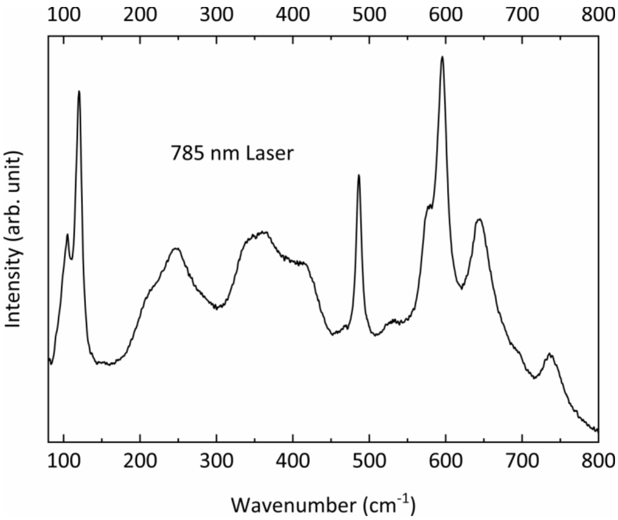

S-Figure 16: Raman spectroscopy measurement of the RTP-sintered composite cathode with a 785 nm laser [27].

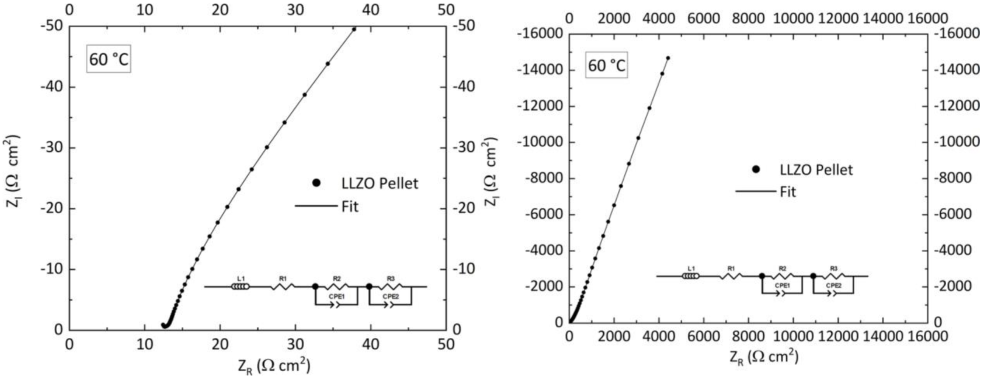

S-Figure 17: Nyquist plot of the LLZO separator pellet before any treatment as a reference for the SSB EIS measurements with two different spectra regions [27].

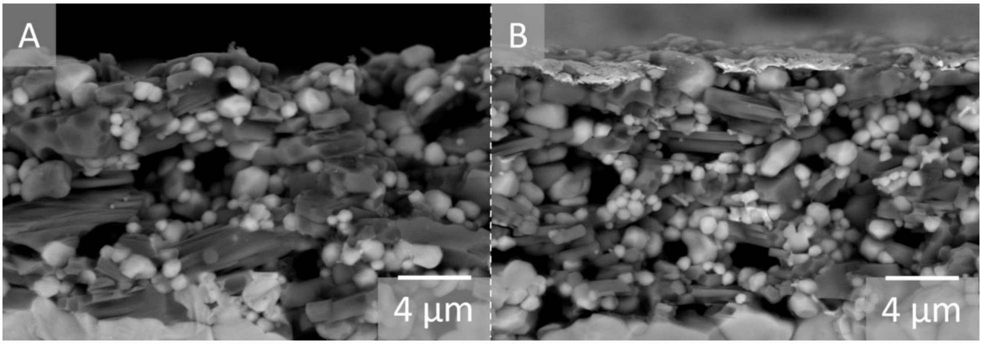

S-Figure 18: SEM images of samples prepared with the optimized sintering parameters. A) back-scattered electron image of a cross-section fracture as prepared; B) back-scattered electron image of a cross-section fracture after 5 cycles with a gold layer on top [27].

Pictures of LCO-LLZO cathode half-cells after thermal processing reveal also a coloration of conventional sintered and FAST/SPS treated samples (S-Figure 19). For the conventional sintering the sample was heated to 1050 °C for 30 min in a tube furnace (NABERTHERM) as in [25]. The FAST/SPS treatment in Ar was performed at 675 °C showing a blue coloration, which turns into brown/black coloration after conventional annealing at 1050 °C for 30 min as in [22]. Images of LCO–LLZO cathode half-cells after thermal processing reveal a coloration of conventionally sintered and FAST/SPS treated samples (S-Figure 19). For the conventional sintering, the sample was heated to 1050 °C for 30 min in a tube furnace (NABERTHERM), as in [25]. The FAST/SPS treatment in Ar was performed at 675 °C, showing a blue coloration that turns into a brown/black coloration after conventional annealing at 1050 °C for 30 min, as in [22].

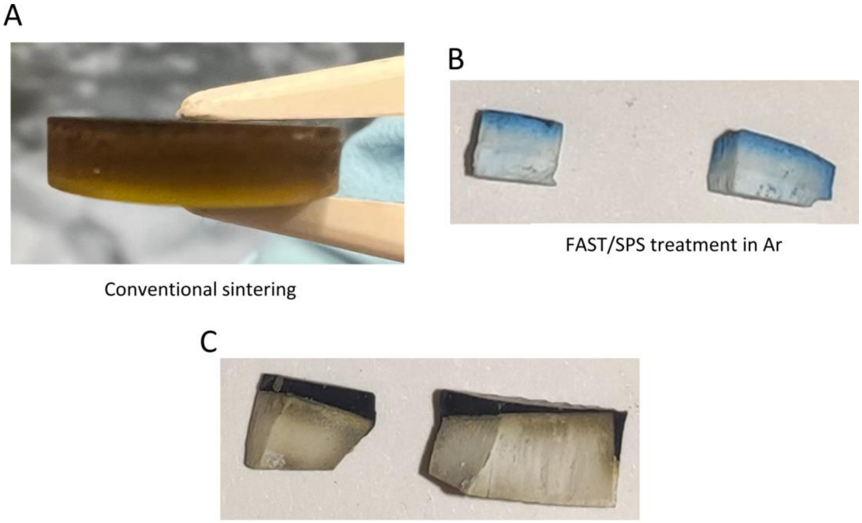

Conventional sintering

FAST/SPS treatment in Ar

Conventional annealing in air of FAST/SPS treated samples in Ar atmosphere

S-Figure 19: Images of LCO–LLZO cathode half-cells after thermal processing. A) Conventional sintering at 1050 °C for 30 min, as in [25]; B) FAST/SPS treatment in Ar at 675 °C, as in [22]; C) the sample of B) after conventional annealing at 1050 °C for 30 min. Copyright Wiley-VCH GmbH. Reproduced with permission [211].

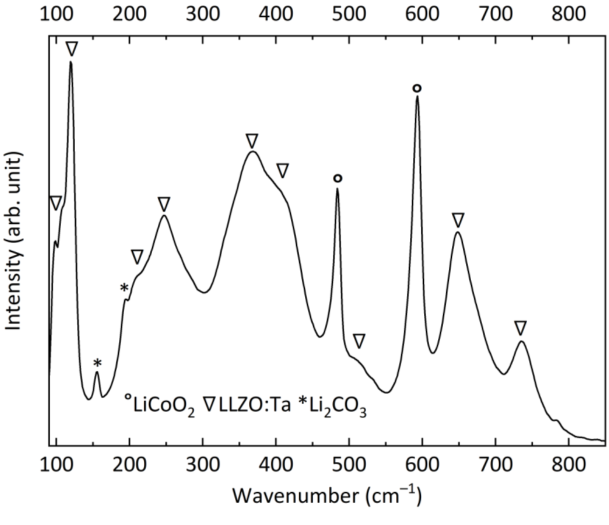

S-Figure 20: Raman spectra of a LCO and LLZO mixture (1:1 wt%) annealed at 500 °C for 1 h in air with signed phases of LCO, c-LLZO with Ta substitution and Li_2CO_3. Copyright Wiley-VCH GmbH. Reproduced with permission [211].

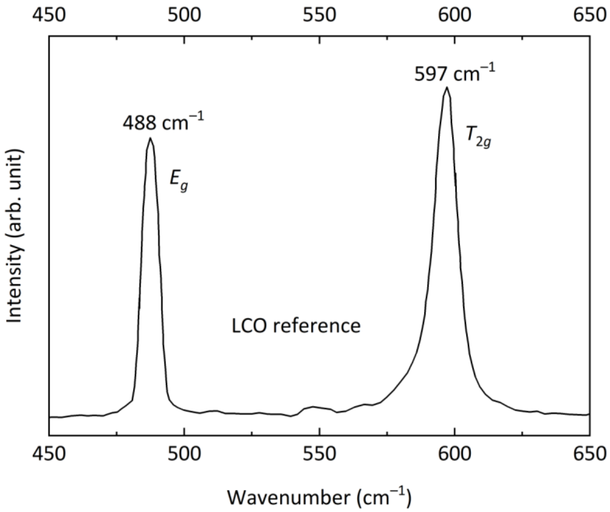

S-Figure 21: Raman reference spectrum of rhombohedral LCO (space group $R\bar{3}m$) with signals at 488 cm⁻¹ (E_g) and 597 cm⁻¹ (T_{2g}) [234, 244]. Copyright Wiley-VCH GmbH. Reproduced with permission [211].

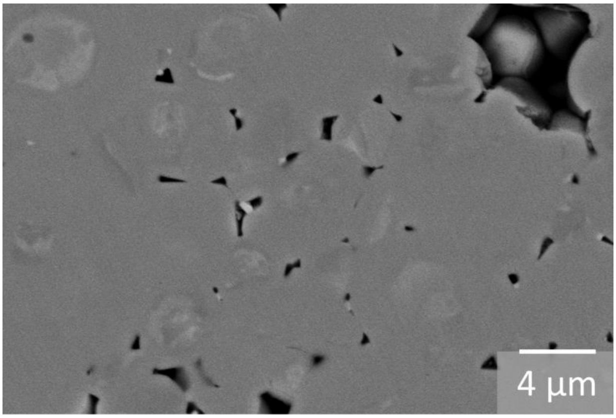

S-Figure 22: SEM image of a sintered, untreated separator LLZO reference without any cathode contact. Copyright Wiley-VCH GmbH. Reproduced with permission [211].

Raman phase localization (Figure 8.4) was used to measure EDS point scans at locations where the phases $Li_{0.5}La_2Co_{0.5}O_4$, LCO, and LLZO:Co occur in order to determine the elemental composition of the LLZO structure in this region (S-Figure 23A-B). In position 1, $Li_{0.5}La_2Co_{0.5}O_4$ was detected by Raman; in position 2 LCO; and in position 3 the photoluminescent LLZO:Co phase. The corresponding spectra 1, 2, and 3 show no difference from each other and no Co signals can be observed. The absence of Co signals and the constant phase composition of the other LLZO elements (La, Zr, Ta, Al) indicate that the observed phases in Raman have to be low in concentration. In the SEM images, several spots with a bright contrast at the grain boundary are present, which are indistinguishable from the surrounding in the Raman mapping. Such a spot is measured in position 4. The element distribution at this location differs strongly from the first three. The Ta and Zr signals are reduced, while the La signal is more pronounced and it is the only position where a Co signal was measured. It could belong to the La_2O_3 phase, which can also be found in sintered LLZO samples without cathode sintering (S-Figure 22). From the element distribution, this phase could also belong to a $LaCoO_3$ phase, but no indication of the $LaCoO_3$ phase was found by Raman or XRD.

Besides the bright areas in the grain boundary regions, regions with a bright contrast exist in the center of the grains and thus have a higher average atomic number compared to the surrounding material, as in position 5. In the corresponding spectra, the Ta signal is more intense, while the Zr signal loses intensity. It can be clearly seen that there is an inhomogeneity in the LLZO material at this point where a proportion of $_{40}Zr$ has been substituted by $_{73}Ta$. This enrichment mainly occurs in the middle of the grains but was also found for LLZO material without cathode sintering (S-Figure 22) and is therefore not associated with it. In contrast, in position 6 an area with a darker contrast is measured close to the area with the bright contrast (position 5). Here, the opposite is observed and a stronger $_{40}Zr$ signal with a less intense $_{73}Ta$ signal is found in the spectrum. The Ta has presumably migrated from this area to the center of the grain and is thus another characteristic of the previously described effect and therefore not attributable to cathode sintering. The fact that hardly any Co signals can be detected by EDS despite the confirmation of their existence by Raman spectroscopy indicates the low concentration of the phases, generated by Co-ion diffusion.

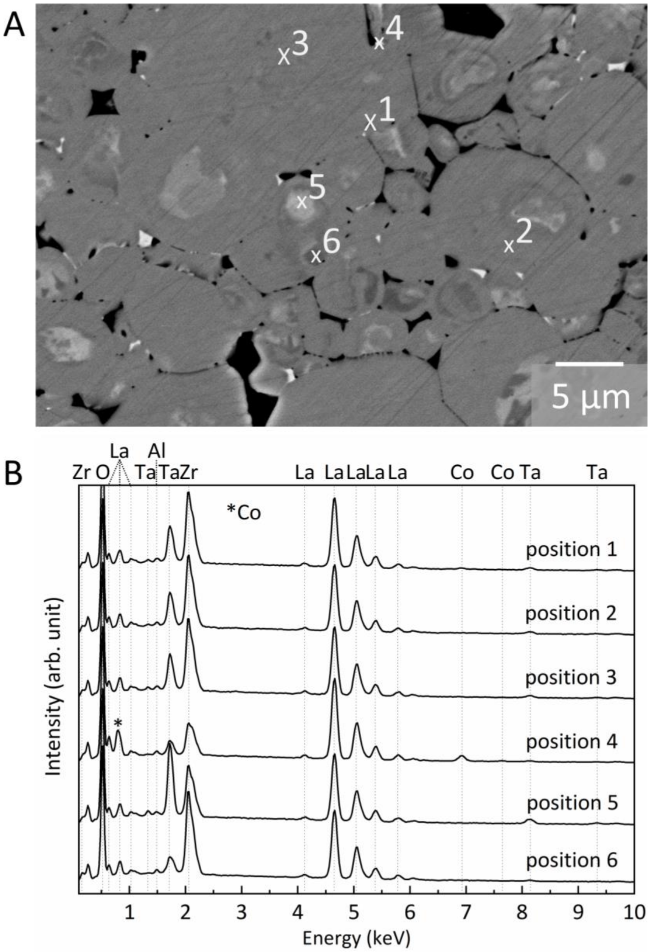

S-Figure 23: EDS point measurements on the cathode side. A) SEM image with the marked EDS positions; B) corresponding EDS spectra with marked elements. Copyright Wiley-VCH GmbH. Reproduced with permission [211].

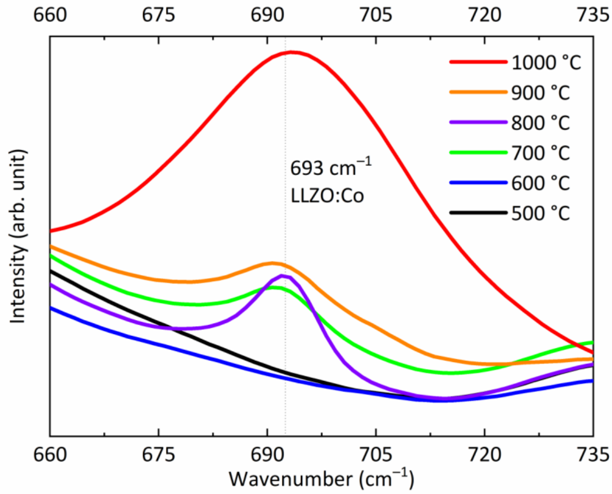

S-Figure 24: Raman spectra of pressed LCO and LLZO powder mixtures (1:1 wt%) conventional annealed at different temperatures (500 °C, 600 °C, 700 °C, 800 °C, 900 °C, and 1000 °C) with a heating rate of 2 K min^{-1} for 1 hour in air. The Raman spectra shows the LLZO:Co photoluminescence signal at 693 cm^{-1}, with its first occurrence at 700 °C. Copyright Wiley-VCH GmbH. Reproduced with permission [211].

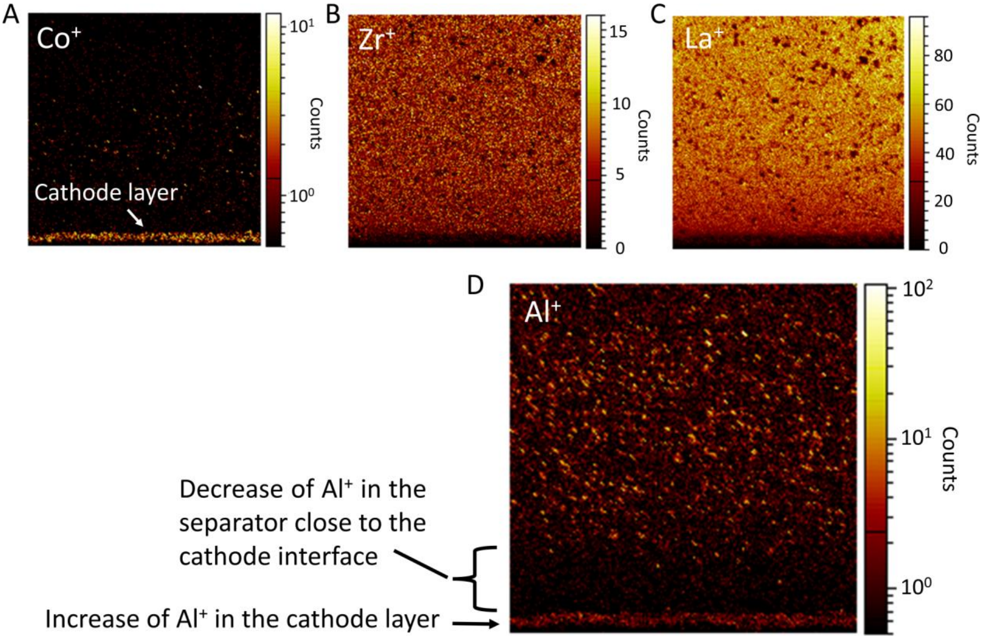

S-Figure 25: 400 µm × 400 µm ToF-SIMS mappings of the LCO-treated separator cross-section including the cathode layer at the bottom of the mappings. A) Co$^+$; B) Zr$^+$; C) La$^+$; D) Al$^+$ with additional explanations. Copyright Wiley-VCH GmbH. Reproduced with permission [211].

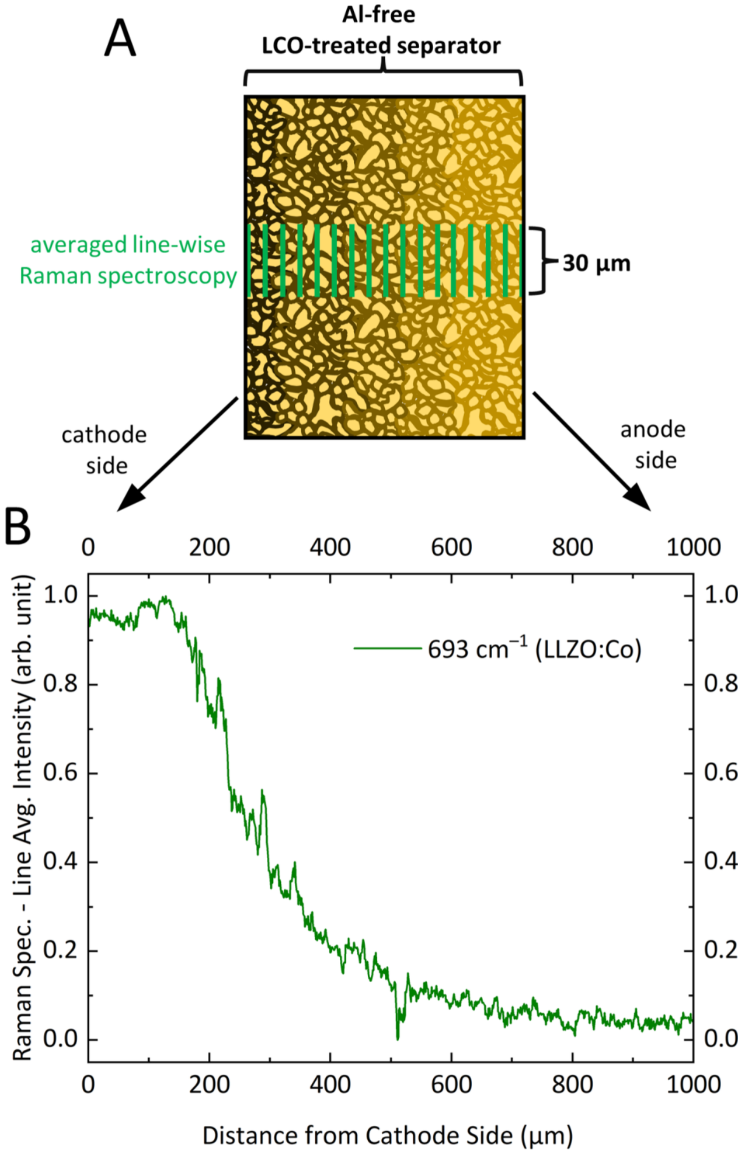

S-Figure 26: Raman measurements to detect Co-ion diffusion into the Al-free LCO-treated separator as a function of distance from the cathode side (starting with 0 µm at the cathode|separator interface). A) scheme of the Raman measurement through the entire cross-section thickness; B) averaged line signal intensity of the LLZO:Co photoluminescence at 693 cm^{-1} (green). Copyright Wiley-VCH GmbH. Reproduced with permission [211].

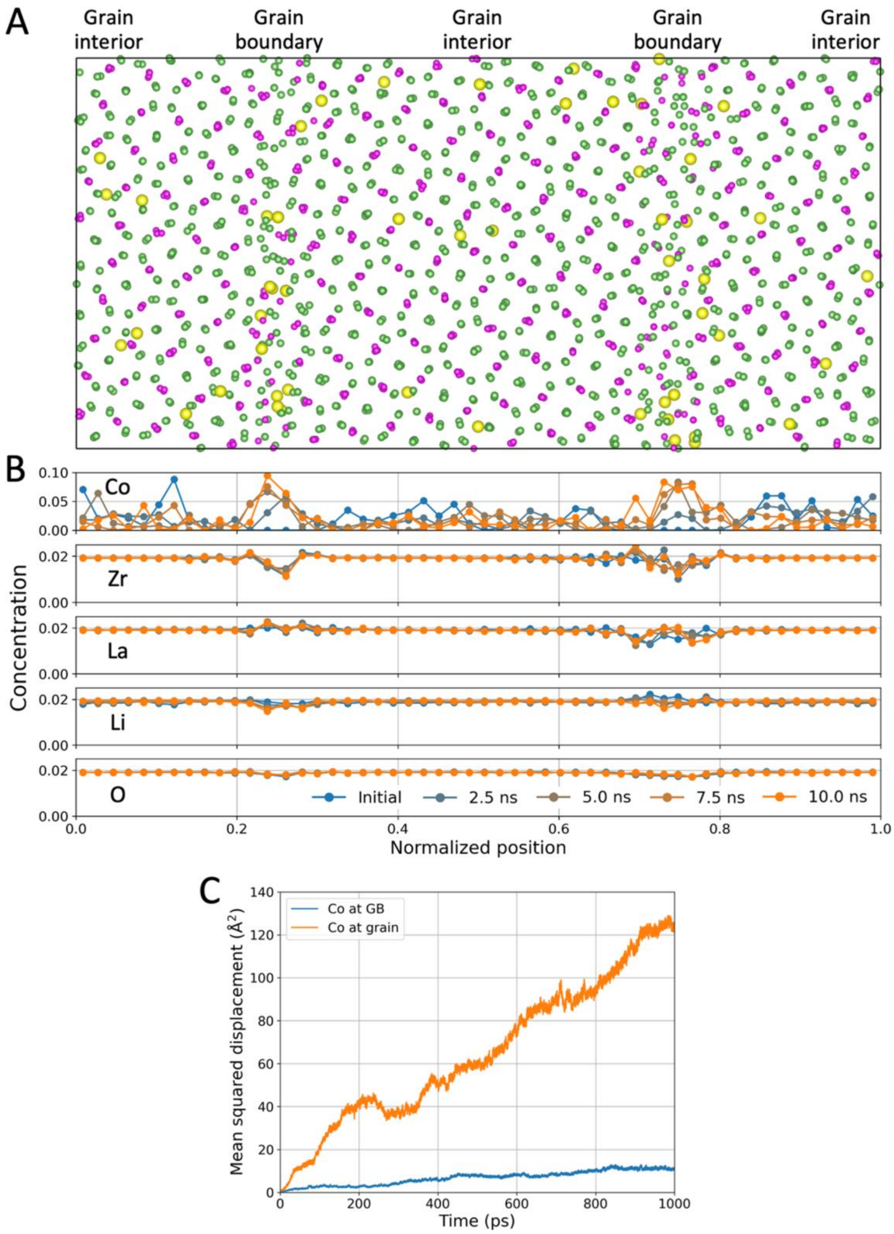

S-Figure 27: A) Atomic structure of ∑13(230)/[001] symmetric tilt grain boundary after 10 ns MD simulation at 1300 K. Magenta, green, and yellow spheres depict Zr, La, and Co-ions, respectively, and Li and O-ions are not shown for simplicity. B) Concentration profiles of each element as a function of position normal to the grain boundary plain. Note that Co-ions were placed at grain interior upon initializing the MD simulation. C) MSD of Co-ions at the grain boundary (GB) and grain interior at 1300 K. An additional 1 ns simulation was performed to evaluate the MSD after the prior 10 ns MD simulation, as shown in A) and B). Copyright Wiley-VCH GmbH. Reproduced with permission [211].

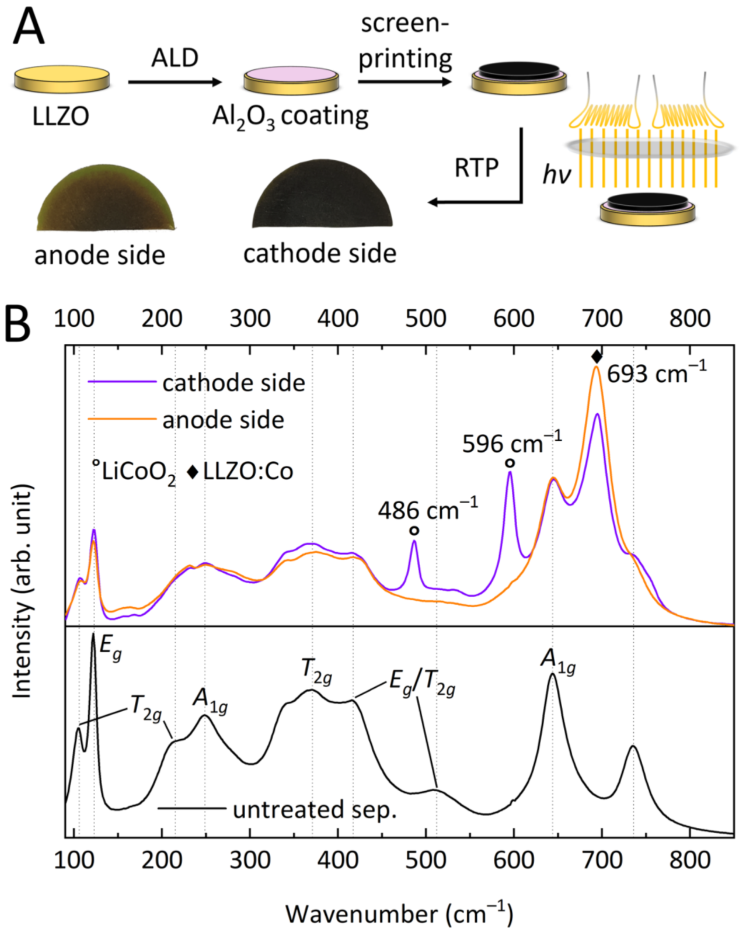

S-Figure 28: Results of the protective coating test. A) Schematic overview of the treatment with the ALD Al_2O_3 coating and the resulting LCO-treated separator with images of the anode and cathode side; B) Raman spectra of the anode and cathode side. Copyright Wiley-VCH GmbH. Reproduced with permission [211].

Curriculum vitae

Personal Information

Name: Walter Sebastian Scheld
Date of birth: 17.01.1994
Place of birth: Siegen
Nationality: German

Education

March 2019 – October 2023	Dissertation in the group of Prof. Dr. Dina Fattakhova-Rohlfing, in Institute of Energy and Climate Research, Materials Synthesis and Processing IEK-1, Research Center Juilich GmbH and Faculty of Engineering and Center for Nanointegration Duisburg-Essen CENIDE, University of Duisburg-Essen • PhD thesis: “Photonic Sintering of Garnet-Based Solid-State Batteries” (grade: *summa cum laude*) • *Doctor rerum naturalium* (Dr. rer. nat.)
October 2016 – September 2018	Master program in chemistry, University of Siegen • Master of Science in chemistry, M. Sc. (grade: 1.3) • Thesis in the group of Prof. Dr. Holger Schönherr, Faculty of Science and Technology, “Development of an Enzyme Responsive Biosensor Based on Photonic Crystals” (grade: 1.0) • Basic subjects: physical and inorganic chemistry • Minor subjects: analytical chemistry
October 2013 – September 2016	Bachelor program in chemistry, University of Siegen • Bachelor of Science in chemistry, B. Sc. (grade: 1.9) • Thesis in the group of Prof. Dr. Jörn Schmedt auf der Günne, Faculty of Science and Technology, “Synthesis and Controlled

Crystallization of Rubidium Cyclophosphates Starting from Rubidium Nitrate, Phosphorus(V) Oxide and Phosphorus(V) Sulfide” (grade: 1.3)

- Basic subjects: General chemistry program

September 2010 – June 2013	„Allgemeine Hochschulreife“ (general qualification for university entrance), Gesamtschule Eiserfeld (grade: 1.7)

Languages

German	Native speaker
English	Business fluent
French	Basic skills

Publications and presentations

Publications

1. *Blacklight Sintering of Garnet-Based Composite Cathodes*
   Walter Sebastian Scheld, Julian Norbert Ebert, Lovro Fulanovic, Michael Scherer, Christian Dellen, Martin Ihrig, Sven Uhlenbruck, Martin Finsterbusch, Olivier Guillon, Wolfgang Rheinheimer, Dina Fattakhova-Rohlfing, *Journal of the European Ceramic Society*, **2023**, in press.
2. *Preparation of Highly Durable Columnar Suspension Plasma Spray (SPS) Coatings by Pre-Oxidation of the CoNiCrAlY Bondcoat*
   Jana Joeris, Walter Sebastian Scheld, Sven Uhlenbruck, Yoo Jung Sohn, Doris Sebold, Olivier Guillon, Robert Vaßen, *Coatings*, **2023**, *13*, 1575.
3. *Low-temperature sintering of* $Li_{0.33}La_{0.55}TiO_3$ *electrolyte for all-solid-state Li batteries*
   Che-an Lin, Martin Ihrig, Kuan-chen Kung, Hsiang-ching Chen, Walter Sebastian Scheld, Ruijie Ye, Martin Finsterbusch, Olivier Guillon, Shih-kang Lin, *J. Eur. Ceram. Soc.*, **2023**, *43*, 7543-7552.
4. *Impact of Ni–Mn–Co–Al-Based Cathode Material Composition on the Sintering with Garnet Solid Electrolytes for All-Solid-State Batteries*
   Alexander Bauer, Sven Uhlenbruck, Sandra Lobe, Yoo Jung Sohn, Doris Sebold, Walter Sebastian Scheld, Dina Fattakhova-Rohlfing, Olivier Guillon, *Chem. Mater.*, **2023**, *35*, 8958-8968.
5. *Enabling metal substrates for garnet-based composite cathodes by laser sintering*
   Walter Sebastian Scheld, Linda Charlotte Hoff, Christian Vedder, Jochen Stollenwerk, Sandra Lobe, Daniel Grüner, Melanie Rosen, Martin Ihrig, Ah-Ram Seok, Martin Finsterbusch, Sven Uhlenbruck, Olivier Guillon, Dina Fattakhova-Rohlfing, *Applied Energy*, **2023**, *345*, 121335.
6. *The Riddle of Dark LLZO: Cobalt Diffusion into the Garnet-based Separator of Solid-State Lithium Batteries*
   Walter Sebastian Scheld, Kwangnam Kim, Christian Schwab, Alexandra C. Moy, Shi-Kai Jiang, Markus Mann, Christian Dellen, Yoo Jung Sohn, Sandra Lobe, Martin Ihrig, Michael Gregory Danner, Chia-Yu Chang, Sven Uhlenbruck, Eric Wachsman, Bing Joe

Hwang, Jeffrey Sakamoto, Liwen Wan, Brandon C. Wood, Martin Finsterbusch, Dina Fattakhova Rohlfing, *Adv. Funct. Mater.*, **2023**, *33*, 2302939.

7. *Cold sintering of* $BaZr_{0.7}Ce_{0.2}Y_{0.1}O_{3-\delta}$ *ceramics by controlling the phase composition of the starting powders*
   M. Kindelmann, Julian Ebert, Walter Sebastian Scheld, Wendelin Deibert, Wilhelm Albert Meulenberg, Wolfgang Rheinheimer, Martin Bram, Joachim Mayer, Olivier Guillon, *Scripta Materialia*, **2023**, *224*, 115147.
8. *Bare Eye Detection of Bacterial Enzymes of Pseudomonas aeruginosa with Polymer Modified Nanoporous Silicon Rugate Filters*
   Qasim Alhusaini, Walter Sebastian Scheld, Zhiyuan Jia, Dipankar Das, Faria Afzal, Mareike Müller, Holger Schönherr, *Biosensors*, **2022**, *12*, 1064.
9. *Rapid thermal processing of garnet-based composite cathodes*
   Walter Sebastian Scheld, Sandra Lobe, Christian Dellen, Martin Ihrig, Grit Häuschen, Linda Charlotte Hoff, Martin Finsterbusch, Sven Uhlenbruck, Olivier Guillon, Dina Fattakhova-Rohlfing, *J. Power Sources*, **2022**, *545*, 231872.
10. *Study of thermal material properties for Ta- and Al-substituted* $Li_7La_3Zr_2O_{12}$ *(LLZO) solid-state electrolyte in dependency of temperature and grain size*
    Julian Neises, Walter Sebastian Scheld, Ah-Ram Seok, Sandra Lobe, Martin Finsterbusch, Sven Uhlenbruck, Roland Schmechel, Niels Benson, *J. Mater. Chem. A*, **2022**, *10*, 12177-12186.
11. *Rapid thermal sintering of screen-printed* $LiCoO_2$ *films*
    Walter Sebastian Scheld, Sandra Lobe, Sven Uhlenbruck, Christian Dellen, Yoo Jung Sohn, Linda Charlotte Hoff, Frank Vondahlen, Olivier Guillon, Dina Fattakhova-Rohlfing, *Thin Solid Films*, **2022**, *749*, 139177.
12. *Polymer−ceramic composite cathode with enhanced storage capacity manufactured by field-assisted sintering and infiltration*
    Martin Ihrig, Ruijie Ye, Alexander M. Laptev, Daniel Grüner, Rayan Guerdelli, Walter Sebastian Scheld, Martin Finsterbusch, Hans-Dieter Wiemhöfer, Dina Fattakhova-Rohlfing, Olivier Guillon, *ACS Appl. Energy Mater.* **2021**, 4, 10428–10432.

13. *$Li_7La_3Zr_2O_{12}$ solid electrolyte sintered by the ultrafast high-temperature method*
    Martin Ihrig, Tarini Prasad Mishra, Walter Sebastian Scheld, Grit Häuschen, Wolfgang Rheinheimer, Martin Bram, Martin Finsterbusch, Olivier Guillon, *J. Eur. Ceram. Soc.*, **2021**, *41*, 6075-6079.

Poster Presentations

1. *Cobalt Diffusion in Garnet Separators during Cathode Sintering*
   Walter Sebastian Scheld, Kwangnam Kim, Christian Schwab, Alexandra C. Moy, Shi-Kai Jiang, Markus Mann, Christian Dellen, Yoo Jung Sohn, Sandra Lobe, Martin Ihrig, Michael Gregory Danner, Chia-Yu Chang, Sven Uhlenbruck, Eric D. Wachsman, Bing Joe Hwang, Jeff Sakamoto, Liwen F. Wan, Brandon C. Wood, Martin Finsterbusch, Dina Fattakhova Rohlfing
   German and United states status meeting (DEUS), **2023**, Frankfurt, Germany.
2. *Rapid thermal processing of garnet-based composite cathodes*
   Walter Sebastian Scheld, Sandra Lobe, Sven Uhlenbruck, Christian Dellen, Yoo Jung Sohn, Linda Charlotte Hoff, Frank Vondahlen, Olivier Guillon, Dina Fattakhova-Rohlfing
   International Bunsen Discussion Meeting "Solid-state Batteries - From Fundamentals to Application (*SSB V*), **2022**, Frankfurt, Germany.
3. *Rapid thermal sintering of screen-printed $LiCoO_2$ films*
   Walter Sebastian Scheld, Sandra Lobe, Sven Uhlenbruck, Christian Dellen, Yoo Jung Sohn, Linda Charlotte Hoff, Frank Vondahlen, Olivier Guillon, Dina Fattakhova-Rohlfing
   97th DKG Annual Meeting (*Ceramics 2022*), **2022**, virtual conference.
   The poster won the 3rd place in the poster competition, which was rewarded with 250 €.

Acknowledgments

First of all, I would like to thank the University of Duisburg-Essen and the Forschungszentrum Jülich for giving me the opportunity to work on my doctoral thesis at these institutions. I would also like to thank the projects OptiKeraLyt, CatSE^1, and CatSE^2, which have funded my work. Further, I would like to thank my colleagues from the IEK-1 and my project partners, who helped me to realize this work.

I want to thank Prof. Dr. Dina Fattakhova-Rohlfing for being my doctoral supervisor, for a very kind collaboration during my PhD time, and for her constant support with my experiments, projects, and publications. Additionally, I want to thank Prof. Dr. Egbert Figgemeier for being the second dissertation examiner, as well as Prof. Dr. Harry Hoster as the third examiner and Prof. Dr. Burak Atakan as exam chair.

Dr. Sandra Lobe and Dr. Sven Uhlenbruck were my scientific advisors and I would like to thank both of them for always taking time for me and my work, and for their constant support with all questions, and publications.

Several other persons were involved in the creation process of my publications and I also want to thank them very much for their support. I want to thank Prof. Dr. Olivier Guillon for his advice and support, Dr. Martin Finsterbusch for his experimental advice and reviewing, Dr. Christian Dellen for his help with several SEM and Raman measurements and analysis, Frank Vondahlen for the maintenance of different devices, Dr. Martin Ihrig for many constructive scientific discussions and his overall support, Grit Häuschen for the synthesis of several powders, Dr. Melanie Rosen for her help with the polymer infiltration, Dr. Daniel Grüner for the infiltrated cross-section analysis, Dr. Yoo Jung Sohn for her XRD analysis, Dr. Christian Schwab for his TOF-SIMS analysis, Dr. Markus Mann for his CCD measurements, Linda Charlotte Hoff for the absorption measurements and the laser sintering experiments, Dr. Christian Vedder for his support with the laser sintering process, Dr. Kwangnam Kim, Dr. Liwen F. Wan, and Dr. Brandon C. Wood for their molecular dynamics simulations, Dr. Alexandra C. Moy, and Prof. Dr. Jeff Sakamoto for their EBSD measurements, Dr. Shi-Kai Jiang, Chia-Yu Chang, and Prof. Dr. Bing Joe Hwang for their XPS measurements, and Michael Gregory Danner, and Prof. Dr. Eric Wachsman for their ALD coating experiments.

My office colleagues in the room 152 deserve my thanks for the exceptionally warm and supportive working atmosphere. Therefore, I want to thank Jens Igel, Alexander Schwiers, Dr. Christoph Dommann, and Dr. Markus Wolf.

I also want to thank many members of the battery department in the IEK-1 for the constantly kind, helpful and very constructive working atmosphere. Many thanks for their support with different methods, processes, scientific questions and joint works to Dr. Michael Küpers, Dr. Christoph Roitzheim, Dr. Ruijie Ye, Yannic Collette, Gerald Dück, Philipp Hecker, Dr. Jana Joeris, Vivien Kiyek, Tobias Lammert, Dr. Chih-Long Tsai, Volker Bader, Dr. Monika Bhardwaj, Dr. Enkhtsetseg Dashjav, Dr. Qianli Ma, Dr. Aikai Yang, Marie-Theres Gerhards, Kaouther Nahr El Touidjine, Dr. Frank Tietz, and Tobias Cohnen.

I am also grateful to many colleagues from other departments at the IEK-1. Therefore, I also would like to thank Dr. Moritz Kindelmann, Prof. Dr. Wolfgang Rheinheimer, Julian Ebert, Werner Herzhof, Mark Kappertz, Michael Xhonneux, Dr. Wendelin Deibert, Jörn Faul, Prof. Dr. Payam Kaghazchi, Dr. Christian Lenser, Yvonne Lichtenfeld, Irmgard Mingers, Dr. Jochen Fiebig, Karl-Heinz Rauwald, Leo Riem, Sigrid Schwartz-Lückge, Andrea Hilgers, Erhan Sucuoglu, Annika Seifert, Dr. Doris Sebold, Vicky Tirtey, and Stefan Weitz.

I also want to thank my project partners Linda Charlotte Hoff, Ah-Ram Seok, Dr. Ralph Dietmar Otterstedt, and Dr. Julian Neises for their constructive and close cooperation in the first years of my doctoral thesis.

I also want to thank my family, partner, and friends.

I would especially like to thank my family, from whom I have constantly received great support, which I greatly appreciate.

My partner Lena Ludwig supported me a lot during my doctoral thesis and especially during the preparation time for the exam, for which I am very grateful.

I would also like to thank my friends for their constant motivation throughout my time as a doctoral student.

Band / Volume 609
Mechanisches Verhalten von Polymer-Elektrolyt-Membran-Elektrolysezellen und -Stacks
S. Holtwerth (2023), x, 251 pp
ISBN: 978-3-95806-697-7

Band / Volume 610
Membrane Reactor Concepts for Power-to-Fuel Processes
H. Huang (2023), VI, 197 pp
ISBN: 978-3-95806-703-5

Band / Volume 611
Deployment of Fuel Cell Vehicles in Road Transport and the Expansion of the Hydrogen Refueling Station Network: 2023 Update
R. C. Samsun, M. Rex (2023), i, 39 pp
ISBN: 978-3-95806-704-2

Band / Volume 612
Behavior/performance of tungsten as a wall material for fusion reactors
M. Gago (2023), X, 120 pp
ISBN: 978-3-95806-707-3

Band / Volume 613
Strategieentwicklung zur Umsetzung der Klimaschutzziele im Verkehrssektor mit dem Fokus Kraftstoffe
M. Decker (2023), ix, 243 pp
ISBN: 978-3-95806-714-1

Band / Volume 614
Joining of tungsten and steel for the first wall of a future fusion reactor
V. Ganesh (2023), xxx, 142, a-v pp
ISBN: 978-3-95806-715-8

Band / Volume 615
Polluter group specific emission optimisation for regional air quality analyses using four-dimensional variational data assimilation
P. M. Backes (2023), xxi, 115 pp
ISBN: 978-3-95806-717-2

Band / Volume 616
Effect of organic soil amendments on increasing soil N retention and reducing N losses from agricultural soils
Z. Li (2023), XI, 134 pp
ISBN: 978-3-95806-721-9

Band / Volume 617
Radiolytic Stability of BTBP-, BTPhen- and DGA-based Ligands for the Selective Actinide Separation by Solvent Extraction
H. Schmidt (2023), ca. 200 pp
ISBN: 978-3-95806-723-3

Band / Volume 618
$Na_5YSi_4O_{12}$-type Na^+ superionic conductors for solid-state batteries
A. Yang (2023), X, 150 pp
ISBN: 978-3-95806-731-8

Band / Volume 619
Development of industry-scalable processes for nanocrystalline silicon oxide in silicon heterojunction solar cells
D. Qiu (2023), 202 pp
ISBN: 978-3-95806-734-9

Band / Volume 620
Photonic Sintering of Garnet-Based Solid-State Batteries
W. S. Scheld (2024), XII, 153 pp
ISBN: 978-3-95806-737-0

Weitere ***Schriften des Verlags im Forschungszentrum Jülich*** unter
http://wwwzb1.fz-juelich.de/verlagextern1/index.asp

Energie & Umwelt / Energy & Environment
Band / Volume 620
ISBN 978-3-95806-737-0

Mitglied der Helmholtz-Gemeinschaft

JÜLICH
Forschungszentrum